

論文 / 著書情報
Article / Book Information

題目(和文)	
Title(English)	Electron transport and near-edge X-ray absorption fine structure study on the effect of structural defects on the electronic structure of graphene
著者(和文)	工藤泰彦
Author(English)	Yasuhiko Kudo
出典(和文)	学位:博士(理学), 学位授与機関:東京工業大学, 報告番号:甲第9383号, 授与年月日:2014年3月26日, 学位の種別:課程博士, 審査員:木口 学,河内 宣之,腰原 伸也,森 健彦,河合 明雄,榎 敏明
Citation(English)	Degree:Doctor (Science), Conferring organization: Tokyo Institute of Technology, Report number:甲第9383号, Conferred date:2014/3/26, Degree Type:Course doctor, Examiner:,,,,,
学位種別(和文)	博士論文
Type(English)	Doctoral Thesis

A Thesis

**Electron Transport And
Near-Edge X-ray Absorption Fine Structure Study On
The Effect Of Structural Defects On
The Electronic Structure Of Graphene**

Submitted to Tokyo Institute of Technology
for a Degree of Doctor of Science

By Yasuhiko Kudo

Department of Chemistry
Graduate School of Science and Engineering
Tokyo Institute of Technology

Supervised by Professor Dr. Manabu Kiguchi

Acknowledgments

This thesis has been executed under the supervision of Professor Emeritus Dr. Toshiaki Enoki and Professor Dr. Manabu Kiguchi. The author would like to express to the supervisors his deepest gratitude for plenty of immeasurably fruitful discussion, advices, instructions, supports, and encouragements.

The author is sincerely grateful to Associate Professor Dr. Kazuyuki Takai in Hosei University, who was previously Assistant Professor of Enoki–Kiguchi laboratory, for his tireless encouragements, significant discussion and advices, and instructions of experimental techniques.

The author would like to considerably thank Dr. Ken-ichi Sakai (University of Tokyo), Assistant Professor Dr. Kazumichi Yokota (Osaka University), Assistant Professor Dr. Yoshikazu Ito (Tohoku University), Dr. V. L. Joseph Joly, Dr. Si-Jia Hao (Tsinghua University), Dr. Yoshiaki Sato (RIKEN), who all previously belonged to Enoki–Kiguchi laboratory, for their greatest coaching and encouragements.

The author would like to thank Prof. Dr. Chuhei Ohshima (Waseda University) and Dr. Genki Odahara for the instruction and advices on chemical preparation of graphene.

The author would like to thank Prof. Dr. Koichi Kusakabe (Osaka University), Prof. Dr. Isao Maruyama (Fukuoka Institute of Technology) and Mr. Gagus Ketut Sunnardianto (Osaka University) for fruitful discussion and suggestions on the electron transport characteristics of hydrogenated graphene from the theoretical point of view.

The author would like to thank Prof. Dr. Kiyoyuki Terakura (Tokyo Institute of Technology) and Dr. Zhufeng Hou (Tokyo Institute of Technology) for fruitful discussion on the X-ray absorption spectroscopy of Ar⁺-irradiated graphite.

The author would like to thank Prof. Dr. Kenta Amemiya (KEK) for kind assistance and advices on X-ray absorption spectroscopy measurements.

Ultimately, the author cannot thank enough Mr. Yu Ishibashi, Mr. Takuya Takahashi, Mr. Yuki Hosoda, Mr. Takanori Mori, Ms. Kaori Sugii, Ms. Tomoka Nakazumi, Mr. Maxim Ziatdinov, Mr. Satoshi Kaneko, Mr. Ryuji Matsushita, Mr. Jun-ichi Takashiro, and all the other colleagues in Enoki–Kiguchi laboratory for encouragements and unforgettably joyful days.

Yasuhiko Kudo
Tokyo, February 2013.

A list of publications

1. Original papers

- 1.1 Yasuhiko Kudo, Kazuyuki Takai, and Toshiaki Enoki, Electron transport properties of graphene with charged impurities and vacancy defects, *Journal of Materials Research* **28**, 1097–1104 (2013).
- 1.2 Yasuhiko Kudo, Manabu Kiguchi, Jun-ichi Takashiro, Kazuyuki Takai, and Toshiaki Enoki, Development of edge state on graphite surface induced by Ar⁺ irradiation studied using near-edge X-ray absorption fine structure spectroscopy, *Carbon*, *in press* (2014), <http://dx.doi.org/10.1016/j.carbon.2014.01.067>
- 1.3 Kazumichi Yokota, Kazuyuki Takai, Yasuhiko Kudo, Yoshiaki Sato, and Toshiaki Enoki, Polaron coupling in graphene field effect transistors on patterned self-assembled monolayer, *Physical Chemistry Chemical Physics*, *in press* (2014).
- 1.4 Jun-ichi Takashiro, Yasuhiko Kudo, Satoshi Kaneko, Kazuyuki Takai, Manabu Kiguchi, Toshiaki Enoki, Takafumi Ishii, and Takashi Kyotani, Heat treatment effect on the electronic and magnetic structures of nanographene sheets investigated with electron spectroscopy and conductance measurements, *accepted for Physical Chemistry Chemical Physics* (2014).
- 1.5 Jun-ichi Takashiro, Yasuhiko Kudo, Si-Jia Hao, Kazuyuki Takai, Manabu Kiguchi, Toshiaki Enoki, *et al.*, Preferential oxidation-induced etching of zigzag edge on nanographene, *in preparation*.

*1.1 and 1.2 are on the scope of this thesis.

Yasuhiko Kudo, Kazuyuki Takai, and Toshiaki Enoki (2013). Electron transport properties of graphene with charged impurities and vacancy defects. *Journal of Materials Research*, 28, pp. 1097–1104 Copyright © Materials Research Society 2013, reproduced with permission.

Reprinted from *Carbon*, Yasuhiko Kudo, Manabu Kiguchi, Jun-ichi Takashiro, Kazuyuki Takai, and Toshiaki Enoki, Development of edge state on graphite surface induced by Ar⁺ irradiation studied using near-edge X-ray absorption fine structure spectroscopy (<http://dx.doi.org/10.1016/j.carbon.2014.01.067>), Copyright (2014), with permission from Elsevier.

A list of presentations

1. International conferences

- 1.1 Yasuhiko Kudo, Yasuhiro Nishimura, Kazuyuki Takai, and Toshiaki Enoki, Electron transport properties of anti-dot graphene, International School and Symposium on Multifunctional Molecule-based Materials, Argonne National Laboratory, USA, March 2011 (Poster presentation).
- 1.2 Yasuhiko Kudo, Kazuyuki Takai, Toshiaki Enoki, Gagus Ketut Sunnardianto, Isao Maruyama, and Koichi Kusakabe, Transport properties of graphene with hydrogenated atomic vacancies, 5th International Conference on Recent Progress in Graphene Research, Tokyo Institute of Technology, Japan, September 2013 (Oral presentation).
- 1.3 Gagus Ketut Sunnardianto, Isao Maruyama, Koichi Kusakabe, Yasuhiko Kudo, Kazuyuki Takai, and Toshiaki Enoki, Curious structure dependence of charge distribution and localized electron modes in hydrogenated graphene and hydrogenated graphene vacancy, 5th International Conference on Recent Progress in Graphene Research, Tokyo Institute of Technology, Japan, September 2013 (Poster presentation).
- 1.4 Yasuhiko Kudo, Kazuyuki Takai, Manabu Kiguchi, Toshiaki Enoki, Gagus Ketut Sunnardianto, Isao Maruyama, and Koichi Kusakabe, Chemical modification of graphene with atomic vacancies, International School and Symposium on Molecular Materials, Tokyo Institute of Technology, Japan, November 2013 (Short-oral and poster presentations).

2. Domestic conferences

- 2.1 工藤泰彦, 西村康寛, 高井和之, 榎敏明, 微細構造グラフェンの電子輸送特性と端効果, 日本物理学会 2010 年秋季大会, 大阪府立大学(大阪), 2010 年 9 月 (口頭発表).
- 2.2 工藤泰彦, 高井和之, 榎敏明, ナノスケール微細構造を有するグラフェンの磁気輸送特性, 配列ナノ空間を利用した新物質科学ユビキタス元素戦略第 4 回若手研究会, 東北大学(宮城), 2011 年 7 月 (ポスター発表).
- 2.3 工藤泰彦, 高井和之, 榎敏明, 欠陥をもつグラフェンの作製とその電子輸送物性, 日本物理学会第 67 回年次大会, 関西学院大学(兵庫), 2012 年 3 月 (口頭発表).
- 2.4 工藤泰彦, 高井和之, 榎敏明, Gagus Ketut Sunnardianto, 丸山勲, 草部浩一, グラフェンの伝導における格子欠陥の化学修飾効果, 日本物理学会第 68 回年次大会, 広島大学(広島), 2013 年 3 月 (口頭発表).
- 2.5 Gagus Ketut Sunnardianto, 丸山勲, 草部浩一, 工藤泰彦, 高井和之, 榎敏明, Electronic state calculation for hydrogenated graphene with atomic vacancy, 日本物理学会第 68 回年次大会, 広島大学(広島), 2013 年 3 月 (口頭発表).
- 2.6 Gagus Ketut Sunnardianto, 森下直樹, 丸山勲, 草部浩一, 工藤泰彦, 高井和之, 榎敏明, Charge distribution of hydrogenated graphene with a vacancy, 日本物理学会 2013 年秋季大会, 徳島大学(徳島), 2013 年 9 月 (口頭発表).

Table of contents

Chapter 1	General introduction	1
	References in Chapter 1	6
Chapter 2	The fundamentals of graphene	9
2.1	Electronic structure of graphene	9
2.1.1	Single-layer graphene	9
2.1.2	Bilayer graphene	13
2.1.3	Multilayer graphene	15
2.2	Transport in graphene	19
2.2.1	Classical basis	19
2.2.2	Boltzmann's transport equation	21
2.2.3	Graphene	28
2.2.4	Presence of magnetic field	29
2.2.5	Charged impurity scattering in graphene	32
2.2.6	Lattice defect scattering in graphene	34
2.3	Nanographene	36
2.3.1	Geometrical structure of nanographene	36
2.3.2	Chemical and physical aspects of edge state in nanographene	37
2.3.3	Electronic structures of zigzag and armchair graphene nanoribbons	40
2.4	Figures in Chapter 2	47
	References in Chapter 2	65
Chapter 3	Experimental developments in graphene researches	67
3.1	Fabrication techniques of graphene	67
3.1.1	Micromechanical exfoliation of graphite	67
3.1.2	Chemical vapor deposition	68
3.1.3	Thermal decomposition of silicon carbide substrate	70
3.2	Determination of the thickness of graphene	71
3.2.1	Optical microscopy	71

3.2.2 Raman spectroscopy.....	73
3.3 Raman spectroscopy in graphene.....	75
3.4 Electron transport in graphene.....	78
3.4.1 Quantum Hall effect in graphene.....	79
3.4.2 High carrier mobility and electron scattering sources in graphene.....	79
3.4.3 Vacancies in graphene as sources of localized spins.....	83
3.4.4 Weak localization effect in graphene.....	84
3.5 Nanographene.....	87
3.5.1 Fabrication techniques of nano-structured graphene.....	87
3.5.2 Observation of the edge state by scanning tunneling microscope.....	89
3.5.3 X-ray absorption spectroscopy.....	90
3.5.4 Magnetic susceptibility originating from edges of nanographene.....	91
3.5.5 Chemical modification of the edge states.....	93
3.6 Scope of this thesis.....	95
3.7 Figures in Chapter 3.....	99
References in Chapter 3.....	132

Chapter 4 Electron scattering sources in antidot graphene and Ar⁺-irradiated graphene.....	146
4.1 Introduction.....	146
4.2 Experimental.....	147
4.3 Results.....	148
4.4 Discussion.....	150
4.4.1. Electron transport without magnetic field.....	150
4.4.2. Magnetoresistance at high magnetic fields.....	152
4.4.3. Magnetoresistance at low magnetic fields.....	153
4.5 Conclusions.....	155
4.6 Complement.....	157
4.7 Figures in Chapter 4.....	158
References in Chapter 4.....	169

Chapter 5 Near-edge X-ray absorption fine structure study of the edge state on Ar⁺-irradiated graphite surface.....	173
5.1 Introduction.....	173

5.2 Experimental	175
5.3 Results	176
5.4 Discussion	179
5.5 Conclusions	183
5.6 Figures in Chapter 5	184
References in Chapter 5	193
Chapter 6 Electron transport study on hydrogen adsorption effect at vacancies in graphene	198
6.1 Introduction	198
6.2 Experimental	201
6.3 Results and discussion	202
6.3.1 Atomic hydrogen exposure to graphene having atomic vacancies	202
6.3.2 Gate-controlled adsorption of hydrogen molecule on graphene	203
6.3.3 Hydrogen molecule exposure to graphene having atomic vacancies	207
6.4 Conclusions	209
6.5 Figures in Chapter 6	210
References in Chapter 6	222
Chapter 7 General conclusions	225
References in Chapter 7	232

Chapter 1

General introduction

It is arrangement of atoms that gives to a substance its characteristic properties. The idea of atom occurred a long time ago. It is said that the Greek philosopher Democritus stated the universe is composed of vacuum and atoms. This statement of Democritus was purely based on his speculation and it was not practical. Then, it was in the beginning of the 19th century that the English chemist J. Dalton hypothesized all substances consist of several different kinds of small particles, called atoms. Dalton succeeded to explain the law of conservation of mass, which was investigated by A. L. Lavoisier, and the law of constant proportions, which was found by J. L. Proust. Moreover, Dalton stated the law of multiple proportions based on his studies. Followed by experimental confirmations of this law, the atomic theory of Dalton was accepted. Dalton's discovery can be regarded as the root of contemporary knowledge on atoms. Thus, Dalton's atomic theory appears to be one of the most priceless accomplishments in a long history of science. Nowadays, we take for granted the existence of atoms thanks to all the former scientists. Since the existence of atoms was verified, one of the dreams that scientists have has been to control arbitrarily the arrangements of various atoms and molecules for creating various substances. Controlling arrangement of atoms in a molecule is mainly performed via chemical reactions. Specific parts in a molecule, which are called as functional groups, can give functions to the molecule. Increasing the number of atoms that participate in the composition of a substance makes usually problems further more complicated, except for the case that regularity exists. One of large-number limits is crystalline substances. In the crystalline state of solids, atoms are arranged in a pattern that repeats itself periodically. Therefore, it is the periodicity of arrangement of the atoms in a crystal that gives rise to the characteristic properties of the crystal.

For a long time, it had been believed that only three-dimensional periodicity is allowed to exist stably, and that a crystalline state having one- or two-dimensional long-range order can be spontaneously broken. Therefore, it was immeasurably surprising that a two-dimensional single layer of graphite can be isolated with a macroscopic size. The

single layer of graphite is now commonly known as graphene. It was A. K. Geim and K. S. Novoselov who succeeded to isolate micrometer-scale flakes of graphene and demonstrated experimental investigations on its electronic properties [1,2]. For their ground breaking experiments regarding the two-dimensional material graphene, the Nobel Prize in Physics was awarded to Geim and Novoselov in 2010. In addition to the stable existence of a two-dimensional graphene, the technique of isolation was again surprising because it was just to exfoliate graphite with adhesive tape and to put it onto a silicon substrate. The impacts brought by Geim and Novoselov caused explosive developments of experimental studies on graphene and stimulated studies on other two-dimensional materials [3–6] such as MoS₂ [7,8] and WS₂ [9].

Graphene is composed of carbon atoms arranged in the two-dimensional honeycomb network. Carbon is the primal element for life. Four valence electrons of a carbon atom give itself the flexible capability for the formation of covalent bonds with various configurations. The enormous diversity of organic compounds is based on this flexibility. A large number of experiments has been performed to understand chemical bonds of carbon. The development of the theory of hybrid bond orbitals around 1930 was of particular excellence. According to this theory, we can understand typical sp^1 -, sp^2 -, and sp^3 -hybridized configurations of carbon and other atoms. Carbon has many allotropes. An allotrope composed by the sp^3 -hybridized carbons is well known as diamond. Another allotrope composed by the sp^1 carbons is called as carbyne [10]. Then, carbon atoms having the sp^2 -hybridized configuration can exist in several forms, *i.e.*, graphite, fullerene [11], nanotube [12], and graphene. Among these sp^2 -carbon allotropes, graphene should be regarded as the particularly important form because the other sp^2 allotropes can be formed by graphene as a fullerene, a nanotube, and a graphite are a wrapped, a rolled, and a stacked graphene, respectively [13]. Therefore, the periodicities of the arrangement of the sp^2 -hybridized carbon atoms in the crystals of these allotropes that give rise to the characteristic properties of themselves are considered to be based on that of graphene.

The crystal structure of graphite was first investigated by J. D. Bernal [14]. In a single sheet of graphite, one carbon atom with four valence electrons has the sp^2 -hybridized configuration, in which three electrons are used to form sp^2 - σ bonds with other three carbon atoms building a honeycomb-arranged plane, so that the other valence electron occupies the $2p_z$ orbital perpendicular to the plane. The overlap among the $2p_z$ orbitals

gives rise to the formation of π network spreading in the entire honeycomb lattice of graphene. Therefore, the electronic structure near the Fermi energy is characterized by these $2p_z$ orbitals of the carbon atoms. The first study on the electronic energy-band structure of a single sheet of graphite was reported by P. R. Wallace in 1947 [15]. It was found that the single sheet can be a semimetal with unusual linear dispersion. During the following years, the study of graphite resulted in the Slonczewski–Weiss–McClure band structure of graphite, which provided a nice description of the electronic properties in graphite [16,17]. This model was followed by correction of the assignments of the electron and the hole states by P. R. Schroeder *et al.* [18]. Thus, the currently accepted electronic structure of graphite was established. It can be viewed that the consideration on the electronic structure of graphene appeared as just a starting point for understanding graphite, probably because graphene was unlikely to exist at that time [19].

The electronic energy in single-layer graphene is linearly dependent of the electronic momentum in the vicinity of the Fermi energy as given by $\varepsilon = \pm v_F p$, where ε is the energy, v_F is the Fermi velocity, and p is the momentum [20], in contrast to the parabolic band structure in conventional two-dimensional electronic systems written as $\varepsilon = p^2 / 2m$, where m is the mass of electron. In other words, it is frequently said that electrons in single-layer graphene follows the relativistic massless Dirac equation in the vicinity of the Fermi energy. This peculiarity originates from the two-dimensional honeycomb bipartite lattice of graphene. The valence and the conduction bands touches each other at zero-energy point, which is called as the Dirac point. The fact that electrons in single-layer graphene are like Dirac fermions has been experimentally evidenced by the observation of anomalous quantum Hall effect [2,21] immediately after the successful isolation of graphene by mechanical cleavage, and by the following angle-resolved photoemission spectroscopy measurements [22] and scanning tunneling spectroscopy measurements [23].

The case that an infinite sheet of graphene is cut into nanometer-scale fragments had been considered prior to the isolation of graphene [24,25]. Such small fragments of graphene, namely nanographene, must have edges. Edges of graphene can be classified into two types of atomic structures, *i.e.*, zigzag- and armchair-shaped arrangements. Theoretical studies [24,25] stated that a non-bonding π electronic state called as the edge state exists at the vicinity of zigzag-shaped edges. The edge state has been experimentally

evidenced utilizing scanning tunneling microscope [26,27]. Besides magnetic properties originating from localized electronic spins of the edge state have been investigated employing nanographite-based materials in terms of magnetic susceptibility [28], near-edge X-ray absorption fine structure [29,30], and so on. Recently the interests in the subjects of the edge state in a single sheet of graphene have appeared to be increasing. One of triggers is the observation of Kondo effect in defective single-layer graphene that evidences the presence of localized spins [31], of which the origin is expected to be the edge state.

More interestingly, edges of graphene give rise to the chances of coupling the unique physics of graphene with chemistry via adding various functional groups. From the point of view of chemistry, the other sp^2 -carbon allotropes, graphite, fullerene, and nanotube, are capable of accommodating guest species into their nano-spaces, *i.e.*, small spaces between the layers of graphite, the inside of a fullerene or a nanotube, resulting in distinct characteristics. Such host–guest interactions have been addressed also in graphene for example in terms of molecular adsorptions on the surface of graphene [32,33]. On the other hand, as another road to chemical modification of graphene, functionalization of graphene edges is hopeful regarding potential applications as well as fundamentals because it would achieve the coexistence of the unconventional electronic behaviors in graphene with magnetic properties arising from edges and their modifications [28,34].

Motivated by above descriptions, the studies in this thesis have highlighted the evolution in the electronic structure of graphene upon the introduction of edges. Several techniques for the introduction of edges into macroscopic graphene flakes can be considered, for example nanofabrications. However, it is not always true that the edge state emerges at edges introduced into a graphene sheet. Moreover, experimental information on whether electronic phenomena originating from edges in a graphene sheet are observable or not is lacking. Accordingly, it needs to be confirmed that such phenomena can be observed, and that the edge state exists at the edges. In addition, chemical structures around the edges should be precisely controlled. These issues are addressed in this thesis. This thesis is based on the following papers: Y. Kudo, K. Takai, and T. Enoki, Electron transport properties of graphene with charged impurities and vacancy defects, *Journal of Materials Research* **28**, 1097 (2013); Y. Kudo, M. Kiguchi, J. Takashiro, K. Takai, and T. Enoki, Development of edge state on graphite surface

induced by Ar^+ irradiation studied using near-edge X-ray absorption fine structure spectroscopy, *Carbon*, *in press* (2014), (<http://dx.doi.org/10.1016/j.carbon.2014.01.067>). In addition, the author has been contributed to the following works: K. Yokota, K. Takai, Y. Kudo, Y. Sato, and T. Enoki, Polaron coupling in graphene field effect transistors on patterned self-assembled monolayer, *Phys. Chem. Chem. Phys.*, *in press* (2014); J. Takashiro, Y. Kudo, S. Kaneko, K. Takai, M. Kiguchi, T. Enoki, T. Ishii, and T. Kyotani, Heat treatment effect on the electronic and magnetic structures of nanographene sheets investigated with electron spectroscopy and conductance measurements, *accepted for Phys. Chem. Chem. Phys.* (2014); J. Takashiro, Y. Kudo, S. J. Hao, K. Takai, M. Kiguchi, T. Enoki, *et al.*, Preferential oxidation-induced etching of zigzag edge on nanographene, *in preparation*.

References in Chapter 1

- [1] K. S. Novoselov, A. K. Geim, S. V. Morozov, D. Jiang, Y. Zhang, S. V. Dubonos, I. V. Grigorieva, and A. A. Firsov, Electric field effect in atomically thin carbon films, *Science* **306**, 666 (2004).
- [2] K. S. Novoselov, A. K. Geim, S. V. Morozov, D. Jiang, M. I. Katsnelson, I. V. Grigorieva, S. V. Dubonos, and A. A. Firsov, Two-dimensional gas of massless Dirac fermions in graphene, *Nature* **438**, 197 (2005).
- [3] R. Mas-Ballesté, C. Gómez-Navarro, J. Gómez-Herrero, and F. Zamora, 2D materials: to graphene and beyond, *Nanoscale* **3**, 20 (2011).
- [4] M. Osada and T. Sasaki, Two-dimensional dielectric nanosheets: novel nanoelectronics from nanocrystal building blocks, *Adv. Mater.* **24**, 210 (2012).
- [5] Q. H. Wang, K. Kalantar-Zadeh, A. Kis, J. N. Coleman, and M. S. Strano, Electronics and optoelectronics of two-dimensional transition metal dichalcogenides, *Nat. Nanotechnol.* **7**, 699 (2012).
- [6] M. Xu, T. Liang, M. Shi, and H. Chen, Graphene-like two-dimensional materials, *Chem. Rev.* **113**, 3766 (2013).
- [7] B. Radisavljevic, A. Radenovic, J. Brivio, V. Giacometti, and A. Kis, Single-layer MoS₂ transistors, *Nat. Nanotechnol.* **6**, 147 (2011).
- [8] M. S. Fuhrer and J. Hone, Measurement of mobility in dual-gated MoS₂ transistors, *Nat. Nanotechnol.* **8**, 146 (2013).
- [9] L. Britnell, R. M. Ribeiro, A. Eckmann, R. Jalil, B. D. Belle, A. Mishchenko, Y. J. Kim, R. V. Gorbachev, T. Georgiou, S. V. Morozov, A. N. Grigorenko, A. K. Geim, C. Casiraghi, A. H. Castro Neto, and K. S. Novoselov, Strong light-matter interactions in heterostructures of atomically thin films, *Science* **340**, 1311 (2013).
- [10] M. Liu, V. I. Artyukhov, H. Lee, F. Xu, and B. I. Yakobson, Carbyne from first principles: chain of C atoms, a nanorod or a nanorope, *ACS Nano* **7**, 10075 (2013).
- [11] H. W. Kroto, J. R. Heath, S. C. O'Brien, R. F. Curl, and R. E. Smalley, C₆₀: Buckminsterfullerene, *Nature* **318**, 162 (1985).
- [12] S. Iijima, Helical microtubules of graphitic carbon, *Nature* **354**, 56 (1991).
- [13] A. K. Geim and K. S. Novoselov, The rise of graphene, *Nat. Mater.* **6**, 183 (2007).
- [14] J. D. Bernal, The structure of graphite, *Proc. Roy. Soc. A* **106**, 749 (1924).
- [15] P. R. Wallace, The band theory of graphite, *Phys. Rev.* **71**, 622 (1947).

- [16] J. W. McClure, Band structure of graphite and de Haas-van Alphen Effect, *Phys. Rev.* **108**, 612 (1957).
- [17] J. C. Slonczewski and P. R. Weiss, Band structure of graphite, *Phys. Rev.* **109**, 272 (1958).
- [18] P. R. Schroeder, M. S. Dresselhaus, and A. Javan, Location of electron and hole carriers in graphite from laser magnetoreflexion data, *Phys. Rev. Lett.* **20**, 1292 (1968).
- [19] N. D. Mermin, Crystalline order in two dimensions, *Phys. Rev.* **176**, 250 (1968).
- [20] A. H. Castro Neto, F. Guinea, N. M. R. Peres, K. S. Novoselov, and A. K. Geim, The electronic properties of graphene, *Rev. Mod. Phys.* **81**, 109 (2009).
- [21] Y. Zhang, Y. W. Tan, H. L. Stormer, and P. Kim, Experimental observation of the quantum Hall effect and Berry's phase in graphene, *Nature* **438**, 201 (2005).
- [22] A. Bostwick, T. Ohta, T. Seyller, K. Horn, and E. Rotenberg, Quasiparticle dynamics in graphene, *Nat. Phys.* **3**, 36 (2007).
- [23] D. L. Miller, K. D. Kubista, G. M. Rutter, M. Ruan, W. A. de Heer, P. N. First, and J. A. Stroscio, Observing the quantization of zero mass carriers in graphene, *Science* **324**, 924 (2009).
- [24] M. Fujita, K. Wakabayashi, K. Nakada, and K. Kusakabe, Peculiar localized state at zigzag graphite edge, *J. Phys. Soc. Jpn.* **65**, 1920 (1996).
- [25] K. Nakada, M. Fujita, G. Dresselhaus, and M. S. Dresselhaus, Edge state in graphene ribbons: nanometer size effect and edge shape dependence, *Phys. Rev. B* **54**, 17954 (1996).
- [26] Y. Kobayashi, K. Fukui, T. Enoki, K. Kusakabe, and Y. Kaburagi, Observation of zigzag and armchair edges of graphite using scanning tunneling microscopy and spectroscopy, *Phys. Rev. B* **71**, 193406 (2005).
- [27] Y. Niimi, T. Matsui, H. Kambara, K. Tagami, M. Tsukada, and H. Fukuyama, Scanning tunneling microscopy and spectroscopy studies of graphite edges, *Appl. Surf. Sci.* **241**, 43 (2005).
- [28] T. Enoki and K. Takai, The edge state of nanographene and the magnetism of the edge-state spins, *Solid State Commun.* **149**, 1144 (2009).
- [29] V. L. J. Joly, M. Kiguchi, S. J. Hao, K. Takai, T. Enoki, R. Sumii, K. Amemiya, H. Muramatsu, T. Hayashi, Y. A. Kim, M. Endo, J. C. Delgado, F. L. Urías, A. B.

- Méndez, H. Terrones, M. Terrones, and M. S. Dresselhaus, Observation of magnetic edge state in graphene nanoribbons, *Phys. Rev. B* **81**, 245428 (2010).
- [30] M. Kiguchi, K. Takai, V. L. J. Joly, T. Enoki, R. Sumii, and K. Amemiya, Magnetic edge state and dangling bond state of nanographene in activated carbon fibers, *Phys. Rev. B* **84**, 045421 (2011).
- [31] J. H. Chen, L. Li, W. G. Cullen, E. D. Williams, and M. S. Fuhrer, Tunable Kondo effect in graphene with defects, *Nat. Phys.* **7**, 535 (2011).
- [32] F. Schedin, A. K. Geim, S. V. Morozov, E. W. Hill, P. Blake, M. I. Katsnelson, and K. S. Novoselov, Detection of individual gas molecules adsorbed on graphene, *Nat. Mater.* **6**, 652 (2007).
- [33] Y. Sato, K. Takai, and T. Enoki, Electrically controlled adsorption of oxygen in bilayer graphene devices, *Nano Lett.* **11**, 3468 (2011).
- [34] K. Kusakabe and M. Maruyama, Magnetic nanographite, *Phys. Rev. B* **67**, 092406 (2003).

Chapter 2

The fundamentals of graphene

2.1 Electronic structure of graphene

2.1.1 Single-layer graphene

The crystal structure of graphite was first investigated by J. D. Bernal in 1924 [1]. The electronic structure of a single sheet of graphite, namely graphene, was described within tight binding approximation [2]. Figure 2.1 shows the honeycomb structure of the single-layer graphene and the first Brillouin zone. The unit cell of the single-layer graphene can be defined as indicated in Fig. 2.1a. Two inequivalent carbon atoms that are labeled as A and B sublattices are included in the unit cell. Two primitive lattice vectors \mathbf{a} and \mathbf{b} are given by

$$\begin{aligned}\mathbf{a} &= a(1, 0), \\ \mathbf{b} &= a\left(-\frac{1}{2}, \frac{\sqrt{3}}{2}\right).\end{aligned}\quad \cdots(2.1)$$

Here, a is the lattice constant given by 2.46 \AA [3–5], which is related to the bond length between adjacent carbon atoms $a_0 = 1.42 \text{ \AA}$ as $a = \sqrt{3}a_0$. The vectors connecting the nearest neighbor carbon atoms $\boldsymbol{\tau}_l$ ($l = 1, 2, 3$) are defined as

$$\begin{aligned}\boldsymbol{\tau}_1 &= a\left(0, \frac{1}{\sqrt{3}}\right), \\ \boldsymbol{\tau}_2 &= a\left(-\frac{1}{2}, -\frac{1}{2\sqrt{3}}\right), \\ \boldsymbol{\tau}_3 &= a\left(\frac{1}{2}, -\frac{1}{2\sqrt{3}}\right).\end{aligned}\quad \cdots(2.2)$$

The primitive reciprocal lattice vectors \mathbf{a}^* and \mathbf{b}^* are given by the followings.

$$\begin{aligned}\mathbf{a}^* &= \frac{2\pi}{a}\left(1, \frac{1}{\sqrt{3}}\right), \\ \mathbf{b}^* &= \frac{2\pi}{a}\left(0, \frac{2}{\sqrt{3}}\right).\end{aligned}\quad \cdots(2.3)$$

The hexagonal first Brillouin zone is shown in Fig. 2.1b. The corners of the Brillouin zone are labeled as two inequivalent \mathbf{K} and \mathbf{K}' points, which are given by,

$$\begin{aligned}\mathbf{K} &= \frac{2\pi}{a} \left(\frac{1}{3}, \frac{1}{\sqrt{3}} \right), \frac{2\pi}{a} \left(\frac{1}{3}, -\frac{1}{\sqrt{3}} \right), \frac{2\pi}{a} \left(-\frac{2}{3}, 0 \right), \\ \mathbf{K}' &= \frac{2\pi}{a} \left(-\frac{1}{3}, -\frac{1}{\sqrt{3}} \right), \frac{2\pi}{a} \left(-\frac{1}{3}, \frac{1}{\sqrt{3}} \right), \frac{2\pi}{a} \left(\frac{2}{3}, 0 \right).\end{aligned}\quad \cdots(2.4)$$

There are the following relationships between $\boldsymbol{\tau}_l$, \mathbf{K} , and \mathbf{K}' .

$$\exp(i\mathbf{K} \cdot \boldsymbol{\tau}_1) = \omega, \quad \exp(i\mathbf{K} \cdot \boldsymbol{\tau}_2) = \omega^{-1}, \quad \exp(i\mathbf{K} \cdot \boldsymbol{\tau}_3) = 1, \quad \cdots(2.5)$$

$$\exp(i\mathbf{K}' \cdot \boldsymbol{\tau}_1) = 1, \quad \exp(i\mathbf{K}' \cdot \boldsymbol{\tau}_2) = \omega^{-1}, \quad \exp(i\mathbf{K}' \cdot \boldsymbol{\tau}_3) = \omega, \quad \cdots(2.6)$$

where, $\omega = \exp(2\pi i / 3)$.

In terms of a tight-binding model [6], electronic wave function in graphene is described as

$$\Psi(\mathbf{r}) = \sum_{\mathbf{R}_A} \psi_A(\mathbf{R}_A) \phi(\mathbf{r} - \mathbf{R}_A) + \sum_{\mathbf{R}_B} \psi_B(\mathbf{R}_B) \phi(\mathbf{r} - \mathbf{R}_B). \quad \cdots(2.7)$$

Here, $\phi(\mathbf{r})$ is the wave function of the $2p_z$ orbital of a carbon atom, $\mathbf{R}_A = n_a \mathbf{a} + n_b \mathbf{b} + \boldsymbol{\tau}_1$ and $\mathbf{R}_B = n_a \mathbf{a} + n_b \mathbf{b}$ with integer n_a and n_b . The first and the second terms correspond to the Bloch waves on A and B sublattices, respectively. Defining the transfer integral between the nearest neighbor carbon atoms as $\gamma_0 \sim 3$ eV [3] and choosing the origin of energy at the carbon $2p_z$ level, we have

$$\begin{aligned}\varepsilon \psi_A(\mathbf{R}_A) &= -\gamma_0 \sum_{l=1}^3 \psi_B(\mathbf{R}_A - \boldsymbol{\tau}_l), \\ \varepsilon \psi_B(\mathbf{R}_B) &= -\gamma_0 \sum_{l=1}^3 \psi_A(\mathbf{R}_B - \boldsymbol{\tau}_l),\end{aligned}\quad \cdots(2.8)$$

where the overlap integral between the nearest carbon atoms is ignored for the simplicity. Because the wave functions $\psi_A(\mathbf{R}_A)$ and $\psi_B(\mathbf{R}_B)$ are the Bloch functions, we can assume $\psi_A(\mathbf{R}_A) \propto f_A(\mathbf{k}) \exp(i\mathbf{k} \cdot \mathbf{R}_A)$ and $\psi_B(\mathbf{R}_B) \propto f_B(\mathbf{k}) \exp(i\mathbf{k} \cdot \mathbf{R}_B)$, so that we obtain,

$$\begin{pmatrix} 0 & h_{AB}(\mathbf{k}) \\ h_{AB}(\mathbf{k})^* & 0 \end{pmatrix} \begin{pmatrix} f_A(\mathbf{k}) \\ f_B(\mathbf{k}) \end{pmatrix} = \varepsilon \begin{pmatrix} f_A(\mathbf{k}) \\ f_B(\mathbf{k}) \end{pmatrix}, \quad \cdots(2.9)$$

$$h_{AB}(\mathbf{k}) = -\gamma_0 \sum_l \exp(-i\mathbf{k} \cdot \boldsymbol{\tau}_l). \quad \cdots(2.10)$$

Thus, the dispersion relation of the electronic energy band in single-layer graphene is given by

$$\varepsilon_{\pm}(\mathbf{k}) = \pm \gamma_0 \sqrt{1 + 4 \cos\left(\frac{ak_x}{2}\right) \cos\left(\frac{\sqrt{3}ak_y}{2}\right) + 4 \cos^2\left(\frac{ak_x}{2}\right)}. \quad \cdots(2.11)$$

This energy band is plotted in Fig. 2.2. The plus and the minus signs correspond to the conduction π^* band and the valence π band, respectively. At the corners of the first Brillouin zone that are denoted as the K and the K' points, $\varepsilon_{\pm}(\mathbf{K})$ and $\varepsilon_{\pm}(\mathbf{K}')$ are equal to zero so that the valence and the conduction bands touch each other at these points. The Fermi level locates at these points so that electronic properties of graphene are mainly governed by electrons in the states near the K and the K' points. We are allowed to write in another way by using the Fermi velocity given as,

$$v_F = \frac{\sqrt{3}a\gamma_0}{2\hbar} = 1.01 \times 10^6 \text{ (m s}^{-1}\text{)}, \quad \cdots(2.12)$$

then,

$$\varepsilon_{\pm}(\mathbf{k}) = \pm \hbar v_F |\mathbf{k}|. \quad \cdots(2.13)$$

For taking a close look at the vicinity of a K point, it is convenient to replace \mathbf{k} with $\mathbf{K} + \mathbf{k}$. Equation (2.9) becomes

$$\begin{pmatrix} 0 & h_{AB}(\mathbf{k} + \mathbf{K}) \\ h_{AB}(\mathbf{k} + \mathbf{K})^* & 0 \end{pmatrix} \begin{pmatrix} f_A(\mathbf{k} + \mathbf{K}) \\ f_B(\mathbf{k} + \mathbf{K}) \end{pmatrix} = \varepsilon \begin{pmatrix} f_A(\mathbf{k} + \mathbf{K}) \\ f_B(\mathbf{k} + \mathbf{K}) \end{pmatrix}, \quad \cdots(2.14)$$

$$h_{AB}(\mathbf{k} + \mathbf{K}) = -\gamma_0 \sum_{l=1}^3 \exp[-i(\mathbf{k} + \mathbf{K}) \cdot \boldsymbol{\tau}_l]. \quad \cdots(2.15)$$

Expanding Eq. (2.13) to the first order of k_x and k_y , which are the ingredients of \mathbf{k} , we obtain the following expression.

$$\begin{aligned} h_{AB}(\mathbf{k} + \mathbf{K}) &= -\gamma_0 \left\{ \omega^{-1} \exp[-i\mathbf{k} \cdot \boldsymbol{\tau}_1] + \omega \exp[-i\mathbf{k} \cdot \boldsymbol{\tau}_2] + \exp[-i\mathbf{k} \cdot \boldsymbol{\tau}_3] \right\} \\ &= -\gamma_0 \left\{ (\omega + \omega^{-1} + 1) + (-i\mathbf{k}) \cdot (\omega^{-1}\boldsymbol{\tau}_1 + \omega\boldsymbol{\tau}_2 + \boldsymbol{\tau}_3) \right\} \\ &= \gamma_0 \frac{\sqrt{3}a}{2} \exp\left(i\frac{\pi}{6}\right) (k_x + ik_y) \\ &= \gamma \exp\left(i\frac{\pi}{6}\right) (k_x + ik_y). \end{aligned} \quad \cdots(2.16)$$

Here, $\gamma = \sqrt{3}a\gamma_0/2$. Similar procedures on $h_{AB}(\mathbf{k} + \mathbf{K})^*$ lead to

$$h_{AB}(\mathbf{k} + \mathbf{K})^* = \gamma \exp\left(i \frac{\pi}{2}\right) (k_x - ik_y). \quad \cdots(2.17)$$

Hence, Eq. (2.14) becomes

$$\begin{pmatrix} 0 & \gamma(\hat{k}_x - i\hat{k}_y) \\ \gamma(\hat{k}_x + i\hat{k}_y) & 0 \end{pmatrix} \begin{pmatrix} F_K^A(\mathbf{r}) \\ F_K^B(\mathbf{r}) \end{pmatrix} = \varepsilon \begin{pmatrix} F_K^A(\mathbf{r}) \\ F_K^B(\mathbf{r}) \end{pmatrix} \quad \cdots(2.18)$$

where $\hat{\mathbf{k}} = -i\nabla$, $F_K^i(\mathbf{r}) = (1/2\pi) \int d\mathbf{k} f_i(\mathbf{k} + \mathbf{K}) \exp(i\mathbf{k} \cdot \mathbf{r})$. Combined with similar calculation in the vicinity of a K' point, the effective Schrödinger equation is given by

$$\begin{pmatrix} 0 & \gamma(\hat{k}_x - i\hat{k}_y) & 0 & 0 \\ \gamma(\hat{k}_x + i\hat{k}_y) & 0 & 0 & 0 \\ 0 & 0 & 0 & \gamma(\hat{k}_x + i\hat{k}_y) \\ 0 & 0 & \gamma(\hat{k}_x - i\hat{k}_y) & 0 \end{pmatrix} \begin{pmatrix} F_K^A(\mathbf{r}) \\ F_K^B(\mathbf{r}) \\ F_{K'}^A(\mathbf{r}) \\ F_{K'}^B(\mathbf{r}) \end{pmatrix} = \varepsilon \begin{pmatrix} F_K^A(\mathbf{r}) \\ F_K^B(\mathbf{r}) \\ F_{K'}^A(\mathbf{r}) \\ F_{K'}^B(\mathbf{r}) \end{pmatrix}. \quad \cdots(2.19)$$

By the use of the Pauli spin matrices,

$$\sigma_x = \begin{pmatrix} 0 & 1 \\ 1 & 0 \end{pmatrix}, \sigma_y = \begin{pmatrix} 0 & -i \\ i & 0 \end{pmatrix}, \sigma_z = \begin{pmatrix} 1 & 0 \\ 0 & -1 \end{pmatrix}, \quad \cdots(2.20)$$

as $\boldsymbol{\sigma} = (\sigma_x, \sigma_y)$, the above equation is rewritten as,

$$\gamma(\boldsymbol{\sigma} \cdot \mathbf{k}) \mathbf{F}^K(\mathbf{r}) = \varepsilon \mathbf{F}^K(\mathbf{r}), \quad \cdots(2.21)$$

$$\gamma(\boldsymbol{\sigma} \cdot \mathbf{k}') \mathbf{F}^{K'}(\mathbf{r}) = \varepsilon \mathbf{F}^{K'}(\mathbf{r}), \quad \cdots(2.22)$$

$$\mathbf{F}^K(\mathbf{r}) = \begin{pmatrix} F_K^A(\mathbf{r}) \\ F_K^B(\mathbf{r}) \end{pmatrix}, \quad \mathbf{F}^{K'}(\mathbf{r}) = \begin{pmatrix} F_{K'}^A(\mathbf{r}) \\ F_{K'}^B(\mathbf{r}) \end{pmatrix}, \quad \cdots(2.23)$$

where $\hat{k}'_x = \hat{k}_x$, and $\hat{k}'_y = -\hat{k}_y$.

Equations (2.19) and (2.20) lead the energy band in the vicinity of the K and the K' points as follows

$$\varepsilon_s(\mathbf{k}) = s\gamma|\mathbf{k}|, \quad \cdots(2.24)$$

where $s = \pm 1$. $s = +1$ corresponds to the conduction band and $s = -1$ corresponds to the valence band. The density of states is given by,

$$D(\varepsilon) = \frac{g_s g_v}{L^2} \sum_{\mathbf{k}, s} \delta(\varepsilon - s\gamma |\mathbf{k}|) = \frac{g_s g_v |\varepsilon|}{2\pi\gamma^2}, \quad \dots(2.25)$$

where L^2 is the area of the target system, $g_s = 2$ is the spin degeneracy, and $g_v = 2$ is the valley degeneracy. It is clear that the density of states is a linear function of the energy and therefore vanishes at $\varepsilon = 0$, at which the valence and the conduction band touch each other. The electronic energy band structure and the density of states of single-layer graphene in the vicinity of the K point are shown in Fig. 2.3.

2.1.2 Bilayer graphene

Next, electronic structure of bilayer graphene is considered. In fact, three-dimensional graphite is a stack of single-layer graphene, and there are two major stacking rules shown in Fig. 2.4. For the most favorable structure, carbon atoms in the second layer are translated with respect to those in the first layer, and the third layer is the exact translation of the first layer. This structure is called as the AB stacking after the regularity that can be denoted as A, B, A, B, \dots , or as the Bernal stacking (Fig. 2.4a) [7]. In contrast, the metastable structure has the regularity of A, B, C, A, B, C, \dots , which is named as the ABC stacking (Fig. 2.4b) [7]. The proportion of the ABC stacking structure in natural graphite is likely to be as much as a few percent. In addition to these structures, one can find a structure having the AA regularity in some graphite intercalated compounds. Here, electronic structure of bilayer graphene having the most favorable AB stacking structure is considered.

The unit cell of bilayer graphene contains four carbon atoms, namely two atoms in the upper layer denoted by \tilde{A} and \tilde{B} as well as two atoms in the lower layer denoted by A and B . The nearest pair between two layers is the vertically neighboring $\tilde{A}-B$, of which the transfer integral is $\gamma_1 = 0.39$ eV [8]. For the other pairs, $\tilde{B}-A$ and $\tilde{A}-A$ ($\tilde{B}-B$) have $\gamma_3 = 0.32$ eV [7] and $\gamma_4 = 0.04$ eV [9], respectively. Figure 2.5 summarizes the geometrical relationships of these transfer integrals together with the intra-layer nearest neighbor one γ_0 .

An effective Hamiltonian of bilayer graphene [10–12] is represented in a basis with components corresponding to atomic sites $A, \tilde{B}, \tilde{A}, B$ in the vicinity of a K point and to $\tilde{B}, A, B, \tilde{A}$ in the vicinity of a K' point

$$H = \xi \begin{pmatrix} \frac{1}{2}u & v_3\pi & 0 & v\pi^\dagger \\ v_3\pi^\dagger & \frac{1}{2}u & v\pi & 0 \\ 0 & v\pi^\dagger & -\frac{1}{2}u & \xi\gamma_1 \\ v\pi & 0 & \xi\gamma_1 & \frac{1}{2}u \end{pmatrix}, \quad \cdots(2.26)$$

where $\pi = \hbar(k_x + ik_y) = (p_x + ip_y)$, $\pi^\dagger = (p_x - ip_y)$, $v = (\sqrt{3}/2)\gamma_0 a / \hbar$, and $v_3 = (\sqrt{3}/2)\gamma_3 a / \hbar$. The asymmetry of the upper and the lower layers is included by distinguishing the on-site energies $\pm(1/2)u$. $\xi = +1$ corresponds to the K point, and $\xi = -1$ corresponds to the K' point. This Hamiltonian determines four energy bands in bilayer graphene described as,

$$\varepsilon_\alpha^2 = \frac{\gamma_1^2}{2} + \frac{u^2}{4} + \left(v^2 + \frac{v_3^2}{2}\right)p^2 + (-1)^\alpha \sqrt{\Gamma}, \quad \cdots(2.27)$$

with

$$\Gamma = \frac{1}{4}(\gamma_1^2 - v_3^2 p^2)^2 + v^2 p^2 [\gamma_1^2 + u^2 + v_3^2 p^2] + 2\xi\gamma_1 v_3 v^2 p^3 \cos 3\varphi. \quad \cdots(2.28)$$

Here φ is an angle of \mathbf{p} , where $\mathbf{p} = |\mathbf{p}|(\cos \varphi, \sin \varphi)$. In the vicinity of the K point, these energy bands are plotted in Fig. 2.6 with v_3 and u set to be zero.

$\alpha = 2$ represents higher-energy bands originated from vertically aligned \tilde{A} and B atoms, which have relatively strong interaction of γ_1 . The minimum (maximum) of the conduction (valence) band of $\alpha = 2$ locates 0.4 eV above (below) the Fermi energy.

$\alpha = 1$ describes the dispersion of lower-energy bands. In the intermediate energy range, $(1/2)\gamma_1(v_3/v)^2 < |\varepsilon_1| < \gamma_1$, Eq. (2.27) can be written in an approximate form of,

$$\varepsilon_1^\pm \approx \pm \frac{1}{2}\gamma_1 \left[\sqrt{1 + 4\frac{v^2 p^2}{\gamma_1^2}} - 1 \right]. \quad \cdots(2.29)$$

In a high wavenumber range, this energy depends mainly on vp , of which linear relation resembles the case of single-layer graphene, while in a low wavenumber range the energy band $\varepsilon_1 \approx p^2 / 2m^*$ has a parabolic dispersion. An effective mass is calculated to be $m^* = \gamma_1 / 2v^2 = 0.0305m_e$ (m_e is the mass of electron), which is comparable with an effective mass of electron $m_e^* = 0.057m_e$ and that of hole $m_h^* = 0.039m_e$ in bulk graphite. The density of electrons and the density of states can be obtained by Eq. (2.29)

as

$$N(\varepsilon) = \frac{g_s g_v}{4\pi v^2 \hbar^2} (\varepsilon \gamma_1 + \text{sgn}(\varepsilon) \varepsilon^2), \quad \cdots (2.30)$$

$$D(\varepsilon) = \frac{1}{\sqrt{3}\pi \gamma_0^2} (2|\varepsilon| + \gamma_1). \quad \cdots (2.31)$$

An interesting feature has been found by focusing attention on the term of the on-site energy theoretically [13] and experimentally [14,15]. The asymmetry can be achieved by applying external electric field perpendicularly to the plane of bilayer graphene. The application of electric field has been performed by means of chemical doping [14] and backgate and topgate electrodes [15]. Under the presence of the external electric field, u cannot be assumed to be zero. The energy bands with various u are plotted in Fig. 2.7. The opening of the energy band gaps is understood.

2.1.3 Multilayer graphene

Finally, the electronic structure of N -layer graphene is referred to [16]. As used in the case of bilayer graphene, the Bernal stacking structure with the AB regularity is again considered, which is shown in Fig. 2.8. In this figure, carbon atoms labeled as A_n and B_n (n is integer) denote A and B sublattices in the n -th layer, respectively. For the description of the electronic structure of bilayer graphene, a basis with components corresponding to atomic sites A, \tilde{B} , \tilde{A} , B in the vicinity of a K point was taken. Similarly for multilayer, taking a basis of the Bloch functions at $A_1, B_1, A_2, B_2, \dots, A_n, B_n$, an effective Hamiltonian for the multilayer graphene at the vicinity of the K point is represented as

$$H = \begin{pmatrix} H_0 & V & & \\ V^\dagger & H_0 & V^\dagger & \\ & V & H_0 & V \\ & & \ddots & \ddots & \ddots \end{pmatrix}, \quad \cdots (2.32)$$

with

$$H_0 = \begin{pmatrix} 0 & vk_- \\ vk_+ & 0 \end{pmatrix}, \quad V = \begin{pmatrix} 0 & 0 \\ \gamma_1 & 0 \end{pmatrix}, \quad \cdots (2.33)$$

where $k_+ = k_x + ik_y$, $k_- = k_x - ik_y$. The effective Hamiltonian around a K' point is written by exchanging k_+ and k_- with each other.

This Hamiltonian Eq. (2.32) can be diagonalized into smaller matrices by choosing

an appropriate basis that is independent on \mathbf{k} . Carbon atoms of multilayer graphene can be divided into two groups as

Group I: A_1, B_2, A_3, \dots ,

Group II: B_1, A_2, B_3, \dots ,

where, the atoms of the group I are vertically aligned along the normal of the stacking plane and those of the group II are above or below the center of hexagons in the neighboring layers, as shown in Fig. 2.8. When the basis is arranged in the order of group I and group II, namely, $B_1, A_2, B_3, \dots; A_1, B_2, A_3, \dots$, the Hamiltonian Eq. (2.32) becomes

$$H = \begin{pmatrix} H_{11} & H_{12} \\ H_{12}^\dagger & H_{22} \end{pmatrix}, \quad \dots(2.34)$$

with H_{ij} being $N \times N$ matrices defined as

$$H_{11} = \gamma_1 \begin{pmatrix} 0 & 1 & & & \\ 1 & 0 & 1 & & \\ & \ddots & \ddots & \ddots & \\ & & 1 & 0 & 1 \\ & & & 1 & 0 \end{pmatrix}, \quad \dots(2.35)$$

$$H_{12} = \gamma \begin{pmatrix} k_+ & & & & \\ & k_- & & & \\ & & k_+ & & \\ & & & \ddots & \\ & & & & k_\pm \end{pmatrix}, \quad \dots(2.36)$$

$$H_{22} = \gamma' \begin{pmatrix} 0 & k_+ & & & \\ k_- & 0 & k_- & & \\ & k_+ & 0 & k_+ & \\ & & \ddots & \ddots & \ddots \\ & & & k_\mp & 0 & k_\mp \\ & & & & k_\pm & 0 \end{pmatrix}, \quad \dots(2.37)$$

where the upper and the lower signs of the subscriptions for k correspond to odd and even N , respectively. At the K point where $\mathbf{k} = 0$, H_{12} and H_{22} vanish. Then, H_{11} is equivalent to the Hamiltonian of a one-dimensional tight-binding chain with the interlayer nearest-neighbor coupling γ_1 . The eigen energies are given by

$$\varepsilon_m = \gamma_1 \lambda_{N,m}, \quad \dots (2.38)$$

$$\lambda_{N,m} = 2 \sin \frac{m\pi}{2(N+1)}, \quad \dots (2.39)$$

$$m = -(N-1), -(N-3), \dots, N-1. \quad \dots (2.40)$$

If the number of layer N is even, m is taken as an odd integer, and vice versa. The corresponding wave function is explicitly written as

$$\psi_m(j) = \sqrt{\frac{2}{N+1}} \sin \left[\frac{(-m+N+1)\pi}{2(N+1)} j \right], \quad \dots (2.41)$$

where $\psi_m(j)$ represents the amplitude at B_1, A_2, B_3, \dots and satisfies

$$\sum_j \psi_m(j) \psi_{m'}(j) = \delta_{mm'}. \quad \dots (2.42)$$

A relationship between the wave functions with the subscription of m and $-m$ is

$$\psi_{-m}(j) = \psi_m(j) (-1)^{j+1}. \quad \dots (2.43)$$

Utilizing these wave functions, the basis can be rewritten as

$$\begin{aligned} |\phi_m^{(I)}\rangle &= \psi_m(1)|A_1\rangle + \psi_m(2)|B_2\rangle + \psi_m(3)|A_3\rangle + \dots, \\ |\phi_m^{(II)}\rangle &= \psi_m(1)|B_1\rangle + \psi_m(2)|A_2\rangle + \psi_m(3)|B_3\rangle + \dots, \end{aligned} \quad \dots (2.44)$$

and the Hamiltonian Eq. (2.32) is modified. The matrix elements within the group I come from H_{11} and become diagonal as is obvious from the definition,

$$\langle \phi_m^{(I)} | H | \phi_m^{(I)} \rangle = \delta_{mm'} \gamma_1 \lambda_{N,m}. \quad \dots (2.45)$$

Off-diagonal elements between $|\phi_m^{(I)}\rangle$ and $|\phi_{m'}^{(II)}\rangle$ are written from H_{12} as

$$\begin{aligned} \langle \phi_{m'}^{(II)} | H | \phi_m^{(I)} \rangle &= \gamma k_x \sum_{j=1}^N \psi_{m'}^*(j) \psi_m(j) + i\gamma k_y \sum_{j=1}^N \psi_{m'}^*(j) \psi_m(j) \times (-1)^j \\ &= \gamma (k_x \delta_{mm'} - ik_y \delta_{m,-m'}). \end{aligned} \quad \dots (2.46)$$

Finally, the matrix elements within group II are obtained from H_{22} as

$$\begin{aligned}
 \langle \phi_m^{(\text{II})} | H | \phi_m^{(\text{II})} \rangle &= \gamma' k_x \sum_{j=1}^{N-1} [\psi_{m'}^*(j+1) \psi_m(j) + \psi_{m'}^*(j) \psi_m(j+1)] \\
 &\quad + \gamma' i k_y \sum_{j=1}^{N-1} (-1)^j [\psi_{m'}^*(j+1) \psi_m(j) - \psi_{m'}^*(j) \psi_m(j+1)] \quad \cdots (2.47) \\
 &= \gamma' \lambda_{N,m} (k_x \delta_{mm'} + i k_y \delta_{m,-m'}).
 \end{aligned}$$

The Hamiltonian is thus closed in the subspace $\{|\phi_m^{(\text{I})}\rangle, |\phi_{-m}^{(\text{I})}\rangle, |\phi_m^{(\text{II})}\rangle, |\phi_{-m}^{(\text{II})}\rangle\}$ for each $|m|$. Particularly, $m = 0$ is special in that the subspace is spanned with only two bases $\{|\phi_0^{(\text{II})}\rangle, |\phi_0^{(\text{I})}\rangle\}$, while this is absent in even-layer graphenes. The submatrix is written as

$$H_{m=0} = \begin{pmatrix} 0 & \gamma k_- \\ \gamma k_+ & 0 \end{pmatrix}. \quad \cdots (2.48)$$

This Hamiltonian Eq. (2.48) is equivalent to that for single-layer graphene, which is independent of γ_1 and γ_3 . For $m > 0$, we can take the basis as

$$\begin{aligned}
 &\left\{ \left(|\phi_m^{(\text{II})}\rangle + |\phi_{-m}^{(\text{II})}\rangle \right) / \sqrt{2}, \left(|\phi_m^{(\text{I})}\rangle + |\phi_{-m}^{(\text{I})}\rangle \right) / \sqrt{2}, \right. \\
 &\left. \left(|\phi_m^{(\text{I})}\rangle - |\phi_{-m}^{(\text{I})}\rangle \right) / \sqrt{2}, \left(|\phi_m^{(\text{II})}\rangle - |\phi_{-m}^{(\text{II})}\rangle \right) / \sqrt{2} \right\}. \quad \cdots (2.49)
 \end{aligned}$$

Then, the Hamiltonian becomes

$$H_m = \begin{pmatrix} 0 & \gamma k_- & 0 & \lambda \gamma' k_+ \\ \gamma k_+ & 0 & \lambda \gamma_1 & 0 \\ 0 & \lambda \gamma_1 & 0 & \gamma k_- \\ \lambda \gamma' k_- & 0 & \gamma k_+ & 0 \end{pmatrix}, \quad \cdots (2.50)$$

with $\lambda = \lambda_{N,m}$. This Hamiltonian Eq. (2.50) is equivalent to that for bilayer graphene while the interlayer coupling γ_1 and γ' ($\propto \gamma_3$) are multiplied by λ .

Thus, the Hamiltonian can be decomposed into those equivalent to single-layer or bilayer subbands. The Hamiltonian of odd-layer graphene is composed of one single-layer-type and $(N-1)/2$ bilayer-type subbands, while that of even-layer graphene is composed of $N/2$ bilayer-type subbands without single-layer-type one. The electronic energy band structures of N -layer graphene ($N = 2, 3, 4$, and 5) are shown in Fig. 2.9 [16].

In the above descriptions, the transfer integral γ_2 included in Fig. 2.8 is not used. γ_2 originates from the interaction between atoms in the next nearest layers. The involvement of γ_2 causes small energy gaps between the conduction and the valence

bands. However, $\gamma_2 = -0.02$ eV [7] is small enough to be neglected for approximation.

2.2 Transport in graphene

2.2.1 Classical basis

Electronic transport is motion of electron in some direction in a solid, which is generally induced by external fields. Motion of electrons is accelerated by external fields and disturbed by various kinds of collisions. Here, a simple case that an electron moves in two-dimensional plane with the speed of v_0 is considered.

The velocity of an electron is $\mathbf{v} = (v_x, v_y)$, the mass is m , the elementary electric charge is e . When a magnetic field is applied perpendicularly to the plane, the equation of motion for the electron contains the Lorentz force, which is written as following.

$$m \frac{d\mathbf{v}}{dt} = -e\mathbf{v} \times \mathbf{B}. \quad \cdots(2.51)$$

The solutions are

$$x(t) = \frac{v_y}{\omega_c}, \quad \cdots(2.52)$$

$$y(t) = \frac{v_x}{\omega_c}, \quad \cdots(2.53)$$

with

$$v_x = v_0 \cos(\omega_c t), \quad \cdots(2.54)$$

$$v_y = v_0 \sin(\omega_c t), \quad \cdots(2.55)$$

$$\omega_c = \frac{eB}{m}, \quad \cdots(2.56)$$

where ω_c is the cyclotron frequency. The radius of cyclotron motion is $v_0 / \omega_c = mv_0 / eB$. In the presence of electric field \mathbf{E} , the equation of motion becomes

$$m \left(\frac{d}{dt} + \frac{1}{\tau} \right) \mathbf{v} = -e(\mathbf{E} + \mathbf{v} \times \mathbf{B}), \quad \cdots(2.57)$$

$$m \left(\frac{d}{dt} + \frac{1}{\tau} \right) v_x = -eE_x - eB_z v_y, \quad \cdots(2.58)$$

$$m \left(\frac{d}{dt} + \frac{1}{\tau} \right) v_y = -eE_y + eB_z v_x, \quad \cdots(2.59)$$

$$m \left(\frac{d}{dt} + \frac{1}{\tau} \right) v_z = -eE_z, \quad \cdots(2.60)$$

where τ is the relaxation time, which involves contributions of scattering events without consideration on detailed mechanisms of these events. In a steady state, time-dependent variations are neglected.

$$v_x = -\frac{e\tau}{m} [E_x + v_y B_z], \quad \cdots(2.61)$$

$$v_y = -\frac{e\tau}{m} [E_y + v_x B_z], \quad \cdots(2.62)$$

$$v_z = -\frac{e\tau}{m} E_z. \quad \cdots(2.63)$$

In this case, the current density $\mathbf{j} = -en\mathbf{v}$ with the concentration of electron n can be written as

$$j_x = \frac{e^2 n \tau}{m} E_x - \frac{e B_z \tau}{m} j_y, \quad \cdots(2.64)$$

$$j_y = \frac{e^2 n \tau}{m} E_y + \frac{e B_z \tau}{m} j_x, \quad \cdots(2.65)$$

$$j_z = \frac{e^2 n \tau}{m} E_z. \quad \cdots(2.66)$$

Then, the solutions are given by

$$(1 + \omega_c^2 \tau^2) j_x = \sigma_0 (E_x - \omega_c \tau E_y), \quad \cdots(2.67)$$

$$(1 + \omega_c^2 \tau^2) j_y = \sigma_0 (E_y + \omega_c \tau E_x), \quad \cdots(2.68)$$

$$j_z = \sigma_0 E_z. \quad \cdots(2.69)$$

Here, the relationship between the current density and the electric field can be understood, which are connected by the conductivity tensor $[\sigma]$ or its inverse tensor, i.e., resistivity tensor $[\rho] = [\sigma]^{-1}$.

$$\begin{pmatrix} j_x \\ j_y \\ j_z \end{pmatrix} = \begin{pmatrix} \sigma_{xx} & \sigma_{xy} & \sigma_{xz} \\ \sigma_{yx} & \sigma_{yy} & \sigma_{yz} \\ \sigma_{zx} & \sigma_{zy} & \sigma_{zz} \end{pmatrix} \begin{pmatrix} E_x \\ E_y \\ E_z \end{pmatrix}, \quad \cdots(2.70)$$

$$\begin{pmatrix} E_x \\ E_y \\ E_z \end{pmatrix} = \begin{pmatrix} \rho_{xx} & \rho_{xy} & \rho_{xz} \\ \rho_{yx} & \rho_{yy} & \rho_{yz} \\ \rho_{zx} & \rho_{zy} & \rho_{zz} \end{pmatrix} \begin{pmatrix} j_x \\ j_y \\ j_z \end{pmatrix}. \quad \cdots(2.71)$$

Compared with Eqs. (2.66), (2.67), and (2.68), the form of the conductivity tensor is as following.

$$[\sigma] = \frac{\sigma_0}{1 + \omega_c^2 \tau^2} \begin{pmatrix} 1 & -\omega_c \tau & 0 \\ \omega_c \tau & 1 & 0 \\ 0 & 0 & 1 + \omega_c^2 \tau^2 \end{pmatrix}. \quad \cdots(2.72)$$

Let us consider a constant current flowing in x direction. In a steady state, the y component of current density is zero $j_y = 0$, so that we can notice the presence of the y component of the electric field, which is called as the Hall electric field.

$$E_y = \left(\frac{\sigma_{xy}}{\sigma_{xx}} \right) E_x. \quad \cdots(2.73)$$

The Hall coefficient is written as

$$R_{\text{Hall}} = \frac{E_y}{j_x B} = \frac{1}{B} \frac{\sigma_{xy}}{\sigma_{xx}^2 + \sigma_{xy}^2} = -\frac{1}{ne}. \quad \cdots(2.74)$$

The signature of the Hall coefficient indicates the signature of major charge carriers. For hole carriers with $+e$, the signature of R_{Hall} is the opposite.

2.2.2 Boltzmann's transport equation [17]

As mentioned above, transport phenomena, such as the flow of electrical current in solids, involve two characteristic mechanisms with opposite effects. One is the driving force for carriers applied by the external fields. The other is the dissipative effect of carrier scatterings by phonons and defects. The interplay between these two mechanisms is described by the Boltzmann's transport equation, so that one can investigate how the distribution of carriers in thermal equilibrium is changed in the presence of external fields and as a result of electron scattering processes.

Under homogeneous temperature conditions and with no external fields, i.e., in thermal equilibrium, the distribution function is simply the Fermi–Dirac type.

$$f_0 \{E(\mathbf{k})\} = \frac{1}{\exp \left[\left(E(\mathbf{k}) - E_F \right) k_B T \right] + 1} . \quad \dots(2.75)$$

One can define the temporal change of wave vector of an electron (\mathbf{k}) by an external field (\mathbf{F}) as

$$\hbar \frac{d\mathbf{k}}{dt} = \mathbf{F} . \quad \dots(2.76)$$

The distribution function depends on wave vector, position, and time as $f(\mathbf{k}, \mathbf{r}, t)$. After the passage of time dt , the position and the wave vector of an electron become $\mathbf{r} + \dot{\mathbf{r}}dt$ and $\mathbf{k} + \dot{\mathbf{k}}dt$. Thus, the temporal variation of the distribution function from $t - dt$ to t is given by

$$\left(\frac{df}{dt} \right)_{\text{drift}} = \frac{f(\mathbf{k} - \dot{\mathbf{k}}dt, \mathbf{r} - \dot{\mathbf{r}}dt, t - dt) - f(\mathbf{k}, \mathbf{r}, t)}{dt} . \quad \dots(2.77)$$

Equation (2.77) is called as the drift term because collisions of carriers are absent. Expanding the first term of the right-hand side, we obtain,

$$f(\mathbf{k} - \dot{\mathbf{k}}dt, \mathbf{r} - \dot{\mathbf{r}}dt, t - dt) = f(\mathbf{k}, \mathbf{r}, t) - \left[\dot{\mathbf{k}} \cdot \frac{\partial f}{\partial \mathbf{k}} + \dot{\mathbf{r}} \cdot \frac{\partial f}{\partial \mathbf{r}} + \frac{\partial f}{\partial t} \right] dt + \dots . \quad \dots(2.78)$$

Here, the first-order term of dt is considered. The drift term is rewritten as

$$\left(\frac{df}{dt} \right)_{\text{drift}} = - \left[\dot{\mathbf{k}} \cdot \nabla_{\mathbf{k}} f + \dot{\mathbf{r}} \cdot \nabla_{\mathbf{r}} f + \frac{\partial f}{\partial t} \right] , \quad \dots(2.79)$$

with

$$\dot{\mathbf{k}} \cdot \nabla_{\mathbf{k}} f = \dot{k}_x \frac{\partial f}{\partial k_x} + \dot{k}_y \frac{\partial f}{\partial k_y} + \dot{k}_z \frac{\partial f}{\partial k_z} , \quad \dots(2.80)$$

$$\dot{\mathbf{r}} \cdot \nabla_{\mathbf{r}} f = \dot{v}_x \frac{\partial f}{\partial x} + \dot{v}_y \frac{\partial f}{\partial y} + \dot{v}_z \frac{\partial f}{\partial z} . \quad \dots(2.81)$$

Using the expression of temporal variation of wave vector as Eq. (2.76), Eq. (2.79) becomes

$$\left(\frac{\partial f}{\partial t} \right)_{\text{drift}} = - \left[\frac{\mathbf{F}}{\hbar} \cdot \nabla_{\mathbf{k}} f + \mathbf{v} \cdot \nabla_{\mathbf{r}} f + \frac{\partial f}{\partial t} \right] . \quad \dots(2.82)$$

If we define the change in f caused by scattering by the term $(\partial f / \partial t)_{\text{scatter}}$,

$$f(\mathbf{k}, \mathbf{r}, dt) = f\left(\mathbf{k} - \frac{\mathbf{F}}{\hbar} dt, \mathbf{r} - \mathbf{v} dt, t - dt\right) + \left(\frac{\partial f}{\partial t} \right)_{\text{scatter}} dt . \quad \dots(2.83)$$

Therefore, $(\partial f / \partial t)_{\text{scatter}}$ is described as following.

$$\left(\frac{\partial f}{\partial t}\right)_{\text{scatter}} = \frac{\partial f}{\partial t} + \frac{\mathbf{F}}{\hbar} \cdot \nabla_{\mathbf{k}} f + \mathbf{v} \cdot \nabla_{\mathbf{r}} f. \quad \cdots(2.84)$$

Equation (2.84) is called as Boltzmann's transport equation.

Next, more detailed expression of the scattering term is considered. The variation of f due to scattering is the sum of electronic transitions from \mathbf{k}' to \mathbf{k} , which increase f , and transitions from \mathbf{k} to \mathbf{k}' , which decrease f , taking over the entire \mathbf{k}' states that is not the \mathbf{k} state. Here, spatial homogeneity of the distribution function is assumed, so that f is independent of \mathbf{r} . Let $P(\mathbf{k}, \mathbf{k}')$ be the probability per unit time to scatter from the state \mathbf{k} to \mathbf{k}' . $P(\mathbf{k}, \mathbf{k}')$ is typically evaluated from the Golden rule of time-dependent perturbation theory.

$$P(\mathbf{k}, \mathbf{k}') = \frac{2\pi}{\hbar} \left| \langle \mathbf{k}' | V_{\mathbf{k}\mathbf{k}'} | \mathbf{k} \rangle \right|^2 \delta[\varepsilon_{\mathbf{k}'} - \varepsilon_{\mathbf{k}}], \quad \cdots(2.85)$$

where $V_{\mathbf{k}\mathbf{k}'}$ is time-dependent perturbation term, $\varepsilon_{\mathbf{k}}$ and $\varepsilon_{\mathbf{k}'}$ are initial- and final-state energy including perturbation, respectively, and the delta function means the conservation of energy. Utilizing $P(\mathbf{k}, \mathbf{k}')$ and $P(\mathbf{k}', \mathbf{k})$, the scattering term is rewritten as

$$\left(\frac{\partial f}{\partial t}\right)_{\text{scatter}} = \sum_{\mathbf{k}'} \left\{ P(\mathbf{k}', \mathbf{k}) f(\mathbf{k}') [1 - f(\mathbf{k})] - P(\mathbf{k}, \mathbf{k}') f(\mathbf{k}) [1 - f(\mathbf{k}')] \right\}. \quad \cdots(2.86)$$

$f(\mathbf{k}') [1 - f(\mathbf{k})]$, which is the coefficient for P , denotes the probability that the initial state \mathbf{k}' is filled and the final state \mathbf{k} is empty.

In thermal equilibrium, the principle of detailed balance is led as following.

$$P(\mathbf{k}', \mathbf{k}) f_0(\mathbf{k}') = P(\mathbf{k}, \mathbf{k}') f_0(\mathbf{k}). \quad \cdots(2.87)$$

Using the principle of detailed balance, Eq. (2.86) becomes

$$\left(\frac{\partial f}{\partial t}\right)_{\text{scatter}} = - \sum_{\mathbf{k}'} P(\mathbf{k}, \mathbf{k}') \left[f(\mathbf{k}) - f(\mathbf{k}') \frac{f_0(\mathbf{k})}{f_0(\mathbf{k}')} \right]. \quad \cdots(2.88)$$

In the form of integral, this equation is written as

$$\left(\frac{\partial f}{\partial t}\right)_{\text{scatter}} = - \frac{V}{(2\pi)^3} \int d^3\mathbf{k}' P(\mathbf{k}, \mathbf{k}') \left[f(\mathbf{k}) - f(\mathbf{k}') \frac{f_0(\mathbf{k})}{f_0(\mathbf{k}')} \right], \quad \cdots(2.89)$$

where V is the volume of crystal.

If the external force is not very strong, the change of the distribution function with respect to its form under thermal equilibrium is small, so that we can put

$$f(\mathbf{k}) = f_0(\mathbf{k}) + f_1(\mathbf{k}) \quad (f_1(\mathbf{k}) \ll f_0(\mathbf{k})). \quad \dots(2.90)$$

Assuming elastic scattering, the variation of energy upon scattering is so small that $\varepsilon_{\mathbf{k}}$ and $\varepsilon_{\mathbf{k}'}$ are approximately equal, and that $f_0(\mathbf{k})$ is also approximately equal to $f_0(\mathbf{k}')$. Thus,

$$\begin{aligned} \left(\frac{\partial f}{\partial t} \right)_{\text{scatter}} &= -f_1(\mathbf{k}) \frac{V}{(2\pi)^3} \int d^3\mathbf{k}' P(\mathbf{k}, \mathbf{k}') \left[1 - \frac{f_1(\mathbf{k}')}{f_1(\mathbf{k})} \right] \\ &\equiv -\frac{f_1(\mathbf{k})}{\tau(\mathbf{k})} \\ &\equiv -\frac{f(\mathbf{k}) - f_0(\mathbf{k})}{\tau(\mathbf{k})}. \end{aligned} \quad \dots(2.91)$$

Here, relaxation time $\tau(\mathbf{k})$ is introduced, which is given by

$$\frac{1}{\tau(\mathbf{k})} = \frac{V}{(2\pi)^3} \int d^3\mathbf{k}' P(\mathbf{k}, \mathbf{k}') \left[1 - \frac{f_1(\mathbf{k}')}{f_1(\mathbf{k})} \right], \quad \dots(2.92)$$

as a function of wave vector of electron, *i.e.*, a function of electronic energy.

Within this relaxation approximation regime, the Boltzmann's transport equation is described as

$$\frac{\partial f}{\partial t} + \frac{\mathbf{F}}{\hbar} \cdot \nabla_{\mathbf{k}} f + \mathbf{v} \cdot \nabla_{\mathbf{r}} f = -\frac{f - f_0}{\tau}. \quad \dots(2.93)$$

In a steady state, the first term of the left-hand side is zero. If crystal is spatially homogeneous, f is independent of \mathbf{r} , providing that the third term of the left side can be ignored. Eventually, we obtain

$$\frac{\mathbf{F}}{\hbar} \cdot \nabla_{\mathbf{k}} f = -\frac{f_1}{\tau}. \quad \dots(2.94)$$

When the direction of the external field is along x axis,

$$f_1 = -\frac{\tau}{\hbar} F_x \frac{\partial f}{\partial k_x}. \quad \dots(2.95)$$

If effective mass of electron is denoted as m^* , electronic energy is $\varepsilon = \hbar^2 k^2 / 2m^*$ with $\hbar k_x = m^* v_x$. Hence we obtain

$$f_1 = -\frac{\tau}{\hbar} F_x \frac{\partial f}{\partial \varepsilon} \frac{\partial \varepsilon}{\partial k_x} = -\tau v_x F_x \frac{\partial f}{\partial \varepsilon}. \quad \dots(2.96)$$

Utilizing the relation of Eq. (2.90),

$$f_1 = -\tau v_x F_x \frac{\partial f_0}{\partial \varepsilon}, \quad \dots(2.97)$$

is derived approximately. Under an assumption of elastic scattering, the relaxation time is written as following,

$$\begin{aligned}\frac{1}{\tau(\mathbf{k})} &= \frac{V}{(2\pi)^3} \int d^3\mathbf{k}' P(\mathbf{k}, \mathbf{k}') \left(1 - \frac{k'_x}{k_x}\right) \\ &= \frac{V}{(2\pi)^3} \int d^3\mathbf{k}' P(\mathbf{k}, \mathbf{k}') (1 - \cos \theta),\end{aligned}\quad \dots(2.98)$$

where k_x and k'_x are x components of wave vectors before and after scattering, respectively, and θ is the angle between vectors \mathbf{k} and \mathbf{k}' .

Letting F_x be equal to $-eE_x$, Eqs. (2.90) and (2.97) lead to

$$f(\mathbf{k}) = f_0(\mathbf{k}) + eE_x \tau v_x \frac{\partial f_0}{\partial \varepsilon}. \quad \dots(2.99)$$

Thus, current density in x direction is given by

$$\begin{aligned}J_x &= \frac{2}{(2\pi)^3} \int (-e) v_x f(\mathbf{k}) d^3\mathbf{k} \\ &= -\frac{e}{4\pi^3} \int v_x f_0(\mathbf{k}) d^3\mathbf{k} - \frac{e^2 E_x}{4\pi^3} \int \tau v_x^2 \frac{\partial f_0}{\partial \varepsilon} d^3\mathbf{k}.\end{aligned}\quad \dots(2.100)$$

The multiplication by 2 indicates up and down spins. The first term of the right-hand side of Eq. (2.100) vanishes because the internal function of the integral is odd. Therefore,

$$J_x = -\frac{e^2 E_x}{4\pi^3} \int \tau v_x^2 \frac{\partial f_0}{\partial \varepsilon} d^3\mathbf{k}. \quad \dots(2.101)$$

If we have spherical symmetry in k space,

$$J_x = -\frac{1}{3} \frac{e^2 E_x}{4\pi^3} \int \tau v_x^2 \frac{\partial f_0}{\partial \varepsilon} d^3k, \quad \dots(2.102)$$

since a volume in \mathbf{k} -space is written as

$$d^3k = \frac{dS d\varepsilon}{|\nabla_{\mathbf{k}} \varepsilon|} = \frac{dS d\varepsilon}{\hbar v_x}, \quad \dots(2.103)$$

where S is an isoenergetic surface area. At sufficiently low temperature, the Fermi–Dirac distribution function is

$$\begin{cases} f_0 \cong 1 & (\varepsilon < \varepsilon_F) \\ f_0 \cong 0 & (\varepsilon > \varepsilon_F) \end{cases} \quad \dots(2.104)$$

and its differential by energy is expressed by using the delta function as

$$\frac{\partial f_0}{\partial \varepsilon} = -\delta(\varepsilon - \varepsilon_F). \quad \dots(2.105)$$

Hence Eq. (2.102) becomes

$$J_x = \frac{e^2 E_x}{12\pi^3 \hbar} \iint \tau v_x \delta(\varepsilon - \varepsilon_F) dS d\varepsilon, \quad \cdots(2.106)$$

then, ultimately,

$$J_x = \frac{e^2 E_x}{12\pi^3 \hbar} (v_F \tau_F 4\pi k_F^2), \quad \cdots(2.107)$$

where the subscript F means that the function is to be evaluated at the Fermi energy. Let n be the number of conducting electrons per unit volume as

$$n = \frac{1}{4\pi^3} \int f_0 d^3 k = \frac{4\pi}{3} k_F^3 \frac{1}{4\pi^3}, \quad \cdots(2.108)$$

we obtain

$$J_x = \frac{ne^2 E_x \tau_F}{m^*} = \sigma E_x, \quad \sigma = \frac{ne^2 \tau_F}{m}, \quad \mu = \frac{e\tau_F}{m^*}. \quad \cdots(2.109)$$

Here σ is the conductivity and μ is the mobility of electron.

If electronic spins are taken into account, the Boltzmann's transport equation Eq. (2.84) and the probability of transition Eq. (2.85) are modified as followings.

$$\left(\frac{\partial f_\sigma}{\partial t} \right)_{\text{scatter}} = \frac{\mathbf{F}}{\hbar} \cdot \nabla_{\mathbf{k}} f_\sigma + \mathbf{v}_\sigma \cdot \nabla_{\mathbf{r}} f_\sigma + \frac{\partial f_\sigma}{\partial t}. \quad \cdots(2.110)$$

$$P(\mathbf{k}\sigma, \mathbf{k}'\sigma') = \frac{2\pi}{\hbar} \left| \langle \mathbf{k}'\sigma' | V_{\mathbf{k}\sigma\mathbf{k}'\sigma'} | \mathbf{k}\sigma \rangle \right|^2 \delta(\varepsilon_{\mathbf{k}'\sigma'} - \varepsilon_{\mathbf{k}\sigma}). \quad \cdots(2.111)$$

Here, σ is defined as electronic spins, not the conductivity. In the case of the presence of degeneration, the equation of the principle of detailed balance is written as

$$P(\mathbf{k}'\sigma', \mathbf{k}\sigma) f_{0,\sigma'}(\mathbf{k}') [1 - f_{0,\sigma}(\mathbf{k})] = P(\mathbf{k}\sigma, \mathbf{k}'\sigma') f_{0,\sigma}(\mathbf{k}) [1 - f_{0,\sigma'}(\mathbf{k}')]. \quad \cdots(2.112)$$

Therefore, Eq. (2.86) can be rewritten as

$$\begin{aligned} \left(\frac{\partial f_\sigma}{\partial t} \right)_{\text{scatter}} &= \sum_{\mathbf{k}'\sigma'} P(\mathbf{k}\sigma, \mathbf{k}'\sigma') f_{0,\sigma}(\mathbf{k}) [1 - f_{0,\sigma'}(\mathbf{k}')] \\ &\times \left\{ \frac{f_{\sigma'}(\mathbf{k}') [1 - f_\sigma(\mathbf{k})]}{f_{0,\sigma'}(\mathbf{k}') [1 - f_{0,\sigma}(\mathbf{k})]} - \frac{f_\sigma(\mathbf{k}) [1 - f_{\sigma'}(\mathbf{k}')] }{f_{0,\sigma}(\mathbf{k}) [1 - f_{0,\sigma'}(\mathbf{k}')] } \right\}. \end{aligned} \quad \cdots(2.113)$$

This equation can be written in the integral form as,

$$\begin{aligned} \left(\frac{\partial f_\sigma}{\partial t} \right)_{\text{scatter}} &= \frac{V}{(2\pi)^3} \sum_{\sigma'} \int d^3\mathbf{k}' P(\mathbf{k}\sigma, \mathbf{k}'\sigma') f_{0,\sigma}(\mathbf{k}) [1 - f_{0,\sigma'}(\mathbf{k}')] \\ &\times \left\{ \frac{f_{\sigma'}(\mathbf{k}') [1 - f_\sigma(\mathbf{k})]}{f_{0,\sigma'}(\mathbf{k}') [1 - f_{0,\sigma}(\mathbf{k})]} - \frac{f_\sigma(\mathbf{k}) [1 - f_{\sigma'}(\mathbf{k}')] }{f_{0,\sigma}(\mathbf{k}) [1 - f_{0,\sigma'}(\mathbf{k}')] } \right\}. \end{aligned} \quad \cdots(2.114)$$

We now define $\varphi_{\mathbf{k}\sigma}$ as

$$f_\sigma(\mathbf{k}) = f_{0,\sigma}(\mathbf{k}) - \varphi_{\mathbf{k}\sigma} \frac{\partial f_{0,\sigma}(\mathbf{k})}{\partial \mathcal{E}_{\mathbf{k}\sigma}}, \quad \cdots(2.115)$$

$$\frac{\partial f_{0,\sigma}(\mathbf{k})}{\partial \mathcal{E}_{\mathbf{k}\sigma}} = -\frac{1}{k_B T} f_{0,\sigma}(\mathbf{k}) [1 - f_{0,\sigma}(\mathbf{k})]. \quad \cdots(2.116)$$

In this case, the interior of the large bracket in Eq. (2.114) can be rewritten as followings

$$\frac{f_{\sigma'}(\mathbf{k}') [1 - f_\sigma(\mathbf{k})]}{f_{0,\sigma'}(\mathbf{k}') [1 - f_{0,\sigma}(\mathbf{k})]} = \left(1 + \varphi_{\mathbf{k}'\sigma'} \frac{1}{k_B T} [1 - f_{0,\sigma'}(\mathbf{k}')] \right) \left(1 - \varphi_{\mathbf{k}\sigma} \frac{1}{k_B T} f_{0,\sigma}(\mathbf{k}) \right), \quad \cdots(2.117)$$

$$\frac{f_\sigma(\mathbf{k}) [1 - f_{\sigma'}(\mathbf{k}')] }{f_{0,\sigma}(\mathbf{k}) [1 - f_{0,\sigma'}(\mathbf{k}')] } = \left(1 + \varphi_{\mathbf{k}\sigma} \frac{1}{k_B T} [1 - f_{0,\sigma}(\mathbf{k})] \right) \left(1 - \varphi_{\mathbf{k}'\sigma'} \frac{1}{k_B T} f_{0,\sigma'}(\mathbf{k}') \right), \quad \cdots(2.118)$$

finally, subtracting Eq. (2.118) from Eq. (2.117), we obtain

$$\begin{aligned} &\frac{f_{\sigma'}(\mathbf{k}') [1 - f_\sigma(\mathbf{k})]}{f_{0,\sigma'}(\mathbf{k}') [1 - f_{0,\sigma}(\mathbf{k})]} - \frac{f_\sigma(\mathbf{k}) [1 - f_{\sigma'}(\mathbf{k}')] }{f_{0,\sigma}(\mathbf{k}) [1 - f_{0,\sigma'}(\mathbf{k}')] } \\ &= \frac{1}{k_B T} (\varphi_{\mathbf{k}'\sigma'} - \varphi_{\mathbf{k}\sigma}) - \left(\frac{1}{k_B T} \right)^2 \varphi_{\mathbf{k}\sigma} \varphi_{\mathbf{k}'\sigma'} \{ f_{0,\sigma}(\mathbf{k}) - f_{0,\sigma'}(\mathbf{k}') \} \end{aligned} \quad \cdots(2.119)$$

The difference of $f_\sigma(\mathbf{k})$ from the Fermi–Dirac function $f_{0,\sigma}(\mathbf{k})$ is assumed to be small to neglect the second term in Eq. (2.119) that contains $\varphi_{\mathbf{k}\sigma} \varphi_{\mathbf{k}'\sigma'}$. Thus, the Boltzmann's transport equation is

$$\begin{aligned} \left(\frac{\partial f_\sigma}{\partial t} \right)_{\text{scatter}} &= \frac{V}{(2\pi)^3} \sum_{\sigma'} \int d^3\mathbf{k}' P(\mathbf{k}\sigma, \mathbf{k}'\sigma') f_{0,\sigma}(\mathbf{k}) [1 - f_{0,\sigma'}(\mathbf{k}')] \\ &\times \frac{1}{k_B T} (\varphi_{\mathbf{k}'\sigma'} - \varphi_{\mathbf{k}\sigma}). \end{aligned} \quad \cdots(2.120)$$

2.2.3 Graphene [18–20]

In the case of two-dimensional system for graphene, the Boltzmann's transport equation for the distribution function $f_{\sigma\mathbf{k}}^E$ in the applied electric field \mathbf{E} is given by

$$\frac{d\mathbf{k}}{dt} \cdot \frac{\partial f_{\sigma\mathbf{k}}^E}{\partial \mathbf{k}} = - \sum_{\sigma'} \int \frac{d\mathbf{k}'}{(2\pi)^2} \left[f_{\sigma\mathbf{k}}^E (1 - f_{\sigma'\mathbf{k}'}^E) - f_{\sigma'\mathbf{k}'}^E (1 - f_{\sigma\mathbf{k}}^E) \right] W(\sigma'\mathbf{k}', \sigma\mathbf{k}), \quad \cdots(2.121)$$

with

$$W(\sigma'\mathbf{k}', \sigma\mathbf{k}) = \frac{2\pi}{\hbar} \left\langle |V_{\sigma'\mathbf{k}', \sigma\mathbf{k}}|^2 \right\rangle \delta(\varepsilon_{\sigma\mathbf{k}} - \varepsilon_{\sigma'\mathbf{k}'}), \quad \cdots(2.122)$$

where $V_{\sigma'\mathbf{k}', \sigma\mathbf{k}}$ is the matrix element of scattering potential, and the triangular bracket denotes the average over configurations of scatterers. Here, the case of elastic scattering is considered for the simplicity. To the lowest order in the applied electric field \mathbf{E} , we have

$$f_{\sigma\mathbf{k}}^E = f_0(\varepsilon_{\sigma\mathbf{k}}) + g_{\sigma\mathbf{k}}, \quad \cdots(2.123)$$

where $f_0(\varepsilon)$ is the Fermi distribution function and $g_{\sigma\mathbf{k}}$ is the deviation proportional to \mathbf{E} . Then,

$$\begin{aligned} \frac{d\mathbf{k}}{dt} \cdot \frac{\partial f_{\sigma\mathbf{k}}^E}{\partial \mathbf{k}} &= -e\mathbf{E} \cdot \left(\frac{\partial \varepsilon_{\sigma\mathbf{k}}}{\hbar \partial \mathbf{k}} \right) \frac{\partial f}{\partial \varepsilon_{\sigma\mathbf{k}}} - \frac{e\mathbf{E}}{\hbar} \cdot \frac{\partial g_{\sigma\mathbf{k}}}{\partial \mathbf{k}} \\ &= -e\mathbf{E} \cdot \mathbf{v}_{\sigma\mathbf{k}} \frac{\partial f}{\partial \varepsilon_{\sigma\mathbf{k}}} - \frac{e}{c\hbar} (\mathbf{v}_{\sigma\mathbf{k}} \times \mathbf{B}) \cdot \frac{\partial g_{\sigma\mathbf{k}}}{\partial \mathbf{k}}, \end{aligned} \quad \cdots(2.124)$$

with the velocity

$$\mathbf{v}_{\sigma\mathbf{k}} = \frac{\partial \varepsilon_{\sigma\mathbf{k}}}{\hbar \partial \mathbf{k}}, \quad \cdots(2.125)$$

and the speed of light c , and the magnetic field perpendicular to the system \mathbf{B} . The transport equation becomes

$$\begin{aligned} &-e\mathbf{E} \cdot \mathbf{v}_{\sigma\mathbf{k}} \frac{\partial f}{\partial \varepsilon_{\sigma\mathbf{k}}} - \frac{e}{c\hbar} (\mathbf{v}_{\sigma\mathbf{k}} \times \mathbf{B}) \cdot \frac{\partial g_{\sigma\mathbf{k}}}{\partial \mathbf{k}} \\ &= - \sum_{\sigma'} \int \frac{d\mathbf{k}'}{(2\pi)^2} \left[f_{\sigma\mathbf{k}}^E - f_{\sigma'\mathbf{k}'}^E \right] W(\sigma'\mathbf{k}', \sigma\mathbf{k}), \end{aligned} \quad \cdots(2.126)$$

$$\begin{aligned} e\mathbf{E} \cdot \mathbf{v}_{\sigma\mathbf{k}} \left(- \frac{\partial f}{\partial \varepsilon_{\sigma\mathbf{k}}} \right) &= \frac{e}{c\hbar} (\mathbf{v}_{\sigma\mathbf{k}} \times \mathbf{B}) \cdot \frac{\partial g_{\sigma\mathbf{k}}}{\partial \mathbf{k}} \\ &\quad - \int \frac{d\mathbf{k}'}{(2\pi)^2} (g_{\sigma\mathbf{k}} - g_{\sigma'\mathbf{k}'}) \frac{2\pi}{\hbar} \left\langle |V_{\sigma'\mathbf{k}', \sigma\mathbf{k}}|^2 \right\rangle \delta(\varepsilon_{\sigma\mathbf{k}} - \varepsilon_{\sigma'\mathbf{k}'}). \end{aligned} \quad \cdots(2.127)$$

Let the relaxation time τ and the cyclotron frequency ω_c be

$$\frac{1}{\tau(\varepsilon_{\sigma\mathbf{k}})} = \frac{2\pi}{\hbar} \int \frac{d\mathbf{k}'}{(2\pi)^2} \left\langle |V_{\sigma\mathbf{k}',\sigma\mathbf{k}}|^2 \right\rangle [1 - \cos(\theta_{\mathbf{k}} - \theta_{\mathbf{k}'})] \delta(\varepsilon_{\sigma\mathbf{k}} - \varepsilon_{\sigma\mathbf{k}'}), \quad \cdots(2.128)$$

$$\omega_c(\varepsilon_{\sigma\mathbf{k}}) = \frac{eBv^2}{c\varepsilon_{\sigma\mathbf{k}}}, \quad \cdots(2.129)$$

where $\theta_{\mathbf{k}}$ and $\theta_{\mathbf{k}'}$ are the angles of wave vectors \mathbf{k} and \mathbf{k}' , respectively. We obtain the solution written as

$$g_{\sigma\mathbf{k}} = -e\tau \left(-\frac{\partial f}{\partial \varepsilon_{\sigma\mathbf{k}}} \right) \frac{1}{1 + \omega_c^2 \tau^2} \mathbf{v}_{\sigma\mathbf{k}} \cdot \left(\mathbf{E} + \omega_c \tau \frac{\mathbf{B}}{B} \times \mathbf{E} \right). \quad \cdots(2.130)$$

Let us define

$$\bar{D} = \frac{g_s g_v}{2\pi\gamma^2} \int \left(-\frac{\partial f}{\partial \varepsilon} \right) |\varepsilon| d\varepsilon, \quad \cdots(2.131)$$

and the average function $\rho(\varepsilon)$ given by

$$\langle \rho(\varepsilon) \rangle \equiv \frac{1}{\bar{D}} \int \left(-\frac{\partial f}{\partial \varepsilon} \right) \frac{g_s g_v}{2\pi\gamma^2} |\varepsilon| \rho(\varepsilon) d\varepsilon. \quad \cdots(2.132)$$

Then, the diagonal conductivity and the Hall conductivity can be written as

$$\sigma_{xx} = \sigma_{yy} = \frac{e^2 \gamma^2}{2\hbar^2} \bar{D} \left\langle \frac{\tau}{1 + \omega_c^2 \tau^2} \right\rangle, \quad \cdots(2.133)$$

$$\sigma_{xy} = -\sigma_{yx} = -\frac{e^2 \gamma^2}{2\hbar^2} \bar{D} \left\langle \frac{\omega_c \tau^2}{1 + \omega_c^2 \tau^2} \right\rangle. \quad \cdots(2.134)$$

These equations are the same expressions with the case of conventional semiconductors or metals except that the cyclotron frequency is strongly dependent of the energy while the velocity remains independent.

2.2.4 Presence of magnetic field

Given that electrons in a material follow cyclotron motions when a magnetic field is applied to the system, the electronic structure of the material is modified. The unconventional electronic structure of graphene shows its modification in an unconventional manner under the presence of a magnetic field, leading to special electronic properties.

The electronic structure of graphene is considered under a magnetic field applied perpendicularly to the plane of graphene [6]. The wave number vector $\hat{\mathbf{k}} = -i\nabla$ needs to be replaced by $\hat{\mathbf{k}} = -i\nabla + (e/\hbar)\mathbf{A}$, where \mathbf{A} is a vector potential giving the magnetic field $\mathbf{B} = \text{rot}\mathbf{A}$. The commutation relation $[\hat{k}_x, \hat{k}_y] = -il^{-2}$ is obtained, where l is the magnetic length given by

$$l = \sqrt{\frac{\hbar}{eB}}. \quad \cdots(2.135)$$

Here B is the strength of the magnetic field and c is the speed of light. It is convenient to define two operators as

$$a = \left(\frac{l}{\sqrt{2}} \right) (\hat{k}_x - i\hat{k}_y), \quad \cdots(2.136)$$

$$a^\dagger = \left(\frac{l}{\sqrt{2}} \right) (\hat{k}_x + i\hat{k}_y). \quad \cdots(2.137)$$

These operators satisfy the commutation relation $[a, a^\dagger] = 1$. The Hamiltonian in the vicinity of the K point in Eq. (2.19) (*i.e.*, left-top 2×2 part) is

$$H_K = \begin{pmatrix} 0 & \gamma(\hat{k}_x - i\hat{k}_y) \\ \gamma(\hat{k}_x + i\hat{k}_y) & 0 \end{pmatrix}. \quad \cdots(2.138)$$

Therefore, by using Eqs. (2.136) and (2.137), this Hamiltonian can be rewritten as,

$$H = \frac{\sqrt{2}\gamma}{l} \begin{pmatrix} 0 & a \\ a^\dagger & 0 \end{pmatrix}. \quad \cdots(2.139)$$

Here, a function $h_n(x, y)$ with n being integer can be defined as

$$h_n(x, y) = \frac{(a^\dagger)^n}{\sqrt{n!}} h_0(x, y), \quad \cdots(2.140)$$

with

$$ah_0(x, y) = 0. \quad \cdots(2.141)$$

The relationships of the function $h_n(x, y)$ and the operators a and a^\dagger are as followings.

$$a^\dagger h_n = \sqrt{n+1} h_{n+1}, \quad \cdots(2.142)$$

$$ah_n = \sqrt{n}h_{n-1}, \quad \dots(2.143)$$

$$a^\dagger ah_n = nh_n. \quad \dots(2.144)$$

Thus, the wave function having the following form

$$F_K(\mathbf{r}) = \begin{pmatrix} 0 \\ h_0 \end{pmatrix}, \quad \dots(2.145)$$

is the wave function for $\varepsilon_0 = 0$. Other Landau levels have the energy

$$\varepsilon_n = \text{sgn}(n) \frac{\sqrt{2}\gamma}{l} \sqrt{|n|}, \quad \dots(2.146)$$

with wave functions

$$F_{K,n}(\mathbf{r}) = \frac{1}{\sqrt{2}} \begin{pmatrix} \text{sgn}(n)h_{|n|-1} \\ h_{|n|} \end{pmatrix}. \quad \dots(2.147)$$

The Hamiltonian in the vicinity of the K' point in Eq. (2.19) (*i.e.*, the right-bottom 2×2 part) is

$$H_{K'} = \begin{pmatrix} 0 & \gamma(\hat{k}_x + i\hat{k}_y) \\ \gamma(\hat{k}_x - i\hat{k}_y) & 0 \end{pmatrix}. \quad \dots(2.148)$$

Hence Eqs. (2.136) and (2.137) modify this Hamiltonian to

$$H = \frac{\sqrt{2}\gamma}{l} \begin{pmatrix} 0 & a^\dagger \\ a & 0 \end{pmatrix}. \quad \dots(2.149)$$

On the basis of the vicinity of the K point, the wave function and the energy for the K' point is given as

$$F_{K'}(\mathbf{r}) = \begin{pmatrix} h_0 \\ 0 \end{pmatrix} \quad (\varepsilon_0 = 0), \quad \dots(2.150)$$

$$F_{K',n}(\mathbf{r}) = \frac{1}{\sqrt{2}} \begin{pmatrix} h_{|n|} \\ \text{sgn}(n)h_{|n|-1} \end{pmatrix} \quad \left(\varepsilon_n = \text{sgn}(n) \frac{\sqrt{2}\gamma}{l} \sqrt{|n|} \right). \quad \dots(2.151)$$

Utilizing Eq. (2.12), $\gamma = \hbar v_F$, the energy is rewritten as

$$\varepsilon_n = \text{sgn}(n) \sqrt{2eB\hbar v_F^2 |n|}. \quad \dots(2.152)$$

The presence of the Landau level at $\varepsilon_0 = 0$ is independent of B . This zero-mode Landau level is a feature of massless Dirac fermion. For comparison, the Landau levels in conventional two-dimensional electrons with a parabolic dispersion relation is written as

$$\varepsilon_n = \hbar \omega_c \left(n + \frac{1}{2} \right), \quad \cdots (2.153)$$

where ω_c is the cyclotron frequency. Plots of the Landau levels for single-layer graphene and conventional two-dimensional systems under various B are shown in Fig. 2.10, including comparison with bilayer graphene.

Then, the Hall conductivity σ_{xy} in conventional two-dimensional system takes quantized value expressed as [21],

$$\sigma_{xy} = n \frac{e^2}{h}, \quad \cdots (2.154)$$

where h is the Planck constant. In bilayer graphene, which has a parabolic dispersion relation in the vicinity of the Fermi energy, quantum Hall effect with this conventional description was observed without having zero-mode plateau [22]. In contrast to bilayer graphene, the electronic structure of graphene is described in terms of the massless Dirac equation in the two-dimensional hexagonal bipartite lattice as written in Eqs. (2.13) or (2.24). The Landau levels of single-layer graphene is written in Eq. (2.152), leading to the Hall conductivity given by

$$\sigma_{xy} = \pm \frac{g_s g_v e^2}{h} \left(n + \frac{1}{2} \right). \quad \cdots (2.155)$$

g_s and g_v are the degeneracies of the spins and the valleys, respectively, both of which are equal to 2. This anomalous half-integer quantum Hall effect was verified [22,23] in the very beginning stage of experimental studies on mechanically exfoliated graphene. These reports [22,23] successfully evidenced the nature of the massless Dirac electrons in single-layer graphene.

2.2.5 Charged impurity scattering in graphene [18–20]

Here we consider the scattering events caused by charged impurities on graphene. For randomly distributed scatterers with potential $V(\mathbf{r})$ and concentration n_{imp} per unit area, the matrix elements can be written as

$$\left\langle \left| V_{\sigma' \mathbf{k}', \sigma \mathbf{k}} \right|^2 \right\rangle = n_{\text{imp}} \left| V(\mathbf{k}' - \mathbf{k}) (\mathbf{F}_{\sigma' \mathbf{k}'}^\dagger \cdot \mathbf{F}_{\sigma \mathbf{k}}) \right|^2, \quad \cdots (2.156)$$

with

$$(\mathbf{F}_{\sigma \mathbf{k}}^\dagger \cdot \mathbf{F}_{\sigma' \mathbf{k}'}) = \frac{1}{2} \left[\exp(i\theta_{\mathbf{k}} - i\theta_{\mathbf{k}'}) + \sigma \sigma' \right], \quad \cdots (2.157)$$

$$V(\mathbf{r}) = \int \frac{d\mathbf{q}}{(2\pi)^2} V(\mathbf{q}) \exp(i\mathbf{q} \cdot \mathbf{r}). \quad \cdots (2.158)$$

The transport relaxation time becomes

$$\frac{1}{\tau(\varepsilon)} = \frac{2\pi n_{\text{imp}}}{\hbar} \frac{|\varepsilon|}{2\pi\gamma^2} \int_0^\pi \frac{d\theta}{\pi} \frac{1}{2} (1 - \cos^2 \theta) |V(q)|^2, \quad \cdots (2.159)$$

where $|V(q)|^2$ is the average taken over different directions of impurities.

The electric potential created by an impurity with electrical charge e can be written in real space as

$$V(r) = \frac{e^2}{4\pi\kappa r}, \quad \cdots (2.160)$$

where r is the distance, and κ is the dielectric constant determined by environmental conditions. The Fourier transform of the potential is

$$V_i(q) = \frac{2\pi e^2}{\kappa q \varepsilon(q)}, \quad \cdots (2.161)$$

where $\varepsilon(q)$ is the dielectric function of graphene. The static dielectric function is written as

$$\varepsilon(q) = 1 + \frac{2\pi e^2}{\kappa q} \Pi(q), \quad \cdots (2.162)$$

with the polarization function given by

$$\Pi(q) = -\frac{g_s g_v}{L^2} \sum_{\sigma, \sigma', \mathbf{k}} (f_{\sigma \mathbf{k}} - f_{\sigma' \mathbf{k}+\mathbf{q}}) \frac{\left| (\mathbf{F}_{\sigma \mathbf{k}}^\dagger \cdot \mathbf{F}_{\sigma' \mathbf{k}+\mathbf{q}}) \right|^2}{\varepsilon_{\sigma \mathbf{k}} - \varepsilon_{\sigma' \mathbf{k}+\mathbf{q}}}. \quad \cdots (2.163)$$

The relaxation time is now written as

$$\frac{1}{\tau(\varepsilon)} = \frac{\pi g_s g_v n_{\text{imp}}}{n_s} \frac{|\varepsilon|}{\hbar} \int_0^\pi \frac{d\theta}{\pi} \frac{1}{2} (1 - \cos^2 \theta) |V(q)|^2, \quad \cdots (2.164)$$

where n_s is the concentration of charge carriers. At sufficiently low temperature, the polarization function can be described within the Thomas-Fermi approximation. Then,

$$\frac{1}{\tau(\varepsilon)} = \frac{\pi g_s g_v n_{\text{imp}} |\varepsilon|}{n_s \hbar} \int_0^\pi \frac{d\theta}{\pi} \frac{1}{2} (1 - \cos^2 \theta) \left(g_s g_v + \frac{\kappa \gamma}{e^2} \frac{q}{k_F} \right)^{-2}. \quad \cdots(2.165)$$

The conductivity and the mobility is described as

$$\sigma_{\text{imp}} = \frac{e^2}{4\pi^2 \hbar} \frac{n_s}{n_{\text{imp}}} \left[\int_0^\pi \frac{d\theta}{\pi} \frac{1}{2} (1 - \cos^2 \theta) \left(g_s g_v + \frac{\kappa \gamma}{e^2} \frac{q}{k_F} \right)^{-2} \right]^{-1}, \quad \cdots(2.166)$$

$$\mu_{\text{imp}} = \frac{e}{4\pi^2 \hbar n_{\text{imp}}} \left[\int_0^\pi \frac{d\theta}{\pi} \frac{1}{2} (1 - \cos^2 \theta) \left(g_s g_v + \frac{\kappa \gamma}{e^2} \frac{q}{k_F} \right)^{-2} \right]^{-1}. \quad \cdots(2.167)$$

The conductivity is linearly dependent of the carrier density, whereas the mobility is independent. Practically, the following form is employed for convenience [24],

$$\sigma_{\text{imp}}(n) = C e \left| \frac{n_s}{n_{\text{imp}}} \right|, \quad \cdots(2.168)$$

where C is a constant. Hwang *et al.* [19] calculated the screened Coulomb potential and C was determined to be $C = 5 \times 10^{15} \text{ V}^{-1} \text{ s}^{-1}$, then, this value was experimentally verified for single-layer graphene [24].

2.2.6 Lattice defect scattering in graphene [20]

Atomic-scale vacancies, edges, or grain boundaries in graphene lattice produce strong potential and give rise to bound states like donor or acceptor states in the vicinity of the Dirac point. These states change the density of states near the Dirac point. Since the density of states in ideal single-layer graphene is zero at the Dirac point, the appearance of localized states induced by impurities give significant contributions to the electronic properties of graphene.

The overlap between the Slater determinants which describe the electronic wave function before and after an introduction of an impurity potential can be reportedly characterized by the number of electrons and the phase shift induced by the potential in the scattered waves at the Fermi level with angular momentum. Scattering from vacancies leads to the following phase shift,

$$\delta_k = -\frac{\pi}{2} \frac{1}{\ln(kR_0)}, \quad \cdots(2.169)$$

where R_0 is the radius of the potential created by a vacancy. For this phase shift with $kR_0 \ll 1$, the relaxation time of scattering is written as

$$\tau_k = \frac{\hbar \rho(E_k)}{2\pi n_{\text{vacancy}}} (\ln kR_0)^2, \quad \dots (2.170)$$

where $\rho(E_k)$ is the density of states at energy E_k , and n_{vacancy} is the concentration of vacancies per unit area. In the case of clean graphene,

$$\rho(E_k) = \frac{g_s g_v |E|}{2\pi (\hbar v_F)^2}, \quad \dots (2.171)$$

where g_s and g_v are the spin and the valley degeneracies, respectively, and v_F is the Fermi velocity in graphene. Thus,

$$\tau_k = \frac{\hbar}{2\pi n_{\text{vacancy}}} \frac{2\hbar v_F k}{\pi (\hbar v_F)^2} (\ln kR_0)^2 = \frac{k}{\pi^2 v_F n_{\text{vacancy}}} (\ln kR_0)^2, \quad \dots (2.172)$$

is led. The logarithmic multiplication leads to a sublinear density dependence of the conductivity,

$$\sigma_{\text{vacancy}} = \frac{2e^2}{h} v_F k_F \tau_F = \frac{2e^2}{h\pi} \frac{n}{n_{\text{vacancy}}} (\ln k_F R_0)^2, \quad \dots (2.173)$$

and the mobility,

$$\mu_{\text{vacancy}} = \frac{2e}{h\pi n_{\text{vacancy}}} (\ln k_F R_0)^2. \quad \dots (2.174)$$

These expressions of the conductivity and the mobility have been experimentally validated [25].

2.3 Nanographene

2.3.1 Geometrical structure of nanographene

Thus far, graphene that have infinite spreading of honeycomb structure has been highlighted. In contrast, graphene having nanometer-scale semi-infinite structure can be regarded an intermediate material between benzene and its derivative molecules and infinite graphene. This semi-infinite-sized graphene has been called as nanographene, and the significance of understanding electronic and magnetic properties of nanographene has been strongly recognized recently. What makes nanographene attractive is its possession of edges [21,26,27].

To the simplest understanding, a nanographene is a graphene cut into small fragment. The structures of nanographene edges are characterized by two types of atomic arrangements having zigzag or armchair shapes, as shown in Fig. 2.11. The presence of electronic state localized at zigzag-shaped edges was theoretically predicted [26,27]. This electronic state is named as the edge state. In general, electronic states appear at crystal surface because the translational symmetry is broken at the surface in the direction perpendicular to the surface plane. For example, semiconductor surface is likely to have surface states that are mainly originated from the presence of dangling bonds [28]. The edge state of graphene seems to have the same origin since in a sense edges can be regarded as a surface in two-dimensional graphene. It can be thought that surface states due to dangling bonds can split into bonding and antibonding states upon terminations of dangling bonds by functional groups, and that states near the Fermi energy do not survive. In graphene, however, edge states do exist with not only dangling bonds but also various functional groups at zigzag edges, although their characteristics, such as dispersion relations, spatial distributions, magnetic properties, and so forth, changes drastically depending upon functional groups.

In order to describe electronic states depending on edge structures of nanographene, it is convenient to use nanoribbon structures that have infinite length and finite width with edge atoms arranged in zigzag- or armchair-shaped forms. The structures of these zigzag or armchair graphene nanoribbons are shown in Fig. 2.12. In Figs. 2.12a and 2.12b, the dashed rectangles denote the unit cells of zigzag and armchair nanoribbons, respectively. Translational vectors of unit cells for armchair- and zigzag-ribbons are represented in Fig. 2.12c as **c** and **d**, respectively, where primitive lattice vectors are taken as **a** and **b**,

$$\mathbf{a} = \left(-\frac{\sqrt{3}a}{2}, \frac{a}{2} \right), \quad \cdots(2.175)$$

$$\mathbf{b} = \left(\frac{\sqrt{3}a}{2}, \frac{a}{2} \right), \quad \cdots(2.176)$$

$$\mathbf{c} = (\sqrt{3}a, 0), \quad \cdots(2.177)$$

$$\mathbf{d} = (0, a), \quad \cdots(2.178)$$

with $a = |\mathbf{a}| = |\mathbf{b}|$. Corresponding reciprocal lattice vectors are written as

$$\mathbf{a}^* = \frac{2\pi}{\sqrt{3}a} (-1, \sqrt{3}), \quad \cdots(2.179)$$

$$\mathbf{b}^* = \frac{2\pi}{\sqrt{3}a} (1, \sqrt{3}), \quad \cdots(2.180)$$

$$\mathbf{c}^* = \frac{2\pi}{\sqrt{3}a} (1, 0), \quad \cdots(2.181)$$

$$\mathbf{d}^* = \frac{2\pi}{a} (0, 1), \quad \cdots(2.182)$$

which are shown in Fig. 2.12d.

In fact, energy band structures of graphene nanoribbons can be simply speculated from the band structure of graphene. A rectangular Brillouin zone that are defined by the reciprocal vectors \mathbf{c}^* and \mathbf{d}^* have a half area of that of infinite graphene, as shown in Fig. 2.12d. The longer (\mathbf{d}^*) and shorter (\mathbf{c}^*) sides of this rectangular Brillouin zone correspond to one-dimensional Brillouin zones of zigzag and armchair nanoribbons, respectively. Energy band structures of zigzag and armchair nanoribbons are suggested to be the projections of band structure of graphene to \mathbf{d}^* and \mathbf{c}^* axes, respectively, as shown in Fig. 2.13 [29]. Namely, a K point of graphene is projected at the Γ point ($k = 0$) for armchair nanoribbon, and at $k = \pm 2\pi/3$ for zigzag nanoribbon.

2.3.2 Chemical and physical aspects of edge state in nanographene [21]

In this section, the edge state of graphene is considered firstly from the chemical point of view, namely in terms of the relationship between aromaticity in small

hydrocarbon molecules and the edge state. The most simple and typical Kekulé molecule is benzene, which is the primary unit of graphene. Molecular orbitals of benzene near the Fermi level are three bonding π orbitals and three antibonding π^* orbitals with a large energy gap between the highest occupied molecular orbital (HOMO) and the lowest unoccupied molecular orbital (LUMO), as shown in Fig. 2.14a. On fusing benzene rings into condensed polycyclic aromatic hydrocarbon molecules, the Kekulé structure with a large HOMO–LUMO energy gap is generally conserved. However, benzene rings can be fused with each other to form non-Kekulé molecules, in which aromatic stabilization fails.

The simplest example is a phenalene molecule. A phenalene molecule consists of three benzene rings arranged in a triangular shape, as shown in Fig. 2.14b. In a phenalene, a half-filled extra π electronic state is present at the Fermi level in the energy gap as a nonbonding π electronic state, which decrease the stability and increase the reactivity. According to Clar's aromatic sextet rule, counting the number of nonbonding π electronic states allows us to discuss comprehensively the aromatic stability of condensed aromatic hydrocarbon molecules. The structure of a polycyclic hydrocarbon molecule is written by tiling aromatic sextets. The aromatic stability is estimated by the number of aromatic sextets tiled on the concerned molecule, and the structure that has the largest number of aromatic sextets is more stable than any other possible structures. A good example should be graphene, which has one aromatic sextet on every three hexagons in the manner of arrangement of a $\sqrt{3} \times \sqrt{3}$ rhombic superstructure as shown in Fig. 2.14c, so that the aromatic stability of graphene is expected to be one third of that of a benzene molecule.

Figure 2.15a shows polycyclic aromatic molecules having armchair-shaped edges. Molecules having 1, 3, 4, and 13 hexagonal rings have 1, 2, 3, and 7 aromatic sextets, respectively. These molecules with armchair-shaped edges are well stabilized as closed shell systems without the nonbonding π -electron state. On the other hand, polycyclic molecules having zigzag-shaped edges have usually small numbers of aromatic sextets. A few examples of zigzag-edged molecules having triangular shapes are on display in Fig. 2.15b. Triangular molecules with 3, 6, and 10 hexagonal rings have only 1, 2, and 4 aromatic sextets, respectively. In addition, these triangular molecules have 1, 2, and 3 nonbonding π electrons, respectively. Thus, it can be understood that polycyclic aromatic molecules with zigzag-shaped edges are open shell systems with the nonbonding π states that locate in the energy gap. It should be noted that spatial distribution of HOMO in

molecules with zigzag edges is mainly populated in zigzag edge region, not in the interior region, as shown in Fig. 2.16 [30]. This large population at the edges is the reason why the nonbonding π electronic state is called as the edge state. In contrast, the armchair-edged molecule has spatially homogeneous distribution as shown in Fig. 2.16 [30]. It should be also noticed that the edge state is magnetic since it is half-filled. In other words, zigzag-edged polycyclic molecules have localized spin states distributed at their edges. Lieb's theorem is helpful for counting the spin states. The spin states are given by $S = (1/2)|N_{\text{starred}} - N_{\text{unstarred}}|$, where N_{starred} and $N_{\text{unstarred}}$ are the numbers of starred and unstarred carbon atoms, respectively, which are the sites belonging to a given subgroup (starred (unstarred)) directly bonded to the sites belonging to another subgroup (unstarred (starred)). Some examples are shown in Fig. 2.17. Polycyclic molecules having armchair-shaped edges in Fig. 2.17a have $S = 0$ as a consequence of $N_{\text{starred}} = N_{\text{unstarred}}$. The triangular molecules consisting of 3, 6, and 10 hexagonal rings have the spin states of $S = 1/2$, 1, and $3/2$, respectively as shown in Fig. 2.17b, so that electronic spin ordering in these molecules can be ferromagnetic. Clar's rule can be applied to nanographene, which is simply regarded as larger polycyclic aromatic hydrocarbon molecule.

It has been shown that the edge state of nanographene can be understood as nonbonding π -electron state from the viewpoint of chemistry. The edge state can be explained in other words. The honeycomb structure of graphene lattice is described in terms of the bipartite lattice which consists of two distinct sublattices labelled as A and B, as discussed before. In infinitely spread graphene, the energy band spectrum is described by the relativistic massless Dirac equation having linear dependence on momentum as $E = v_F \sigma \mathbf{p}$, where v_F is the Fermi velocity, \mathbf{p} is the momentum, and σ is the Pauli spin matrices for a pseudospin, which comes from the degree of freedom 2 in the bipartite lattice. The pseudospin is not the real electronic spin, although it can be coupled with a magnetic field via the transformation of \mathbf{p} to $\mathbf{p} + e\mathbf{A}$ (\mathbf{A} is the corresponding potential), resulting in similar behavior with the real spin. Even in the absence of an external magnetic field, structural disorders can induce an additional field. The most typical example should be edges of nanographene. In the case of zigzag edges, only one of the sublattices, namely A or B, locates at the edge, whereas armchair-shaped edges always have the pair of A and B sublattices. This fact means that the symmetry of the pseudospin is broken in the zigzag edge, resulting in the creation of the magnetic edge state.

2.3.3 Electronic structures of zigzag and armchair graphene nanoribbons [29]

The electronic structures of zigzag and armchair graphene nanoribbons, of which geometrical structures are shown in Figs. 2.12a and 2.12b, respectively, are considered under the assumption that each edge carbon atom is terminated by one hydrogen atom. The widths (N) of the armchair and the zigzag nanoribbons are defined as the number of the dimer lines for armchair one, and as the number of the zigzag lines for zigzag one. The sublattices A and B in the n -th line are labelled as nA and nB , respectively. Attention should be paid to the fact that the widths of N -wide armchair and zigzag nanoribbons are different from each other if the widths are measured in the same unit of length, namely,

$$W = \begin{cases} \frac{\sqrt{3}}{2}Na - \frac{a}{\sqrt{3}} \equiv W_z & (\text{zigzag nanoribbons}) \\ \frac{a}{2}(N-1) \equiv W_a & (\text{armchair nanoribbons}) \end{cases}, \quad \cdots(2.183)$$

where W , W_z , and W_a are the widths in the scale of length (e.g. nanometer), and a is the lattice constant. For the following calculations, the honeycomb lattice of graphene is transformed into the brick-type lattice for simplicity, as shown in Fig. 2.18 [29]. This transformation does not change the topology of the lattice.

The Schrödinger equation of graphene having translational symmetry along the zigzag direction is considered. A creation operator can be defined as following,

$$c_\alpha(i) = \frac{1}{\sqrt{L}} \sum_k \exp[ik_y r_{\alpha i}] \gamma_k(i), \quad \cdots(2.184)$$

meaning creation of an electron on the site i in the unit cell α . $r_{\alpha i}$ is the coordinate of the site i in the unit cell α . The one-particle wave function can be defined as

$$|\Psi(k)\rangle = \sum_m [\Psi_{mA}(k) \gamma_k^\dagger(mA) + \Psi_{mB}(k) \gamma_k^\dagger(mB)] |0\rangle. \quad \cdots(2.185)$$

Putting Eqs. (2.184) and (2.185) into the Schrödinger equation $H\Psi = E\Psi$, three equations are derived,

$$\varepsilon \Psi_{mB} = \Psi_{(m+1)A} + \exp\left[i2\pi \frac{m}{2} \phi\right] \Psi_{mA} + \exp\left[-i2\pi \frac{m}{2} \phi\right] \Psi_{mA}, \quad \cdots(2.186)$$

$$\varepsilon \Psi_{mA} = \Psi_{(m-1)B} + \exp\left[i2\pi \frac{m}{2} \phi\right] \Psi_{mB} + \exp\left[-i2\pi \frac{m}{2} \phi\right] \Psi_{mB}, \quad \cdots(2.187)$$

$$\varepsilon \Psi_{(m+1)A} = \Psi_{mB} + \exp\left[i2\pi \frac{m}{2} \phi\right] \Psi_{(m+1)B} + \exp\left[-i2\pi \frac{m}{2} \phi\right] \Psi_{(m+1)B}, \quad \cdots(2.188)$$

where ε is the eigen energy, and ϕ is the magnetic flux. The terms relevant to the site

A can be removed, leading to

$$\lambda \Psi_m(k_y) = a_m \Psi_{m+1}(k_y) + b_m \Psi_m(k_y) + a_{m-1} \Psi_{m-1}(k_y), \quad \cdots (2.189)$$

where $\lambda = \varepsilon^2 - 3$, $a_m(k_y) = 2 \cos(k_y / 2 + m\pi\phi)$, and $b_m(k_y) = 2 \cos(k_y + 2m\pi\phi)$. Ψ_{mB} is written as Ψ_m in this equation. If ϕ is assumed to be an irreducible fraction $\phi = p/q$, Eq. (2.189) can be regarded as a simple one-dimensional tight-binding model for the superperiodic lattice with $2q$ periodicity in x -direction. For the convenience, $m\pi\phi$ needs to be replaced by $[(N-1)/2 - m + 1]\pi\phi$ to keep the symmetry of the band structure at the Γ point. This replacement corresponds to set the origin of the x -axis on the center of the target zigzag graphene nanoribbons. The band structure is invariant for the operations $\varepsilon \rightarrow -\varepsilon$ and $\phi \rightarrow \phi + n$ (n is integer). The band structure in the Brillouin zone has the following symmetry.

$$\varepsilon\left(k_y + \frac{2\pi}{q}\right) = \varepsilon(k_y). \quad \cdots (2.190)$$

The similar calculations lead to the similar equation to Eq. (2.189) for the armchair direction, given by

$$\lambda \Psi_m(k_y) = \Psi_{m+2}(k_y) + a_m \Psi_{m+1}(k_y) + a_m \Psi_{m-1}(k_y) + \Psi_{m-2}(k_y), \quad \cdots (2.191)$$

where $\lambda = \varepsilon^2 - 3$, and $a_m(k_y) = 2 \cos[k_y / 2 + (m-1/2)\pi\phi] \exp[-i\pi\phi/2]$. In this case of the armchair direction, the symmetry of the band structure at the Γ point is retained by the replacement of $a_m(k_y) = 2 \cos[k_y / 2 + \{(N-1)/2 - 2m + 3\}\pi\phi] \exp[-i\pi\phi]$.

No boundary condition has been imposed yet. We can chose appropriate boundary conditions for target situation. Above descriptions can be applied to graphene sheet under appropriate conditions.

Infinite graphene sheet

Taking translational invariance along x direction into account, the following solutions are given from Eqs. (2.189) and (2.191),

$$\varepsilon = \pm \sqrt{3 + 2 \cos(k_y) + 4 \cos\left(\frac{k_y}{2}\right) \cos(k_x)}, \quad (\text{zigzag}) \quad \cdots (2.192)$$

$$\varepsilon = \pm \sqrt{3 + 2 \cos(2k_x) + 4 \cos\left(\frac{k_y}{2}\right) \cos(k_x)}, \quad (\text{armchair}) \quad \cdots(2.193)$$

with no magnetic field ($\phi = 0$). In fact, it can be shown that the energy band structures expressed by Eqs. (2.192) and (2.193) have the same shapes with the projections of the band structure of infinite graphene sheet to zigzag and armchair directions, as already shown in Fig. 2.13 [29]. The linear dispersion relation in graphene can be seen in the vicinities of $k = \pm 2\pi/3$ for zigzag and of $k = 0$ for armchair.

Edge state of zigzag graphene nanoribbon

Next, Eq. (2.189) is applied to the zigzag graphene nanoribbon having the width of N . Equation (2.189) can be rewritten in the following transfer-matrix from,

$$\begin{pmatrix} \Psi_{m+1} \\ \Psi_m \end{pmatrix} = \begin{pmatrix} \frac{1}{a_m}(\lambda - \tilde{b}_m) & \frac{a_{m-1}}{a_m} \\ 1 & 0 \end{pmatrix} \begin{pmatrix} \Psi_m \\ \Psi_{m-1} \end{pmatrix}, \quad \cdots(2.194)$$

with

$$\tilde{b}_m = \begin{cases} b_m - 1 & (m = 1, N) \\ b_m & (\text{the other}) \end{cases}, \quad \cdots(2.195)$$

under the boundary conditions of the steep potential barriers with the infinite energy height along the zigzag lines 0 and $N+1$ ($\Psi_0 = \Psi_{N+1} = 0$),

$$\begin{pmatrix} \Psi_1 \\ \Psi_0 \end{pmatrix} = \begin{pmatrix} 1 \\ 0 \end{pmatrix}. \quad \cdots(2.196)$$

When the energy is zero ($\varepsilon = 0$), the amplitude of the wave function of a π electron at the n -th site counted from the zigzag edge is given by

$$\Psi_n = D_k^{n-1}, \quad \cdots(2.197)$$

$$D_k = -2 \cos\left(\frac{k}{2}\right). \quad \cdots(2.198)$$

Here, $|D_k| \leq 1$ is required for the convergence. In order to satisfy this condition, the range of the wave number is limited in $2\pi/3 \leq k \leq \pi$ (or $-\pi \leq k \leq -2\pi/3$). This condition

provides the flat dispersion at the Fermi energy of graphene ($\varepsilon = 0$). The two-dimensional mappings of the squared amplitude of Ψ_n with various wave numbers are shown in Fig. 2.19 [29]. The edge state is absolutely localized at the zigzag edge with $k = \pi$. It starts to penetrate toward the interior of the graphene sheet with k changing from π to $2\pi/3$. Then, ultimately it becomes delocalized with $k = 2\pi/3$.

When the edge states of the zigzag nanoribbon having the width of N are considered, the edge states arise from both edges with overlapping each other. This overlap results in the energetic separation of the edge states into bonding and antibonding states. This is equivalent to the generation of the energy band gap. The magnitude of the overlap is dependent of N as well as k . Equation (2.197) enables us to express the amplitude of the wave function on the n -th zigzag line counted from the 1st line as

$$\Psi_n = D_k^{n-1} \equiv \Psi_A, \quad \cdots(2.199)$$

which is the wave function localized only on the A sites. In contrast, the amplitude of the wave function on the n -th line counted from the N -th line is given by

$$\Psi_{N-n} = D_k^{n-1} \equiv \Psi_B, \quad \cdots(2.200)$$

which is localized only on the B sites. The eigen energy of the edge states E_k can be calculated from the matrix element $\sum \langle \Psi_A | H | \Psi_B \rangle$ by taking the summation for the entire carbon sites in the unit cell as

$$\sum \langle \Psi_A | H | \Psi_B \rangle = -2tND_k^{N-1} \left(1 - \frac{D_k}{2} \right) = T_k, \quad \cdots(2.201)$$

therefore,

$$\begin{pmatrix} 0 & T_k \\ T_k & 0 \end{pmatrix} \begin{pmatrix} C_1 \\ C_2 \end{pmatrix} = E_k \begin{pmatrix} C_1 \\ C_2 \end{pmatrix}, \quad \cdots(2.202)$$

$$E_k = \pm 2tND_k^{N-1} \left(1 - \frac{D_k}{2} \right). \quad \cdots(2.203)$$

Here t is the transfer integral. The positive and the negative signatures correspond to the conduction and the valence bands, respectively. The density of states related to the edge states ($\rho(E_k)$) is given by

$$\rho(E_k) = \frac{\partial k}{\partial E_k} \sim \frac{1}{N} E_k^\alpha, \quad \cdots(2.204)$$

where $\alpha = 1/N - 1$. $\rho(E_k)$ has the dependence on $1/N$. If the width of the zigzag

nanoribbon is too narrow, the overlap between the edge states from two edges is so effective that the edge states are shifted from the Fermi energy and the number of the edge states decreases. On the other hand, increasing N means approaching to infinite graphene sheet, in which the contribution of the edge state is negligibly small. A numerical calculation revealed that the contribution of the edge state is likely to be the most effective in the nanoribbon having $N = 7$ (i.e., approximately as narrow as 1.3 nm) [27].

Energy band gap of zigzag graphene nanoribbon at $k = 2\pi/3$

As described above, zigzag graphene nanoribbon possesses the edge states at two edges. The energy of the edge states are $\varepsilon = 0$ at $k = \pi$, resulting in the absence of the energy band gap. In contrast, when k approaches from π to $2\pi/3$, the overlap of the edge states can cause the splitting into bonding and antibonding states with gap. The Hamiltonian for zigzag graphene nanoribbons at $k = \pm 2\pi/3$ is given by

$$H = -t \sum_{i=1}^{2N} (a_i^\dagger a_{i+1} + h.c.), \quad \cdots (2.205)$$

which is equivalent to the case for one-dimensional chain model having $2N$ lattice sites. Odd i corresponds to iA , and even one does iB . The Hamiltonian Eq. (2.205) gives the eigen energy and the eigen function

$$\varepsilon = -2t \cos\left(\frac{n\pi}{2N+1}\right), \quad n = 1, 2, \dots, 2N \quad \cdots (2.206)$$

$$\Psi_j = B \sin\left(\frac{nj\pi}{2N+1}\right), \quad \cdots (2.207)$$

where Ψ_j is the eigen function at the j -th site, and B is a normalization coefficient. The energy band gap (Δ_z) is given as the energy difference between $n = N$ and $N + 1$,

$$\Delta_z = 4t \cos\left(\frac{N\pi}{2N+1}\right). \quad \cdots (2.208)$$

Using W_z in Eq. (2.183) and expanding Eq. (2.208) under $1/N \ll 1$, Eq. (2.208) is rewritten as

$$\Delta_z \sim \frac{\pi}{N} = \frac{\sqrt{3}}{2} \frac{\pi}{\frac{W_z}{a} + \frac{1}{\sqrt{3}}}. \quad \cdots (2.209)$$

As expected, when W_z approaches to infinity, the energy gap becomes zero, as in the case

of infinite graphene sheet.

Armchair graphene nanoribbons

The Hamiltonian for armchair graphene nanoribbon at the Γ point is written as

$$H = -t \sum_{j=1}^N \left[\sum_{\mu=1}^2 \left(a_{j,\mu}^\dagger a_{j+1,\mu} + h.c. \right) + a_{j,1}^\dagger a_{j,2} + h.c. \right], \quad \cdots(2.210)$$

which is equivalent to the tight-binding Hamiltonian in the case of the ladder model with N rungs as shown in Fig. 2.20. The index $\mu = 1, 2$ has the same meaning as the sublattice A and B in the structure of graphene. The eigen energy and the eigen function are given by

$$\varepsilon^\pm = -2t \cos\left(\frac{n\pi}{N+1}\right) \pm t, \quad n = 1, 2, \dots, N \quad \cdots(2.211)$$

$$\Psi_{j,\mu} = (\mp 1)^{\mu+1} B \sin\left(\frac{nj\pi}{N+1}\right), \quad \cdots(2.212)$$

where B is the normalization coefficient. As a consequence, it is found that the system is metallic (i.e., zero band gap) when $3m-1$ because the energy levels ε^+ or ε^- can be zero for $n = m$ and $2m$. Therefore, the energy band gap of the armchair graphene nanoribbon (Δ_a) having the width of N is summarized as

$$\Delta_a = \begin{cases} 0 & (N = 3m-1) \\ 2 \left[2t \cos\left(\frac{m+1}{3m+1}\pi\right) - t \right] & (N = 3m) \\ 2 \left[2t \cos\left(\frac{m+1}{3m+2}\pi\right) - t \right] & (N = 3m+1) \end{cases} \quad \cdots(2.213)$$

Using W_a in Eq. (2.183) and expanding Eq. (2.213) under $1/N \ll 1$, the followings are obtained.

$$\Delta_a \sim \begin{cases} 0 & (N = 3m-1) \\ \frac{\pi}{W_a + 3} & (N = 3m) \\ \frac{\pi}{W_a} & (N = 3m+1) \end{cases} \quad \cdots(2.214)$$

Thus, it can be clearly understood that Δ_a is inversely proportional to W_a .

Ultimately, Fig. 2.21 represents the electronic energy band structure of graphene nanoribbons having armchair- or zigzag-shaped edges with the width of $N = 20$ [26]. Figure 2.21 should be compared with Fig. 2.13, which shows the band structures obtained by simply projecting that of graphene. The band structures of the armchair nanoribbon (Figs. 2.13b and 2.21a) have the similar dispersion relation. Those of the zigzag nanoribbon (Figs. 2.13a and 2.21b) are also similar with each other except for the presence of additional state in the vicinity of the Fermi energy in Fig. 2.21b. This state is the edge state, which has been derived in above descriptions.

2.4 Figures in Chapter 2

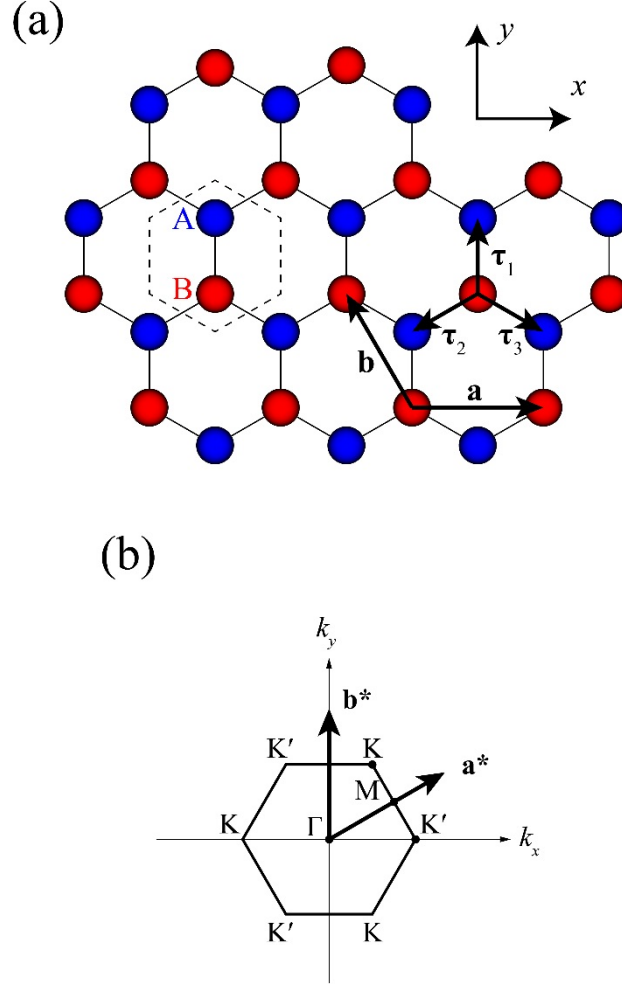


Figure 2.1. (a) The honeycomb structure of single-layer graphene. The sublattices A and B are denoted as the blue and the red circles, respectively. The unit cell is represented as the dashed hexagon. The lattice vectors are denoted as \mathbf{a} and \mathbf{b} . The vectors from a certain atom toward three neighboring sites are denoted as $\boldsymbol{\tau}_1$, $\boldsymbol{\tau}_2$, and $\boldsymbol{\tau}_3$. (b) The first Brillouin zone. \mathbf{a}^* and \mathbf{b}^* are the reciprocal lattice vectors.

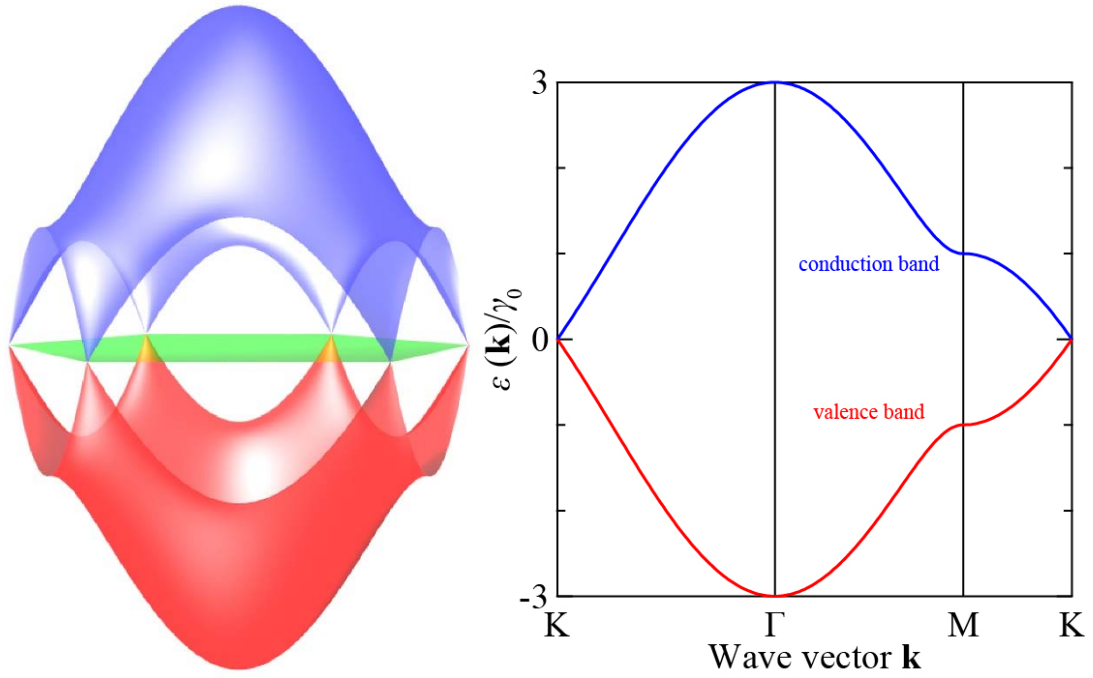


Figure 2.2. The dispersion of the electronic energy band of single-layer graphene plotted on the basis of Eq. (2.11). The green hexagon denotes the Brillouin zone. The red and the blue bands correspond to the valence and the conduction bands, respectively.

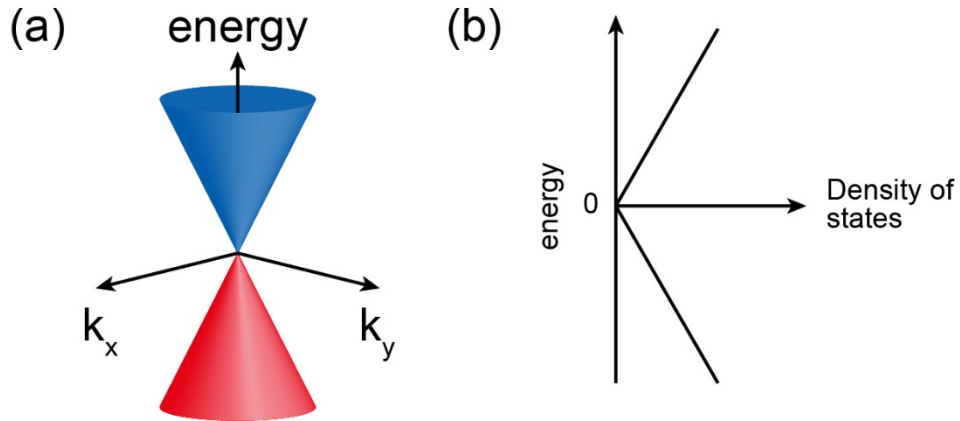


Figure 2.3. (a) The electronic energy band structure of single-layer graphene in the vicinity of the K point. The point at which the valence and the conduction bands touches each other is called the Dirac point. (b) The density of states plotted with respect to the energy.

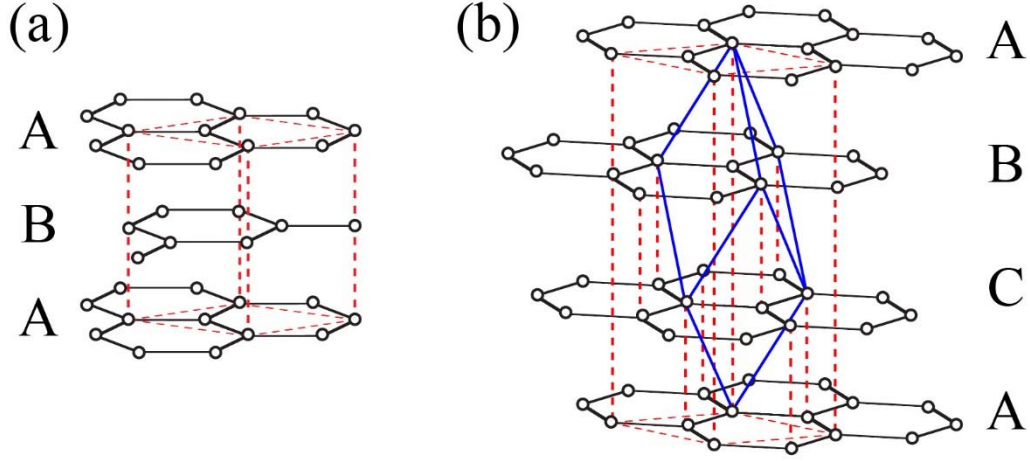


Figure 2.4. The regularities of (a) the AB stacking and (b) the ABC stacking.

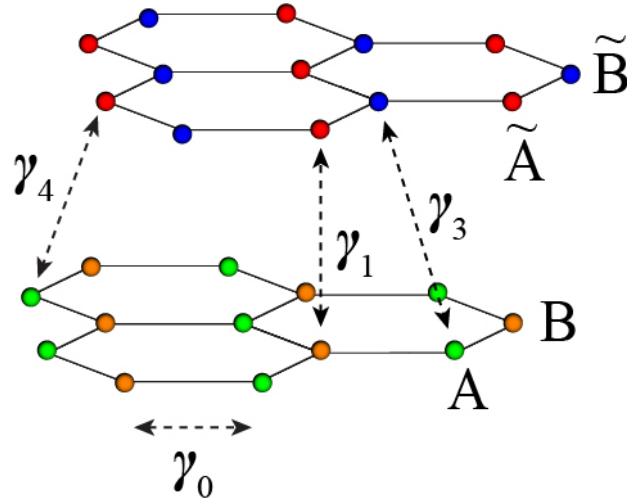


Figure 2.5. The AB stacking structure of bilayer graphene with various transfer integrals: $\gamma_0 = 3$ eV [3] is between the nearest neighbor carbon atoms A and B; $\gamma_1 = 0.39$ eV [8] is between the vertically neighboring pair $\tilde{A}-B$; $\gamma_3 = 0.32$ eV [7] is between \tilde{B} and A; $\gamma_4 = 0.04$ eV [9] is between the pair $\tilde{A}-A$ ($\tilde{B}-B$).

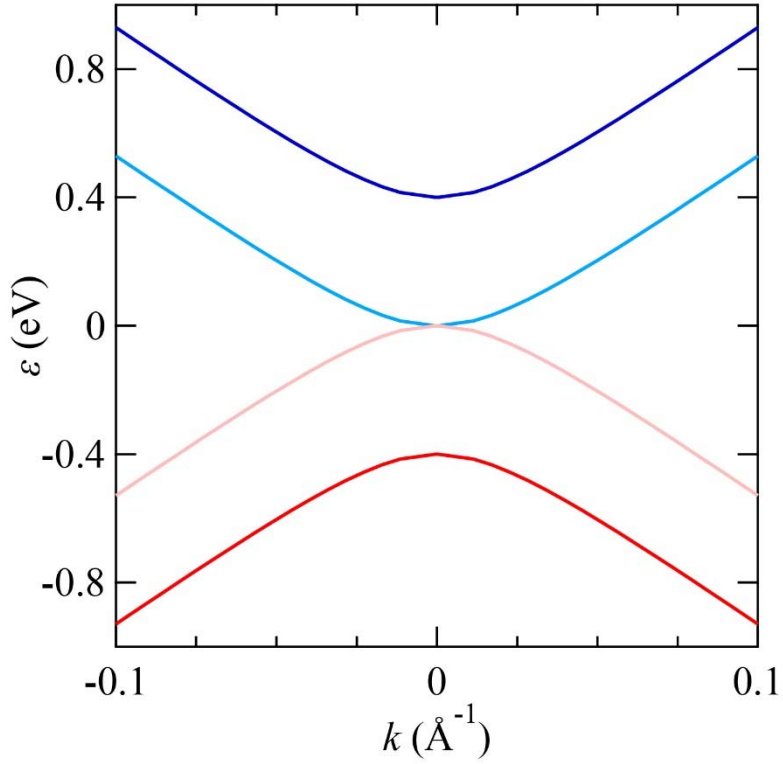


Figure 2.6. The electronic energy band of bilayer graphene in the vicinity of the K point described by Eq. (2.27) under $\gamma_1 = 0.40$ eV, $\gamma_3 = 0$ eV, and $u = 0$. The blue and the light-blue bands represent the high- and the low-energy conduction bands, respectively. The red and the pink bands represent the high- and the low-energy valence bands, respectively.

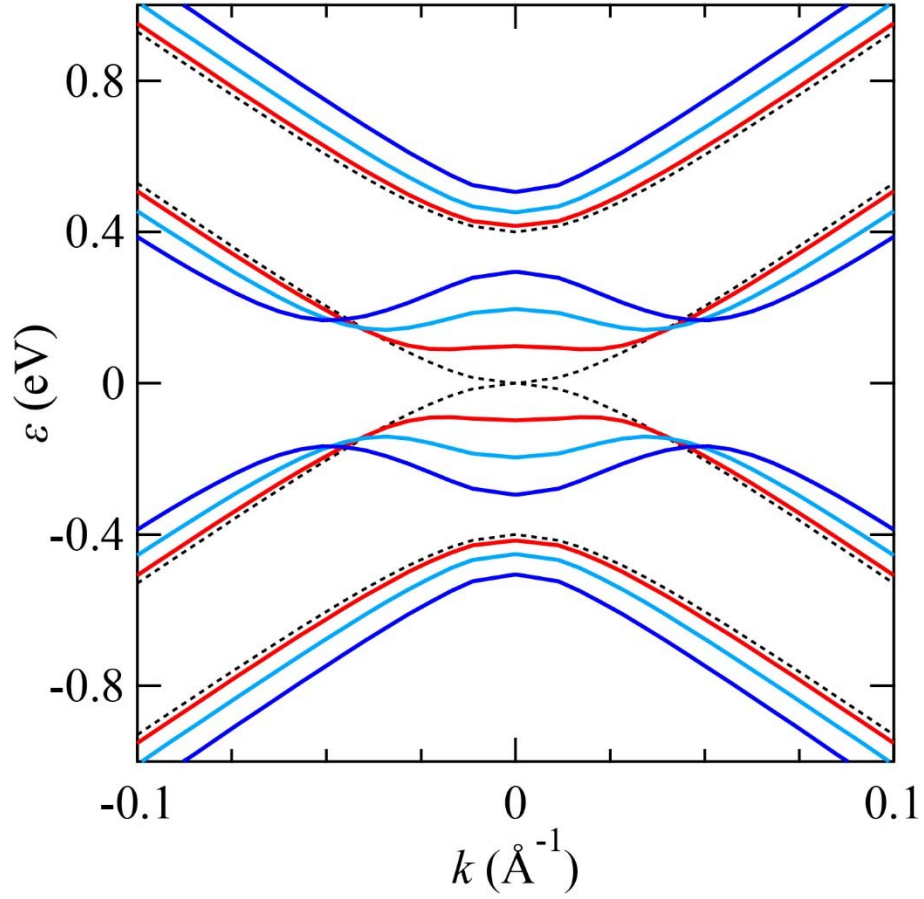


Figure 2.7. The electronic energy band of bilayer graphene in the vicinity of the K point described by Eq. (2.27) under $\gamma_1 = 0.40$ eV, $\gamma_3 = 0$ eV with $u = 0$ (dotted curves), 0.2 (red curves), 0.4 (light-blue curves), and 0.6 (blue curves).

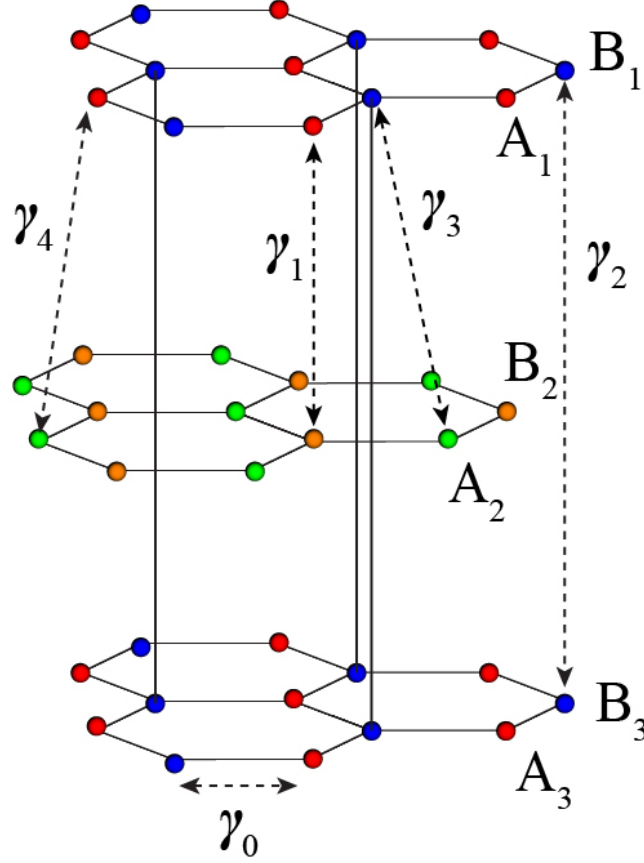


Figure 2.8. The AB stacking structure of multilayer graphene with various transfer integrals. In addition to γ_0 , γ_1 , γ_3 , and γ_4 , there is an interaction between atoms in the top and the bottom layers B_1 – B_3 , which is denoted as $\gamma_2 = -0.02$ eV [7].

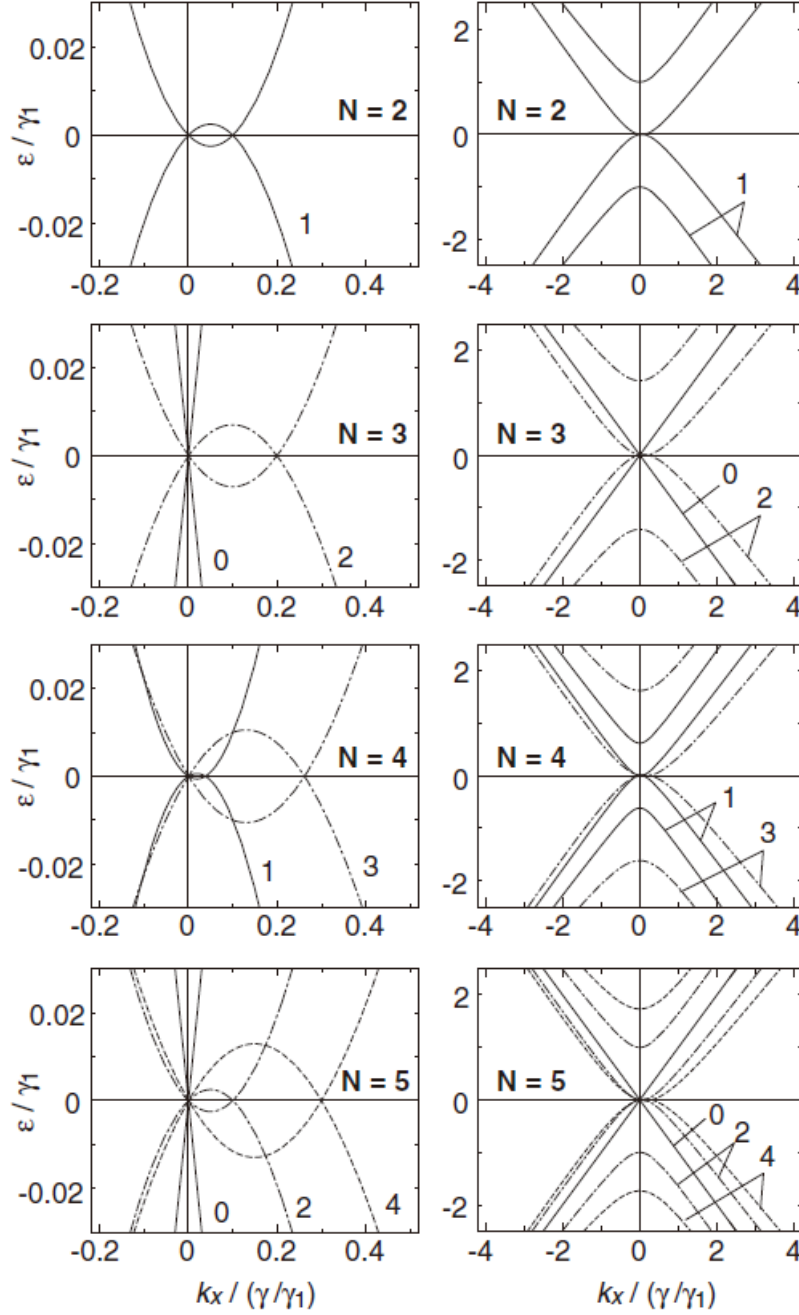


Figure 2.9. Band structures of N -layer graphenes ($N = 2, 3, 4$, and 5) with $\gamma_3/\gamma_0 = 0.1$, around the K point (taken as origin) along the k_x axis. Right panel shows a zoom out of the left. Numbers assigned to curves indicate m . Reprinted figure with permission from M. Koshino and T. Ando, Orbital diamagnetism in multilayer graphenes: systematic study with the effective mass approximation, *Physical Review B* **76**, 085425 (2007) [16]. Copyright (2006) by the American Physical Society.

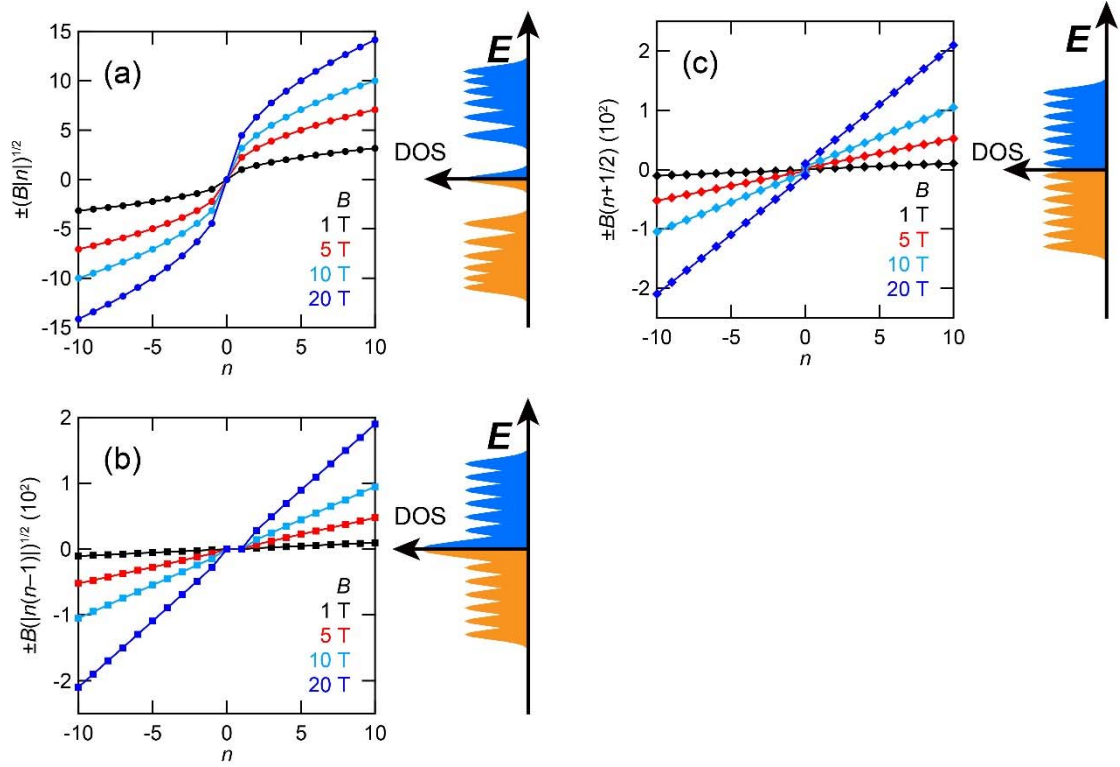


Figure 2.10. Plots of the Landau-level sequences under various magnetic fields B . (a) The case of single-layer graphene described by Eq. (2.152), $\varepsilon_n = \text{sgn}(n) \sqrt{2eB\hbar v_F^2 |n|} \propto \pm \sqrt{B|n|}$. $\varepsilon_n = 0$ corresponds to the Fermi energy. The right side of (a) is a schematic illustration of the density of states (DOS) of Landau levels under $B = 20$ T. (b) The case of bilayer graphene described by $\varepsilon_n = \text{sgn}(n) (\hbar e B / m) \sqrt{n(n-1)} \propto \pm B \sqrt{n(n-1)}$. Here, $\varepsilon_n = 0$ also corresponds to the Fermi energy. The right side of (b) is a schematic illustration of DOS of Landau levels under $B = 20$ T. Note that the Landau levels with indices 0 and 1 are degenerated at the Fermi energy. Except for this degenerated states at the Fermi energy, the series of the Landau levels for bilayer graphene is similar to that of conventional two-dimensional systems. (c) The case of conventional two-dimensional systems described by Eq. (2.153), $\varepsilon_n = (\hbar e B / m) (n + 1/2) \propto B(n + 1/2)$. The origins of the energy and n are chosen for ease of comparison with (a) and (b). The right side of (c) is a schematic illustration of DOS of Landau levels under $B = 20$ T. The zero-mode state is absent in this case.

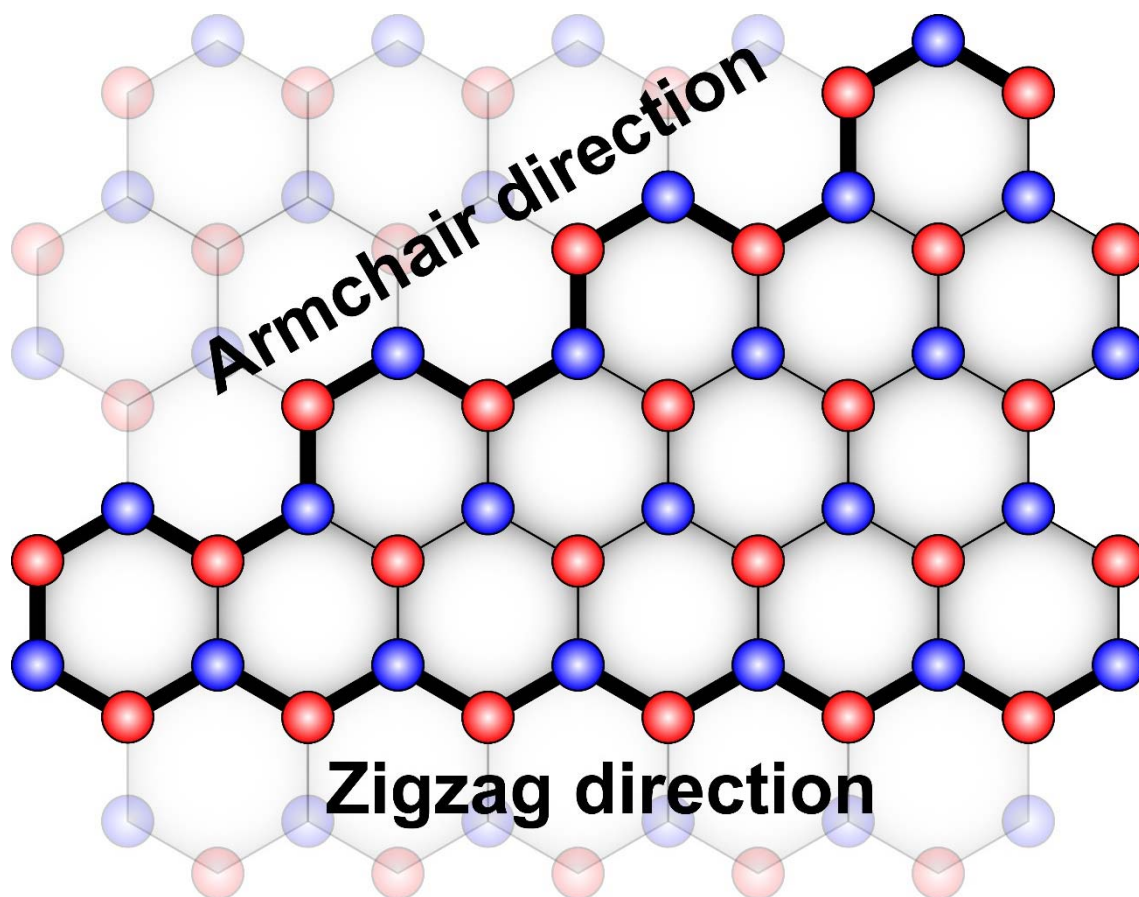


Figure 2.11. Schematic illustration of zigzag and armchair directions in graphene sheet.

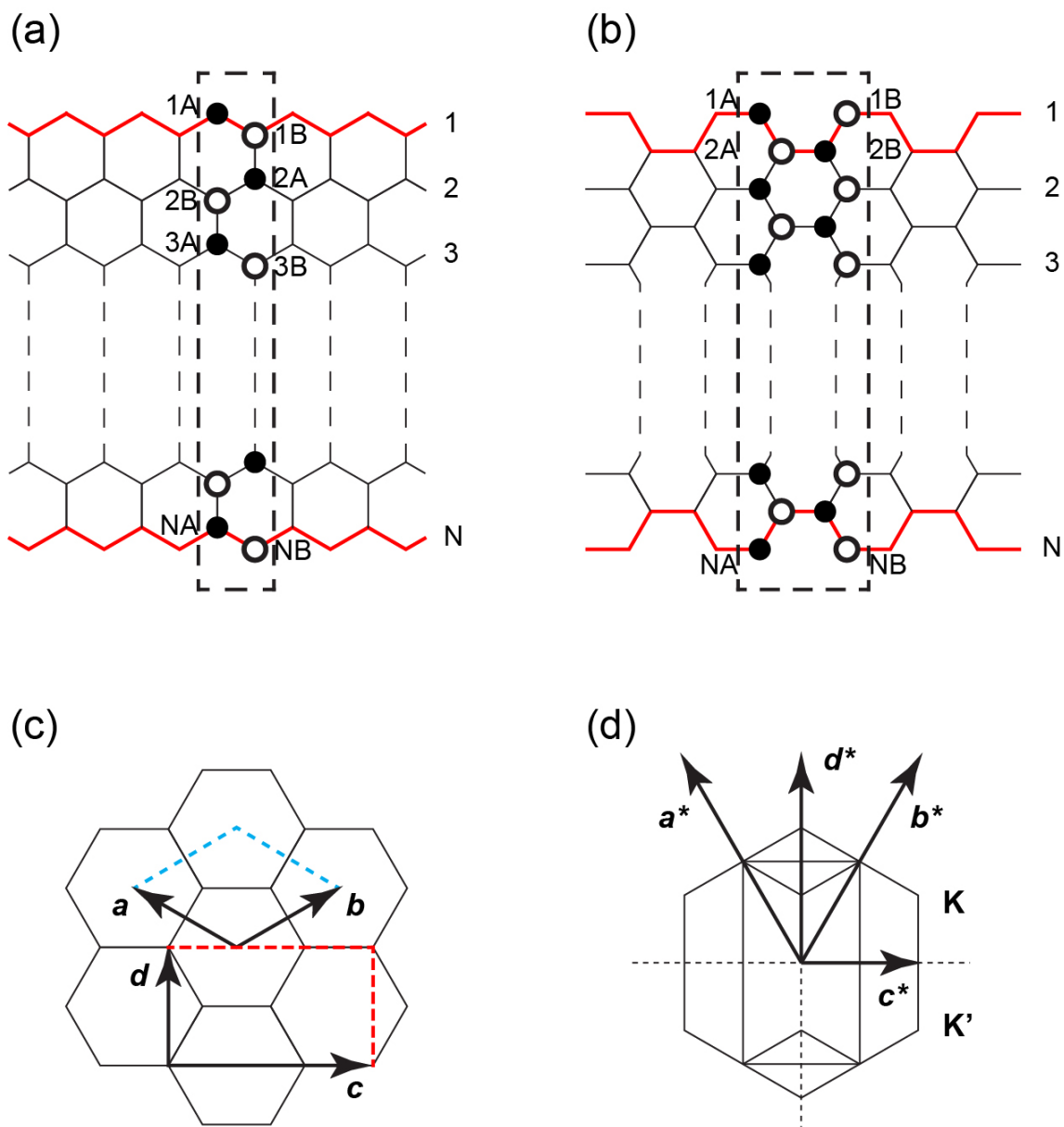


Figure 2.12. The structures of graphene nanoribbons with (a) zigzag-shaped edges and (b) armchair-shaped edges. The dashed rectangles denote the unit cell for each nanoribbon. The unit cells in (c) real space and (d) reciprocal space of graphene sheet is shown. The vectors \mathbf{c} and \mathbf{c}^* (\mathbf{d} and \mathbf{d}^*) are related to the armchair (zigzag) direction.

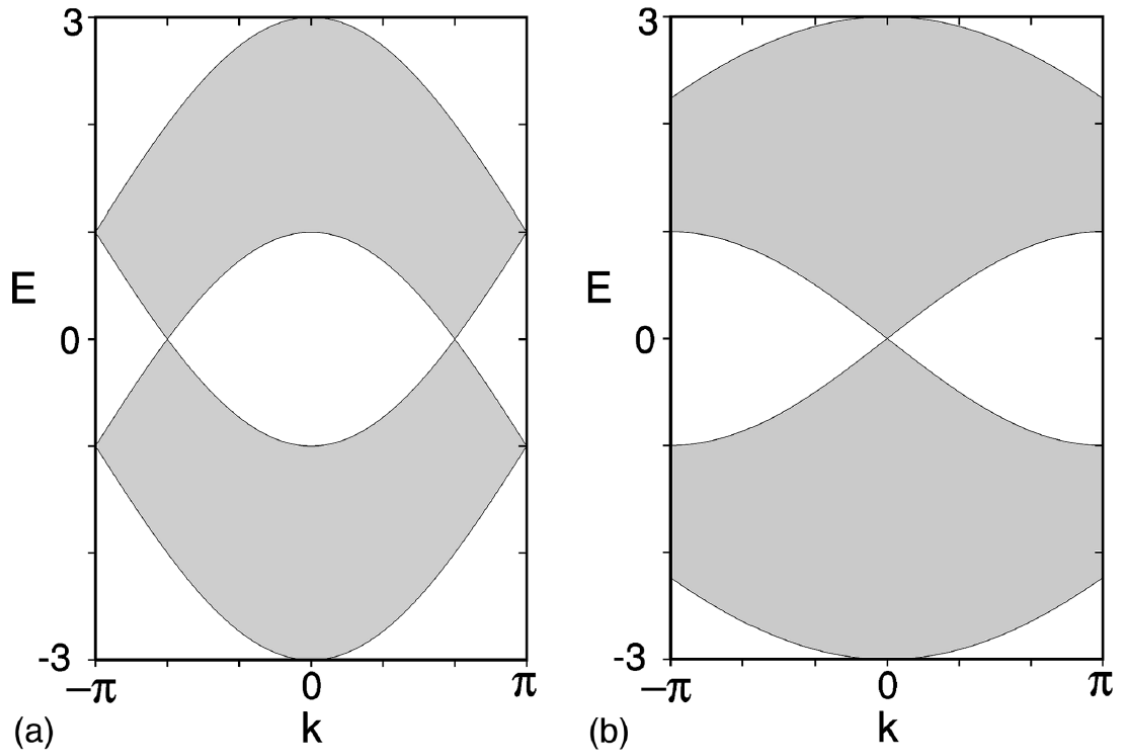


Figure 2.13. The energy band structures of infinite graphene projected to (a) the zigzag direction and (b) the armchair direction. Reprinted figure with permission from K. Wakabayashi, M. Fujita, H. Ajiki, and M. Sigrist, Electronic and magnetic properties of nanographite ribbons, *Physical Review B* **59**, 8271 (1999) [29]. Copyright (1999) by the American Physical Society.

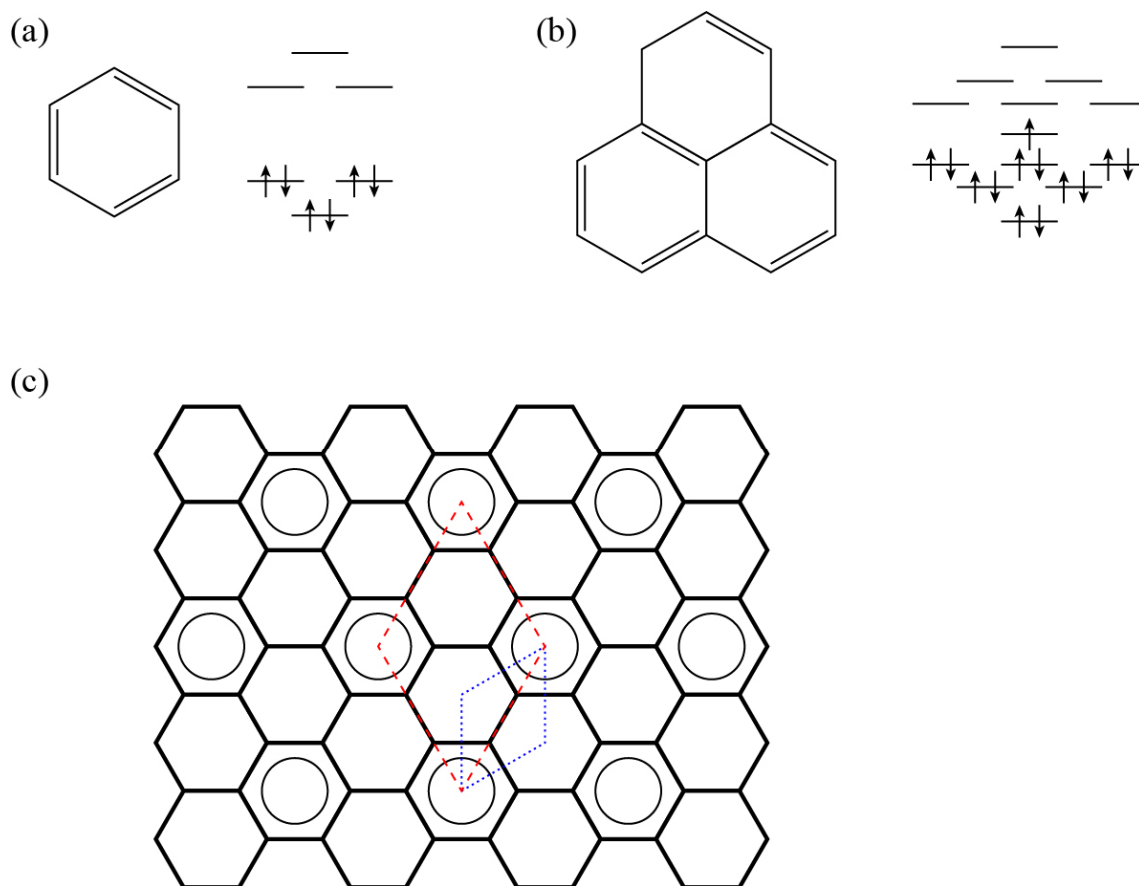


Figure 2.14. (a) Schematic illustrations of a benzene molecule and the energy levels of its molecular orbitals near the Fermi level. There is a large HOMO–LUMO energy gap. (b) Schematic illustrations of a phenalene molecule and the energy levels of its molecular orbitals near the Fermi level. There is a half-filled state with nonbonding nature at the center of the HOMO–LUMO gap. (c) Tiling of aromatic sextets in a graphene sheet. There is one aromatic sextet for every three benzene rings. The blue dotted rhombus denotes the unit cell of graphene. The red dashed rhombus denotes the periodicity of the aromatic sextets, having a $\sqrt{3} \times \sqrt{3}$ superperiodicity with respect to the unit cell of graphene.

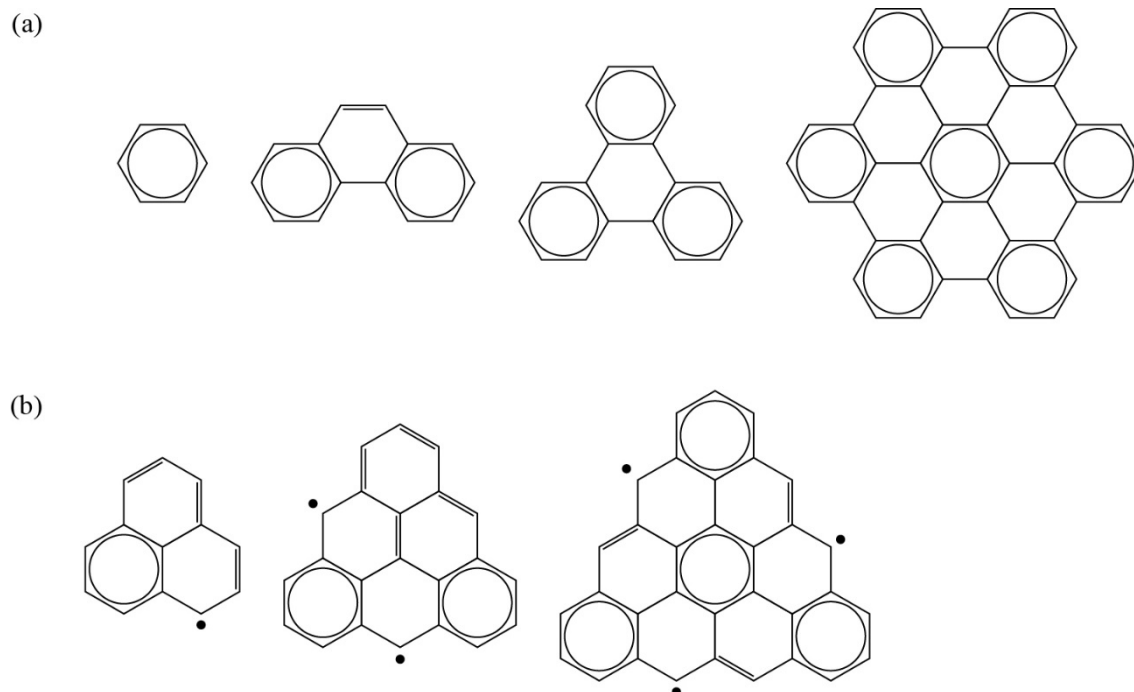


Figure 2.15. (a) Polycyclic aromatic molecules having armchair-shaped edges. (b) Polycyclic aromatic molecules having zigzag-shaped edges. The black dots denote electrons in the nonbonding π states.

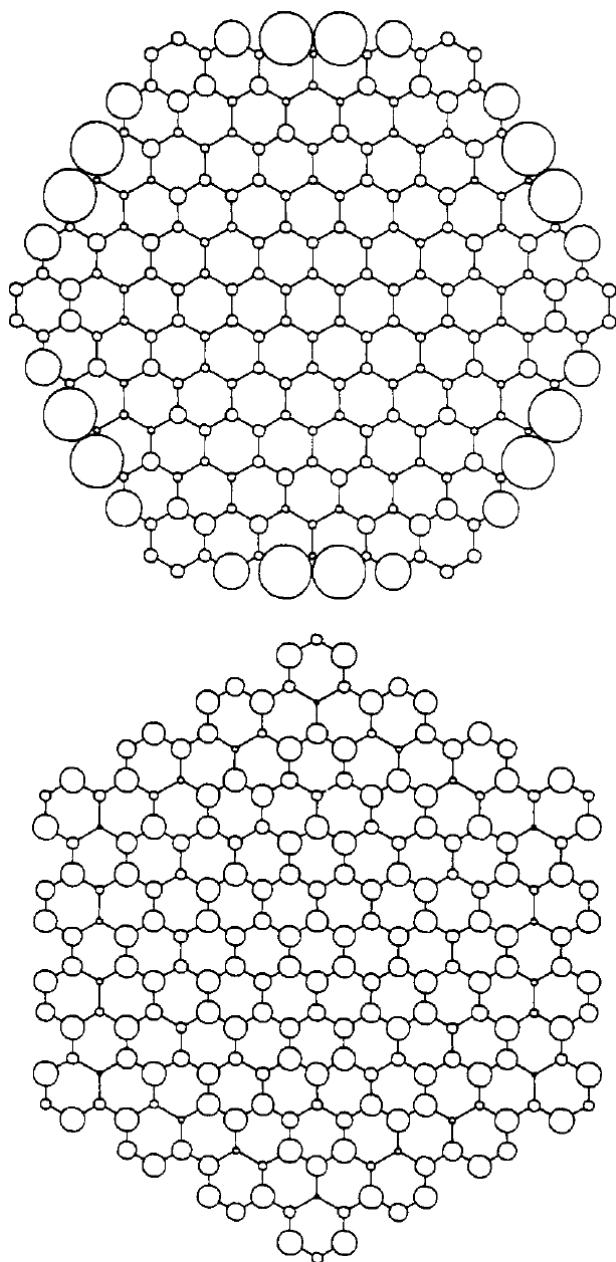


Figure 2.16. Spatial distribution of HOMO in nanographene sheets having (upper) zigzag-shaped edges or (lower) armchair-shaped edges. Reprinted with permission from S. E. Stein and R. L. Brown, π -Electron properties of large condensed polycyclic aromatic hydrocarbons, *Journal of the American Chemical Society* **109**, 3721 (1987) [30]. Copyright 1987 American Chemical Society.

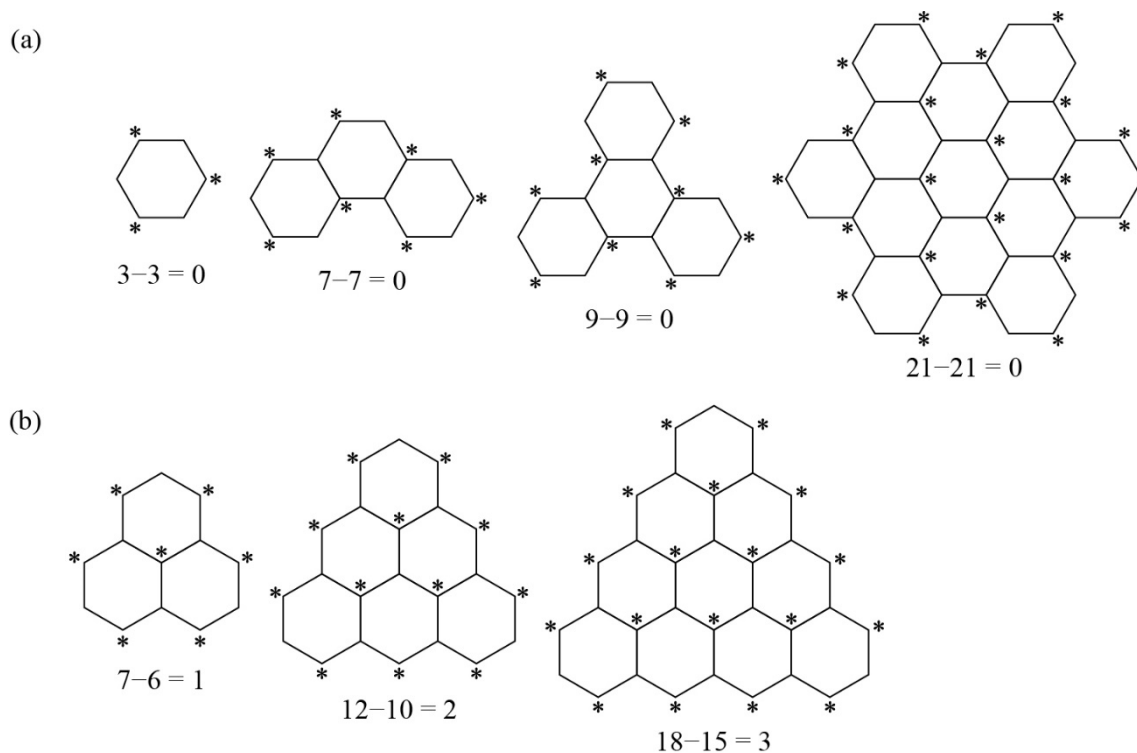


Figure 2.17. (a) Armchair-edged polycyclic aromatic molecules with starred carbon atoms. For these molecules, the numbers of the starred and the unstarred carbon atoms are exactly the same (*e.g.*, $3-3=0$ for benzene). As a consequence, there is no spin state. (b) Zigzag-edged polycyclic aromatic molecules with starred carbon atoms. For these molecules, the similar calculation does not lead to zero (*e.g.*, $7-6=1$ for phenylene), so that there are the spin states.

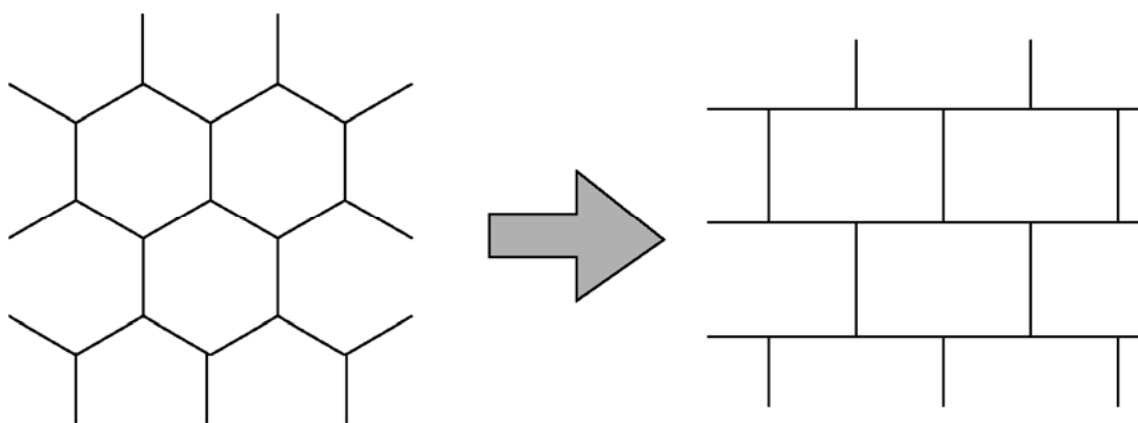


Figure 2.18. The transformation from the honeycomb lattice to the brick-type lattice. This transformation does not change the topology of the lattice. Reprinted figure with permission from K. Wakabayashi, M. Fujita, H. Ajiki, and M. Sigrist, Electronic and magnetic properties of nanographite ribbons, *Physical Review B* **59**, 8271 (1999) [29]. Copyright (1999) by the American Physical Society.

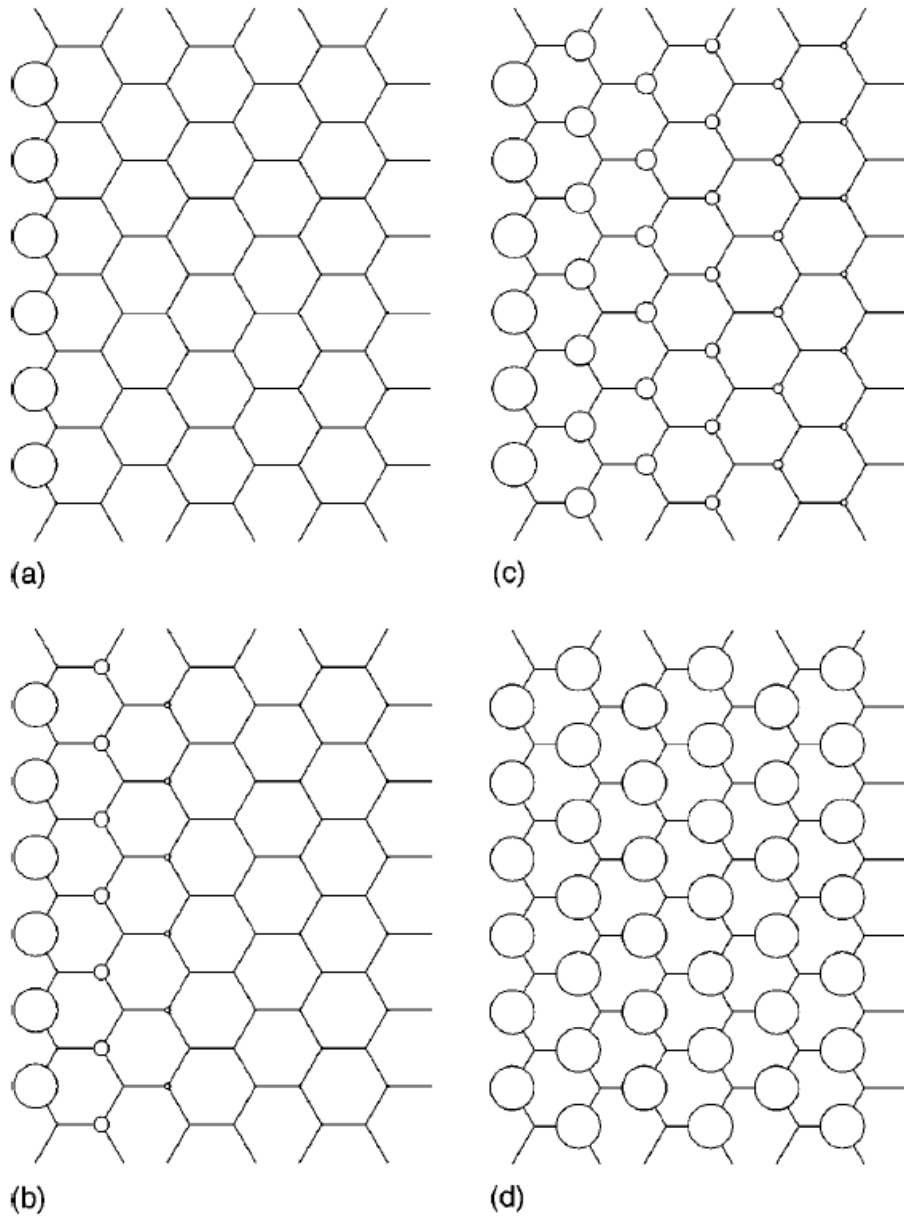


Figure 2.19. The charge density of the edge state at (a) $k = \pi$, (b) $k = 8\pi / 9$, (c) $k = 7\pi / 9$, (d) $k = 2\pi / 3$, where the radius of the circle means the magnitude of the charge density. Reprinted figure with permission from K. Wakabayashi, M. Fujita, H. Ajiki, and M. Sigrist, Electronic and magnetic properties of nanographite ribbons, *Physical Review B* **59**, 8271 (1999) [29]. Copyright (1999) by the American Physical Society.

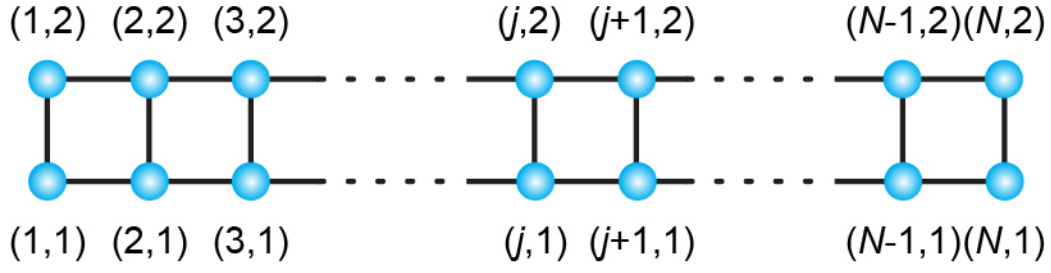


Figure 2.20. Two-leg ladder lattice model having N rungs.

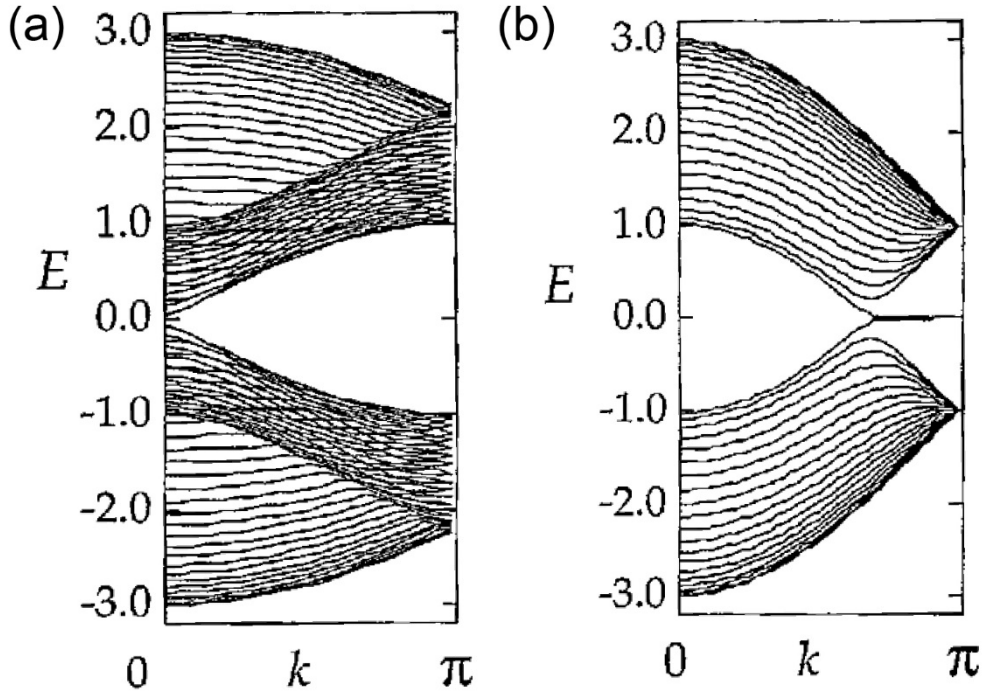


Figure 2.21. Band structure of (a) armchair and (b) zigzag ribbons with width $N = 20$. Compared with the projected band structures of graphene sheet in Fig. 2.13, it can be seen that the armchair nanoribbon has the similar dispersion relation, whereas the zigzag nanoribbon has the edge state at the Fermi energy in the region of the wavenumber $2\pi/3 \leq k \leq \pi$. Reprinted from *Journal of the Physical Society of Japan*, Vol. 65, No. 7, 1996, pp. 1920–1923, M. Fujita, K. Wakabayashi, K. Nakada, and K. Kusakabe, Peculiar localized state at zigzag graphite edge [26], with the permission from The Physical Society of Japan. Copyright 1996, The Physical Society of Japan.

References in Chapter 2

- [1] J. D. Bernal, The structure of graphite, *Proc. Roy. Soc. A* **106**, 749 (1924).
- [2] P. R. Wallace, The band theory of graphite, *Phys. Rev.* **71**, 622 (1947).
- [3] J. W. McClure, Band structure of graphite and de Haas-van Alphen effect, *Phys. Rev.* **108**, 612 (1957).
- [4] J. C. Slonczewski and P. R. Weiss, Band structure of graphite, *Phys. Rev.* **109**, 272 (1958).
- [5] D. D. L. Chung, Review graphite, *J. Mater. Sci.* **37**, 1475 (2002).
- [6] T. Ando, Theory of electronic states and transport in carbon nanotubes, *J. Phys. Soc. Jpn.* **74**, 777 (2005).
- [7] M. S. Dresselhaus and G. Dresselhaus, Intercalation compounds of graphite, *Adv. Phys.* **51**, 1 (2002).
- [8] A. Misu, E. E. Mendez, and M. S. Dresselhaus, Near infrared reflectivity of graphite under hydrostatic pressure. I. Experiment, *J. Phys. Soc. Jpn.* **47**, 199 (1979).
- [9] E. Mendez, A. Misu, and M. S. Dresselhaus, Magnetoreflexion study of graphite under pressure, *Phys. Rev. B* **21**, 827 (1980).
- [10] E. McCann and V. I. Fal'ko, Landau-level degeneracy and quantum Hall effect in a graphite bilayer, *Phys. Rev. Lett.* **96**, 086805 (2006).
- [11] E. McCann, D. S. L. Abergel, and V. I. Fal'ko, The low energy electronic band structure of bilayer graphene, *Eur. Phys. J. Special Topics* **148**, 91 (2007).
- [12] V. I. Fal'ko, Electronic properties and the quantum Hall effect in bilayer graphene, *Phil. Trans. R. Soc. A* **366**, 205 (2008).
- [13] E. McCann, Asymmetry gap in the electronic band structure of bilayer graphene, *Phys. Rev. B* **74**, 161403 (2006).
- [14] T. Ohta, A. Bostwick, T. Seyller, K. Horn, and E. Rotenberg, Controlling the electronic structure of bilayer graphene, *Science* **313**, 951 (2006).
- [15] Y. Zhang, T. T. Tang, C. Girit, Z. Hao, M. C. Martin, A. Zettl, M. F. Crommie, Y. R. Shen, and F. Wang, Direct observation of a widely tunable bandgap in bilayer graphene, *Nature* **459**, 820 (2009).
- [16] M. Koshino and T. Ando, Orbital diamagnetism in multilayer graphenes: systematic study with the effective mass approximation, *Phys. Rev. B* **76**, 085425

- (2007).
- [17] J. Patterson and B. Bailey, Solid-state physics: introduction to the theory, *Springer* (2007).
 - [18] T. Ando, Screening effect and impurity scattering in monolayer graphene, *J. Phys. Soc. Jpn.* **75**, 074716 (2006).
 - [19] E. H. Hwang, S. Adam, and S. Das Sarma, Carrier transport in two-dimensional graphene, *Phys. Rev. Lett.* **98**, 186806 (2007).
 - [20] T. Stauber, N. M. R. Peres, and F. Guinea, Electronic transport in graphene: a semiclassical approach including midgap states, *Phys. Rev. B* **76**, 205423 (2007).
 - [21] T. Enoki and T. Ando, Physics and chemistry of graphene: graphene to nanographene, *Pan Stanford publishing* (2013).
 - [22] K. S. Novoselov, A. K. Geim, S. V. Morozov, D. Jiang, M. I. Katsnelson, I. V. Grigorieva, S. V. Dubonos, and A. A. Firsov, Two-dimensional gas of massless Dirac fermions in graphene, *Nature* **438**, 197 (2005).
 - [23] Y. Zhang, Y. W. Tan, H. L. Stormer, and P. Kim, Experimental observation of the quantum Hall effect and Berry's phase in graphene, *Nature* **438**, 201 (2005).
 - [24] J. H. Chen, C. Jang, S. Adams, M. S. Fuhrer, E. D. Williams, and M. Ishigami, Charged-impurity scattering in graphene, *Nat. Phys.* **4**, 377 (2008).
 - [25] J. H. Chen, W. G. Cullen, C. Jang, M. S. Fuhrer, and E. D. Williams, Defect scattering in graphene, *Phys. Rev. Lett.* **102**, 236805 (2009).
 - [26] M. Fujita, K. Wakabayashi, K. Nakada, and K. Kusakabe, Peculiar localized state at zigzag graphite edge, *J. Phys. Soc. Jpn.* **65**, 1920 (1996).
 - [27] K. Nakada, M. Fujita, G. Dresselhaus, and M. S. Dresselhaus, Edge state in graphene ribbons: nanometer size effect and edge shape dependence, *Phys. Rev. B* **54**, 17954 (1996).
 - [28] A. Zangwill, Physics at surfaces, *Cambridge Univ. Press* (1988).
 - [29] K. Wakabayashi, M. Fujita, H. Ajiki, and M. Sigrist, Electronic and magnetic properties of nanographite ribbons, *Phys. Rev. B* **59**, 8271 (1999).
 - [30] S. E. Stein and R. L. Brown, π -Electron properties of large condensed polyaromatic hydrocarbons, *J. Am. Chem. Soc.* **109**, 3721 (1981).

Chapter 3

Experimental developments in graphene researches

3.1 Fabrication techniques of graphene

The first successful isolation of single-layer graphene was performed by Novoselov *et al.* by means of the well-known scotch-tape exfoliation of graphite [1,2]. Because this method is quite easy and obtained graphene flakes have sufficiently high quality, their report is regarded as the trigger of experimental studies on graphene. However, when it comes to potential industrial applications of graphene, the scotch-tape method is inadequate because of, *e.g.*, the very low yield. Prior to the success of the scotch-tape method, in fact, preparation techniques of graphene had been already attractive themes of studies. In this section, several important techniques for preparation of graphene are referred to.

3.1.1 Micromechanical exfoliation of graphite

Novoselov *et al.* prepared graphenes including a single layer by using adhesive scotch tape to exfoliate highly-oriented pyrolytic graphite (HOPG) [1,2]. Because it had been believed that one- or two-dimensional crystals are instable and likely to decompose readily [3], the stable existence of macroscopic-sized single-layer graphene was quite attractive, together with the ease of the way of isolation. This method is now very commonly used for studies on graphene, particularly its fundamental properties, because graphene samples obtained by this method are usually high-quality, that is to say, exfoliated graphene have quite small amount of disorders. In addition, this method has appeared to be applicable for the preparation of atomically thin layers of other materials having two-dimensional periodicities [4–7]. For this mechanical exfoliation method, actually it should be mentioned that the use of adhesive tape to obtain thin flakes of

graphite was performed, probably for the first time, in 1971 by a Japanese group in Keio University [8]. In this study, the graphite flakes were deposited on a transparent glass substrate, on which extremely thin graphene flakes were hardly visible. In contrast, Novoselov *et al.* used SiO₂/Si substrates, on which even single-layer graphene can be found with optical microscope [1,2]. The visibility of graphene on a SiO₂ substrate is mentioned in Section 3.2.1. The sizes of deposited graphene flakes are distributed over the range from a few micrometers to 0.1 millimeters. Usually, flakes of 10–20 micrometers in length and width are large enough to be employed for example as a field-effect transistor device. Optical microscope images of a typical sample of an as-prepared single-layer graphene flake and the identical graphene with Au/Cr electrodes attached by means of photolithography are shown in Fig. 3.1.

Although this micromechanical exfoliation is excellent from the viewpoints of its ease and the high quality of prepared graphene flakes, arbitrarily controlling the thickness, the size and the position of a graphene flake is absolutely impossible, so that alternative methods need strongly to be developed for commercial applications of graphene. Considerable effort has been dedicated for production of large-scale homogeneously high-quality graphene sheets.

3.1.2 Chemical vapor deposition

Since 1960s, it has been indicated that chemical vapor deposition (CVD) of hydrocarbon molecules on various metal substrates produces graphitic layers. Many hydrocarbon molecules such as methane, ethylene, benzene, and so forth have been selected as a source of graphene. Similarly, various substrates including nickel, platinum, palladium, copper, and so on, have been explored.

In early studies for producing graphene via CVD, the formations of graphitic layers were observed using nickel substrates [9–11], soon followed by using platinum [12,13]. It was found that the formation of graphitic layers was the consequence of diffusion and segregation of carbon atoms from the bulk to the surface during the annealing and cooling processes. Given that the solubility of carbon atoms is strongly dependent of the temperature, the segregation of carbon atoms on the surface can be caused by lowering the temperature [14]. The solubility is also dependent of the kind of metal for the substrate

[14]. The growth of graphene has been demonstrated on many kinds of metals such as cobalt [14], nickel [15–16], platinum [14,17,18], and palladium [14,19,20] by means of thermal dissociation of hydrocarbon molecules on the surface followed by the segregation of carbons on the surface upon cooling down. The solubility of carbons in the metal and the growth conditions determine the mechanism of deposition.

For low-cost large-scale production of graphene films, ambient pressure CVD with polycrystalline catalytic metals is favorable. CVD on polycrystalline nickel was first performed recently [21–23]. One can use thermally deposited film of nickel on insulating substrate with lithographical patterning as a substrate for CVD, so that patterned graphene can be obtained as shown in Fig. 3.2 [21]. However, because nickel is capable for accommodating large amount of carbons, single- and few-layer graphene can be formed when diffused carbon atoms segregates on the surface. This inhomogeneity of the number of layers of produced graphene can be disadvantageous for the use of nickel as a substrate for CVD. In contrast, one can use polycrystalline copper foils for uniform growth of moderate-quality single-layer graphene films [24]. The initial [24] and the following studies [25–32] demonstrated that CVD-grown graphene on copper can be homogeneously single-layer over areas as large as 30 inches. This growth on copper is easily utilized because thin copper foil is inexpensive. Moreover, thin foil can be easily etched with acids in order to transfer onto other substrates, for example, insulating SiO₂/Si substrate for measurements of electron transport properties. Therefore, copper is regarded as the most attractive material for CVD growth of graphene.

Finally, how to transfer graphene prepared on a metal substrate should be referred to. One needs to isolate the produced graphene from the metal substrate for practical use. The transfer of CVD-grown graphene layers to an arbitrary substrate has been carried out by means of wet-etching the catalytic metal substrate, as shown in Fig. 3.3 [28]. After CVD, a graphene grown on metal substrate is covered with a supporting material such as a polymer layer. Poly(methyl methacrylate), which is known as a resist compound for electron-beam lithography, is frequently employed as a supporting layer. Then, the metal substrate is etched by immersing it in a solution of acid, for example FeCl₃. The resulting graphene with the supporting layer can be transferred onto arbitrary place. When, the supporting layer is removed chemically, one obtains the graphene sample on a favorable substrate.

Although graphene samples grown by CVD have generally lower quality than exfoliated ones, great effort has been devoted to improve the quality, and so that one may expect the production of sufficiently nice graphene by CVD. The CVD method is regarded as the most promising, inexpensive approach for industrial production of large-scale homogeneously single-layer graphene films.

3.1.3 Thermal decomposition of silicon carbide substrate

In addition to the CVD method, epitaxial growth of graphene is achievable on SiC(0001) [33,34]. SiC is a wide-gap semiconductor and is composed of stacking basal planes of bilayers of silicon and carbon atoms. When an SiC substrate is annealed at high temperature (typically 1200–1600°C) in ultra-high vacuum [35] or in an Ar atmosphere [36], silicon atoms desorb from the substrate and graphitization of remaining carbon atoms occurs. Because SiC is a stack of bilayers of silicons and carbons, there are two types of surface, namely, silicon-terminated surface and carbon-terminated surface. In the case of silicon-terminated surface, the growth of graphene is slow and finished soon, resulting in few-layer graphene. In contrast, carbon-terminated surface can produce rapidly thick graphene, of which the number of layers may reach several tens. The structure of graphene grown on silicon-terminated surface is also different from that on carbon-terminated one. On silicon-terminated surface, there is a buffer layer, which is the layer between grown graphene and the substrate having strong interaction with the substrate. Due to the buffer layer, the upper graphene layers are separated from the SiC substrate, so that their electronic states are almost identical to those of single- or multi-layer graphene. On the other hand, the surface structure depends strongly on the growth conditions for carbon-terminated surface. When graphene is grown in ultra-high vacuum, three-dimensional structures are obtained [37]. In contrast, successive layers are flat if it is grown in graphitic furnace.

Epitaxial graphene on SiC(0001) has been demonstrated high mobilities, especially in multilayered graphene films. Single-layer graphene over a large area on SiC has been shown to exhibit high mobility and quantum Hall effect [38]. Production of wafer-scale epitaxial graphene has been appeared for example as a high-frequency device [39].

3.2 Determination of the thickness of graphene

Usually, the number of layers of a graphene flake is determined by means of comparing the contrast in optical image and/or measuring Raman spectrum. In addition to these methods, one can determine the thickness by measurements of quantum Hall effect, and direct measurements of the height with atomic force microscopy. Herein, the methods of optical microscopy and Raman spectroscopy, which are sufficiently precise and highly practical, are referred to.

3.2.1 Optical microscopy

The thickness of a single-layer graphene is as thin as approximately 0.3 nm. In spite of the thinness, it can be identified by optical microscope if it lies on a SiO₂/Si substrate with a certain thickness of the oxide layer. Furthermore, the difference in optical contrast is clear even between single- and bi-layer graphene flakes.

The visibility of graphene on a SiO₂/Si substrate has been explained quantitatively in virtue of a model based on the Fresnel law, in which the reflection of light at the boundary of different materials is taken into account [40–42]. The visibility of graphene has been found to be strongly dependent of the thickness of the oxide layer of the substrate as well as the wavelength of the illuminating light.

Figure 3.4 shows the tri-layered model of a stack of graphene/SiO₂/Si. The case that the incident light comes into the system perpendicularly to the plane of the surface is considered. The refractive index of the air (n_{Air}) is set to be one. The depth of the silicon layer is assumed to be semi-infinite with the complex refractive index ($n_{\text{Si}}(\lambda)$), which depends upon the wavelength of the incident light. The thickness and the refractive index of the SiO₂ layer are denoted as d_{SiO_2} and $n_{\text{SiO}_2}(\lambda)$, respectively. For example, $n_{\text{Si}}(\lambda = 400 \text{ nm}) \approx 5.6 - 0.4i$ and $n_{\text{SiO}_2}(\lambda = 400 \text{ nm}) \approx 1.47$ [40]. The thickness and the complex refractive index of graphene are defined as d_{g} and $n_{\text{g}}(\lambda)$, respectively. Here, the intensity of the reflected light $I(n_{\text{g}})$ is written as following.

$$\begin{aligned}
 I(n_g) = & \left| \left\{ r_1 \exp \left[i \left(\Phi_g + \Phi_{\text{SiO}_2} \right) \right] + r_2 \exp \left[-i \left(\Phi_g - \Phi_{\text{SiO}_2} \right) \right] \right. \right. \\
 & + r_1 r_2 r_3 \exp \left[i \left(\Phi_g - \Phi_{\text{SiO}_2} \right) \right] \left. \right\} \times \left\{ \exp \left[i \left(\Phi_g + \Phi_{\text{SiO}_2} \right) \right] \right. \\
 & + r_1 r_2 \exp \left[-i \left(\Phi_g - \Phi_{\text{SiO}_2} \right) \right] + r_1 r_3 \exp \left[-i \left(\Phi_g + \Phi_{\text{SiO}_2} \right) \right] \\
 & \left. \left. + r_2 r_3 \exp \left[i \left(\Phi_g - \Phi_{\text{SiO}_2} \right) \right] \right\} \right|^2
 \end{aligned} \quad \cdots(3.1)$$

with the relative refractive indices r_1 , r_2 , and r_3 , and the phase differences Φ_g and Φ_{SiO_2} ,

$$r_1 = \frac{n_{\text{Air}} - n_g}{n_{\text{Air}} + n_g}, \quad \cdots(3.2)$$

$$r_2 = \frac{n_g - n_{\text{SiO}_2}}{n_g + n_{\text{SiO}_2}}, \quad \cdots(3.3)$$

$$r_3 = \frac{n_{\text{SiO}_2} - n_{\text{Si}}}{n_{\text{SiO}_2} + n_{\text{Si}}}, \quad \cdots(3.4)$$

$$\Phi_g = \frac{2\pi n_g d_g}{\lambda}, \quad \cdots(3.5)$$

$$\Phi_{\text{SiO}_2} = \frac{2\pi n_{\text{SiO}_2} d_{\text{SiO}_2}}{\lambda}. \quad \cdots(3.6)$$

Then, the optical contrast (C) is defined as the relative intensity of the reflected light with graphene ($n_g \neq 1$) with respect to the case without graphene ($n_g = n_{\text{Air}} = 1$),

$$C = \frac{I(n_g = 1) - I(n_g)}{I(n_g = 1)}. \quad \cdots(3.7)$$

Blake *et al.* [40] calculated C with $d_{\text{SiO}_2} = 300$ nm, 200 nm, and 90 nm, $d_g = 0.34$ nm, and $n_g(\lambda) \approx 2.6 - 1.3i$ adopted from the value of bulk graphite, which showed excellent agreements with experimental results. The complex refractive index of bulk graphite is known to be independent of the wavelength of the incident light, so that the λ -dependence of C is appeared to be determined by $n_{\text{Si}}(\lambda)$ and $n_{\text{SiO}_2}(\lambda)$. Figure 3.5 shows the color plot of Eq. (3.7) [40]. When green light with the approximate wavelength of 540 nm is employed for illumination, $d_{\text{SiO}_2} \approx 90$ nm or 280 nm have appeared to provide the best visibility of graphene [40].

An example is shown in Fig. 3.6. Figure 3.6a is an optical microscope image of graphene flakes on a SiO₂/Si substrate having a 300-nm-thick oxide layer taken with white illumination. Figure 3.6b is the same area taken using a green filter. When the red and the blue components of Fig. 3.6b are omitted and the green component is extracted, the image in Fig. 3.6c is obtained. Then, Fig. 3.6d represents the distribution of the green indices over the image of Fig. 3.6c. The SiO₂ substrate has the highest index of 237. Graphene flakes labeled as A, B, and C have indices of 223, 209, and 179, respectively. In this sample, the unit spacing between green indices is approximately 14, so that graphene A, B, and C are determined to be single-layer, bi-layer, and four-layer flakes, respectively.

3.2.2 Raman spectroscopy

Raman spectroscopy technique is widely applied for studies of graphene [43–45] because it gives us many information about not only the number of layers, but also the quality of crystal, the amount of charge transfer between graphene and surrounding impurities and substrates, and the direction of edges. Here, only how to decide the number of layers by Raman spectroscopy is briefly written. Details on Raman spectroscopy in graphene is described in Section 3.3.

Figure 3.7 shows typical Raman spectra of a defective graphene sample. In order to determine the thickness of the flake, attention should be focused on the G and the 2D bands.

- (i) The ratio of the intensity of the G band to that of the 2D band
- (ii) The Raman shift and the spectral shape of the 2D band

For (i), given that the intensity of the G band is relatively sensitive to the amount of graphitic carbons, the ratio of the G band to the 2D band (*i.e.*, I_G / I_{2D}) reflects the number of layers. This ratio usually increases with the increase of the number of layers. However, the intensities of these peaks are likely to be affected by contaminants on the sample graphene. Thus, (ii) is usually easier to define the thickness than (i). The 2D band reflects sensitively the difference in the electronic structures of graphenes with different numbers of layers. The 2D band of a single-layer graphene consists of a single symmetric peak. In contrast, because bi- or thicker-layer graphene has multiple energy bands, the 2D

band consists of several ingredients involving multiple transitions between the multiple energy bands. Because the 2D band in Fig. 3.7 has nearly symmetric shape with its central energy at about 2680 cm^{-1} , this graphene sample is single-layer. (ii) also has the same drawback with (i), namely, the extrinsic effects on the intensities of the 2D-band ingredients. However, discrimination between single-, bi-, and tri-layer graphene sheets is sufficiently clear. These small numbers of layers are of particular interest in graphene studies.

Coupling the optical contrast method with Raman spectroscopy, the number of layers of a graphene can be quite easily estimated, and this estimation is known to be sufficiently accurate.

3.3 Raman spectroscopy in graphene

When monochromatic light with the frequency of ν_0 impinges to a material, the scattered light has not only the frequency ν_0 but also $\nu_0 \pm \nu$. The former process is called Rayleigh scattering and the latter is called Raman scattering including Stokes scattering of $\nu_0 - \nu$ and anti-Stokes scattering of $\nu_0 + \nu$. This shift of the frequency ν includes information on vibrational modes in the material.

The phonon dispersion relation of graphene is shown in Fig. 3.8 [46]. Six branches are shown in this figure originating from two carbon atoms in the unit cell of graphene. Three of them are acoustic phonon branches (A) and the other three are optic phonon branches (O). One of A branches and one of O branches correspond to the out-of-plane (o) vibrational modes. The other four branches are the in-plane (i) modes. There are another classifications of longitudinal (L) and transverse (T) modes. For the L modes, the direction of the vibration is parallel with the carbon-carbon directions. For the T modes, on the other hand, the direction of the vibration is perpendicular to the carbon-carbon direction. Thus, six branches are assigned to iLO, iTO, iLA, iTA, oTO, and oTA modes as indicated in Fig. 3.8 [43].

Figure 3.9 shows several Raman processes which can be observed in graphene [43]. The G band (Fig. 3.9 (left)) is the most obvious feature in Raman spectrum of graphene. It appears at around 1580 cm^{-1} as shown in Fig. 3.7. The G band is associated with the doubly degenerated phonon mode (iTO and iLO) at the center of the Brillouin zone (*i.e.*, the Γ point). The G' band (Fig. 3.9 (right-top)), which is also called 2D band, is also generally observed for graphene. The position of the 2D band is around 2700 cm^{-1} as shown in Fig. 3.7. The 2D band originates from a second-order process, involving two iTO phonons near the K point. The 2D band of single-layer graphene is simple because only two Dirac cones (*i.e.*, the neighboring K and K' points) are involved in this process. In contrast, The 2D band of multi-layer graphene is complicated because the number of the energy bands that participate in this double-resonance process increases. Figure 3.10 shows the 2D bands of single-, bi-, tri-, and four-layer graphene, and graphite. The 2D band of single-layer graphene consists of only single ingredient, and is symmetric. In contrast, multi-layer graphene have various ingredients contributing to the 2D band. These ingredients originate from the branches of the electronic energy bands, resulting in various double-resonance processes. Above two bands, *i.e.*, the G and the 2D bands are

typical features in a Raman spectrum of graphene, and these bands can be used for the determination of the number of layers of the target graphene as mentioned in Section 3.2.2. In the special case of graphene, where the valence and the conduction bands are very symmetric with respect to the Dirac point, the Raman process of the scattering of holes can occur, leading to the triple-resonance G' process shown in Fig. 3.9 (right bottom).

In the case that the target graphene contains structural disorders, such as vacancies, and grain boundaries, additional features appear. One is the D band at approximately 1350 cm^{-1} and the other is the D' band at approximately 1620 cm^{-1} as shown in Fig. 3.7. The D band has its origin as a second-order process, involving one iTO phonon and one elastic scattering event due to a defect. For the D band, two Dirac cones at the adjacent K and K' points are involved as shown in Fig. 3.9 (center top), so that the elastic scattering event of the D band is intervalley scattering. On the other hand, the D'-band process consists of one iLO phonon and one elastic intravalley scattering event within one Dirac cone as shown in Fig. 3.9 (center bottom).

It was found that the ratio of the intensity of the D band to that of the G band (I_D / I_G) was inversely proportional to the crystallite sizes (L_a) by Raman and X-ray diffraction studies [47]. The following studies revealed the dependence of I_D / I_G on the energy of the excitation laser [48] and derived an empirical equation that enabled one to estimate L_a from I_D / I_G as $L_a = 44 \times (I_D / I_G)^{-1}$ [49]. Finally, the relation between L_a and I_D / I_G was generalized by involving the correction for the dependence of I_D / I_G on the wavelength of the excitation laser (λ_{laser} in unit of nanometer) as [50],

$$L_a = (2.4 \times 10^{-10}) \times \lambda_{\text{laser}}^4 \left(\frac{I_D}{I_G} \right)^{-1} \text{ (nm)}. \quad \cdots (3.8)$$

Although Eq. (3.8) was established via experiments on nanographite samples consisting of more than several layers, it has been used in various studies on graphene containing single layer with nice agreements [51–53]. In the case of graphene, L_a should be regarded as the average spacing between defect sites, rather than the crystallite size.

Provided that the D band originates from defects in graphene, edges of graphene, which are regarded as defects, should show the D band in its Raman spectrum. This expectation is both correct and incorrect. It was previously reported that differences in the intensity of the D band were observed in Raman spectra measured at distinct areas of graphite including step edges, as shown in Fig. 3.11 [54]. The regions 1 and 2

corresponded to step edges of graphite, and the region 3 was the interior terrace. It can be easily understood that only the G band appeared with no defect-related feature in the region 3, and that the D band (and the D' band) appeared in the spectra of the regions 1 and 2. However, the intensity of the D band in the region 1 was much larger than that in the region 2. The similar feature has been observed in isolated graphene samples [55–58]. It has been revealed that the intensity of the D band at edges of graphene depends on the direction of edges, namely zigzag or armchair. Figure 3.12 shows Raman imaging results measured at edges of single-layer graphene sheets forming various angles [55]. By comparing 30° and 90° corners that are composed of a zigzag and an armchair edges shown in Figs. 3.12a and 3.12c, respectively, and by comparing two distinct 60° corners that are composed of two zigzag edges or two armchair edges shown in Figs. 3.12b and 3.12d, respectively, it can be clearly seen that the intensity of the D band is strong for armchair edges whereas it is weak for zigzag edges. This dependence of the intensity of the D band on the direction of edges has been theoretically explained in terms of the direction of the elastic intervalley scattering. Figure 3.13a shows the wave vectors \vec{d}_a and \vec{d}_z , which are perpendicular to the direction of armchair- and zigzag-shaped edges of graphene, respectively [58]. Figure 3.13b shows the D-band process and Fig. 3.13c represents the directions of \vec{d}_a and \vec{d}_z in k -space [58]. Because the D-band process connects the adjacent K and K' points by involving one iTO phonon and one elastic intervalley scattering, it is induced at armchair edges that have \vec{d}_a directing from a K point to the neighboring K' point. On the other hand, \vec{d}_z of zigzag edges directs from a K point to another K point, so that the D band is likely to be suppressed at zigzag edges. It should be noted that an edge of graphene is not purely composed of either armchair or zigzag. For Raman measurements, the spot size of the excitation laser is usually as large as 1 μm in diameter. In this scale, edges of graphene must be regarded as mixtures of the armchair and zigzag arrangements, although the directions of mainly armchair structure and mainly zigzag structure can be estimated depending upon the angle between two edges, as in Fig. 3.12 [55].

3.4 Electron transport in graphene

Electron transport measurements are the most frequently employed method for elucidating fundamentals of electronic behaviors in graphene described as the massless Dirac fermions in the vicinity of the Dirac point. Because graphene samples prepared by mechanical exfoliation are usually on SiO₂/doped-Si substrates, it is convenient to fabricate field-effect-transistor (FET) devices of graphene, in which metal electrodes are attached to a graphene sample and heavily-doped silicon layer is used as a backgate electrode, as shown in Fig. 3.14.

According to the simple Drude equation, the electrical conductivity (σ) is written as

$$\sigma = en\mu, \quad \cdots(3.9)$$

where e is the elementary electrical charge, n is the concentration of the charge carrier, and μ is the mobility of the carrier. When a backgate voltage (V_g) is applied to the graphene FET device, n is controlled like a parallel-plate capacitor. The relationship between V_g and the number of the carriers (N) is written as

$$V_g = \frac{eN}{C}, \quad \cdots(3.10)$$

with

$$\frac{1}{C} = \frac{1}{C_g} + \frac{1}{C_q}, \quad \cdots(3.11)$$

$$C_g = \frac{\epsilon_0 \epsilon_{\text{SiO}_2} A}{d}, \quad \cdots(3.12)$$

where C is the capacitance, C_g is the form of general capacitor, and C_q is the quantum capacitance [59–61], which contributes significantly if the distance between two parallel plates is very small (several nanometers). ϵ_0 is the dielectric constant of vacuum, ϵ_{SiO_2} is the relative dielectric constant of the dielectric SiO₂ layer (usually 3.9–4.0), d is the thickness of the SiO₂ layer, and A is the area. d is usually large enough (more than ~ 100 nm) to ignore C_q . To consider the concentration of the carrier density, the relationship $n = N / A$ is used. Thus, we obtain

$$\sigma = \mu \times \left(\frac{\epsilon_0 \epsilon_{\text{SiO}_2} V_g}{d} \right) = \mu \times (7.4 \times 10^{10} \times V_g) \quad (d = 300 \text{ nm}). \quad \cdots(3.13)$$

Based on Eq. (3.13), electron transport properties of graphene can be examined in terms of the dependence on the carrier density, *i.e.*, the position of the Fermi energy.

3.4.1 Quantum Hall effect in graphene

Immediately after the report on successful isolation of graphene and electrical measurements [1], unconventional half-integer quantum Hall effect in single-layer graphene was experimentally observed by two groups at the same time [62,63]. As mentioned in Section 2.2.4, when a strong magnetic field is applied perpendicularly to the plane of two-dimensional electron system, cyclotron motion of moving electrons occur in virtue of the Lorentz force, and the energy of electrons are quantized as Landau levels. The Hall conductivity σ_{xy} for conventional two-dimensional system has a factor of n , which is an integer. If the spin and the valley degeneracies of graphene are taken into account for Eq. (2.154), $\sigma_{xy} = n(4e^2/h)$ is expected, although this expression is incorrect. The observed sequence has a half-integer feature as $\sigma_{xy} = (4e^2/h)(n+1/2)$ [62,63] as a consequence of the linear electronic band structure of single-layer graphene leading to the Landau levels in a distinct manner as written in Eq. (2.152) $\varepsilon_n = \text{sgn}(n)\sqrt{2eB\hbar v_F^2 |n|}$. This half-integer quantum Hall effect is an obvious evidence that electrons in single-layer graphene can be described as massless Dirac fermion in the vicinity of the intersection between the valence and the conduction bands (*i.e.*, the Dirac point). In contrast, bilayer graphene has parabolic energy band in the vicinity of the Fermi energy, resulting in the Landau quantization, $\varepsilon_N = \pm\hbar\omega_c\sqrt{|n(n-1)|}$, where the cyclotron frequency is $\omega_c = eB/m^*$ and m^* is the effective mass. Thus, conventional integer quantum Hall effect was observed in bilayer graphene except for the absence of zero-mode plateau because of the presence of the zero-mode Landau level with $n = 0$ and $+1$ [62,64].

3.4.2 High carrier mobility and electron scattering sources in graphene

Although graphene is expected to be applied as high-speed electronic devices owing to its potential higher mobility than conventional materials, effects of scattering sources that limits the mobility of the charge carriers are significant, so that scattering mechanisms in graphene need strongly to be well understood. Various scattering sources in graphene have been theoretically [65–67] and experimentally studied, such as charged impurities [68–71], lattice defects [51,72,73], phonons [74,75], and so on.

Charged impurities are inevitably contained on or beneath a graphene sheet through

the preparation processes and create long-range Coulomb potentials. The gate-voltage dependence of the conductivity of an as-prepared graphene FET device shows usually a characteristic of hole donation due to charged impurities such as oxygen molecules in the atmosphere or resists for lithography. Although the basis of the concentration of the carriers is defined as the gate voltage that gives the minimum of the conductivity (V_{\min}), this hole donation is likely to move V_{\min} out of the range of V_g sweeping, thus is crucially disturbing. In order to remove charged impurities, hydrogen annealing is a frequently employed process [76]. In this process, a graphene sample is heated up to 300–500°C in H_2 (or $Ar + H_2$ mixture) atmosphere for at least few hours. This hydrogen annealing is known to work effectively for the removal of adsorbed impurities, as shown in Fig. 3.15 [76]. In the case that the hydrogen annealing cannot be used, current-induced annealing can be an alternative method for cleaning graphene [77]. In this method, a relatively large current is applied to a graphene sample at low temperature, so that the temperature of the graphene rises quite locally. It is mentioned that the temperature of the graphene may reach as high as 600°C [77]. Figures 3.16a–c show atomic force microscope images taken at various stages of the current-induced cleaning [77]. The removal of adsorbates on graphene was obviously seen. Figure 3.16d shows the conductance traces obtained before and after the cleaning [77]. In the trace before the cleaning, V_{\min} could not be determined owing to a large amount of hole donations, whereas it appeared near zero backgate voltage, meaning that impurities that can donate holes were removed. Figure 3.16e shows the variation of the current flowing the sample during the cleaning process [77]. The steep reduction of the current up to 100 seconds indicated the increase of the resistance as a consequence of the removal of hole-donating impurities.

Apart from the methods for the removal of charged impurities on graphene, the influence of charged impurities on the conductivity of graphene was examined by Chen *et al.* [68]. They deposited potassium atoms onto the surface of graphene with varying the amount and measured the backgate-voltage dependence of the conductivity. Then, they found that the mobility significantly reduces with the increase of the amount of potassium atoms, and that it is nearly constant in the vicinity of the Dirac point. Hwang *et al.* [67] theoretically predicted that the charged impurity scattering in graphene gives the dependence of the conductivity on the density of the carriers and the density of the impurities as [68],

$$\sigma(n) = Ce \left| \frac{n}{n_{\text{impurity}}} \right| + \sigma_{\text{residual}}, \quad \dots(3.14)$$

where $C = 5 \times 10^{15} \text{ V}^{-1} \text{ s}^{-1}$, e is the elementary electrical charge, n is the density of the carriers, n_{impurity} is the density of the charged impurities, and σ_{residual} is the residual conductivity at $n = 0$ (*i.e.*, the Fermi energy is set to the Dirac point). Chen *et al.* verified this expression and the value of C experimentally [68]. They also showed that the magnitudes of the reductions of the electron and the hole mobilities are different because potassium atoms are positively charged. This difference was theoretically proposed prior to their report as a characteristic feature for massless charge carriers [78].

Lattice defects include vacancies of carbon atoms, grain boundaries, ripples, wrinkles, the formation of chemical bond between adsorbates and interior carbon atoms, and so on. For micromechanically exfoliated graphene, although defects are unavoidably contained [73], the amount of such defects are likely to be quite small. However, in order to control electronic transport in graphene, vacancies or adatoms have been artificially introduced. For example, the irradiation of noble gas ions to graphene has been utilized [51]. Chen *et al.* [51] examined the variation of the conductivity of graphene upon increasing the duration of exposure of noble gas ions to the graphene samples. There have been a number of studies about the creation of carbon vacancies on the surface of graphite upon noble-gas irradiations with various kinetic energies. As widely accepted currently, when a surface of graphite is exposed to noble-gas ions with low kinetic energy (typically 100 eV or less), single atomic vacancies are mainly created predominantly in the outermost surface [79]. Such atomic vacancies act as steep potential barriers in graphene. It was theoretically predicted that the conductivity of graphene having atomic vacancies is given by [66],

$$\sigma(n) = \frac{2e^2}{\pi h} \left(\frac{n}{n_{\text{defect}}} \right) (\ln k_F R)^2, \quad \dots(3.15)$$

where h is the Planck constant, n_{defect} is the density of the vacancies, k_F is the Fermi wave number, and R is the radius of potential wall created by a vacancy [51]. Chen *et al.* systematically studied the reduction of the conductivity of graphene upon increasing n_{defect} , and validated Eq. (3.15) [51]. For another example, if a graphene sample is exposed to hydrogen plasma, the sp^2 -hybridized carbons are transformed into the sp^3 configuration,

which is called graphane being an electrical insulator because of the band-gap opening [73,79]. For graphene prepared via other processes, for example CVD or decomposition of SiC, the amount of defects contained is relatively large so that the mobility of the carriers is strongly limited.

Phonons, especially interfacial phonons between graphene and substrate, has been addressed. Chen *et al.* [74] examined the low contribution of intrinsic phonons in graphene to the conductivity, even at room temperature. On the other hand, the surface phonons originating from the SiO₂ substrate works effectively for the restriction of the mobility. Chen *et al.* stated the importance of the selection of the substrate material for improving the quality of the graphene device. One solution is to remove the substrate beneath the graphene sheet via chemical treatments [81,82] This so-called suspended graphene has shown extremely high mobility as high as 200,000 cm² V⁻¹ s⁻¹ [82]. However, making graphene suspended imposes strongly geometrical constraint. As an alternative to suspended graphene, the use of hexagonal boron nitride (h-BN) as substrate is appealing [83]. h-BN is an electrical insulator, is atomically smooth, and is relatively free from surface adsorbates. In addition, the lattice constant of h-BN well matches that of graphene. As a consequence of these advantages, it has been reported that the mobility of graphene on h-BN can be almost an order of magnitude higher than that on SiO₂ [83]. Although this method also has difficulties at present, the considerable developments in CVD preparation of graphene and h-BN are hopeful. Finally, reported mobilities of various graphene samples are summarized in Table 3.1.

Table 3.1. Reported mobilities of graphene samples prepared via various techniques.

Substrates	Preparation methods	Reported mobilities (10 ³ cm ² V ⁻¹ s ⁻¹)
SiO ₂ /Si	Mechanical exfoliation	10 [1]
Suspended on SiO ₂ /Si	Mechanical exfoliation	200 [82]
h-BN	Mechanical exfoliation	25–140 [83]
SiO ₂ /Si	CVD on Cu and transfer	0.5–1 [28]
SiC	Thermal decomposition	2 [36]

3.4.3 Vacancies in graphene as sources of localized spins

As mentioned in the previous section, it is possible to create single atomic vacancies in graphene [51,79]. Figure 3.17 shows a schematic illustration of a single atomic vacancy in graphene. The lack of a carbon atom of the A sublattice leads to the sublattice asymmetry as in the case of zigzag edges. Therefore, atomic vacancies are expected to act as localized magnetic impurities.

Kondo effect is a well-known phenomenon that can be observed by electron transport measurements at low temperature. For traditional diluted alloys, Kondo effect is understood as the interaction between the conducting s -electrons and the localized impurities having d -electronic spins, resulting in an anomalous temperature dependence in the resistivity. Kondo effect in graphene with the edge states [84,85] has been theoretically predicted [86]. In addition, it has been also theoretically stated that atomic vacancies in graphene can be the sources of localized magnetic moments possibly to cause Kondo effect [87–90]. Figure 3.18 shows an STM image taken at a single-atomic vacancy in the surface of graphite created by Ar^+ irradiation and STS spectra of local density of states measured at the surface of graphite and at a vacancy [90]. For the STS spectrum at the vacancy, the enhancement of local density of states at the Dirac point can be seen [90]. Then, the electron transport of graphene with atomic vacancies has been experimentally examined, leading to the observation of Kondo effect [91].

Chen *et al.* [91] employed single-layer graphene FET devices irradiated by 500-eV He^+ at low temperature and measured the conductivity in terms of the position of the Fermi energy. They could observe the temperature dependence of the resistivity as a function of $\ln T$ (T denotes temperature) at low temperature range, and finally the saturation of the resistivity. This temperature dependence is typical for Kondo effect. They found their observations could be fitted by the following equations,

$$\rho(V_g, T) = \rho_c(V_g) + \frac{\rho_{K,0}(V_g)}{2} \left[1 - 0.470 \ln \left(\frac{1.2T}{T_K(V_g)} \right) \right], \quad \cdots (3.16)$$

$$\rho(V_g, T) = \rho_c(V_g) + \rho_{K,0}(V_g) \left[1 - \left(\frac{\pi}{2} \right)^4 \left(\frac{T}{T_K(V_g)} \right)^2 \right], \quad \cdots (3.17)$$

where $\rho(V_g, T)$ is the backgate-voltage- and temperature-dependent resistivity, $\rho_c(V_g)$ is the non-temperature-dependent part of the resistivity (e.g., impurity

scatterings), $\rho_{K,0}(V_g)$ is the Kondo resistivity at zero temperature, and $T_K(V_g)$ is the backgate-dependent Kondo temperature. Equation (3.16) is for the intermediate temperature from 10 K to nearly 100 K, and Eq. (3.17) is for the lowest temperature below 10 K. They found that $\rho(V_g, T)$ shows a single functional form below $T_K(V_g)$ regardless of the value of V_g , which is the evidence of Kondo effect.

Although their results are excellent, there still are issues to be clarified. A theoretical study indicated that the origin of localized spins can be sp^2 bonds of carbon atoms which surround a vacancy [92]. This statement differs from the fact that the edge state originates from the nonbonding π electronic states, so that the sources of localized spin are still controversial. In addition, the edge states are likely to be strongly affected by functional groups [93–96]. Because of this point, the terminating species of carbon atoms surrounding a vacancy need to be well defined. Further effort is strongly required for the elucidation of the interaction of edge-state spins and conducting π electrons.

3.4.4 Weak localization effect in graphene

The weak localization is a quantum interference phenomenon, which is usually observed in mesoscopic systems. Quantum interference effects affect the electron transport properties in a system. The case that an electron is traveling in a conductor involving impurities is considered. There should be possible electron back-scattering paths in which an electron repeatedly hits impurities and goes back to the direction of its incidence, as shown in Fig. 3.19. In a back-scattering path, the electron can go both clockwise and counterclockwise (*i.e.*, time-reversal symmetry). Electrons in conventional two-dimensional systems have the same phase on both trajectories and interfere with one another, resulting in an increased probability of back-scattering compared to the value expected in the simple case that electrons go through impurities with various scattering processes but without back-scatterings. This increase of the back-scattering probability corresponds to the increase of the resistivity. Here, the removal of the impurities should be the only one solution to improve the conductivity. Then, when a magnetic field is applied perpendicularly to this two-dimensional system, the interference is destroyed because phase difference emerges between the two paths, so that the conductivity increases. This improvement of the conductivity due to the application of a magnetic field

is the weak localization effect. The weak localization is usually observed in a low magnetic field at low temperature. The emergence of phase difference is related to the Aharonov–Bohm effect [97], which has been observed in metal [98], semiconductor [99], and carbon nanotubes [100]. The Aharonov–Bohm effect has also been examined in graphene [101–104].

The issue of the weak localization is different in graphene from conventional systems owing to the unconventional electronic structure. The honeycomb bipartite lattice of graphene leads to the involvement of pseudospins, which makes electrons chiral in graphene. Given that the back-scattering in a valley requires a flip of a pseudospin, it is not allowed in graphene, working for the suppression of the weak localization. However, it has been predicted that elastic scattering events by defects permit the pseudospin flip in a valley, resulting in the increase of the resistivity under a low magnetic field (weak antilocalization) [105]. This weak antilocalization effect was experimentally observed in single-layer graphene [106,107]. In the case of bilayer graphene, it was predicted that the weak localization is also suppressed due to the asymmetry in the momentum (trigonal warping) [108]. However, the weak localization has been experimentally observed in single-layer and bilayer graphene [109–115]. This occurrence of the weak localization is understood as the defect- and impurity-induced occurrence of the intra- and the inter-valley scattering events that ignore the breaking of the chirality and give rise to back-scattering paths.

The magnetoresistance of the weak localization can be evaluated by the theoretically-derived expression [105] as

$$\Delta\rho(B) = -\frac{e^2\rho(0)^2}{\pi h} \left[F\left(\frac{B}{B_\varphi}\right) - F\left(\frac{B}{B_\varphi + 2B_{iv}}\right) - 2F\left(\frac{B}{B_\varphi + B_{iv} + B_*}\right) \right], \quad \cdots(3.18)$$

$$F(z) = \ln z + \psi\left(\frac{1}{2} + \frac{1}{z}\right), \quad \cdots(3.19)$$

$$B_{\varphi, iv, *} = \frac{\hbar}{4eD} L_{\varphi, iv, *}^2, \quad \cdots(3.20)$$

where $\Delta\rho(B) = \rho(B) - \rho(0)$ is the difference in the resistivity at a magnetic field B with respect to zero field, e is the elementary electrical charge, h is the Planck constant, \hbar is that divided by 2π , $\psi(z)$ is the digamma function, B_x (x : φ , iv , $*$) is defined as Eq. (3.20), D is the diffusion constant, and L_x (x : φ , iv , $*$) is characteristic scattering

lengths. The subscriptions φ , iv, and * denote the inelastic scattering event, the elastic intervalley scattering event, and the elastic scattering events including intravalley process, respectively. L_x is related to the scattering rates τ_x by $L_{\varphi,iv,*}^2 = D\tau_{\varphi,iv,*}$. Equation (3.18) has been employed to fit the magnetoresistance within a low magnetic field, and to extract information on electron scattering events in a sample. It should be noted that the weak localization requires $L_{\varphi} > L_{iv,*}$, because elastic electron scattering paths having time-reversal symmetry need to emerge before the occurrence of an inelastic scattering events.

3.5 Nanographene

In Section 2.3, it is mentioned that the peculiar electronic states emerges upon decreasing the size of graphene, *i.e.*, nanographene. Graphene itself is expected to be applied to transparent devices such as touch screens and flexible electronic papers in the near future and fast electronic devices in the future [25,116]. Chemical vapor deposition technique has been intensively studied for inexpensive mass-production of large-area high-quality homogeneous graphene sheets. On the other hand, the shrinkage of graphene is also of particular importance from the viewpoint of potential applications, for example if it is considered that graphene-based fast electronic devices partly replace contemporary silicon technology extended to nearly 10-nm scale. In nanographene with such a small-sized structure, the contribution of the edge state will be large enough, and magnetic properties originating from the sublattice asymmetry will emerge. In the present section, various studies focusing on nanographene are referred to.

3.5.1 Fabrication techniques of nano-structured graphene

The preparation of nano-structured graphene is of importance for the elucidation of the electronic properties originating from the presence of edges and the following applications as devices. Several methods have been proposed to prepare nano-structured graphene [117], including chemical exfoliation of graphene [118], chemical vapor deposition (CVD) [119,120], nanofabrication of graphene oxide [121–123], unzipping of carbon nanotubes [124–126], nanofabrication with electron–beam lithography [127,128], lithography with scanning tunneling microscope (STM) and atomic force microscope (AFM) [129–132], bottom-up production from aromatic molecules [133–135], and many other attempts. Here in this section, several techniques for preparing nano-structured graphene are written.

CVD is a technique expected for industrial application of graphene because one can produce large-area homogeneously single-layer graphene via this technique as written in Section 3.1.2. Additionally speaking, nano-structured graphene can be prepared by employing a nano-sized area on a surface of a single-crystal substrate via CVD. It was reported that single sheets of graphene nanoribbons were formed on a TiC(111)-faceted surface and TiC(410) surface with extremely narrow width corresponding to

approximately three-time multiplication of the unit cell width of graphene ($0.74\text{ nm} \sim 3 \times 0.246\text{ nm}$) [119]. As in the case of the production of large-area graphene, CVD process on a metallic substrate needs to be followed by transfer of graphene to other convenient substrate arbitrarily. Recently, it has been reported that dielectric insulators can be employed as substrates for the CVD growth of graphene [120].

Electron-beam lithography is frequently used for fabricating graphene devices. It can draw nano-scale patterns with its narrowest width being a few tens nanometers, so that it can be applicable for preparation of nano-structured graphene samples. However, new lithographical method has been demonstrated recently, which uses scanning tunneling microscope (STM) or atomic force microscope (AFM) [129–132]. In this STM/AFM lithography, graphene sheet is cut into nanostructure by electrochemical oxidation of graphene triggered and controlled by an STM/AFM tip. Nano-structured graphene with narrower widths than the electron-beam lithography method can be obtained. Figure 3.20 shows graphene nanoribbons cut by means of STM lithography [130]. Extremely narrow ribbons could be successfully prepared. Moreover, STM/AFM lithography has a great advantage for cutting graphene with edges of arbitrary directions. Because electronic structures of nanographene is dependent of the geometrical structures of edges, this advantage is of importance. However, at present, the quality of nanographene sheets obtained by STM/AFM lithography is not sufficiently high. In addition, the low yield of nanographene via STM/AFM lithography is also a critical drawback. These issues make it unlikely for this method to be applied for large-scale production.

Finally, bottom-up production of graphene nanoribbons from aromatic monomers is explained. Bieri *et al.* [133] recently developed the technique which involves small aromatic molecules with halogen groups as precursor monomers. These monomers are deposited on a metal substrate. Figure 3.21 shows the case of hexaiodo-substituted cyclohexa-*m*-phenylene monomer [133]. This monomer can reportedly adsorb on Cu, Au, and Ag substrate with its C–I bond dissociated at room temperature. By heating up the substrate, the fusion of monomers occurs, resulting in graphene-like fragments as shown in Figure 3.22 [133]. Cai *et al.* [134] employed monomers containing bromine. Through heating up the substrate to cause dehalogenation and cyclodehydrogenation steps, graphene nanoribbons purely with armchair-shaped edges are formed. This method can produce graphene nanoribbons with well controlled widths and various shapes, both of

which depends upon the chemical structure of a precursor monomer. However, further effort should be devoted to create graphene nanoribbons having solely zigzag-shaped edges for fundamental studies on the edge state, and to make this method applicable for fabricating or transferring nanoribbons on an arbitrary substrate.

3.5.2 Observation of the edge state by scanning tunneling microscope

It was theoretically stated by Fujita *et al.* that localized electronic states exist in the vicinity of zigzag-shaped edges of nanographene [84,85]. This state is called the edge state. The following experimental studies have been verified that zigzag edges of graphene indeed possess this state by means of scanning tunneling microscopy and spectroscopy (STS) [136–139].

Kobayashi *et al.* [136] employed nanographite samples prepared on a highly oriented pyrolytic graphite (HOPG) substrate by means of a combination of electrophoretic deposition and heat treatment of diamond nano-particles [140]. For the STM observation under an ultra-high vacuum condition, the sample was heated up to around 800°C in order to eliminate functional groups at the edges and on the surface of the sample. Moreover, the sample was immediately exposed to atomic hydrogen flow, which was produced by cracking of hydrogen molecules with a heated tungsten filament, so that the edges of the sample were terminated by hydrogens. After cleaning and hydrogenating the sample, the edges of the sample were observed by STM. The edges of the sample were sufficiently clean to determine the precise structures, namely zigzag or armchair. In STM images taken by constant-height mode shown in Fig. 3.23 [136], it was obviously found that step edges with zigzag structures had bright spots in the vicinity of edges, whereas those with armchair shapes did not have such brightness. These bright spots were explained as the large local density of states originating from the edge state of zigzag edges. Furthermore, an STS spectrum measured at a zigzag region (Fig. 3.23b [136]) obviously had a flat band at the Dirac point, which was unambiguously assigned to the edge state. Figures 3.24a–c show STM images of armchair-shaped edges [136]. The absence of bright spots at the armchair edges was again confirmed. An STS spectrum taken at an armchair region did not show any state at the Dirac point (Fig. 3.24d [136]). These STM/STS observations of zigzag and armchair edges nicely agreed with theoretical predictions.

3.5.3 X-ray absorption spectroscopy

It has been reported that the edge state can be identified by carbon K-edge near-edge X-ray absorption fine structure (NEXAFS) spectroscopy [141–143]. X-ray absorption spectroscopy is known as a powerful element-specific method. Among X-ray-based spectroscopic techniques, NEXAFS is relatively young, which was developed in the 1980s. NEXAFS probes the absorption of X-ray by transition of core electrons into unoccupied states. NEXAFS is regarded as a powerful tool that provides information on electronic structures of unoccupied states, molecular alignments at surfaces or thin films, and so on [144]. NEXAFS of graphite has been widely studied [145–147] and applied to graphene recently [148–151].

Typically, C K-edge NEXAFS spectra of graphite and graphene possess two characteristic features originating from transitions of $1s$ core electron to unoccupied states having π - and σ -symmetry, which locate approximately at 285.5 eV and 292.0 eV, respectively. These features can be seen in the C K-edge NEXAFS spectra of graphene shown in Fig. 3.25 [148]. Given that these orbitals spread in different directions, namely the π^* state is perpendicular to the plane of the graphene sheet and the σ^* state distribute within the plane, opposing dependence of the intensities of these peaks can be observed upon the direction of the electric field vector of the incident X-ray [144,145]. Figure 3.26 shows the polarization dependence of the C K-edge NEXAFS spectra of graphite [145]. When the angle of the incidence, the electric field vector of the incident X-ray, and the surface normal vector are α , \mathbf{E} , and \mathbf{n} , respectively, the transitions from the carbon $1s$ state to the π -symmetry final states are enhanced with $\mathbf{E} \parallel \mathbf{n}$ (*i.e.*, α close to 90°). Contrarily, those to the σ -symmetry final states appears clearly with $\mathbf{E} \perp \mathbf{n}$ (*i.e.*, α close to 0°).

In the spectra for nanographene samples, an extra ingredient is observed at 284.5 eV in the vicinity of the Fermi level at 284.36 eV. This extra ingredient has been assigned to the edge state [141–143]. Joly *et al.* employed thick graphene nanoribbon samples and examined the variation of the edge-state ingredient upon high-temperature treatments of the sample [142]. Prior to this study, it was revealed that nanographite-based systems showed the fusion of the edges of nanographite domains by high-temperature treatment [152,153]. Joly *et al.* confirmed that the edge state ingredient survives up to 1000°C , tends to decrease at further higher temperatures, and ultimately disappears above 2000°C as

shown in Fig. 3.27 [142]. The integrated intensity of the edge state peak are shown in Fig. 3.28 [143]. Thus, the threshold temperature for graphitization was determined as around 1500°C [142]. This study also evidenced that NEXAFS technique is sufficiently sensitive to the edge state in nano-structured graphite, and that it is capable for detecting structural modifications of nanographite systems in terms of the evolution in the intensity of the edge-state ingredient.

3.5.4 Magnetic susceptibility originating from edges of nanographene

In nano-structured graphene, magnetic properties appear significantly owing to the localized spins of the edge state. For experimental investigations of magnetism in nanographene, activated carbon fibers (ACFs) have been frequently employed [154–156]. ACFs consist of a three-dimensional disordered network of nanographite domains, each of which is a stack of 3–4 nanographene sheets with the mean in-plane size of about 3 nm, as shown in Fig 3.29 [155]. Assuming a circular nanographene fragment of 3 nm in diameter, it is composed of approximately 300 carbon atoms, and nearly 90 carbons out of 300 are at the periphery (*i.e.*, edges). The high ratio of the edge carbons to the interior carbons ~30% leads to the large contribution of magnetic properties originating from the edge states. In addition to the large proportion of edge carbon atoms, ACFs have huge specific surface areas in the range of 1000–3000 m² g⁻¹ owing to nano-sized interstitial spaces, namely nanopores, which are distributed between nanographite domains. Such nanopores are capable of accommodating various chemical species, enabling us to modify the characteristics of ACFs via so-called host–guest interactions [157,158].

As an example, a study on the variation of magnetic susceptibility of ACFs coupled with conductivity measurements upon heat treatments is referred to [152,153]. Shibayama *et al.* revealed the heat-induced structural evolution of ACFs by Raman spectroscopy. Figure 3.30 shows the variation of the in-plane crystallite size (L_a) of the nanographite domains in ACFs upon the heat-treatment temperature (HTT) [152]. L_a was evaluated by an equation in [49]. For the pristine ACFs sample, $L_a \sim 3$ nm as expected. By increasing HTT above 1000°C, L_a also increased strikingly, indicating the fusion of the nanographite domains. This heat-induced graphitization in ACFs could be verified in terms of the conductivity. The conductivity in ACFs had been examined and described as

the Coulomb-gap-type variable range hopping process between nanographite domains in the Anderson insulator regime given by [155],

$$\sigma \propto \exp\left[-\left(\frac{T_0}{T}\right)^{1/2}\right], \quad \cdots(3.21)$$

$$T_0 = \frac{6e^2}{4\pi^2 k_B \varepsilon \xi}, \quad \cdots(3.22)$$

where ε is the dielectric constant of the medium and ξ is the localization length of the wave function of conducting electrons. Figure 3.31 shows the plot of the temperature dependences of the conductivities of ACFs samples before and after heat treatments at various HTTs [152]. ACFs samples heat-treated below 1000°C showed thermally-activated conductivities. The common-logarithmic conductivities of these samples showed linear dependence on $T^{-1/2}$, as expected by Eq. (3.21). In contrast, the conductivities of ACFs samples heat-treated above 1300°C were nearly independent of the temperature. This change was explained by the insulator-to-metal transition due to heat-induced fusion of the nanographite domains [152]. The threshold HTT for this transition was determined as ~1200°C.

This structural evolution by annealing was expected to have direct correlation with magnetic properties of ACFs samples because fusion of nanographite domains corresponded to the decrease of the edge ratio. The behavior of the magnetic susceptibility in pristine ACFs obeys the paramagnetic Curie–Weiss law [155], namely the temperature dependence of the magnetic susceptibility contains the Curie-Weiss term $C/(T-\Theta)$, where C is the Curie constant and Θ is the Weiss temperature. Figure 3.32 shows the temperature dependence of the magnetic susceptibility (χ) of ACFs samples heat-treated at various HTTs [153]. For ACFs samples up to HTT = 1100°C, χ followed the Curie–Weiss law in the entire temperature range. However, χ of the samples above HTT = 1200°C deviated from the law below 20 K. This change in the temperature dependence of χ was explained on the basis that the Curie–Weiss behavior with localized edge-state spins in the insulating regime was converted to the less temperature dependent susceptibility of conduction electrons in the metallic regime [153].

3.5.5 Chemical modification of the edge states

In a monohydrogenated zigzag-edged nanoribbon, localized electronic spins of the edge state at one zigzag edge is ferromagnetically aligned. It can be understood in terms of the sublattice asymmetry, that is to say, only A (or B) sublattice locates at one zigzag edge. For the other zigzag edge of the nanoribbon, however, only B (or A) sublattice are settled, which has opposite pseudospin. This coexistence of up and down spins at two zigzag edges of the nanoribbon corresponds to antiferromagnetic structure, so that the zigzag nanoribbon does not have spontaneous magnetization.

Kusakabe and Maruyama theoretically predicted that chemical modifications of the edges of graphene nanoribbons can give rise to ferrimagnetic ordering [159,160]. The upper panel of Fig. 3.33 shows the distribution of the spin density in a zigzag-edged nanoribbon with one of its edge dihydrogenated [160]. When one zigzag edge is dihydrogenated, the densities of the up and down spins are not compensated, resulting in a ferrimagnetic structure. The rise of a ferrimagnetic structure is also achieved in the case of asymmetric fluorination of the zigzag nanoribbon as shown in the lower panel of Fig. 3.33 [160]. A clear difference from the case of hydrogenation is that the edge state spin disappears completely at the difluorinated edge.

The evolution of the edge state upon fluorination has been experimentally investigated with ACFs in terms of the edge state peak in NEXAFS spectra [143] and the concentration of localized spins from magnetic susceptibility measurements [93]. Figures 3.34a and 3.34b show the schematic models of fluorinated ACFs at low and high ratio of fluorine atoms to carbon atoms (F/C), respectively [143]. Figure 3.34c shows the intensities of the edge state peak, the σ -dangling bond peak, and the π^* peak measured by NEXAFS [143]. Figure 3.34d shows the concentration of localized spins [93,143]. At low F/C up to 0.4, fluorination occurs only at the edges of nanographite domains in ACFs, resulting in difluorinated edges. As difluorinated sites increases, the edge state is expected to be destroyed [160]. This theoretical expectation was nicely evidenced in Figs. 3.34c and 3.34d as the reduction of the intensity of the edge state and as the reduction of the spin concentration, respectively. At high F/C above 0.4, fluorine atoms are likely to attack the interior carbon atoms, breaking the π network and creating dangling bonds. The intensity of the π^* peak reduced significantly, reflecting the destruction of the π network, whereas the intensity of the σ -dangling bonds took its maximum at F/C \sim 0.8 owing to

the creation of the interior dangling bonds, as shown in Fig. 3.34c [143]. The enhancement in the spin concentration, which can be viewed in Fig. 3.34d [93,143], was also a strong support for this suggestion. On further increasing F/C above 0.8, the intensity of the σ -dangling bond state and the spin concentration decreased similarly, as a consequence of the disappearance of the interior dangling bonds by fluorination.

3.6 Scope of this thesis

It has been viewed that the periodicity of the honeycomb bipartite structure of graphene results in exotic electronic properties based on the unconventional electronic structure described by the relativistic massless Dirac equation. Since the electronic structure of graphene in the vicinity of the Dirac point is composed of the p_z orbitals of carbon atoms that have perpendicular spreading to the plane of graphene, it is likely to be strongly affected by the surrounding environment, for example supporting substrates and adsorbed molecules. On the one hand, the removal of the surrounding environment has been achieved. The removal of the substrate leads to suspended graphene [81,82] and the removal of adsorbates has been performed by hydrogen annealing [76] or current-induced cleaning [77]. These approaches are for understanding fundamental properties of pure graphene such as anomalous quantum Hall effect [62–64] due to massless charge carriers [161,162], and extremely high mobility of charge carriers [82]. However, such processes are complicated and unlikely to be practical. On the other hand, making the use of the control of the surrounding environment has also provided fruitful information. Hexagonal boron nitride, which have advantages of small surface roughness and small amount of surface adsorbates with respect to conventional silicon wafer, is now regarded as the most favorable supporting substrate [83], and the combination of chemical vapor deposited graphene with chemical vapor deposited hexagonal boron nitride is expected to be commercially applied in the near future. Patterned decoration of the substrate by self-assembled monolayer [163–168] has been opened a new way of spatial modulation of a graphene sheet without damaging. Adding impurities onto graphene helps us acquiring how the mobility in graphene is influenced by them [51,68,69,72,73]. Drastic changes in the conductivity of graphene upon molecular adsorption [169–171] can be utilized as sensitive gas sensors. Great effort has been devoted to control graphene via its surrounding environment for applications.

Damaging a material is usually losing its advantages, hence is unfavorable. In the case of graphene, it is also true, but is false if attention is focused on the appearance of edge state. The edge state is a localized electronic state around zigzag-shaped edges of graphene having nonbonding π -orbital nature. The breaking symmetry of the sublattices at zigzag edges makes the edge state magnetic. In addition to the electronic and magnetic properties of the edge state, edges of graphene give rise to the chances of chemical

modification via decorating edge carbons by various functional groups. Since the theoretical predictions of the edge state appeared [84,85], the edge state has been evidenced by scanning tunneling microscope observations [136–139] and investigated in terms of electronic and magnetic structures and chemical modification [154–156]. However, most of the experimental studies focusing on the edge state have employed nanographite-based samples such as activated carbon fibers and nanographite ribbons, which have by nature a large ratio of edge carbon atoms to interior carbon atoms. This abundance of edges is advantageous for magnetic measurements because of the abundance of magnetic moments at edges, whereas it is disadvantageous in terms of, *e.g.*, electron transport, edge pollution, and difficulty in applications. Electron transport in nanographite-based materials is governed by variable range hopping mechanism [152], thus is totally different from graphene. In addition, electric-field-effect control of conducting carriers is not utilized. Pollution of edges due to high chemical activity is also problematic, leading to the lack of controllability and the requirement of severe conditions, *e.g.*, high temperature for cleaning or highly reactive agent for edge decoration. In anticipation of graphene as future electronic devices coupled with spintronic aspects arising from the edges, it is indispensable to discover how to make the edge state emerge in graphene. Several techniques for the introduction of edges into a single sheet of graphene have been considered. However, the edge state is unlikely to always emerge at edges introduced into the graphene sheet. For example, the energetic advantage of armchair-shaped edges, which do not have the edge state, should be one of the reasons. Moreover, experimental information is lacking on whether electronic phenomena originating from edges in the graphene sheet is observable or not.

Therefore, the first scope of this thesis is to conclude what kind of nanostructure of graphene are the most likely to have a large contribution of edges. For this purpose, nanofabrications by electron-beam lithography were employed to prepare edge-enriched antidot graphene samples having nanostructure of several tens to 100 nanometer scale. For comparison with the antidot samples having artificially controlled nanostructures, another method was also utilized, that is to say, graphene samples having atomic vacancies were prepared by means of irradiation of 100-eV Ar^+ ions. Under the hypothesis that the contribution of graphene edges appears as electronic scattering events, the electrical conductivities of these samples were measured at low temperature under a

magnetic field with the advantage of tuning the concentration of charge carriers by applying backgate voltages. Raman spectroscopy measurements were also performed under an ambient condition. Then, it has been concluded that dominant scatterers in antidot samples and graphene with atomic vacancies are charged impurities and edges of vacancies, respectively, so that the contribution of the edge state can be expected in graphene with atomic vacancies. The results have been published [Y. Kudo, K. Takai, and T. Enoki, Electron transport properties of graphene with charged impurities and vacancy defects, *Journal of Materials Research* **28**, 1097–1104 (2013)], and are written in Chapter 4.

The second scope is the verification of the emergence of the edge state over a macroscopic extent upon the creation of atomic vacancies. In order to figure out how the edge state contribution emerges upon creation of structural defects, the surface of HOPG was observed upon Ar^+ irradiation with various kinetic energies using near-edge X-ray absorption fine structure spectroscopy. It has been clearly found that the edge state peak emerges by low energy Ar^+ irradiation, which produces vacancies in the outermost layer of HOPG. It has also been observed the surface of HOPG changes into an amorphous-like structure by increasing the kinetic energy of Ar^+ ions. Interestingly, the edge state contribution has appeared to survive even in the amorphous-like state. Consequently, it has been verified that low energy Ar^+ irradiation can be utilized to make the edge state emerge significantly in graphene. The results have been submitted [Y. Kudo, M. Kiguchi, J. Takashiro, K. Takai, and T. Enoki, Development of edge state on graphite surface induced by Ar^+ irradiation studied using near-edge X-ray absorption fine structure spectroscopy, *Carbon*, *in press* (2014), <http://dx.doi.org/10.1016/j.carbon.2014.01.067>], and are written in Chapter 5.

In virtue of the studies described above, Ar^+ irradiation to graphene has been regarded as the most reliable method for the emergence of the edge state contribution over a single-layer graphene. Then, because the electronic and the magnetic structures of the edge state are sensitively dependent of functional groups [93–96,143,154–156,159,160], it is strongly required to examine the edge state properties under the precise control of the chemical structures at edges. Thus, the third scope of this thesis is to establish a method for decorating the vacancies in Ar^+ -irradiated graphene, which is applicable to various functionalizations. Hydrogen has been chosen as a starting point because there has already

been a method to hydrogenate edges of HOPG, which was previously used for the STM observations of the edge state [136,138]. Electrical conductivity measurements have been again employed in terms of backgate-aided control of carrier density, expecting to detect evolutions in scattering behavior. Then, it has been found that the atomic hydrogen method are likely to cause impurity adsorptions on graphene unintentionally. Given that the high reactivity of carbon atoms at vacancies allows hydrogen molecules to adsorb dissociatively, an exposure of graphene samples to hydrogen molecules has been performed immediately after Ar^+ irradiation. The resulting characteristics in the electrical conductivity have appeared to agree with what is expected theoretically. It has been concluded that atomic vacancies can be hydrogenated by exposure to molecular hydrogen. Moreover, this simple method can be applied to other gas species.

3.7 Figures in Chapter 3

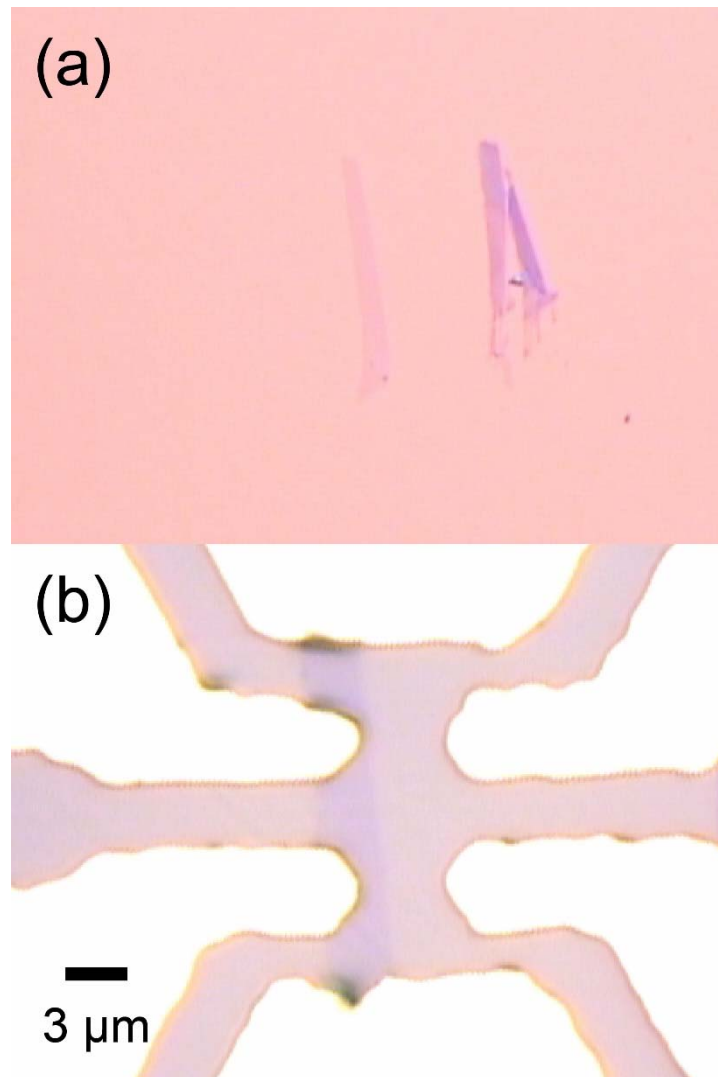


Figure 3.1. (a) An optical microscope image of an as-prepared single-layer graphene flake on a Si substrate covered with a 285-nm-thick SiO₂ layer typically obtained by the author. The single-layer graphene locates in the center of the image, together with thicker flakes nearby. (b) An optical microscope image of the identical graphene flake taken after the attachment of Au/Cr electrodes by means of photolithography. Cr is an adhesion layer directly attached to the sample with the typical thickness of below 5 nm. Au is deposited on Cr.

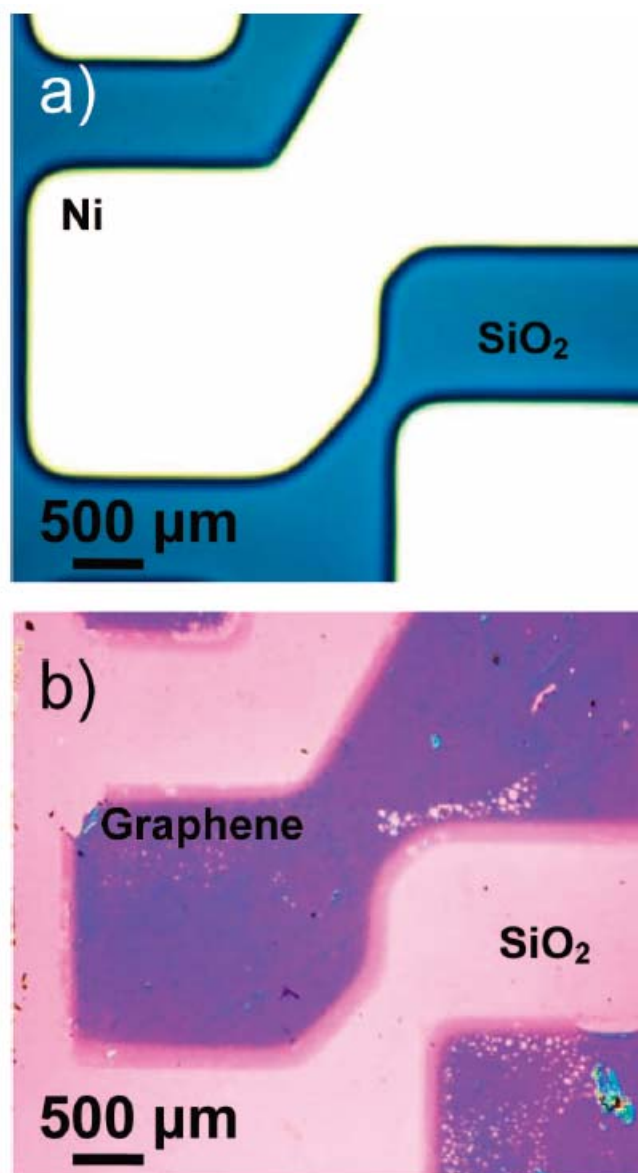


Figure 3.2. (a) An optical microscope image of a patterned Ni film on SiO₂/Si. CVD graphene is grown on the surface of the Ni pattern. (b) An optical microscope image of the CVD graphene transferred from the Ni surface in (a) to another SiO₂/Si substrate. Reprinted with permission from A. Reina, X. Jia, J. Ho, D. Nezich, H. Son, V. Bulovic, M. S. Dresselhaus, and J. Kong, Large area, few-layer graphene films on arbitrary substrates by chemical vapor deposition, *Nano Letters* **9**, 30 (2009) [21]. Copyright 2009 American Chemical Society.

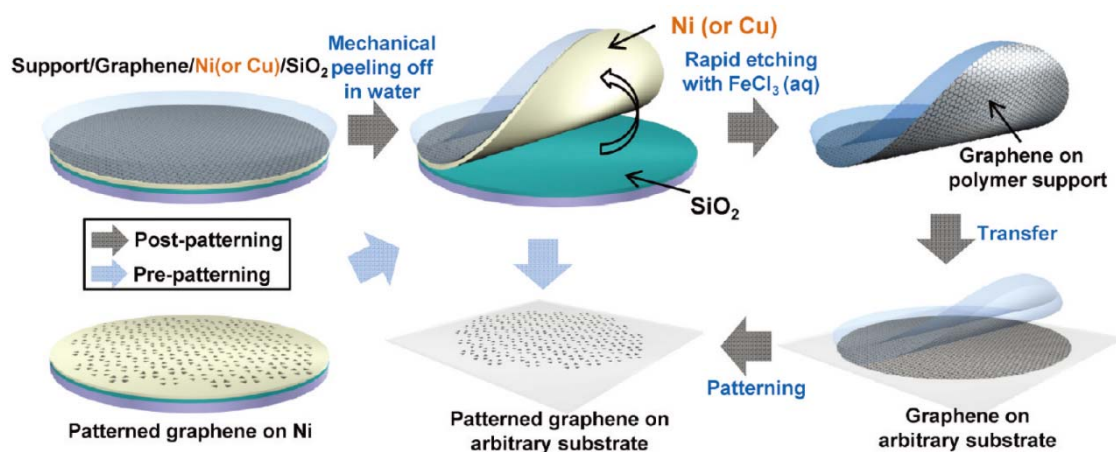


Figure 3.3. Schematic illustration of transferring CVD graphene. (left-top) CVD graphene on a non-patterned metal film deposited on a SiO_2/Si substrate. The grown graphene is covered with a supporting polymer layer. (center-top) The polymer/graphene/metal stack is mechanically peeled off the substrate. (right-top) Then, by etching the metal layer using acid, the polymer/graphene stack is isolated. (right-bottom) The isolated stack can be deposited on an arbitrary substrate. After the removal of the supporting polymer, the graphene on an arbitrary substrate is obtained. (center-bottom) After the following patterning of graphene, the arbitrarily patterned graphene on an arbitrary substrate is obtained. There is another way to achieve this (center-bottom) situation more conveniently, namely pre-patterning of the metal layer. (left-bottom) CVD graphene on a patterned metal film on a SiO_2/Si substrate. The grown graphene is covered with a supporting polymer layer. This polymer/patterned-graphene/patterned-metal stack is also mechanically peeled off the substrate as in (center-top). Via chemical etching of the metal layer and removing the supporting polymer, the arbitrarily patterned graphene on an arbitrary substrate is obtained as in (center-bottom). Reprinted with permission from Y. Lee, S. Bae, H. Jang, S. Jang, S. E. Zhu, S. H. Sim, Y. I. Song, B. H. Hong, and J. H. Ahn, Wafer-scale synthesis and transfer of graphene films, *Nano Letters* **10**, 490 (2010) [28]. Copyright 2010 American Chemical Society.

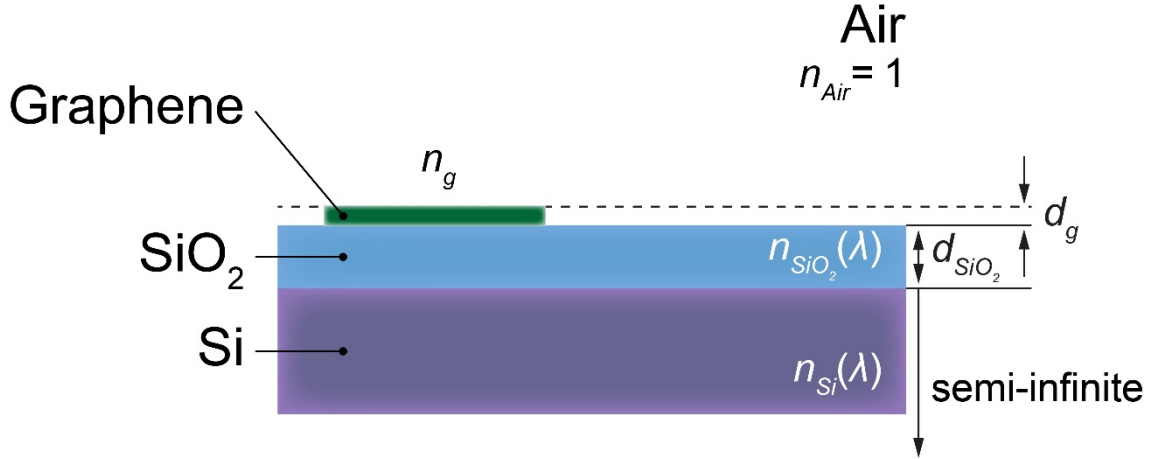


Figure 3.4. A schematic illustration of a model of graphene on a SiO₂/Si substrate.

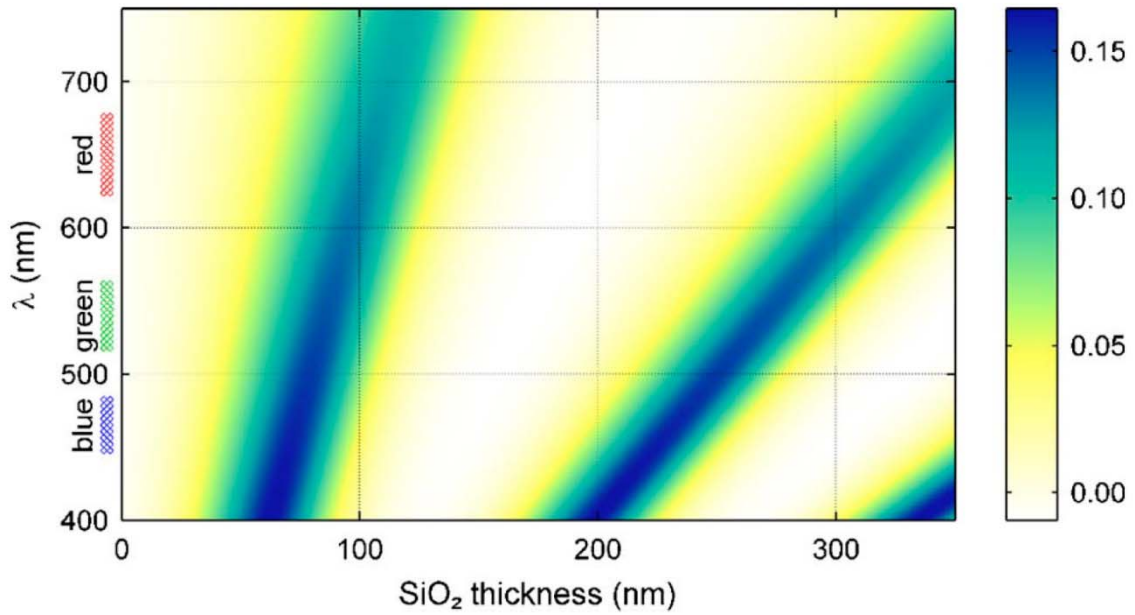


Figure 3.5. Color plot of the optical contrast as a function of wavelength and SiO₂ thickness given by Eq. (3.7). The color scale on the right shows the expected contrast. Reprinted with permission from P. Blake, E. W. Hill, A. H. C. Neto, K. S. Novoselov, D. Jiang, R. Yang, T. J. Booth, and A. K. Geim, Making graphene visible, *Applied Physics Letters* **91**, 063124 (2007) [40]. Copyright 2007, AIP Publishing LLC.

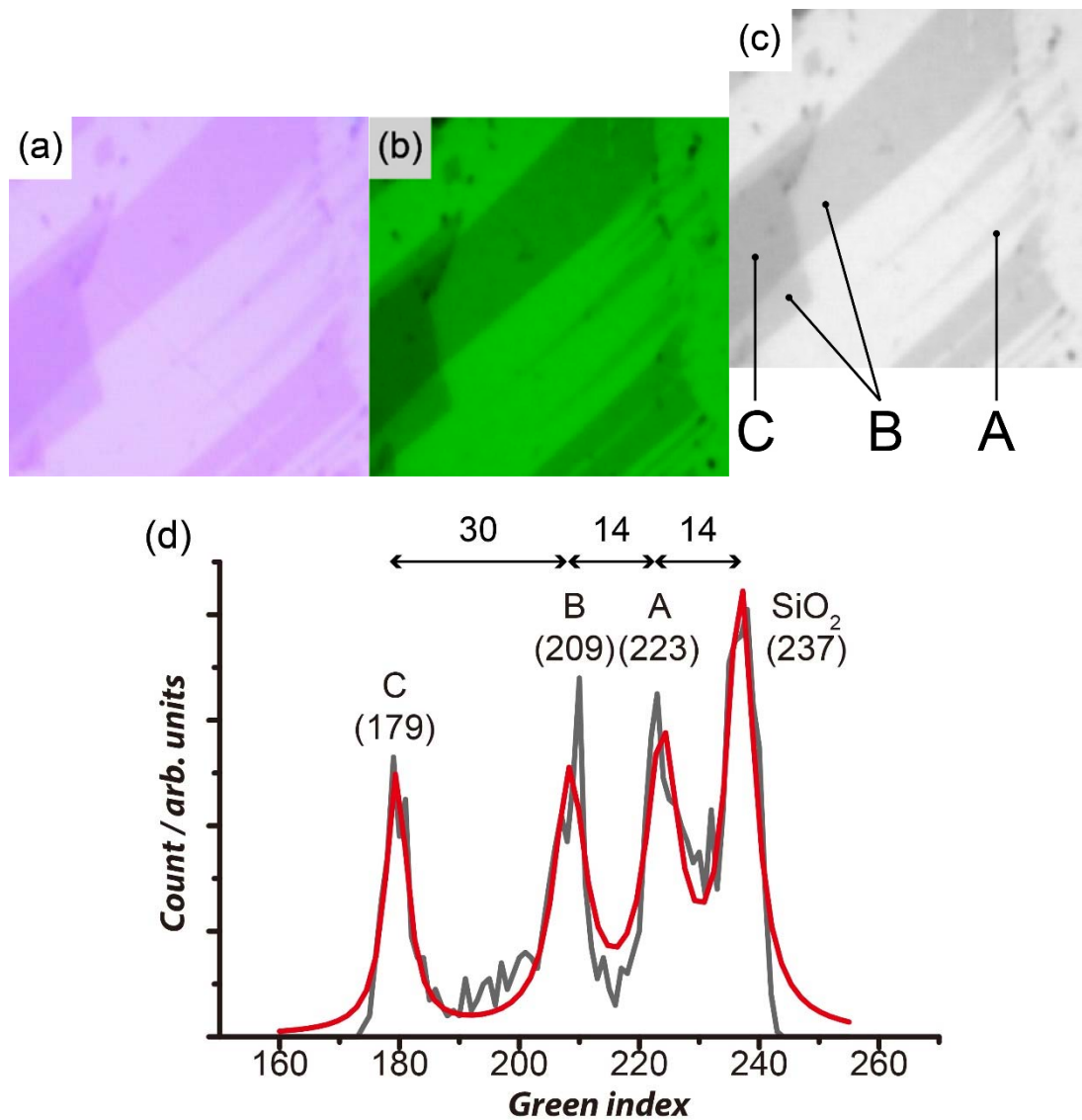


Figure 3.6. An example of the determination of graphene thickness by optical microscope images done by the author. (a) An optical microscope image of graphene flakes. (b) An image taken with a green filter. (c) An image of green component extracted from (b). (d) A plot of the distribution of the values of green indices in (c).

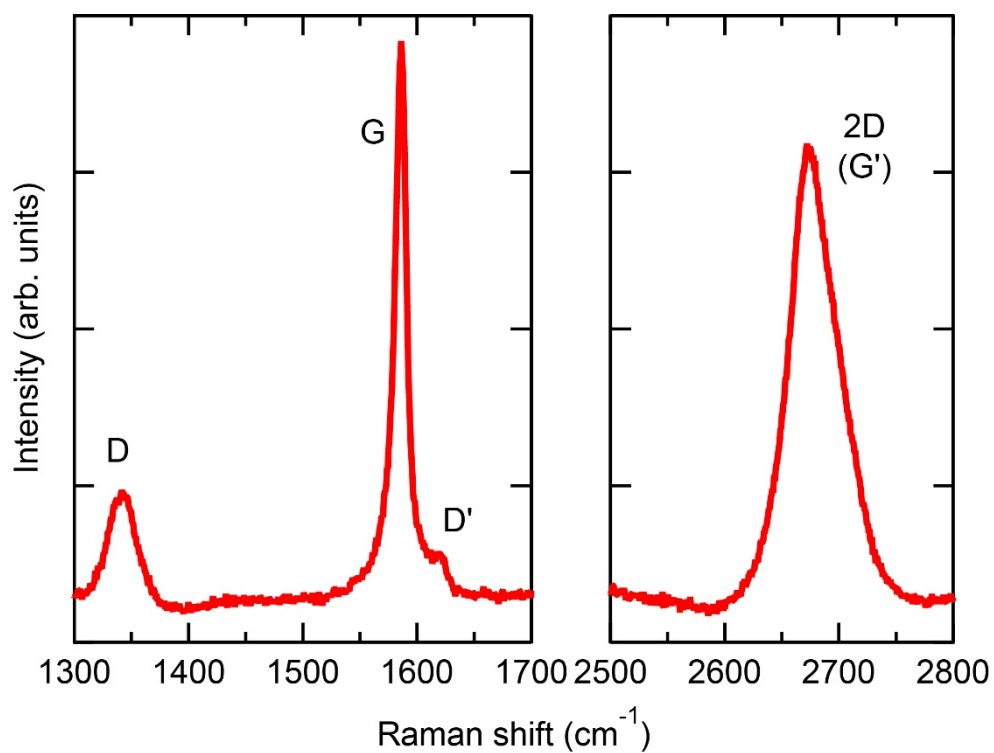


Figure 3.7. The typical Raman spectra of a defective graphene sample measured by the author. In the left panel, the main G band is clearly observed together with the D and D' bands both of which are correlated with the presence of defects. In the right panel, the 2D band, which is called G' at times, is observed.

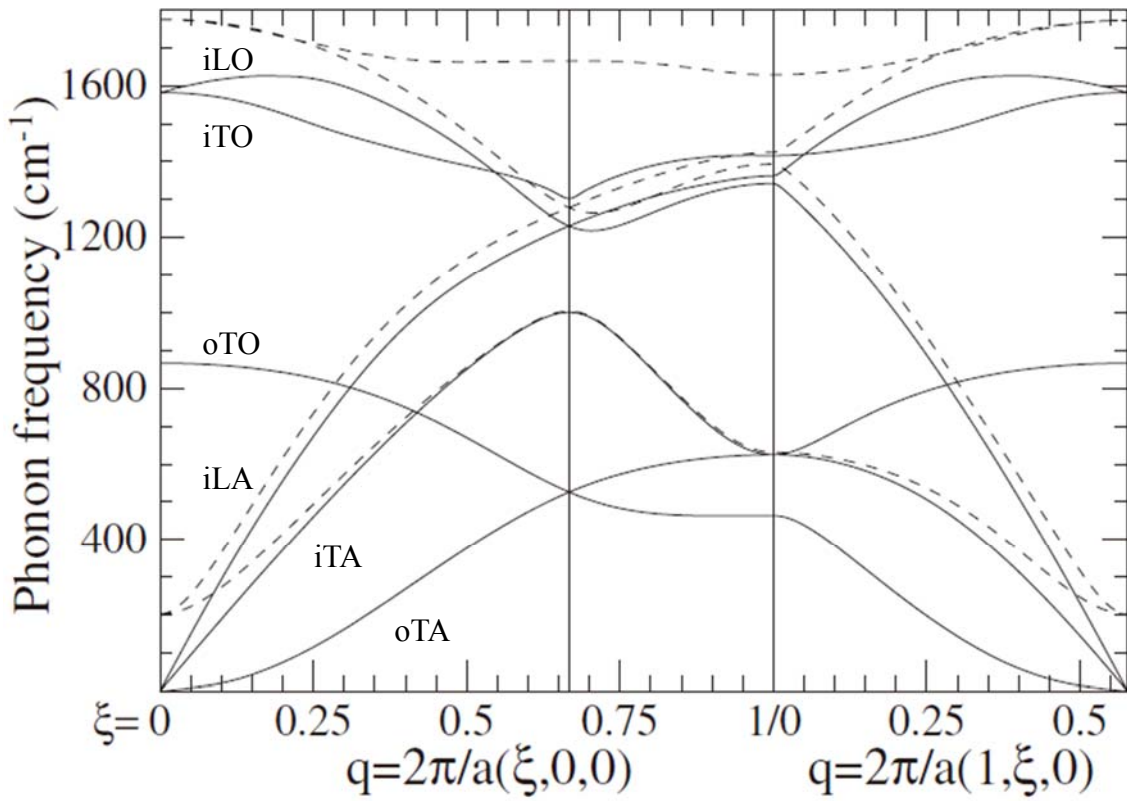


Figure 3.8. Calculated phonon dispersion relation of graphene with the labels of phonon branches. Reprinted figure with permission from M. Lazzeri, C. Attaccalite, L. Wirtz, and F. Mauri, Impact of the electron-electron correlation on phonon dispersion: failure of LDA and GGA DFT functionals in graphene and graphite, *Physical Review B* **78**, 081406 (2008) [46]. Copyright (2008) by the American Physical Society.

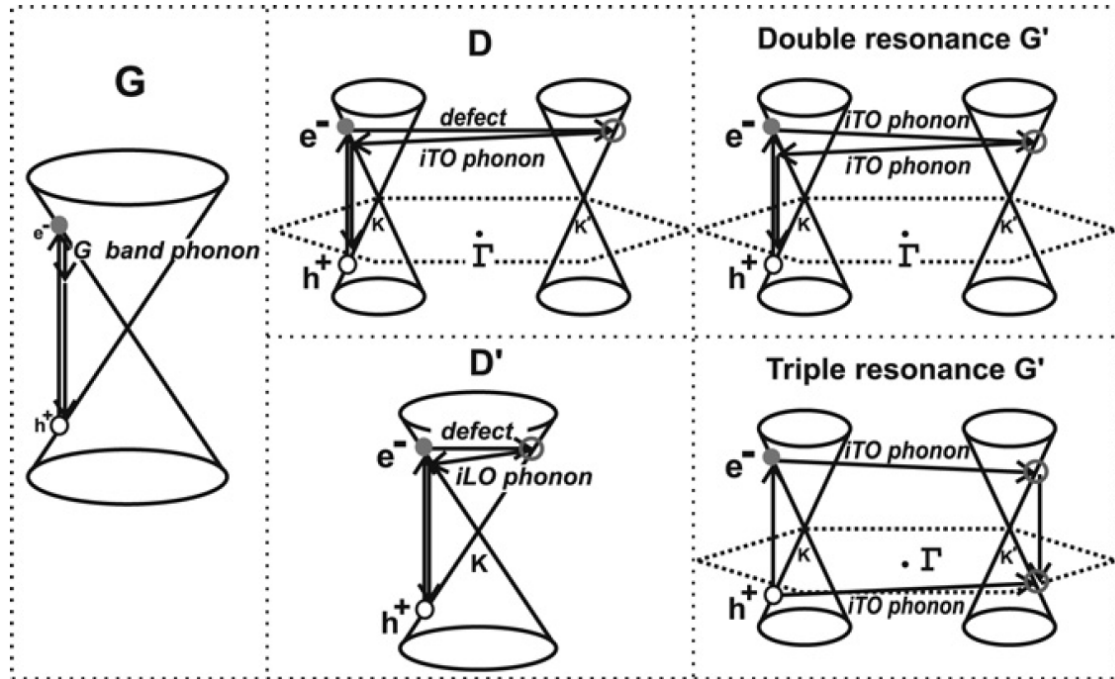


Figure 3.9. (Left) First-order G-band process and (center) one-phonon second-order double-resonance process for the D band (intervalley process) (top) and for the D' band (intravalley process) (bottom), and (right) two-phonon second-order resonance Raman spectral processes (top) for the double-resonance G' process, and (bottom) for the triple resonance G'-band process for single-layer graphene. Reprinted from *Physics Reports*, **473**, L. M. Malard, M. A. Pimenta, G. Dresselhaus, and M. S. Dresselhaus, Raman spectroscopy in graphene, 51, Copyright (2009), with permission from Elsevier [43].

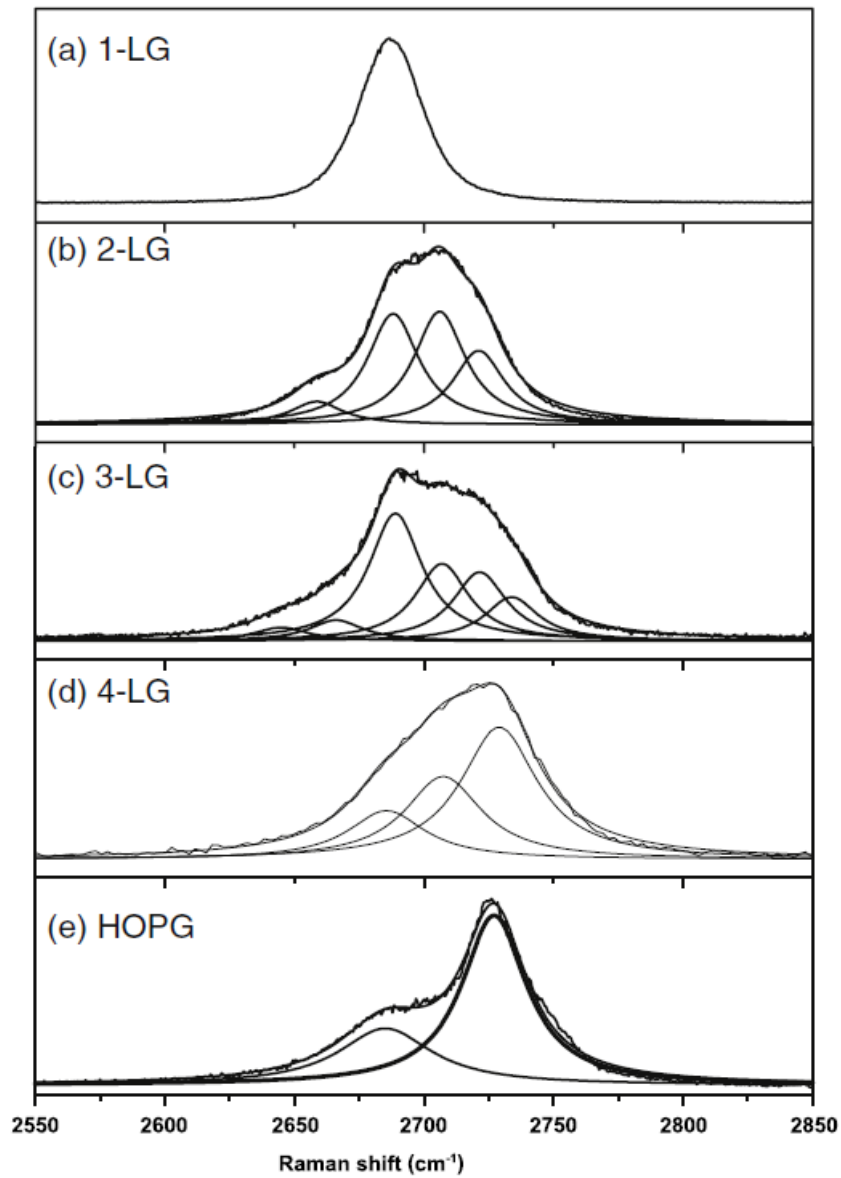


Figure 3.10. Typical 2D bands for (a) single-layer graphene, (b) bilayer graphene, (c) trilayer graphene, (d) four-layer graphene, and (e) HOPG. Reprinted from *Physics Reports*, **473**, L. M. Malard, M. A. Pimenta, G. Dresselhaus, and M. S. Dresselhaus, Raman spectroscopy in graphene, 51, Copyright (2009), with permission from Elsevier [43].

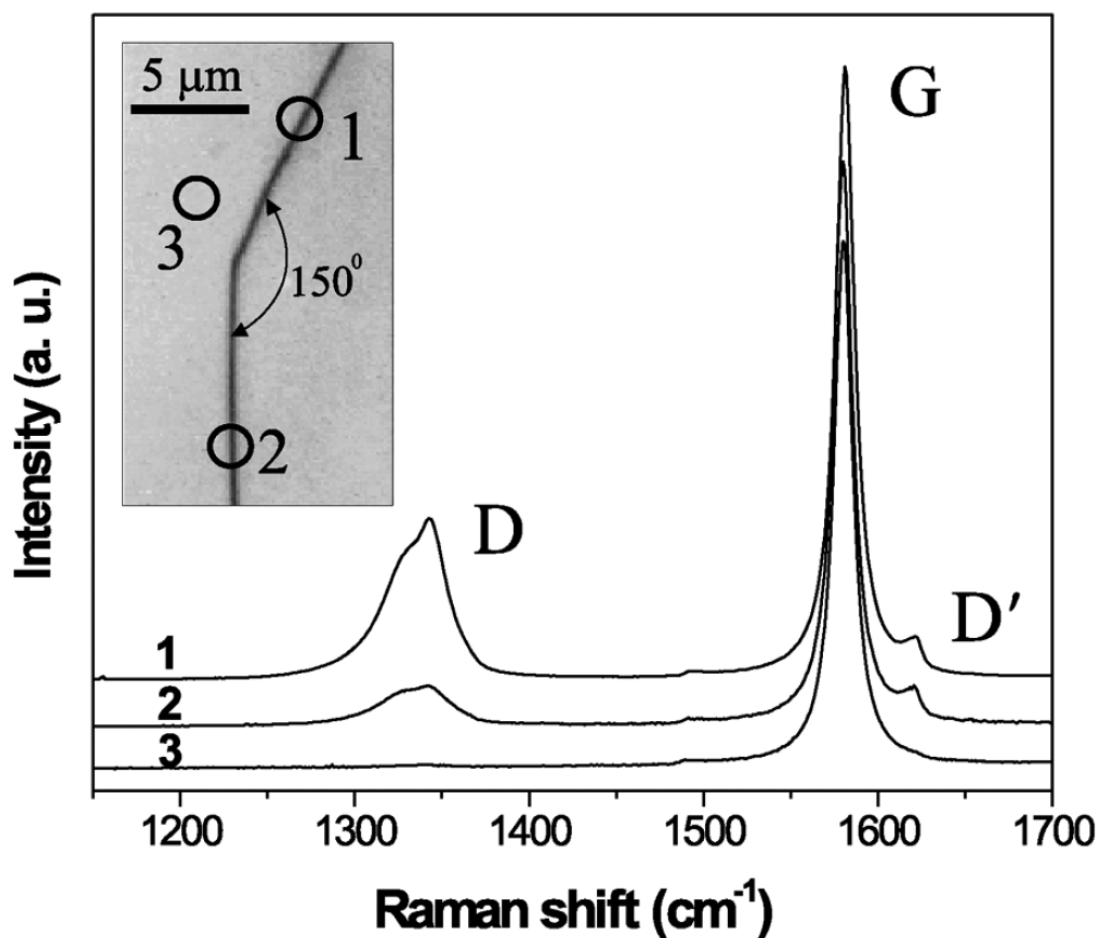


Fig. 3.11. Raman spectra of an HOPG obtained in three distinct regions. The inset shows an optical microscope image of the regions 1, 2, and 3, where spectra 1, 2, and 3 were taken, respectively. Reprinted figure with permission from L. G. Cançado, M. A. Pimenta, B. R. A. Neves, M. S. S. Dantas, and A. Jorio, Influence of the atomic structure of the Raman spectra of graphite edges, *Physical Review Letters* **93**, 247401 (2004) [54]. Copyright (2004) by the American Physical Society.

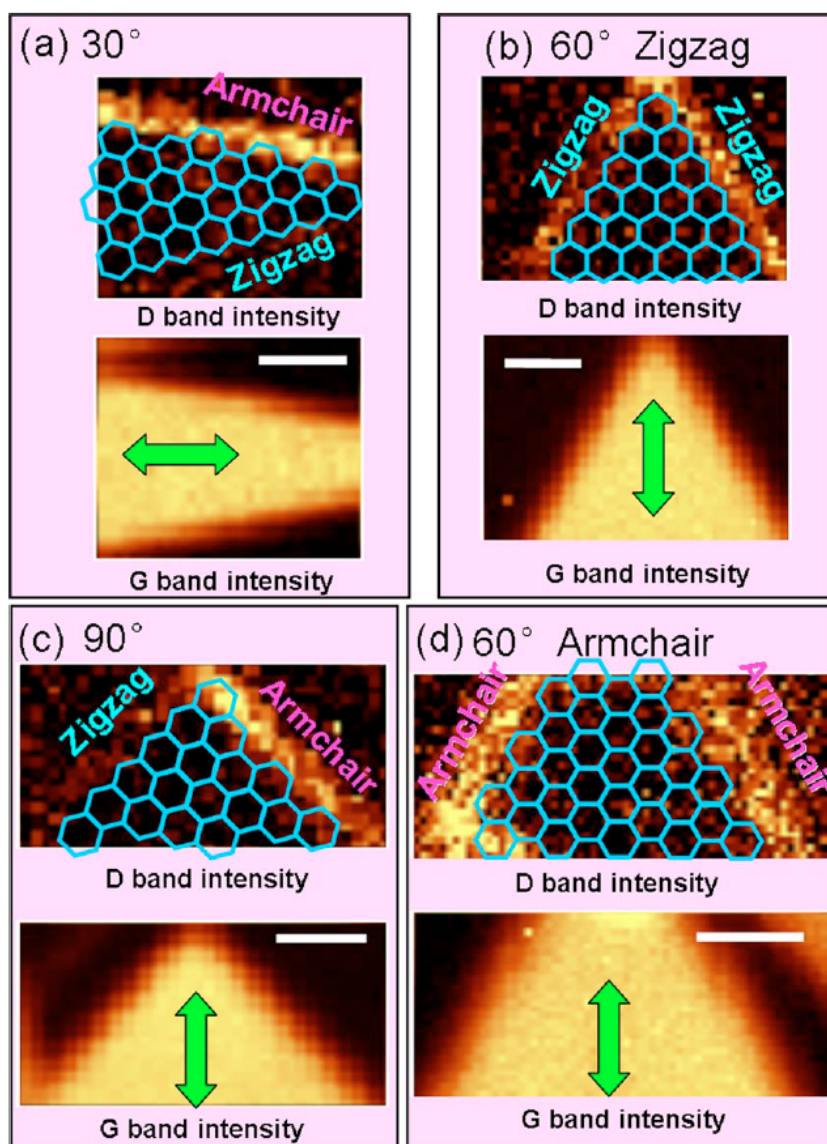


Figure 3.12. Raman imaging results from edges with angles (a) 30° , (b) 60° (zigzag), (c) 90° , and (d) 60° (armchair). The images constructed by the G band intensity show the positions and shapes of single-layer graphene sheets. The laser polarization is indicated by the green arrows. The super-imposed frameworks are guides for the eye indicating the atomic arrangements at the edges. Note that the arrangements of (b) and (d) were determined by the other pair of edges (not shown) with $30^\circ/90^\circ$ on the same piece of single-layer graphenes. The scale bar is $1\ \mu\text{m}$. Reprinted with permission from Y. M. You, Z. H. Ni, T. Yu, and Z. X. Shen, Edge chirality determination of graphene by Raman spectroscopy, *Applied Physics Letters* **93**, 163112 (2008) [55]. Copyright 2008, AIP Publishing LLC.

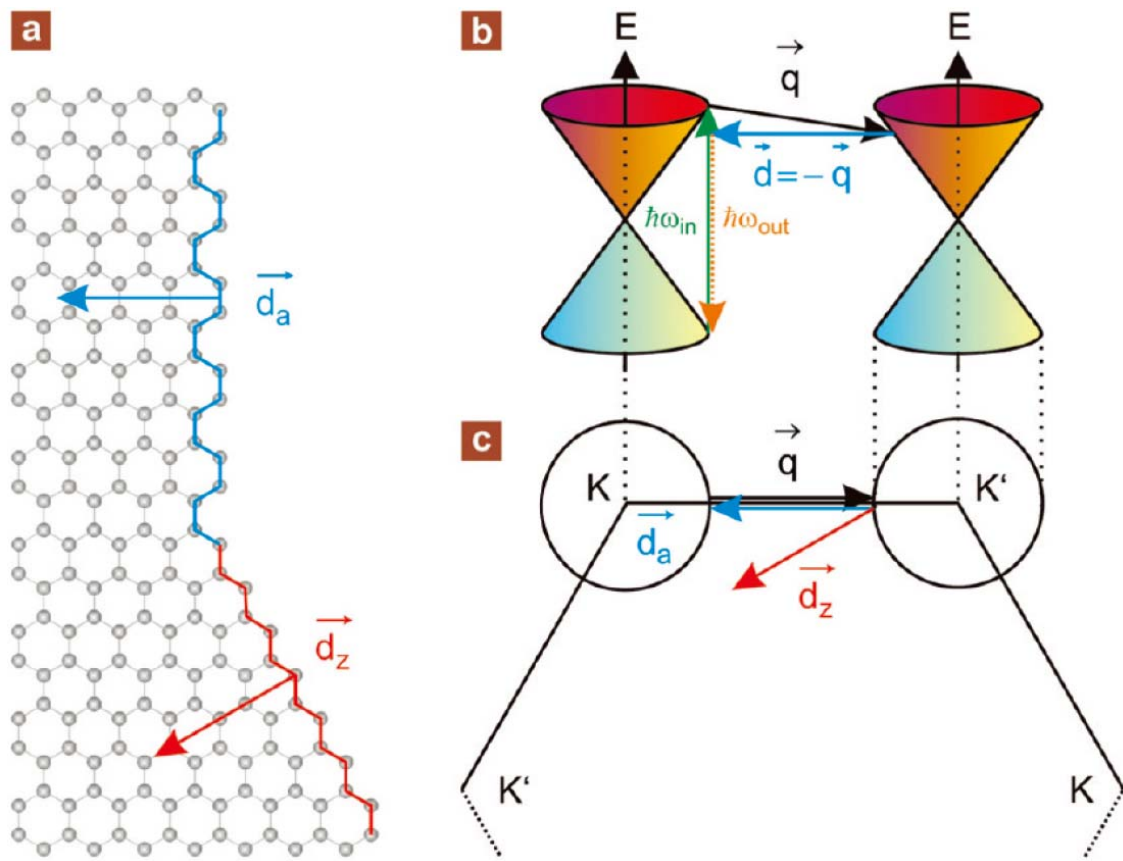


Figure 3.13. (a) Atomic structure of the edge with armchair (blue) and zigzag (red) arrangements. The edge can transfer momentum along the defect wave vectors \vec{d}_a and \vec{d}_z (blue and red arrows, respectively). (b) Schematic illustration of the D-band process. (c) First Brillouin zone of graphene and the D-band process in top view. Reprinted with permission from B. Krauss, P. B. Incze, V. Skakalova, L. P. Biro, K. von Klitzing, and J. H. Smet, Raman scattering at pure graphene zigzag edges, *Nano Letters* **10**, 4544 (2010) [58]. Copyright 2010 American Chemical Society.

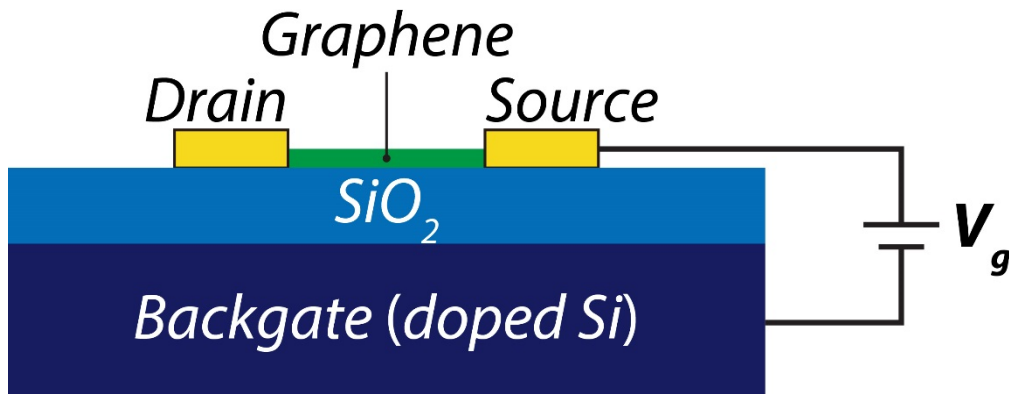


Figure 3.14. Schematic illustration of a typical FET device of a graphene sample. A graphene sample prepared by micromechanical exfoliation is generally deposited on a SiO₂/doped-Si substrate. Metal electrodes can be attached to the graphene via lithography process, which are denoted as Source and Drain here. A typical example of top view of this graphene FET structure is shown in Fig. 3.1b. The heavily doped Si layer is conductive, so that it can be utilized as a backgate electrode. Application of backgate voltage (V_g) enables us to control the Fermi energy of the graphene, as a capacitor.

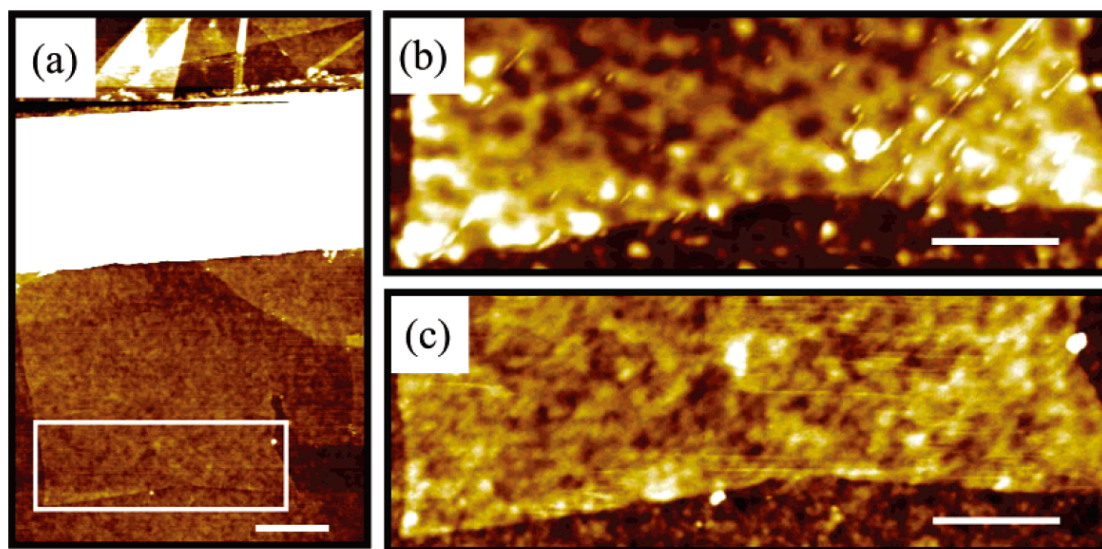


Figure 3.15. (a) AFM topography of graphene deposited on SiO₂. Thin graphite flakes are generated using the mechanical exfoliation technique on thermally grown SiO₂ with the thickness of 300 nm. Single-layer graphene flakes are located using optical and atomic force microscopy. The electron-beam lithography defined electrode, approximately 80 nm in height and 1.5 μ m in width, is the white are nearly horizontal to the image. The white square indicates the region shown in (b) and (c). The scale bar is 500 nm. (b) Graphene sheet prior to hydrogen annealing. The scale bar is 300 nm. (c) Graphene sheet after hydrogen annealing. The standard deviation of the height variation in a square of side 600 nm is approximately 3 Å after the treatment compared to 8 Å before the treatment. The scale bar is 300 nm. Images (a)–(c) were acquired using intermittent-contact mode atomic force microscope in air. Reprinted with permission from M. Ishigami, J. H. Chen, W. G. Cullen, M. S. Fuhrer, and E. D. Williams, Atomic structure of graphene on SiO₂, *Nano Letters* **7**, 1643 (2007) [76]. Copyright 2007 American Chemical Society.

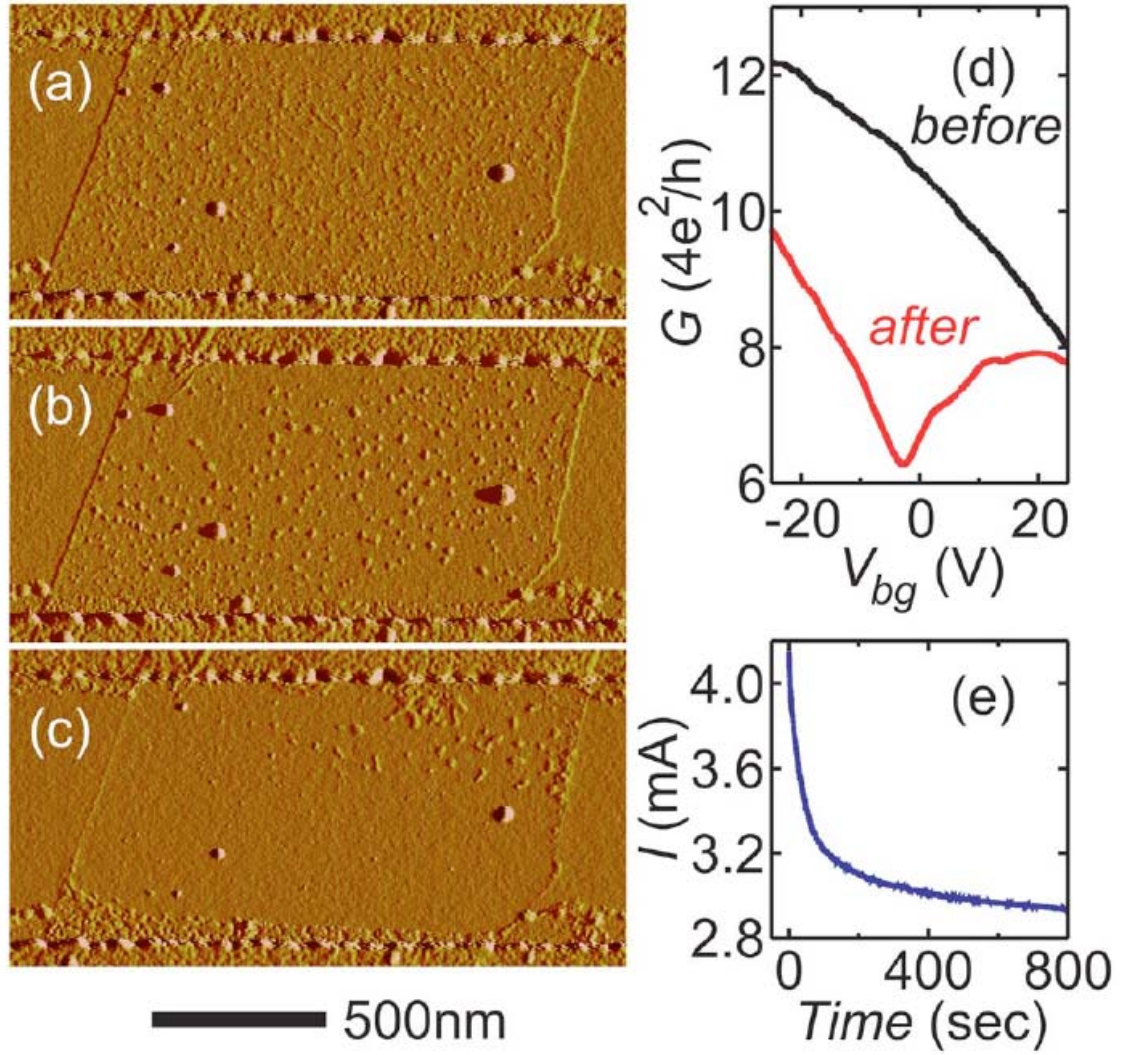


Figure 3.16. (a)–(c) Atomic force microscopy signal amplitude scans captured at various stages of the current-induced cleaning process in air. (d) Two-point conductance G as a function of backgate voltage V_{bg} before and after the application of a large current in helium atmosphere and at $T = 76$ K. (e) Time dependence of current I at fixed bias $V = 5$ V. Reprinted with permission from J. Moser, A. Barreiro, and A. Bachtold, Current-induced cleaning of graphene, *Applied Physics Letters* **91**, 163513 (2007) [77]. Copyright 2007, AIP Publishing LLC.

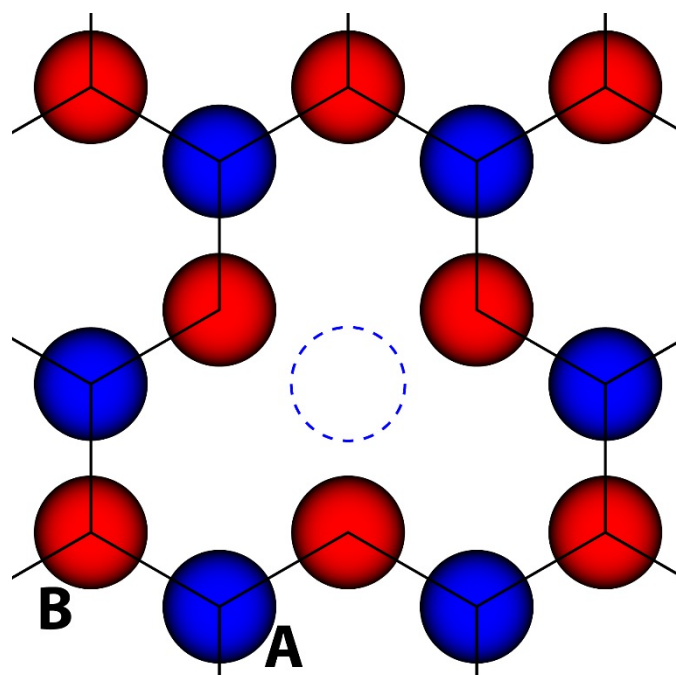


Figure 3.17. A schematic illustration of a single atomic vacancy in graphene. The blue and the red circles denote the sublattices A and B, respectively. The blue dashed circle at the center denotes the vacancy of a carbon atom of the A sublattice.

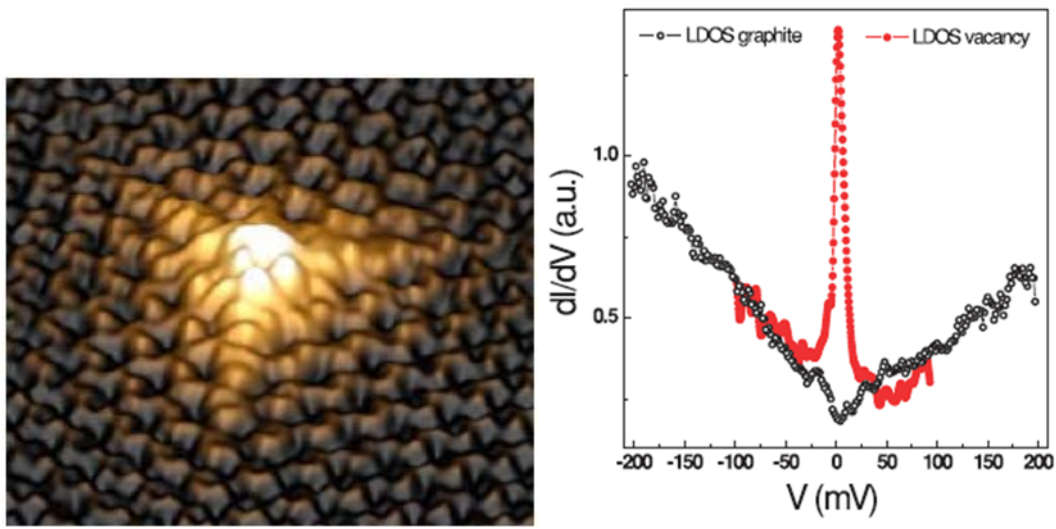


Figure 3.18. (left) An STM image of a single atomic vacancy in the surface of graphite. (right) STS spectra of local density of states (LDOS) measured at the surface of graphite (black) and at a vacancy (red). Reprinted figure with permission from M. M. Ugeda, I. Brihuega, F. Guinea, and J. M. G. Rodríguez, Missing atom as a source of carbon magnetism, *Physical Review Letters* **104**, 096804 (2010) [90]. Copyright (2010) by the American Physical Society.

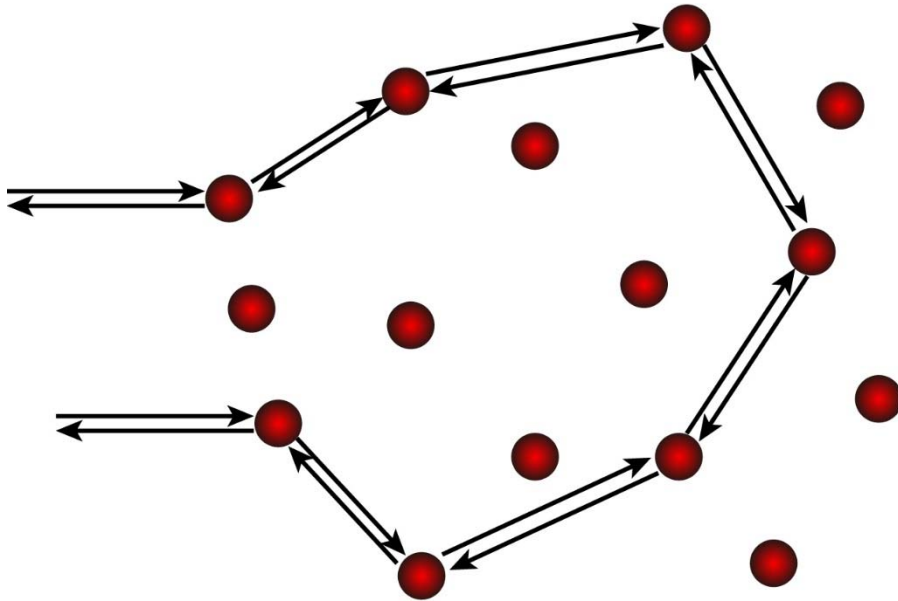


Figure 3.19. A schematic illustration of a possible electron back-scattering path in a conductor having impurities (red circles). Arrows denote the scattering path of an electron with time-reversal symmetry.

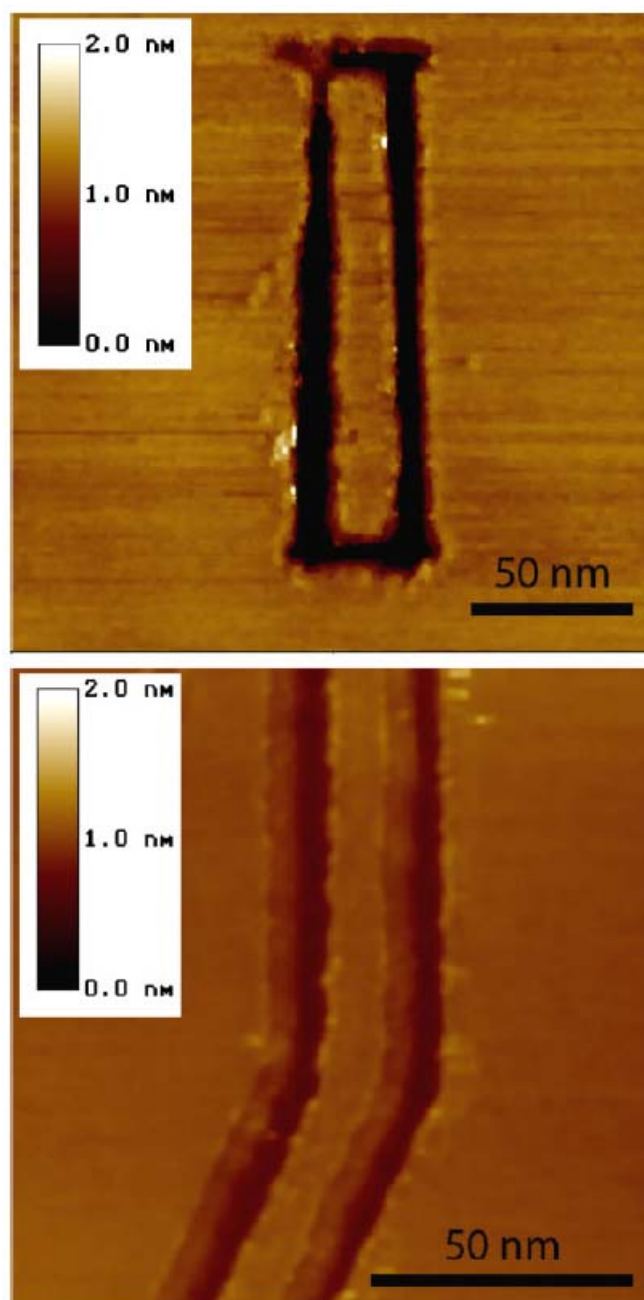


Figure 3.20. Graphene nanoribbons prepared by cutting graphene using STM lithography. Top: A 10-nm-wide straight graphene nanoribbon. Bottom: An 8-nm-wide knee-shaped graphene nanoribbon. Reprinted with permission of John Wiley and Sons from G. Dobrik, L. Tapastó, P. Nemes-Incze, P. Lambin, and L. P. Biró, Crystallographically oriented high resolution lithography of graphene nanoribbons by STM lithography, *Physica Status Solidi (B)* **247**, 896 (2010) [130]. Copyright 2010, John Wiley & Sons, Inc.

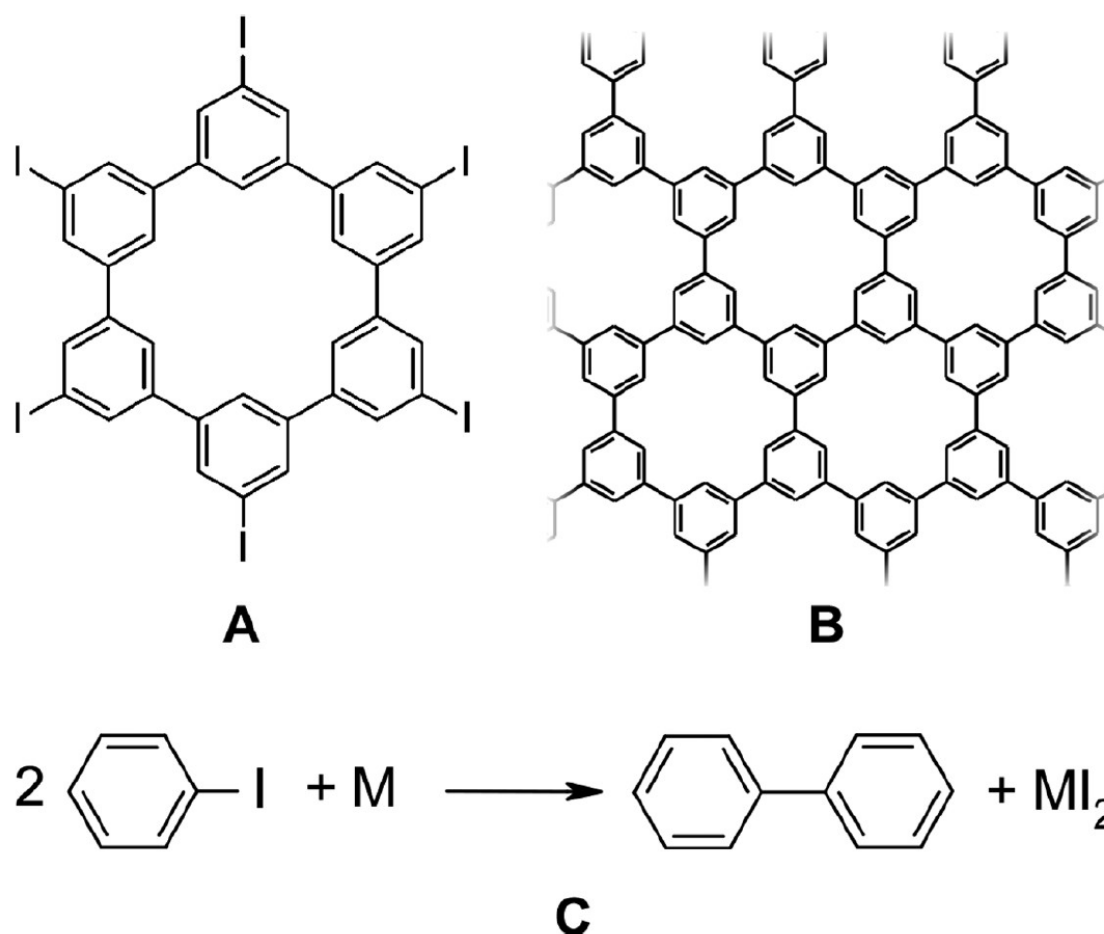


Figure 3.21. (A) Structure of hexaiodo-substituted cyclohexa-*m*-phenylene. (B) Structure of the polyphenylene. (C) Mechanism of the surface-assisted coupling of iodobenzene to biphenyl (M represents Cu, Au, or Ag). Reprinted with permission from M. Bieri, M. T. Nguyen, O. Gröning, J. Cai, M. Treier, K. A. Mansour, P. Ruffieux, C. A. Pignedoli, D. Passerone, M. Kastler, K. Müllen, and R. Fasel, Two-dimensional polymer formation on surfaces: insight into the roles of precursor mobility and reactivity, *Journal of the American Chemical Society* **132**, 16669 (2010) [133]. Copyright 2010 American Chemical Society.

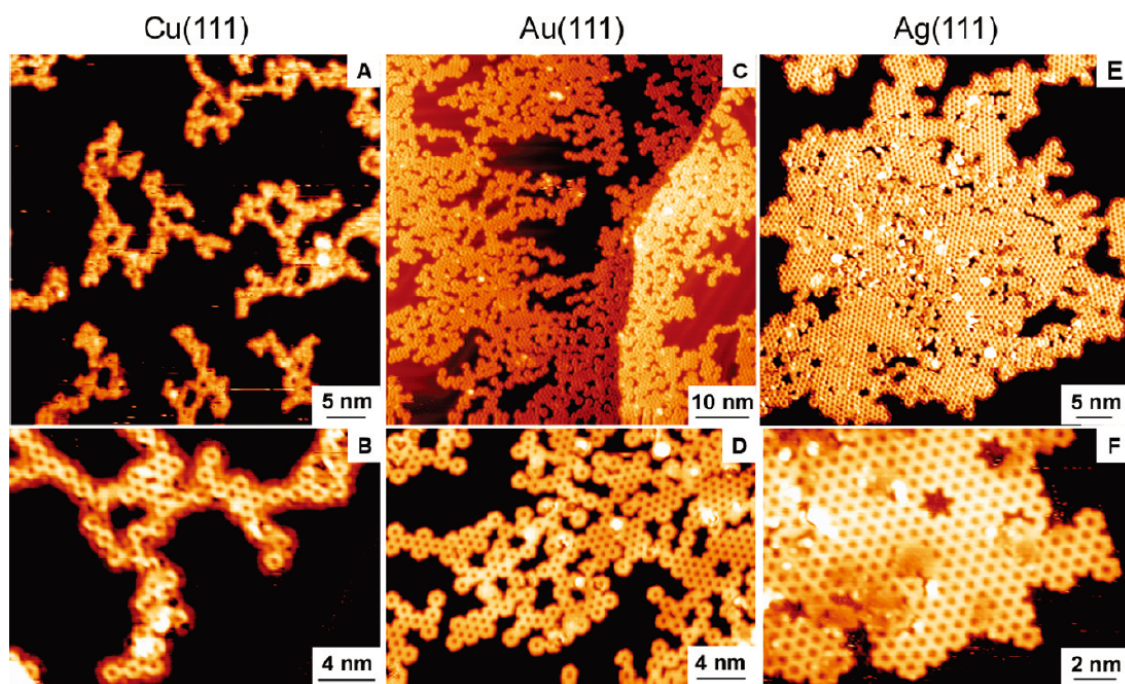


Figure 3.22. (A,C,E) STM images of polyphenylene on Cu(111), Au(111), and Ag(111), respectively. (B,D,F) High-resolution STM images of the polyphenylene shown above. Reprinted with permission from M. Bieri, M. T. Nguyen, O. Gröning, J. Cai, M. Treier, K. A. Mansour, P. Ruffieux, C. A. Pignedoli, D. Passerone, M. Kastler, K. Müllen, and R. Fasel, Two-dimensional polymer formation on surfaces: insight into the roles of precursor mobility and reactivity, *Journal of the American Chemical Society* **132**, 16669 (2010) [133]. Copyright 2010 American Chemical Society.

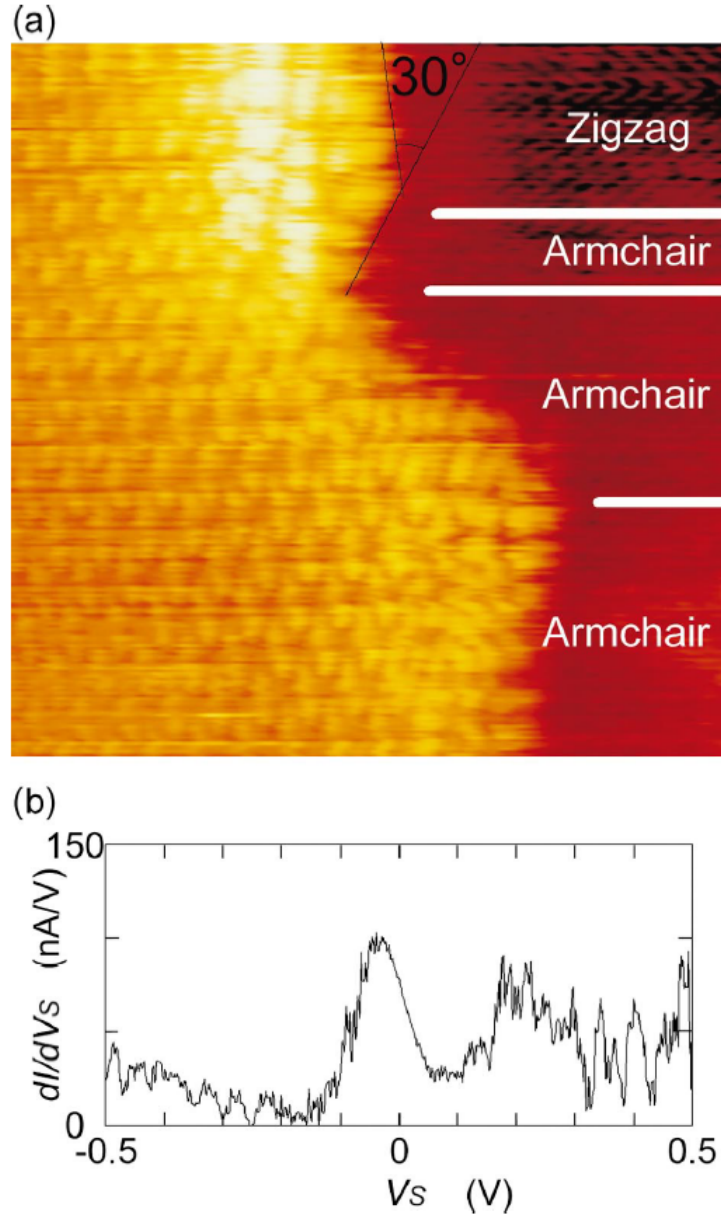


Figure 3.23. (a) An atomically resolved STM image of zigzag and armchair edges (9×9 nm²). (b) Typical dI/dV_s curve from STS data at a zigzag edge (I is the tunneling current, and V_s is the sample bias voltage). $V_s \sim 0$ V corresponds the Dirac point. Reprinted figure with permission from Y. Kobayashi, K. Fukui, T. Enoki, K. Kusakabe, and Y. Kaburagi, Observation of zigzag and armchair edges of graphite using scanning tunneling microscopy and spectroscopy, *Physical Review B* **71**, 193406 (2005) [136]. Copyright (2005) by the American Physical Society.

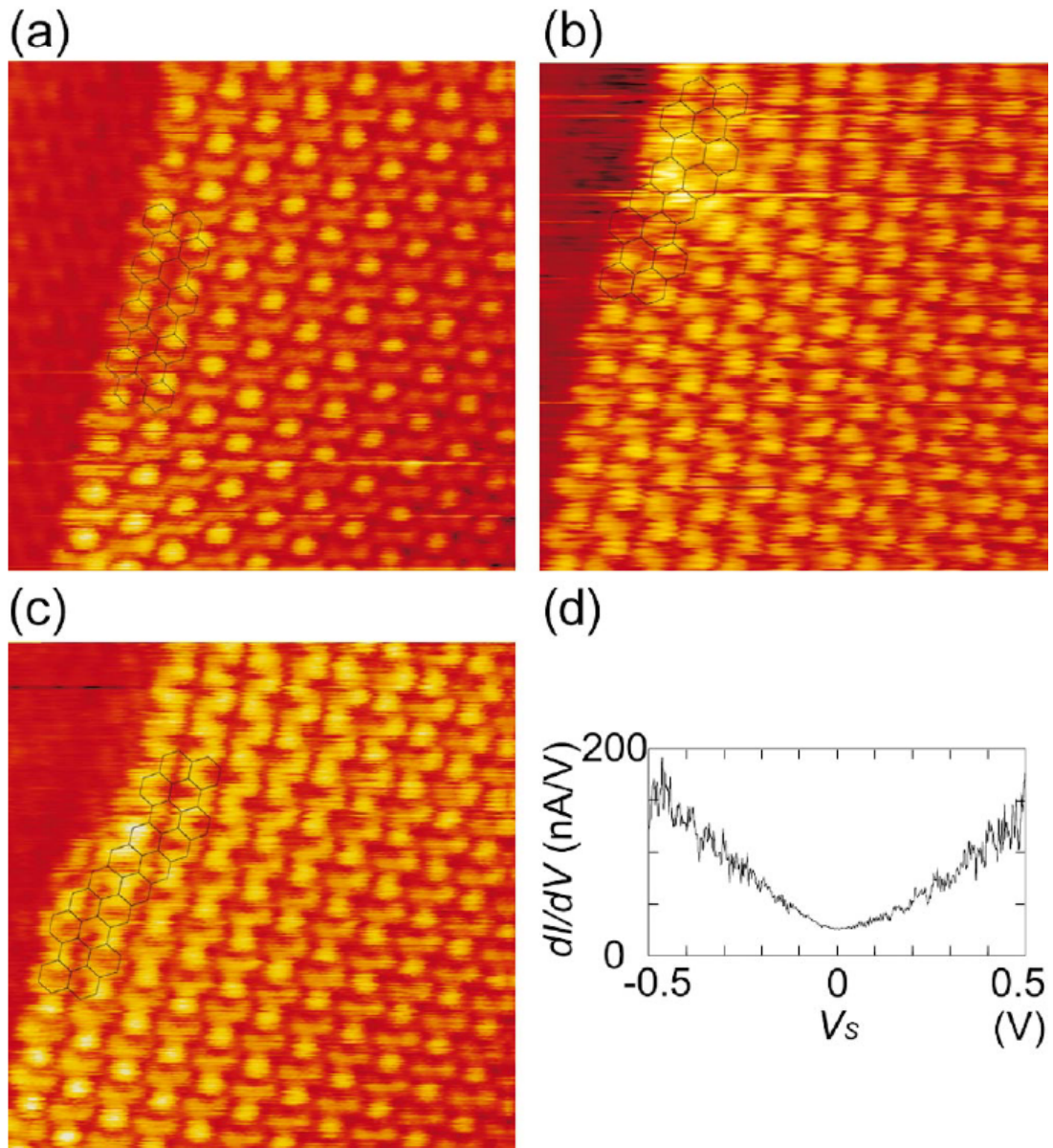


Figure 3.24. Atomically resolved STM images ($5.6 \times 5.6 \text{ nm}^2$) of (a) a homogeneously arranged armchair edge and (b,c) armchair edges with defect points. For clarity of edge structures, models of the honeycomb lattice are drawn on each image. (d) A dI/dV_s curve from STS taken at the armchair edge in (a). Reprinted figure with permission from Y. Kobayashi, K. Fukui, T. Enoki, K. Kusakabe, and Y. Kaburagi, Observation of zigzag and armchair edges of graphite using scanning tunneling microscopy and spectroscopy, *Physical Review B* **71**, 193406 (2005) [136]. Copyright (2005) by the American Physical Society.

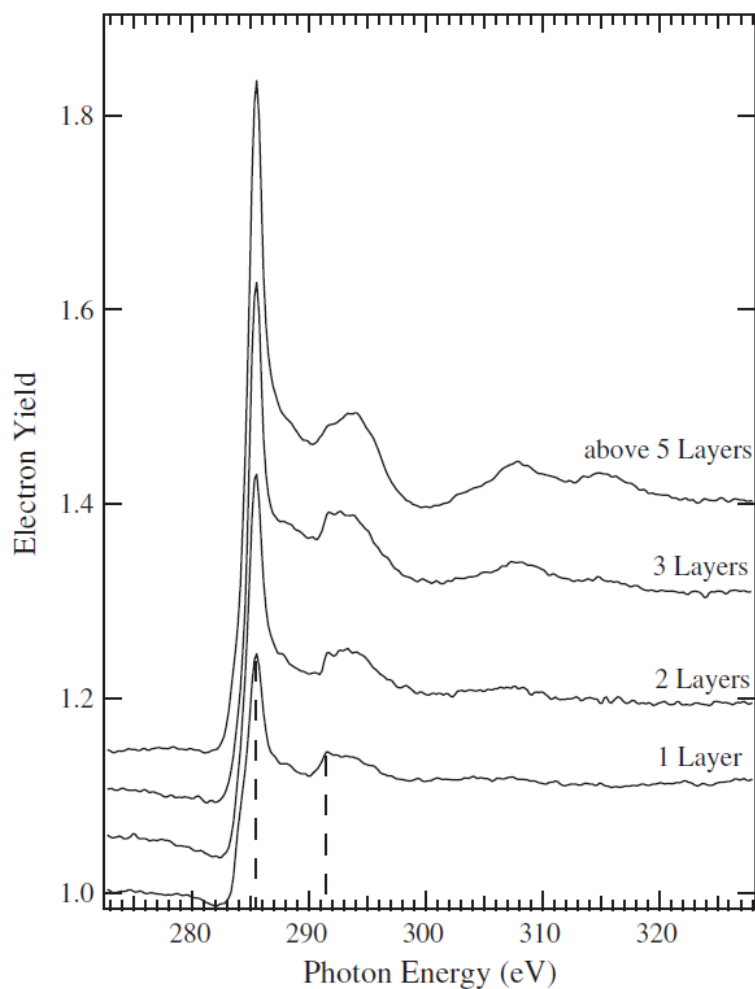


Figure 3.25. The C K-edge NEXAFS spectra of single-layer graphene, bilayer graphene, and few-layer graphenes from the bottom to the top. The dashed lines at ~ 285.5 eV and ~ 292 eV indicate the transitions from C $1s$ to the π^* and the σ^* final states, respectively. Reprinted figure with permission from D. Pacilé, M. Papagno, A. F. Rodríguez, M. Grioni, L. Papagno, Ç. Ö. Girit, J. C. Meyer, G. E. Begtrup, and A. Zettl, Near-edge X-ray absorption fine-structure investigation of graphene, *Physical Review Letters* **101**, 066806 (2008) [148]. Copyright (2008) by the American Physical Society.

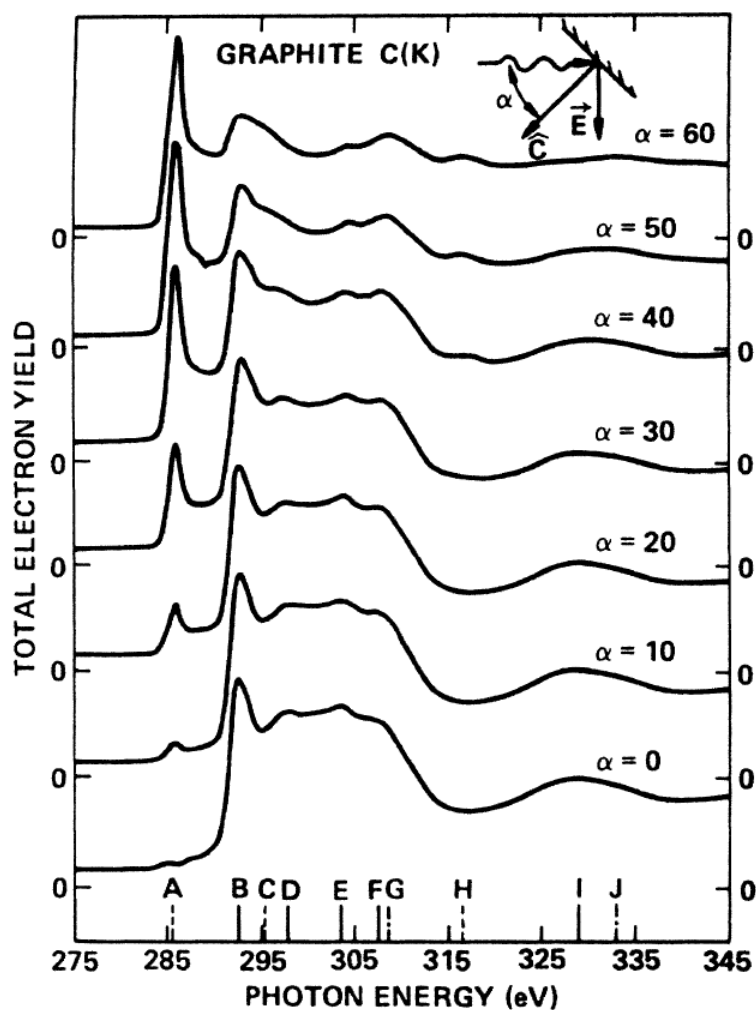


Figure 3.26. The C K-edge NEXAFS spectra of graphite at various angles of incidence α . At the bottom of the figure are lines showing the peak energies: dashed lines represent the transitions to the final states having π symmetry, while solid lines represent the transitions to the final states having σ symmetry. Reprinted figure with permission from R. A. Rosenberg, P. J. Love, and V. Rehn, Polarization-dependent C(K) near-edge x-ray-absorption fine structure of graphite, *Physical Review B* **33**, 4034 (1986) [145]. Copyright (1986) by the American Physical Society.

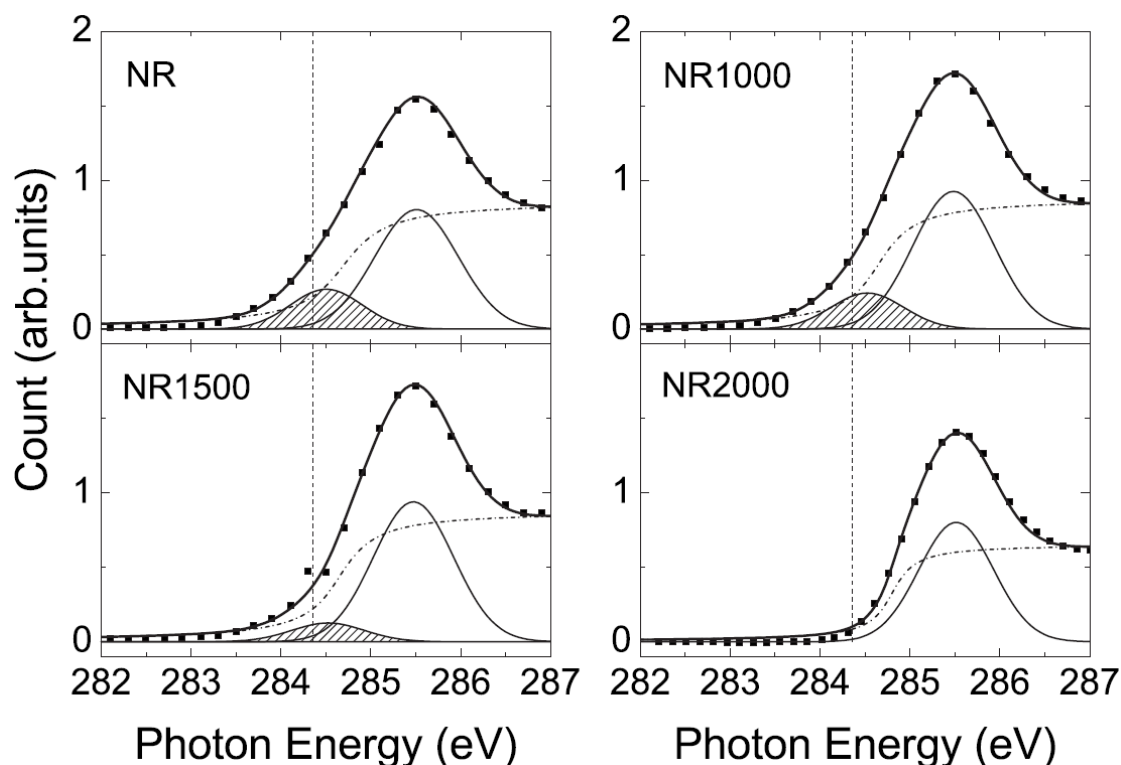


Figure 3.27. The close-up of the C $1s$ to π^* peak in the C K-edge NEXAFS spectra under different annealing conditions of thick graphene nanoribbon (NR) samples. NR1000, NR1500, and NR2000 denote the annealing temperatures at 1000°C, 1500°C, and 2000°C, respectively. The deconvolution comprises two Gaussian peaks corresponding to the edge state (shaded) and the π^* state (unshaded), and a step function (dashed-dotted curve). The vertical dashed lines indicate the Fermi level of HOPG (284.36 eV). Reprinted figure with permission from V. L. J. Joly, M. Kiguchi, S. J. Hao, K. Takai, T. Enoki, R. Sumii, K. Amemiya, H. Muramatsu, T. Hayashi, Y. A. Kim, M. Endo, J. Campos-Delgado, F. López-Urías, A. Botello-Méndez, H. Terrones, M. Terrones, and M. S. Dresselhaus, Observation of magnetic edge state in graphene nanoribbons, *Physical Review B* **81**, 245428 (2010) [142]. Copyright (2010) by the American Physical Society.

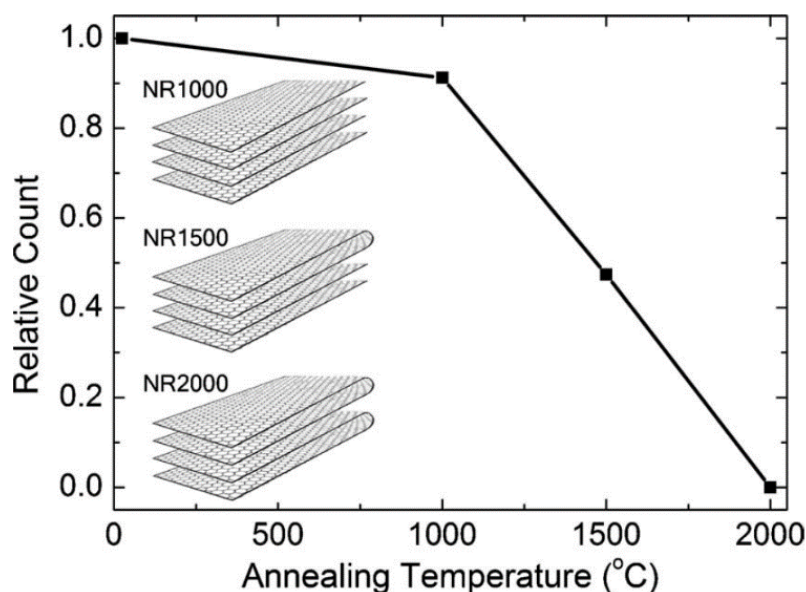


Figure 3.28. The integrated intensity of the edge-state peak normalized to that of the pristine sample. The schematic model of the fusion of edges on annealing is given in the insets. Reprinted figure with permission from V. L. J. Joly, M. Kiguchi, S. J. Hao, K. Takai, T. Enoki, R. Sumii, K. Amemiya, H. Muramatsu, T. Hayashi, Y. A. Kim, M. Endo, J. Campos-Delgado, F. López-Urías, A. Botello-Méndez, H. Terrones, M. Terrones, and M. S. Dresselhaus, Observation of magnetic edge state in graphene nanoribbons, *Physical Review B* **81**, 245428 (2010) [142]. Copyright (2010) by the American Physical Society.

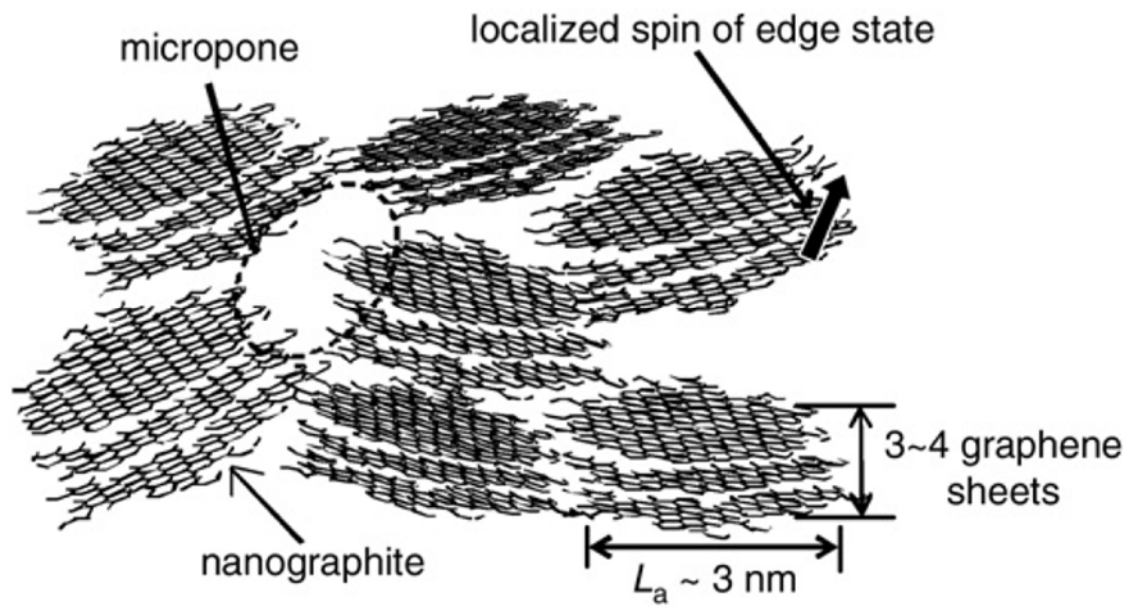


Figure 3.29. Structural model of ACFs. L_a denotes the mean in-plane size of each nanographite domain. Reprinted from *Solid State Communications*, **149**, T. Enoki and K. Takai, The edge state of nanographene and the magnetism of the edge-state spins, 1144, Copyright (2009), with permission from Elsevier [155].

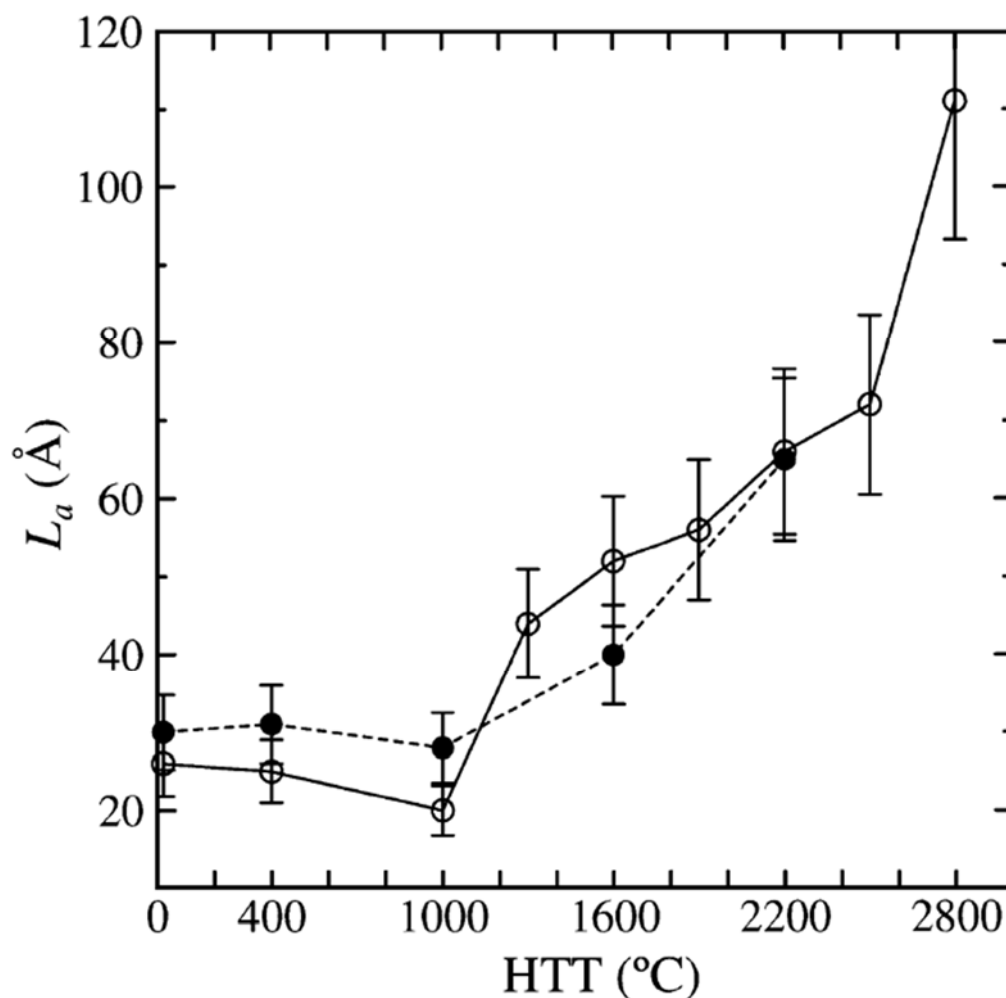


Figure 3.30. The plot of the in-plane crystallite size of nanographite domains in ACFs (L_a) versus the heat-treatment temperature (HTT). Reprinted from *Journal of the Physical Society of Japan*, Vol. 69, No. 3, 2000, pp. 754–767, Y. Shibayama, H. Sato, T. Enoki, X. X. Bi, M. S. Dresselhaus, and M. Endo, Novel electronic properties of a nanographite disordered network and their iodine doping effect [152], with the permission from The Physical Society of Japan. Copyright 2000, The Physical Society of Japan.

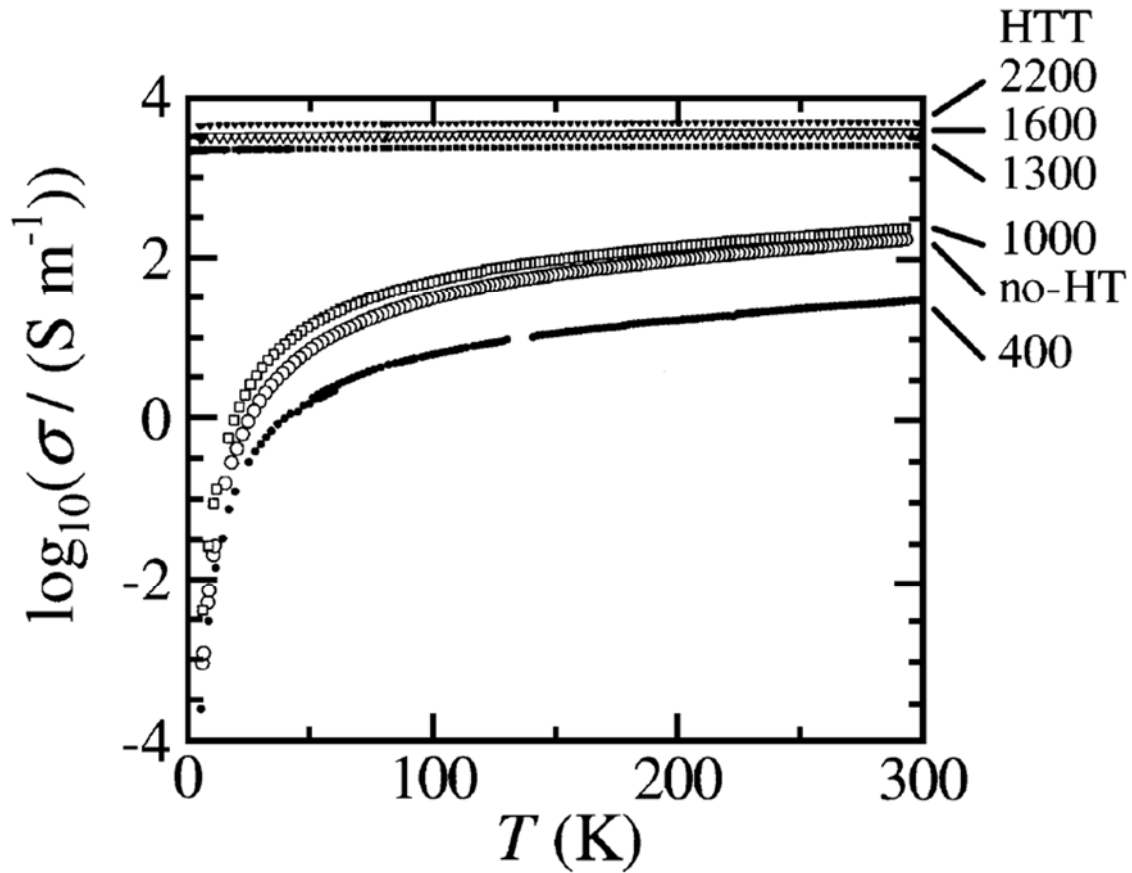


Figure 3.31. The plot of the common-logarithmic conductivity ($\log_{10} \sigma$) versus the temperature for ACFs before (no-HT) and after heat treatments at $\text{HTT} = 400^\circ\text{C}$, 1000°C , 1300°C , 1600°C , and 2200°C . Reprinted from *Journal of the Physical Society of Japan*, Vol. 69, No. 3, 2000, pp. 754–767, Y. Shibayama, H. Sato, T. Enoki, X. X. Bi, M. S. Dresselhaus, and M. Endo, Novel electronic properties of a nano-graphite disordered network and their iodine doping effect [152], with the permission from The Physical Society of Japan. Copyright 2000, The Physical Society of Japan.

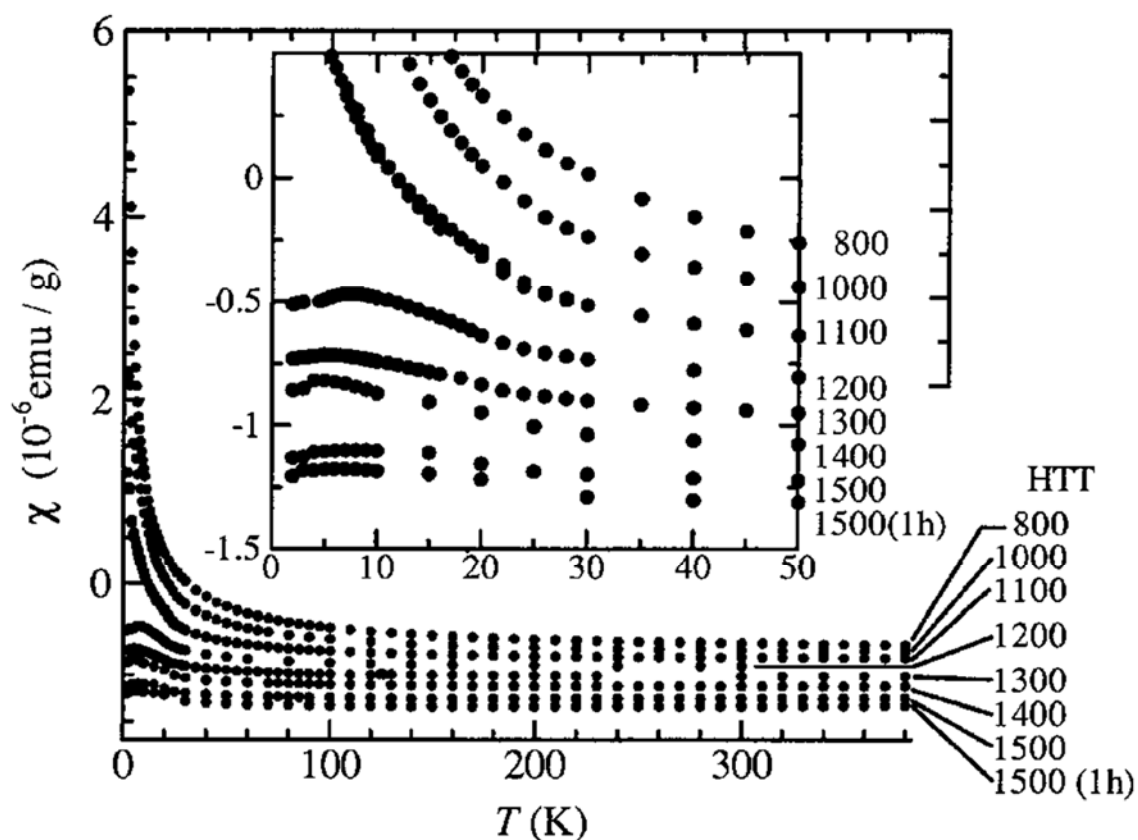


Figure 3.32. Temperature dependence of the magnetic susceptibility (χ) of ACFs heat treated at various HTTs. Detailed behavior at low temperatures is shown in the inset. Reprinted figure with permission from Y. Shibayama, H. Sato, T. Enoki, and M. Endo, Disordered magnetism at the metal-insulator threshold in nano-graphite-based carbon materials, *Physical Review Letters* **84**, 1744 (2000) [153]. Copyright (2000) by the American Physical Society.

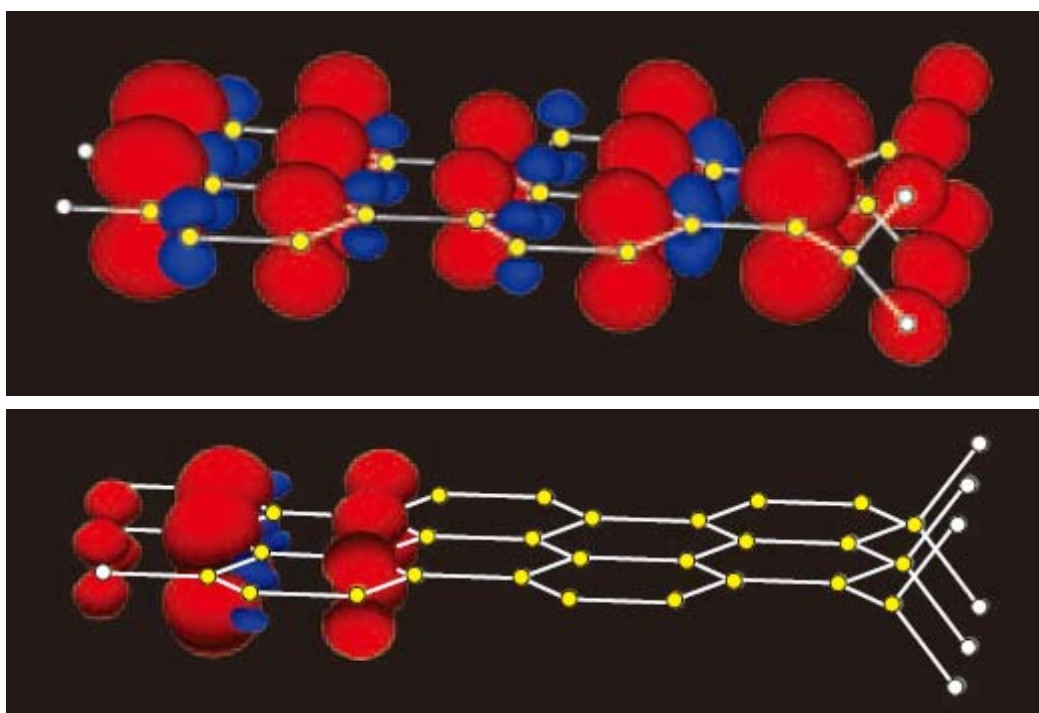


Figure 3.33. Distributions of spin densities in (upper panel) a hydrogenated zigzag nanoribbon and (lower panel) a fluorinated zigzag nanoribbon. Yellow circles denote carbon atoms. White circles in upper and lower panels denote hydrogen atoms and fluorine atoms, respectively. Isosurfaces of spin-up density and spin-down density are colored red and blue, respectively. Ferrimagnetic spin structures are realized. Reprinted from *Journal of the Physical Society of Japan*, Vol. 73, No. 3, 2004, pp. 656–663, M. Maruyama and K. Kusakabe, Theoretical prediction of synthesis methods to create magnetic nanographite [160], with permission from The Physical Society of Japan. Copyright 2004, The Physical Society of Japan.

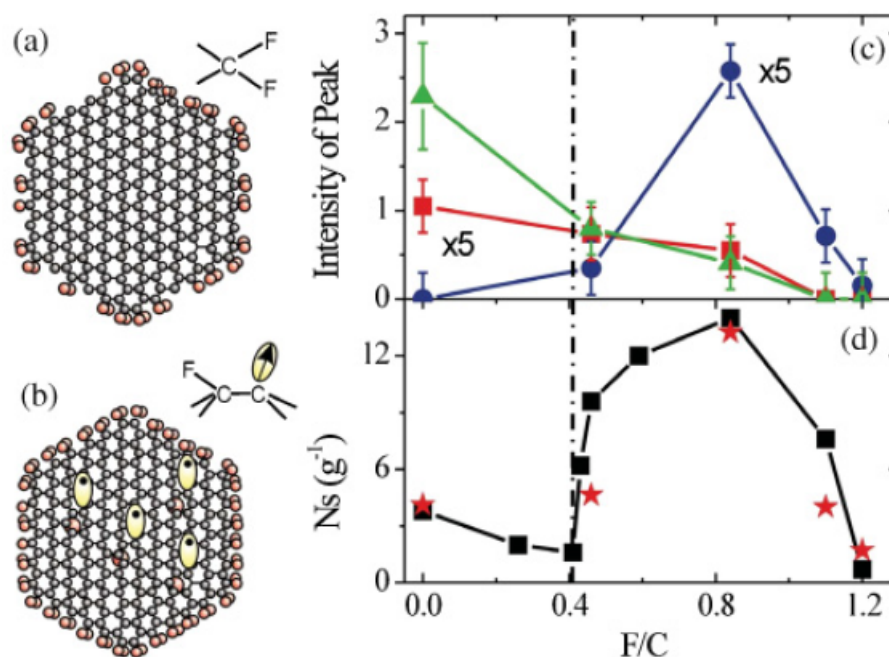


Figure 3.34. Schematic model of the fluorinated ACFs at (a) the ratio of F to C (F/C) < 0.4, and (b) $F/C = 0.4$ –0.8. Carbon and fluorine atoms are denoted as gray and red circles, respectively. σ -dangling bonds are denoted as yellow ellipsoids with a dot inside. (c) The intensities of the edge state (red squares), the σ -dangling bond state (blue circles), and the π^* state (green triangles) peaks as a function of F/C measured by NEXAFS. (d) The total localized spin concentration (black squares) as a function of F/C . The expected total density of magnetic moments in the fluorinated ACFs is denoted as red stars. Reprinted figure with permission from M. Kiguchi, K. Takai, V. L. J. Joly, T. Enoki, R. Sumii, and K. Amemiya, Magnetic edge state and dangling bond state of nanographene in activated carbon fibers, *Physical Review B* **84**, 045421 (2011) [143]. Copyright (2011) by the American Physical Society. The data in the panel (d) are reprinted from *Journal of the Physical Society of Japan*, Vol. 70, No. 1, 2001, pp. 175–185, K. Takai, H. Sato, T. Enoki, N. Yoshida, F. Okino, H. Touhara, and M. Endo, Effect of fluorination on nano-sized π -electron systems [93], with the permission from The Physical Society of Japan. Copyright 2001, The Physical Society of Japan.

References in Chapter 3

- [1] K. S. Novoselov, A. K. Geim, S. V. Morozov, D. Jiang, Y. Zhang, S. V. Dubonos, I. V. Grigorieva, and A. A. Firsov, Electric field effect in atomically thin carbon films, *Science* **306**, 666 (2004).
- [2] K. S. Novoselov, D. Jiang, F. Schedin, T. J. Booth, V. V. Khotkevich, S. V. Morozov, and A. K. Geim, Two-dimensional atomic crystals, *Proc. Nat. Acad. Sci.* **102**, 10451 (2005).
- [3] N. D. Mermin, Crystalline order in two dimensions, *Phys. Rev.* **176**, 250 (1968).
- [4] R. Mas-Ballesté, C. Gómez-Navarro, J. Gómez-Herrero, and F. Zamora, 2D materials: to graphene and beyond, *Nanoscale* **3**, 20 (2011).
- [5] M. Osada and T. Sasaki, Two-dimensional dielectric nanosheets: novel nanoelectronics from nanocrystal building blocks, *Adv. Mater.* **24**, 210 (2012).
- [6] Q. H. Wang, K. Kalantar-Zadeh, A. Kis, J. N. Coleman, and M. S. Strano, Electronics and optoelectronics of tow-dimensional transition metal dichalcogenides, *Nat. Nanotechnol.* **7**, 699 (2012).
- [7] M. Xu, T. Liang, M. Shi, and H. Chen, Graphene-like two-dimensional materials, *Chem. Rev.* **113**, 3766 (2013).
- [8] S. Mizushima, Y. Fujibayashi, and K. Shiiki, Electric resistivity and Hall coefficient of very thin graphite crystals, *J. Phys. Soc. Jpn.* **30**, 299 (1971).
- [9] B. C. Banerjee, T. J. Hirt, and P. L. Walker Jr., Pyrolytic carbon formation from carbon suboxide, *Nature* **192**, 450 (1961).
- [10] A. E. Karu and M. Beer, Pyrolytic formation of highly crystalline graphite films, *J. Appl. Phys.* **37**, 2179 (1966).
- [11] S. D. Robertson, Graphite formation from low temperature pyrolysis of methane over some transition metal surfaces, *Nature* **221**, 1044 (1969).
- [12] S. Hagstrom, H. B. Lyon, and G. A. Somorjai, Surface structures on the clean platinum (100) surface, *Phys. Rev. Lett.* **15**, 491 (1965).
- [13] A. E. Morgan, and G. A. Somorjai, Low energy electron diffraction studies of gas adsorption on the platinum (100) single crystal surface, *Surf. Sci.* **12**, 405 (1968).
- [14] J. C. Hamilton and J. M. Blakely, Carbon segregation to single crystal surfaces of Pt, Pd and Co, *Surf. Sci.* **91**, 199 (1980).
- [15] M. Eizenberg and J. M. Blakely, Carbon monolayer phase condensation on Ni(111),

- Surf. Sci.* **82**, 228 (1979).
- [16] A. N. Obraztsov, E. A. Obraztsova, A. V. Tyurnina, and A. A. Zolotukhin, Chemical vapor deposition of thin graphite films of nanometer thickness, *Carbon* **45**, 2017 (2007).
- [17] H. Ueta, M. Saida, C. Nakai, Y. Yamada, M. Sasaki, and S. Yamamoto, Highly oriented monolayer graphite formation on Pt(111) by a supersonic methane beam, *Surf. Sci.* **560**, 183 (2004).
- [18] D. E. Starr, E. M. Pazhetnov, A. I. Stadnichenko, A. I. Boronin, and S. K. Shaikhutdinov, Carbon films grown on Pt(111) as supports for model cold catalysts, *Surf. Sci.* **600**, 2688 (2006).
- [19] S. Y. Kwon, C. V. Ciobanu, V. Petrova, V. B. Shenoy, J. Bareño, V. Gambin, I. Petrov, and S. Kodambaka, Growth of semiconducting graphene on Palladium, *Nano Lett.* **9**, 3985 (2009).
- [20] X. An, F. Liu, Y. J. Jung, and S. Kar, Large-area synthesis of graphene on Palladium and their Raman spectroscopy, *J. Phys. Chem. C* **116**, 16412 (2012).
- [21] A. Reina, X. Jia, J. Ho, D. Nezich, H. Son, V. Bulovic, M. S. Dresselhaus, and J. Kong, Large area, few-layer graphene films on arbitrary substrates by chemical vapor deposition, *Nano Lett.* **9**, 30 (2009).
- [22] Q. Yu, J. Lian, S. Siriponglert, H. Li, Y. P. Chen, and S. S. Pei, Graphene segregated on Ni surfaces and transferred to insulators, *Appl. Phys. Lett.* **93**, 113103 (2008).
- [23] K. S. Kim, Y. Zhao, H. Jang, S. Y. Lee, J. M. Kim, K. S. Kim, J. H. Ahn, P. Kim, J. Y. Choi, and B. H. Hong, Large-scale pattern growth of graphene films for stretchable transparent electrodes, *Nature* **457**, 706 (2009).
- [24] X. Li, W. Cai, J. An, S. Kim, J. Nah, D. Yang, R. Piner, A. Velamakanni, I. Jung, E. Tutuc, S. K. Banerjee, L. Colombo, and R. S. Ruoff, Large-area synthesis of high-quality and uniform graphene films on copper foils, *Science* **324**, 1312 (2009).
- [25] S. Bae, H. Kim, Y. Lee, X. Xu, J. S. Park, Y. Zheng, J. Balakrishnan, T. Lei, H. R. Kim, Y. I. Song, Y. J. Kim, K. S. Kim, B. Özyilmaz, J. H. Ahn, B. H. Hong, and S. Iijima, Roll-to-roll production of 30-inch graphene films for transparent electrodes, *Nat. Nanotechnol.* **5**, 574 (2010).
- [26] M. P. Levendorf, C. S. Ruiz-Vargas, S. Garg, and J. Park, Transfer-free batch fabrication of single layer graphene transistors, *Nano Lett.* **9**, 4479 (2009).

-
- [27] A. Ismach, C. Druzgalski, S. Penwell, A. Schwartzberg, M. Zheng, A. Javey, J. Bokor, and Y. Zhang, Direct chemical vapor deposition of graphene on dielectric surfaces, *Nano Lett.* **10**, 1542 (2010).
- [28] Y. Lee, S. Bae, H. Jang, S. Jang, S. E. Zhu, S. H. Sim, Y. I. Song, B. H. Hong, and J. H. Ahn, Wafer-scale synthesis and transfer of graphene films, *Nano Lett.* **10**, 490 (2010).
- [29] A. Srivastava, C. Galande, L. Ci, L. Song, C. Rai, D. Jariwala, K. F. Kelly, and P. M. Ajayan, Novel liquid precursor-based facile synthesis of large-area continuous, single, and few-layer graphene films, *Chem. Mater.* **22**, 3457 (2010).
- [30] Y. H. Lee and J. H. Lee, Scalable growth of free-standing graphene wafers with copper (Cu) catalyst on SiO₂/Si substrate: thermal conductivity of the wafers, *Appl. Phys. Lett.* **96**, 083101 (2010).
- [31] H. Cao, Q. Yu, L. A. Jauregui, J. Tian, W. Wu, Z. Liu, R. Jalilian, D. K. Benjamin, Z. Jiang, J. Bao, S. S. Pei, and Y. P. Chen, Electronic transport in chemical vapor deposited graphene synthesized on Cu: quantum hall effect and weak localization, *Appl. Phys. Lett.* **96**, 122106 (2010).
- [32] V. P. Verma, S. Das, I. Lahiri, and W. Choi, Large-area graphene on polymer film for flexible and transparent anode in field emission device, *Appl. Phys. Lett.* **96**, 203108 (2010).
- [33] A. J. V. Bommel, J. E. Crombeen, and A. V. Tooren, LEED and Auger electron observations of the SiC(0001) surface, *Surf. Sci.* **48**, 463 (1975).
- [34] W. A. de Heer, C. Berger, X. Wu, P. N. First, E. H. Conrad, X. Li, T. Li, M. Sprinkle, J. Hass, M. L. Sadowski, M. Potemski, and G. Martinez, Epitaxial graphene, *Solid State Commun.* **143**, 92 (2007).
- [35] T. Ohta, F. E. Gabaly, A. Bostwick, J. L. McChesney, K. V. Emtsev, A. K. Schmid, T. Seyller, K. Horn, and E. Rotenberg, Morphology of graphene thin film growth on SiC(0001), *New J. Phys.* **10**, 023034 (2008).
- [36] K. V. Emtsev, A. Bostwick, K. Horn, J. Jobst, G. L. Kellogg, L. Ley, J. L. McChesney, T. Ohta, S. A. Reshanov, J. Röhl, E. Rotenberg, A. K. Schmid, D. Waldmann, H. B. Weber, and T. Seyller, Towards wafer-size graphene layers by atmospheric pressure graphitization of silicon carbide, *Nat. Mater.* **8**, 203 (2009).
- [37] S. Irle, Z. Wang, G. Zheng, K. Morokuma, and M. Kusunoki, Theory and

- experiment agree: single-walled carbon nanotube caps grow catalyst-free with chirality preference on a SiC surface, *J. Chem. Phys.* **125**, 044702 (2006).
- [38] X. Wu, Y. Hu, M. Ruan, N. K. Madiomanana, J. Hankinson, M. Sprinkle, C. Berger, and W. A. de Heer, Half integer quantum Hall effect in high mobility single layer epitaxial graphene, *Appl. Phys. Lett.* **95**, 223108 (2009).
- [39] Y. M. Lin, C. Dimitrakopoulos, K. A. Jenkins, D. B. Farmer, H. Y. Chiu, A. Grill, and P. Avouris, 100-GHz transistors from wafer-scale epitaxial graphene, *Science* **327**, 662 (2010).
- [40] P. Blake, E. W. Hill, A. H. Castro Neto, K. S. Novoselov, D. Jiang, R. Yang, T. J. Booth, and A. K. Geim, Making graphene visible, *Appl. Phys. Lett.* **91**, 063124 (2007).
- [41] Z. H. Ni, H. M. Wang, J. Kasim, H. M. Fan, T. Yu, Y. H. Wu, Y. P. Feng, and Z. X. Shen, Graphene thickness determination using reflection and contrast spectroscopy, *Nano Lett.* **7**, 2758 (2007).
- [42] I. Jung, M. Pelton, R. Piner, D. A. Dikin, S. Stankovich, S. Watcharotone, M. Hausner, and R. S. Ruoff, Simple approach for high-contrast optical imaging and characterization of graphene-based sheets, *Nano Lett.* **7**, 3569 (2007).
- [43] L. M. Malard, M. A. Pimenta, G. Dresselhaus, and M. S. Dresselhaus, Raman spectroscopy in graphene, *Phys. Rep.* **473**, 51 (2009).
- [44] M. A. Pimenta, G. Dresselhaus, M. S. Dresselhaus, L. G. Cançado, A. Jorio, and R. Saito, Studying disorder in graphite-based systems by Raman spectroscopy, *Phys. Chem. Chem. Phys.* **9**, 1276 (2007).
- [45] A. C. Ferrari and D. M. Basko, Raman spectroscopy as a versatile tool for studying the properties of graphene, *Nat. Nanotechnol.* **8**, 235 (2013).
- [46] M. Lazzeri, C. Attaccalite, L. Wirtz, and F. Mauri, Impact of the electron-electron correlation on phonon dispersion: failure of LDA and GGA DFT functionals in graphene and graphite, *Phys. Rev. B* **78**, 081406 (2008).
- [47] F. Tuinstra and J. L. Koenig, Raman spectrum of graphite, *J. Chem. Phys.* **53**, 1126 (1970).
- [48] T. P. Mernagh, R. P. Cooney, and R. A. Johnson, Raman spectra of graphon carbon black, *Carbon* **22**, 39 (1984).
- [49] D. S. Knight and W. B. White, Characterization of diamond films by Raman

- spectroscopy, *J. Mater. Res.* **4**, 385 (1989).
- [50] L. G. Cançado, K. Takai, T. Enoki, M. Endo, Y. A. Kim, H. Mizusaki, A. Jorio, L. N. Coelho, R. M. Paniago, and M. A. Pimenta, General equation for the determination of the crystallite size L_a of nanographite by Raman spectroscopy, *Appl. Phys. Lett.* **88**, 163106 (2006).
- [51] J. H. Chen, W. G. Cullen, C. Jang, M. S. Fuhrer, and E. D. Williams, Defect scattering in graphene, *Phys. Rev. Lett.* **102**, 236805 (2009).
- [52] T. Terasawa and K. Saiki, Growth of graphene on Cu by plasma enhanced chemical vapor deposition, *Carbon* **50**, 869 (2012).
- [53] X. C. Yang, H. M. Wang, T. R. Wu, F. Q. Huang, J. Chen, X. X. Kang, Z. Jin, X. M. Xie, and M. H. Jiang, Magnetotransport of polycrystalline graphene: Shubnikov-de Haas oscillation and weak localization study, *Appl. Phys. Lett.* **102**, 233503 (2013).
- [54] L. G. Cançado, M. A. Pimenta, B. R. A. Neves, M. S. S. Dantas, and A. Jorio, Influence of the atomic structure on the Raman spectra of graphite edges, *Phys. Rev. Lett.* **93**, 247401 (2004).
- [55] Y. M. You, Z. H. Ni, T. Yu, and Z. X. Shen, Edge chirality determination of graphene by Raman spectroscopy, *Appl. Phys. Lett.* **93**, 163112 (2008).
- [56] A. K. Gupta, T. J. Russin, H. R. Gutiérrez, and P. C. Eklund, Probing graphene edges via Raman scattering, *ACS Nano* **3**, 45 (2009).
- [57] C. Casiraghi, A. Hartschuh, H. Qian, S. Piscanec, C. Georgi, A. Fasoli, K. S. Novoselov, D. M. Basko, and A. C. Ferrari, Raman spectroscopy of graphene edges, *Nano Lett.* **9**, 1433 (2009).
- [58] B. Krauss, P. N. Incze, V. Skakalova, L. P. Biro, K. von Klitzing, and J. H. Smet, Raman scattering at pure graphene zigzag edges, *Nano Lett.* **10**, 4544 (2010).
- [59] J. Xia, F. Chen, J. Li, and N. Tao, Measurement of the quantum capacitance of graphene, *Nat. Nanotechnol.* **4**, 505 (2009).
- [60] S. Dröschner, P. Roulleau, F. Molitor, P. Studerus, C. Stampfer, K. Ensslin, and T. Ihn, Quantum capacitance and density of states of graphene, *Appl. Phys. Lett.* **96**, 152104 (2010).
- [61] H. Xu, Z. Zhang, and L. M. Peng, Measurements and microscopic model of quantum capacitance in graphene, *Appl. Phys. Lett.* **98**, 133122 (2011).
- [62] K. S. Novoselov, A. K. Geim, S. V. Morozov, D. Jiang, M. I. Katsnelson, I. V.

- Grigorieva, S. V. Dubonos, and A. A. Firsov, Two-dimensional gas of massless Dirac fermions in graphene, *Nature* **438**, 197 (2005).
- [63] Y. Zhang, Y. W. Tan, H. L. Stormer, and P. Kim, Experimental observation of the quantum Hall effect and Berry's phase in graphene, *Nature* **438**, 201 (2005).
- [64] K. S. Novoselov, E. McCann, S. V. Morozov, V. I. Fal'ko, M. I. Katsnelson, U. Zeitler, D. Jiang, F. Schedin, and A. K. Geim, Unconventional quantum Hall effect and Berry's phase of 2π in bilayer graphene, *Nat. Phys.* **2**, 177 (2006).
- [65] T. Ando, Screening effect and impurity scattering in monolayer graphene, *J. Phys. Soc. Jpn.* **75**, 074716 (2006).
- [66] T. Stauber, N. M. R. Peres, and F. Guinea, Electronic transport in graphene: a semiclassical approach including midgap states, *Phys. Rev. B* **76**, 205423 (2007).
- [67] E. H. Hwang, S. Adam, and S. Das Sarma, Carrier transport in two-dimensional graphene layers, *Phys. Rev. Lett.* **98**, 186806 (2007).
- [68] J. H. Chen, C. Jang, S. Adam, M. S. Fuhrer, E. D. Williams, and M. Ishigami, Charged-impurity scattering in graphene, *Nat. Phys.* **4**, 377 (2008).
- [69] S. Xiao, J. H. Chen, S. Adam, E. D. Williams, and M. S. Fuhrer, Charged impurity scattering in bilayer graphene, *Phys. Rev. B* **82**, 041406 (2010).
- [70] S. V. Morozov, K. S. Novoselov, M. I. Katsnelson, F. Schedin, D. C. Elias, J. A. Jaszczak, and A. K. Geim, Giant intrinsic carrier mobilities in graphene and its bilayer, *Phys. Rev. Lett.* **100**, 016602 (2008).
- [71] J. Yan and M. S. Fuhrer, Correlated charged impurity scattering in graphene, *Phys. Rev. Lett.* **107**, 206601 (2011).
- [72] J. Katoch, J. H. Chen, R. Tsuchikawa, C. W. Smith, E. R. Mucciolo, and M. Ishigami, Uncovering the dominant scatterer in graphene sheets on SiO₂, *Phys. Rev. B* **82**, 081417 (2010).
- [73] Z. H. Ni, L. A. Ponomarenko, R. R. Nair, R. Yang, S. Anissimova, I. V. Grigorieva, F. Schedin, P. Blake, Z. X. Shen, E. H. Hill, K. S. Novoselov, and A. K. Geim, On resonant scatterers as a factor limiting carrier mobility in graphene, *Nano Lett.* **10**, 3868 (2010).
- [74] J. H. Chen, C. Jang, S. Xiao, M. Ishigami, and M. S. Fuhrer, Intrinsic and extrinsic performance limits of graphene devices on SiO₂, *Nat. Nanotechnol.* **3**, 206 (2008).
- [75] D. K. Efetov and P. Kim, Controlling electron-phonon interactions in graphene at

- ultrahigh carrier densities, *Phys. Rev. Lett.* **105**, 256805 (2010).
- [76] M. Ishigami, J. H. Chen, W. G. Cullen, M. S. Fuhrer, and E. D. Williams, Atomic structure of graphene on SiO₂, *Nano Lett.* **7**, 1643 (2007).
- [77] J. Moser, A. Barreiro, and A. Bachtold, Current-induced cleaning of graphene, *Appl. Phys. Lett.* **91**, 163513 (2007).
- [78] D. S. Novikov, Numbers of donors and acceptors from transport measurements in graphene, *Appl. Phys. Lett.* **91**, 102102 (2007).
- [79] J. R. Hahn and H. Kang, Vacancy and interstitial defects at graphite surfaces: scanning tunneling microscopic study of the structure, electronic property, and yield for ion-induced defect creation, *Phys. Rev. B* **60**, 6007 (1999).
- [80] D. C. Elias, R. R. Nair, T. M. G. Mohiuddin, S. V. Morozov, P. Blake, M. P. Halsall, A. C. Ferrari, D. W. Boukhvalov, M. I. Katsnelson, A. K. Geim, and K. S. Novoselov, Control of graphene's properties by reversible hydrogenation: evidence for graphane, *Science* **323**, 610 (2009).
- [81] X. Du, I. Skachko, A. Barker, and E. Y. Andrei, Approaching ballistic transport in suspended graphene, *Nat. Nanotechnol.* **3**, 491 (2008).
- [82] K. I. Bolotin, K. J. Sikes, Z. Jiang, M. Klima, G. Fudenberg, J. Hone, P. Kim, and H. L. Stormer, Ultrahigh electron mobility in suspended graphene, *Solid State Commun.* **146**, 351 (2008).
- [83] C. R. Dean, A. F. Young, I. Meric, C. Lee, L. Wang, S. Sorgenfrei, K. Watanabe, T. Taniguchi, P. Kim, K. L. Shepard, and J. Hone, Boron nitride substrates for high-quality graphene electronics, *Nat. Nanotechnol.* **5**, 722 (2010).
- [84] M. Fujita, K. Wakabayashi, K. Nakada, and K. Kusakabe, Peculiar localized state at zigzag graphite edge, *J. Phys. Soc. Jpn.* **65**, 1920 (1996).
- [85] K. Nakada, M. Fujita, G. Dresselhaus, and M. S. Dresselhaus, Edge state in graphene ribbons: nanometer size effect and edge shape dependence, *Phys. Rev. B* **54**, 17954 (1996).
- [86] K. Sengupta and G. Baskaran, Tuning Kondo physics in graphene with gate voltage, *Phys. Rev. B* **77**, 045417 (2008).
- [87] V. M. Pereira, F. Guinea, J. M. B. L. dos Santos, N. M. R. Peres, and A. H. Castro Neto, Disorder induced localized states in graphene, *Phys. Rev. Lett.* **96**, 036801 (2006).

-
- [88] O. V. Yazyev and L. Helm, Defect-induced magnetism in graphene, *Phys. Rev. B* **75**, 125408 (2007).
- [89] M. Hentschel and F. Guinea, Orthogonality catastrophe and Kondo effect in graphene, *Phys. Rev. B* **76**, 115407 (2007).
- [90] M. M. Ugeda, I. Brihuega, F. Guinea, and J. M. G. Rodríguez, Missing atom as a source of carbon magnetism, *Phys. Rev. Lett.* **104**, 096804 (2010).
- [91] J. H. Chen, L. Li, W. G. Cullen, E. D. Williams, and M. S. Fuhrer, Tunable Kondo effect in graphene with defects, *Nat. Phys.* **7**, 535 (2011).
- [92] T. Kanao, H. Matsuura, and M. Ogata, Theory of defect-induced Kondo effect in graphene: numerical renormalization group study, *J. Phys. Soc. Jpn.* **81**, 063709 (2012).
- [93] K. Takai, H. Sato, T. Enoki, N. Yoshida, F. Okino, H. Touhara, and M. Endo, Effect of fluorination on nano-sized π -electron systems, *J. Phys. Soc. Jpn.* **70**, 175 (2001).
- [94] K. Takai, H. Kumagai, H. Sato, and T. Enoki, Bromine-adsorption-induced change in the electronic and magnetic properties of nanographite network systems, *Phys. Rev. B* **73**, 035435 (2006).
- [95] M. Ohtsuka, S. Fujii, M. Kiguchi, and T. Enoki, Electronic state of oxidized nanographene edge with atomically sharp zigzag boundaries, *ACS Nano*, **7**, 6868 (2013).
- [96] M. Ziatdinov, S. Fujii, K. Kusakabe, M. Kiguchi, T. Mori, and T. Enoki, Visualization of electronic states on atomically smooth graphitic edges with different types of hydrogen termination, *Phys. Rev. B* **87**, 115427 (2013).
- [97] Y. Aharonov and D. Bohm, Significance of electromagnetic potentials in the quantum theory, *Phys. Rev.* **115**, 485 (1959).
- [98] R. A. Webb, S. Washburn, C. P. Umbach, and R. B. Laibowitz, Observation of h/e Aharonov–Bohm oscillations in normal-metal rings, *Phys. Rev. Lett.* **54**, 2696 (1985).
- [99] S. Datta, M. R. Melloch, S. Bandyopadhyay, and R. Noren, Novel interference effects between parallel quantum wells, *Phys. Rev. Lett.* **55**, 2344 (1985).
- [100] A. Bachtold, C. Strunk, J. P. Salvetat, J. M. Bonard, L. Forró, T. Nussbaumer, and C. Schönenberger, Aharonov–Bohm oscillations in carbon nanotubes, *Nature* **397**, 673 (1999).

- [101] J. S. Yoo, Y. W. Park, V. Skákalová, and S. Roth, Shubnikov–de Haas and Aharonov Bohm effects in a graphene nanoring structure, *Appl. Phys. Lett.* **96**, 143112 (2010).
- [102] M. Huefner, F. Molitor, A. Jacobsen, A. Pioda, C. Stampfer, K. Ensslin, and T. Ihn, The Aharonov–Bohm effect in a side-gated graphene ring, *New J. Phys.* **12**, 043054 (2010).
- [103] F. de Juan, A. Cortijo, M. A. H. Vozmediano, and A. Cano, Aharonov–Bohm interferences from local deformations in graphene, *Nat. Phys.* **7**, 810 (2011).
- [104] V. H. Nguyen, Y. M. Niquet, and P. Dollfus, Aharonov–Bohm effect and giant magnetoresistance in graphene nanoribbon rings, *Phys. Rev. B* **88**, 035408 (2013).
- [105] E. McCann, K. Kechedzhi, V. I. Fal’ko, H. Suzuura, T. Ando, and B. L. Altshuler, Weak-localization magnetoresistance and valley symmetry in graphene, *Phys. Rev. Lett.* **97**, 146805 (2006).
- [106] S. V. Morozov, K. S. Novoselov, M. I. Katsnelson, F. Schedin, L. A. Ponomarenko, D. Jiang, and A. K. Geim, Strong suppression of weak localization in graphene, *Phys. Rev. Lett.* **97**, 016801 (2006).
- [107] X. Wu, X. Li, Z. Song, C. Berger, and W. A. de Heer, Weak antilocalization in epitaxial graphene: evidence for chiral electrons, *Phys. Rev. Lett.* **98**, 136801 (2007).
- [108] K. Kechedzhi, V. I. Fal’ko, E. McCann, and B. L. Altshuler, Influence of trigonal warping on interference effects in bilayer graphene, *Phys. Rev. Lett.* **98**, 176806 (2007).
- [109] D. W. Horsell, F. V. Tikhonenko, R. V. Gorbachev, and A. K. Savchenko, Weak localization in monolayer and bilayer graphene, *Phil. Trans. R. Soc. A* **366**, 245 (2008).
- [110] F. V. Tikhonenko, D. W. Horsell, R. V. Gorbachev, and A. K. Savchenko, Weak localization in graphene flakes, *Phys. Rev. Lett.* **100**, 056802 (2008).
- [111] R. V. Gorbachev, F. V. Tikhonenko, A. S. Mayorov, D. W. Horsell, and A. K. Savchenko, Weak localization in bilayer graphene, *Phys. Rev. Lett.* **98**, 176805 (2007).
- [112] D.K. Ki, D. Jeong, J. H. Choi, and H. J. Lee, Inelastic scattering in a monolayer graphene sheet: a weak-localization study, *Phys. Rev. B* **78**, 125409 (2008).
- [113] Y. F. Chen, M. H. Bae, C. Chialvo, T. Dirks, A. Bezryadin, and N. Mason, Magnetoresistance in single-layer graphene: weak localization and universal

- conductance fluctuation studies, *J. Phys. Condens. Matter* **22**, 205301 (2010).
- [114] Z. M. Liao, B. H. Han, H. C. Wu, and D. P. Yu, Gate voltage dependence of weak localization in bilayer graphene, *Appl. Phys. Lett.* **97**, 163110 (2010).
- [115] Y. F. Chen, M. H. Bae, C. Chialvo, T. Dirks, A. Bezryadin, N. Mason, Negative and positive magnetoresistance in bilayer graphene: effects of weak localization and charge inhomogeneity, *Physica B* **406**, 785 (2011).
- [116] K. S. Novoselov, V. I. Fal'ko, L. Colombo, P. R. Gellert, M. G. Schwab, and K. Kim, A roadmap for graphene, *Nature* **490**, 192 (2012).
- [117] X. Jia, J. Campos-Delgado, M. Terrones, V. Meunier, and M. S. Dresselhaus, Graphene edges: a review of their fabrication and characterization, *Nanoscale* **3**, 86 (2011).
- [118] X. Li, X. Wang, L. Zhang, S. Lee, and H. Dai, Chemically derived, ultrasmooth graphene nanoribbon semiconductors, *Science* **319**, 1229 (2008).
- [119] M. Terai, N. Hasegawa, M. Okusawa, S. Otani, and C. Oshima, Electronic states of monolayer micrographite on TiC(111)-faceted and TiC(410) surfaces, *Appl. Surf. Sci.* **130–132**, 876 (1998).
- [120] M. H. Rummeli, A. Bachmatiuk, A. Scott, F. Börrnert, J. H. Warner, V. Hoffman, J. H. Lin, G. Cuniberti, and B. Büchner, Direct low-temperature nanographene CVD synthesis over a dielectric insulator, *ACS Nano* **7**, 4206 (2010).
- [121] J. L. Li, K. N. Kudin, M. J. McAllister, R. K. Prud'homme, I. A. Aksay, and R. Car, Oxygen-driven unzipping of graphitic materials, *Phys. Rev. Lett.* **96**, 176101 (2006).
- [122] Z. Li, W. Zhang, Y. Luo, J. Yang, and J. G. Hou, How graphene is cut upon oxidation?, *J. Am. Chem. Soc.* **131**, 6320 (2009).
- [123] S. Fujii and T. Enoki, Cutting of oxidized graphene into nanosized pieces, *J. Am. Chem. Soc.* **132**, 10034 (2010).
- [124] M. Terrones, Nanotubes unzipped, *Nature* **458**, 845 (2009).
- [125] D. V. Kosynkin, A. L. Higginbotham, A. Sinitskii, J. R. Lomeda, A. Dimiev, B. K. Price, and J. M. Tour, Longitudinal unzipping of carbon nanotubes to form graphene nanoribbons, *Nature* **458**, 872 (2009).
- [126] L. Jiao, L. Zhang, X. Wang, G. Diankov, and H. Dai, Narrow graphene nanoribbons from carbon nanotubes, *Nature* **458**, 877 (2009).
- [127] M. Y. Han, B. Özyilmaz, Y. Zhang, and P. Kim, Energy band-gap engineering of

- graphene nanoribbons, *Phys. Rev. Lett.* **98**, 206805 (2007).
- [128] K. Takai, Y. Nishimura, and T. Enoki, Anomalous magnetotransport in nanostructured graphene, *Physica E* **42**, 680 (2010).
- [129] L. P. Biró and P. Lambin, Nanopatterning of graphene with crystallographic orientation control, *Carbon* **48**, 2677 (2010).
- [130] G. Dobrik, L. Tapasztó, P. Nemes-Incze, P. Lambin, and L. P. Biró, Crystallographically oriented high resolution lithography of graphene nanoribbons by STM lithography, *Phys. Status Solidi B* **247**, 896 (2010).
- [131] L. Tapasztó, G. Dobrik, P. Lambin, and L. P. Biró, Tailoring the atomic structure of graphene nanoribbons by scanning tunneling microscope lithography, *Nat. Nanotechnol.* **3**, 397 (2008).
- [132] S. Masubuchi, M. Ono, K. Yoshida, K. Hirakawa, and T. Machida, Fabrication of graphene nanoribbon by local anodic oxidation lithography using atomic force microscope, *Appl. Phys. Lett.* **94**, 082107 (2009).
- [133] M. Bieri, M. T. Nguyen, O. Gröning, J. Cai, M. Treier, K. A. Mansour, P. Ruffieux, C. A. Pignedoli, D. Passerone, M. Kastler, K. Müllen, and R. Fasel, Two-dimensional polymer formation on surfaces: insight into the roles of precursor mobility and reactivity, *J. Am. Chem. Soc.* **132**, 16669 (2010).
- [134] J. Cai, P. Ruffieux, R. Jaafar, M. Bieri, T. Braun, S. Blankenburg, M. Mouth, A. P. Seitsonen, M. Saleh, X. Feng, K. Müllen, and R. Fasel, Atomically precise bottom-up fabrication of graphene nanoribbons, *Nature* **466**, 470 (2010).
- [135] M. S. Fuhrer, Ribbons piece-by-piece, *Nat. Mater.* **9**, 611 (2010).
- [136] Y. Kobayashi, K. Fukui, T. Enoki, K. Kusakabe, and Y. Kaburagi, Observation of zigzag and armchair edges of graphite using scanning tunneling microscopy and spectroscopy, *Phys. Rev. B* **71**, 193406 (2005).
- [137] Y. Niimi, T. Matsui, H. Kambara, K. Tagami, M. Tsukada, and H. Fukuyama, Scanning tunneling microscopy and spectroscopy studies of graphite edges, *Appl. Surf. Sci.* **241**, 43 (2005).
- [138] Y. Kobayashi, K. Fukui, T. Enoki, and K. Kusakabe, Edge state on hydrogen-terminated graphite edges investigated by scanning tunneling microscopy, *Phys. Rev. B* **73**, 125415 (2006).
- [139] Y. Niimi, T. Matsui, H. Kambara, K. Tagami, M. Tsukada, and H. Fukuyama,

- Scanning tunneling microscopy and spectroscopy of the electronic local density of states of graphite surfaces near monoatomic step edges, *Phys. Rev. B* **73**, 085421 (2006).
- [140] A. M. Affoune, B. L. V. Prasad, H. Sato, T. Enoki, Y. Kaburagi, and Y. Hishiyama, Experimental evidence of a single nano-graphene, *Chem. Phys. Lett.* **348**, 17 (2001).
- [141] S. Entani, S. Ikeda, M. Kiguchi, K. Saiki, G. Yoshikawa, I. Nakai, H. Kondoh, and T. Ohta, Growth of nanographite on Pt(111) and its edge state, *Appl. Phys. Lett.* **88**, 153126 (2006).
- [142] V. L. J. Joly, M. Kiguchi, S. J. Hao, K. Takai, T. Enoki, R. Sumii, K. Amemiya, H. Muramatsu, T. Hayashi, Y. A. Kim, M. Endo, J. Campos-Delgado, F. López-Urías, A. Botello-Méndez, H. Terrones, M. Terrones, and M. S. Dresselhaus, Observation of magnetic edge state in graphene nanoribbons, *Phys. Rev. B* **81**, 245428 (2010).
- [143] M. Kiguchi, K. Takai, V. L. J. Joly, T. Enoki, R. Sumii, and K. Amemiya, Magnetic edge state and dangling bond state of nanographene in activated carbon fibers, *Phys. Rev. B* **84**, 045421 (2011).
- [144] G. Hähner, Near edge X-ray absorption fine structure spectroscopy as a tool to probe electronic and structural properties of thin organic films and liquids, *Chem. Soc. Rev.* **35**, 1244 (2006).
- [145] R. A. Rosenberg, P. J. Love, and V. Rehn, Polarization-dependent C(K) near-edge x-ray-absorption fine structure of graphite, *Phys. Rev. B* **33**, 4034 (1986).
- [146] D. A. Fischer, R. M. Wentzcovitch, R. G. Carr, A. Continenza, and A. J. Freeman, Graphitic interlayer states: a carbon K near-edge x-ray-absorption fine-structure study, *Phys. Rev. B* **44**, 1427 (1991).
- [147] S. Banerjee, T. Hemraj-Benny, S. Sambasivan, D. A. Fischer, J. A. Misewich, and S. S. Wong, Near-edge X-ray absorption fine structure investigations of order in carbon nanotube-based systems, *J. Phys. Chem. B* **109**, 8489 (2005).
- [148] D. Pacilé, M. Papagno, A. F. Rodríguez, M. Grioni, L. Papagno, Ç. Ö. Girit, J. C. Meyer, G. E. Begtrup, and A. Zettl, Near-edge X-ray absorption fine-structure investigation of graphene, *Phys. Rev. Lett.* **101**, 066806 (2008).
- [149] M. Papagno, A. F. Rodríguez, Ç. Ö. Girit, J. C. Meyer, A. Zettl, and D. Pacilé, Polarization-dependent C K near-edge X-ray absorption fine-structure of graphene, *Chem. Phys. Lett.* **475**, 269 (2009).

- [150] V. Lee, C. Park, C. Jaye, D. A. Fischer, Q. Yu, W. Wu, Z. Liu, J. Bao, S. S. Pei, C. Smith, P. Lysaght, and S. Banerjee, Substrate hybridization and rippling of graphene evidenced by near-edge X-ray absorption fine structure spectroscopy, *J. Phys. Chem. Lett.* **1**, 1247 (2010).
- [151] V. Lee, R. V. Dennis, C. Jaye, X. Wang, D. A. Fischer, A. N. Cartwright, and S. Banerjee, In situ near-edge x-ray absorption fine structure spectroscopy investigation of the thermal defunctionalization of graphene oxide, *J. Vac. Sci. Technol. B* **30**, 061206 (2012).
- [152] Y. Shibayama, H. Sato, T. Enoki, X. X. Bi, M. S. Dresselhaus, and M. Endo, Novel electronic properties of a nano-graphite disordered network and their iodine doping effect, *J. Phys. Soc. Jpn.* **69**, 754 (2000).
- [153] Y. Shibayama, H. Sato, T. Enoki, and M. Endo, Disordered magnetism at the metal-insulator threshold in nano-graphite-based carbon materials, *Phys. Rev. Lett.* **84**, 1744 (2000).
- [154] T. Enoki and K. Takai, Unconventional electronic and magnetic functions of nanographene-based host-guest systems, *Dalton Trans.* 3773 (2008).
- [155] T. Enoki and K. Takai, The edge state of nanographene and the magnetism of the edge-state spins, *Solid State Commun.* **149**, 1144 (2009).
- [156] T. Enoki, Role of edges in the electronic and magnetic structures of nanographene, *Phys. Scr.* **T146**, 014008 (2012).
- [157] S. J. Hao, K. Takai, V. L. J. Joly, and T. Enoki, Magnetism of HNO₃-adsorbed nanoporous network of nanographene sheets, *J. Phys. Chem. Solids* **73**, 1432 (2012).
- [158] S. J. Hao, K. Takai, V. L. J. Joly, K. Yokota, M. Kiguchi, and T. Enoki, Magnetic properties and interplay between nanographene host and nitric acid guest in nanographene-based nanoporous carbon, *Bull. Chem. Soc. Jpn.* **85**, 376 (2012).
- [159] K. Kusakabe and M. Maruyama, Magnetic nanographite, *Phys. Rev. B* **67**, 092406 (2003).
- [160] M. Maruyama and K. Kusakabe, Theoretical prediction of synthesis methods to create magnetic nanographite, *J. Phys. Soc. Jpn.* **73**, 656 (2004).
- [161] A. Bostwick, T. Ohta, T. Seyller, K. Horn, and E. Rotenberg, Quasiparticle dynamics in graphene, *Nat. Phys.* **3**, 36 (2007).
- [162] D. L. Miller, K. D. Kubista, G. M. Rutter, M. Ruan, W. A. de Heer, P. N. First, and

- J. A. Strosio, Observing the quantization of zero mass carriers in graphene, *Science* **324**, 924 (2009).
- [163] K. Yokota, K. Takai, and T. Enoki, Carrier control of graphene driven by the proximity effect of functionalized self-assembled monolayers, *Nano Lett.* **11**, 3669 (2011).
- [164] Z. Yan, Z. Sun, W. Lu, J. Yao, Y. Zhu, and J. M. Tour, Controlled modulation of electronic properties of graphene by self-assembled monolayers on SiO₂ substrates, *ACS Nano* **5**, 1535 (2011).
- [165] J. Park, W. H. Lee, S. Huh, S. H. Sim, S. B. Kim, K. Cho, B. H. Hong, and K. S. Kim, Work-function engineering of graphene electrodes by self-assembled monolayers for high-performance organic field-effect transistors, *J. Phys. Chem. Lett.* **2**, 841 (2011).
- [166] R. Wang, S. Wang, D. Zhang, Z. Li, Y. Fang, and X. Qiu, Control of carrier type and density in exfoliated graphene by interface engineering, *ACS Nano* **5**, 408 (2011).
- [167] J. Baltazar, H. Sojoudi, S. A. Paniagua, J. Kowalik, S. R. Marder, L. M. Tolbert, S. Graham, and C. L. Henderson, Facile formation of graphene p-n junctions using self-assembled monolayers, *J. Phys. Chem. C* **116**, 19095 (2012).
- [168] H. Sojoudi, J. Baltazar, L. M. Tolbert, C. L. Henderson, and S. Graham, Creating graphene p-n junctions using self-assembled monolayers, *ACS Appl. Mater. Interfaces* **4**
- [169] F. Schedin, A. K. Geim, S. V. Morozov, E. W. Hill, P. Blake, M. I. Katsnelson, and K. S. Novoselov, Detection of individual gas molecules adsorbed on graphene, *Nat. Mater.* **6**, 652 (2007).
- [170] Y. Sato, K. Takai, and T. Enoki, Electrically controlled adsorption of oxygen in bilayer graphene devices, *Nano Lett.* **11**, 3468 (2011).
- [171] I. Silvestre, E. A. de Morais, A. O. Melo, L. C. Campos, A. M. B. Goncalves, A. R. Cadore, A. S. Ferlauto, H. Chacham, M. S. C. Mazzoni, and R. G. Lacerda, Asymmetric effect of oxygen adsorption on electron and hole mobilities in bilayer graphene: long- and short-range scattering mechanisms, *ACS Nano* **7**, 6597 (2013).

Chapter 4

Electron scattering sources in antidot graphene and Ar⁺-irradiated graphene

4.1 Introduction

Graphene, a single sheet of graphite, is a two-dimensional crystal of carbon atoms arranged in a honeycomb structure. Since macroscopic flakes of single-layer or multilayer graphene were first isolated by micromechanical exfoliation of graphite, followed by the discovery of the anomalous quantum Hall effect [1–3], many studies have been performed to elucidate the electron behavior described by the massless Dirac equation. The electron transport properties of graphene, in which carrier mobility reaches as high as 200,000 cm² V⁻¹ s⁻¹ [4], are highly attractive topics and the electron scattering mechanisms have been studied experimentally and theoretically. The electrostatic potentials of charged impurities, which are inevitably introduced during device fabrication processes, act as long-range scattering sources [5,6]. The gentle decay of the Coulomb potential created by these charged impurities is closely related to the intravalley scattering process, in which electrons are scattered within a valley in the first Brillouin zone of graphene. Here, the effect of the scattering potential depends strongly on the electrostatic screening effect, which is modulated by the charge carrier density. On the other hand, a steep potential induced by structural defects, such as vacancies and grain boundaries in graphene, causes larger changes in the electron momentum, including backscattering, which corresponds to the K-to-K' transition (*i.e.*, intervalley scattering). Such defects form midgap states in graphene, which reportedly contribute to the conductivity [7,8]. In addition, these structural defects have been experimentally and theoretically examined as the origin of localized magnetic moments in various carbon materials as well as graphene [9,10]. Chen *et al.* [11] recently reported experimental observations of carrier scattering by vacancy defects as magnetic impurities in graphene; the defects were introduced by irradiation of noble gas ions. Edge states, which are spin-polarized electronic states localized at the

zigzag edges of graphene [12–14], have been considered to be the sources of magnetic moments in graphene. Magnetic moments at atomic vacancies are likely to be due to these edge states. Although the correlation between edge states and electron scattering properties is of importance from the viewpoint of electronics and spintronics devices applications as well as fundamental physics, experimental information is still lacking.

For the elucidation of this issue, electron transport characteristics have been measured in edge-enriched graphene devices such as antidot structures, in which artificial periodic potential barriers and edge boundaries are introduced into graphene [15–18]. Indeed, the commensurability effect and Aharonov-Bohm-type oscillation, which are related to the antidot structure were reportedly observed in antidot graphene samples. Although Shen *et al.* [15] estimated the carrier density on the basis of the commensurability peaks, and Eroms and Weiss [19] determined it using variations in the conductivity with the application of a gate voltage, further investigation of the dependence of electron transport characteristics on the carrier density is needed to understand the dominant scattering mechanism in antidot graphene for deriving edge effects.

In this study, antidot and Ar⁺-irradiated graphene samples were fabricated, and the Fermi energy was determined from the gate voltage dependence of the conductivity. Antidot sample had long-range continuous edges. Ar⁺ irradiation created atomic vacancies in graphene honeycomb lattice. The author hypothesized both of these samples show electron transport characteristics related to the presence of edges and edge states. The electron scattering sources were investigated in terms of the carrier density for both samples and found to exhibit essential differences.

4.2 Experimental

Graphene flakes were prepared on an *n*-Si substrate with an SiO₂ layer of 285 or 90 nm thickness by micromechanical exfoliation of kish graphite. For the antidot structured graphene sample, an Au/Cr mask (40 nm and 10 nm thick, respectively) was fabricated on the graphene by electron beam lithography, followed by etching in reactive oxygen plasma and removal of the metal mask by chemical etching. A graphene sample having vacancy defects was fabricated by irradiation with a 100 eV Ar⁺ ion beam in a high

vacuum (1.0×10^{-8} Torr). Au/Cr electrodes with thicknesses of 40/5 nm, respectively, were attached to the samples by photolithography. Doped-Si layer was used as backgate electrode. Contaminants were removed by current-induced annealing of graphene [20]. Raman spectra were measured with excitation lasers at 514.5 nm and 532 nm (Jobin Yvon T64000, Tokyo Instruments Nanofinder 30) for the antidot samples and Ar⁺-irradiated samples, respectively, under ambient conditions at room temperature. The dependence on the wave length of the excitation laser was corrected [21]. Magnetotransport measurements were performed by applying a gate voltage between -60 and $+60$ V under a magnetic field of up to 15 T applied perpendicularly to the graphene plane in the temperature range from 1.5 K to 30 K.

As shown later, the author used bilayer and single-layer graphenes for antidot and Ar⁺-irradiated samples, respectively, in the experiments due to the difficulty in the sample preparations and appropriateness in the discussion of the physical properties (see Section 4.6 Complement).

4.3 Results

Figure 4.1a shows a typical optical microscope image of an antidot graphene sample with source–drain electrodes. No difference was observed between optical images taken before and after the nanofabrication processes in either antidot or Ar⁺-irradiated samples. The antidot array of 100×100 nm² rectangular holes with 200-nm pitches in the graphene was clearly seen in the scanning electron microscope image shown in Fig. 4.1b. Considering the contrast in the optical microscope image [22], antidot and Ar⁺-irradiated samples were defined as bilayers and a monolayer, respectively. Observation of the Raman 2D bands in both samples confirmed these results regarding the number of layers [23].

Figure 4.2 shows the backgate voltage (V_g) dependence of the sheet conductivity (σ) for the antidot sample. The blue circles denote the data obtained for the as-prepared antidot sample. σ of the as-prepared sample decreased monotonically with respect to the increase of V_g without having a minimum. After the current-induced annealing, σ exhibited its minimum value with $V_g = 0$, as shown as the red circles in Fig. 4.2. The value of V_g with which σ is the minimum is defined as the charge neutrality point (V_{CNP}). The

carrier mobility (μ) is derived from the Drude equation,

$$\mu = \frac{\sigma}{en}, \quad \dots(4.1)$$

where e is the elementary electrical charge and n is the carrier density described as

$$n = 7.6 \times 10^{10} (V_g - V_{\text{CNP}}) \text{ (cm}^{-2}\text{)}, \quad \dots(4.2)$$

for the 285-nm thick SiO₂ substrate used for the antidot sample. The calculated values of the hole and electron mobilities are approximately 400 cm² V⁻¹ s⁻¹ and 180 cm² V⁻¹ s⁻¹, respectively. For the Ar⁺-irradiated sample, V_{CNP} appeared at $V_g = +42$ V, as shown in Fig. 4.3. The author used a 90-nm thick SiO₂ substrate for the Ar⁺-irradiated sample; this corresponds to a much wider field-effect modulation of the carrier density, which is given by

$$n = 2.4 \times 10^{11} (V_g - V_{\text{CNP}}) \text{ (cm}^{-2}\text{)}. \quad \dots(4.3)$$

For the Ar⁺-irradiated sample, the calculated hole mobility is approximately 600 cm² V⁻¹ s⁻¹. The electron mobility cannot be extracted because the data are insufficient.

Figures 4.4 and 4.5 show the magnetoresistance ($\Delta\rho(B)/\rho(0)$), for the antidot and Ar⁺-irradiated samples with various backgate voltages, respectively, where $\Delta\rho(B) = \rho(B) - \rho(0)$, and $\rho(B)$ is the resistivity under the applied magnetic field B , namely, $\rho(0)$ is the resistivity under zero magnetic field. At high magnetic fields, the antidot sample shows Shubnikov-de Haas (SdH) oscillation, whereas the Ar⁺-irradiated sample does not. At low magnetic fields (below approximately 1 T), the magnetoresistance of both samples decreases steeply as the magnetic field increases. The strength of the negative magnetoresistance is approximately 0.1 at 1 T for both samples. The magnetoresistance of the antidot sample remains negative in the entire magnetic field range.

The Raman spectra of the antidot and the Ar⁺-irradiated samples are shown in Fig. 4.6. The G band appears clearly at approximately 1590 cm⁻¹ in both samples. Both Raman spectra show D band features at approximately 1350 cm⁻¹, which originate from the intervalley scatterings induced by vacancies, grain boundaries, and so on [23]. The integrated intensity ratios of the D band to the G band (I_D/I_G) are 0.26 and 0.48 for the antidot and the Ar⁺-irradiated samples, respectively. The average distance between the intervalley scattering sources (L_a) is derived from I_D/I_G

$$L_a = 2.4 \times 10^{-10} \lambda_{\text{laser}}^4 \left(\frac{I_D}{I_G} \right)^{-1} \text{ (nm)}, \quad \dots(4.4)$$

where the dependence on the wave length of the excitation laser in nanometer units (λ_{laser}) is corrected for the D band intensity [24]. The estimated values of L_a for the antidot and the Ar⁺-irradiated samples are approximately 65 nm and 40 nm, respectively. In addition, the D' band, which is correlated with intravalley scattering [25,26], appears at 1631 cm⁻¹ in the spectrum of the Ar⁺-irradiated sample. The selective presence of the D' band in the spectrum of the Ar⁺-irradiated sample is related to the difference in the wave length of the excitation laser [27].

4.4 Discussion

4.4.1. Electron transport without magnetic field

The sheet conductivity under V_g tuning in Fig. 4.2 yields a mean free path (l) of 10 nm for the antidot sample according to the equation

$$l = \frac{\hbar k_F \mu}{e}, \quad \dots(4.5)$$

where \hbar is the Planck constant divided by 2π , and k_F is the Fermi wave number. This value is much smaller than that obtained from the Raman spectrum, $L_a = 65$ nm. For the Ar⁺-irradiated sample, however, l is calculated as 20–30 nm, which is comparable with $L_a = 40$ nm. Because L_a is estimated from the D band intensity of the Raman spectra, which arises from intervalley scattering sources such as vacancies, it has been concluded that carrier scattering in the Ar⁺-irradiated sample is governed by intervalley scattering. In contrast, the large carrier scattering rate indicated by the smaller mean free path in the antidot sample, which has a weak D band contribution, is attributed mainly to the intravalley process, which is not related to the Raman D band [28]. Charged impurities are the most likely scattering sources responsible for intravalley scattering in the antidot sample [29]. The sample fabrication processes, which involved chemical treatments and oxygen plasma exposure, could unintentionally introduce charged impurities into the antidot sample.

For single-layer graphene, theoretical and experimental studies have shown that the

conductivity varies with the carrier density as

$$\sigma(n) = Ce \left| \frac{n}{n_{\text{imp}}} \right|, \quad \dots(4.6)$$

where $C = 5 \times 10^{15} \text{ Vs}^{-1}$, and n_{imp} is the density of charged impurities [5,6]. In bilayer graphene, $\sigma(n)$ has a linear dependence on carrier density as in monolayer graphene [30], although a nonlinear relationship due to a change in C as a function of n has also been reported [31]. Although the scattering source in bilayer graphene on an SiO₂ substrate remains controversial, the author simply use Eq. (4.6) with $C = 5 \times 10^{15} \text{ Vs}^{-1}$ to fit the data for the antidot sample, which was identified as bilayer graphene, to estimate the density of impurities. The resulting fit is shown in Fig. 4.2. The observed electron–hole asymmetry yields $n_{\text{imp}} = 1.6 \times 10^{13} \text{ cm}^{-2}$ and $7.7 \times 10^{13} \text{ cm}^{-2}$ for negative and positive V_g , respectively. The electron–hole asymmetry can be attributed to an inhomogeneous distribution of the charged impurities. The author applied a relatively high voltage to heat and clean the antidot sample. However, the source and the drain electrodes are likely to act as heat sinks during this process and reduce the sample temperature in the region close to the electrodes relative to that in the central region; thus, contaminants may remain near the electrodes and cause hole doping [20,29]. When V_g is negative, the conductivity in the central region of the sample (see Fig. 4.7), which is relatively clean, is predominant. In contrast, the dirty region contributes much more to the conductivity of electron carriers when V_g is positive. Given the long channel length of the antidot sample (6 μm), for all practical purposes, the asymmetry in conductivity due to the difference in the work functions of graphene and metal electrodes can be ignored [32].

In contrast, for the single-layer Ar⁺-irradiated sample, l of 20–30 nm is comparable with $L_a = 40 \text{ nm}$. Given the extremely low concentration of atomic vacancies (0.004%), which is estimated from the squared ratio of the lattice constant ($a = 0.246 \text{ nm}$) to the average distance between vacancy defects [40 nm; hence, a squared ratio of $(a/40)^2$], and the small size of the vacancies (0.25 nm) [33], it has been confirmed that the intrinsic electronic structure of graphene is preserved. During fabrication, the Ar-sputtered sample is not exposed to chemical reactions such as the removal of metal masks, which introduce many charged impurities. This is consistent with the suggestion that intervalley scattering by vacancy defects created during Ar⁺ irradiation dominates the conductivity in the Ar⁺-

irradiated sample. However, charged impurities are also inevitably contained in the Ar⁺-irradiated sample. They form electron-hole puddles that produce a spatially inhomogeneous distribution of V_{CNP} , which results in a broadening of the V_g - σ curve in the region around the Dirac point. Here, modulation of the carrier density dependence of the conductivity due to vacancy defects is fitted by a function of the form

$$\sigma(n) = \left(\frac{2e^2}{\pi h} \right) \left| \frac{n}{n_d} \right| \ln^2(k_F R), \quad \cdots (4.7)$$

as shown in Fig. 4.3, where n_d is the density of vacancy defects, and R is the radius of the potential [7,8]. The formation of mono-atomic-scale vacancy defect by ion irradiation is well accepted. Assuming an R -value of 0.25 nm, which corresponds to single atom vacancies [33], the density of vacancy defects is $n_d = 9.0 \times 10^{12} \text{ cm}^{-2}$.

4.4.2. Magnetoresistance at high magnetic fields

Differences in the origin of electron scattering in each sample are associated with differences in the change of the electron momentum during the carrier scattering event. This can be seen in the SdH oscillation of the conductivity at high fields. SdH oscillations are observed in the antidot sample, in which charged impurities mainly contribute to carrier scattering. Their shallow potential causes a small change in electron momentum, and the average cyclotron motions are less disturbed in k -space. In contrast, in the Ar⁺-irradiated sample, the larger electron momentum change caused by the intervalley scattering induced by vacancy defects completely breaks the cyclotron orbits of the carriers, so that the SdH oscillation is not observed in the Ar⁺-irradiated sample.

To analyze the SdH oscillation, the author defined the envelope curve of the resistivity by taking the average of adjacent data points with a window width of 60 points, corresponding to a range of 0.9 T around a certain magnetic field. By subtracting the envelope curve from the magnetic field dependence of the sheet resistance, the author obtained the SdH oscillation with $V_g = -50 \text{ V}$ at 1.5 K, as shown in Fig. 4.8a. The author derived the dominant frequency of the SdH oscillation by applying a fast Fourier transform (FFT) to the data. The power spectrum (i.e., FFT intensity versus oscillation frequency) obtained with $V_g = -50 \text{ V}$ is plotted in Fig. 4.8b. The broad SdH oscillation peak around 50–100 T indicates inhomogeneity in the spatial distribution of charges in

the sample. A linear relationship between the oscillation frequency (B_F) and the carrier density,

$$B_F = \frac{hn}{4e}, \quad \dots(4.8)$$

has been reported for bulk graphene samples [2]. However, the estimated values of B_F in the antidot sample are 50–95 T with a minimum at a gate voltage of 30 V, as shown in Fig. 4.8c. The estimated frequency yields a carrier density of $n = 4.8\text{--}9.2 \times 10^{12} \text{ cm}^{-2}$, which disagrees with that obtained from the sheet resistance. In particular, the carrier density estimated from the SdH oscillation becomes $n = 6.8 \times 10^{12} \text{ cm}^{-2}$ at $V_{\text{CNP}} = 0 \text{ V}$ (the Dirac point), although it should be zero. In a nanoribbon-structured graphene sample, such an anomalous SdH oscillation was observed with V_g set to the Dirac point, in contrast to that in a bulk graphene sample [34]. The anomaly was ascribed to the indirect contribution of edges. The chemical species introduced in the lithography process, which affect the chemically active edge in particular, can cause locally high carrier doping; this in turn results in the presence of Landau states with modified orbits, which produce the large oscillation frequency at the Dirac points. Although antidot graphene is rich in graphene edges, the sample shows no anomaly related to nonbonding edge states localized near the edge region depending on the edge geometry [12]. This is attributed to the presence of inhomogeneously distributed scattering sources in the interior region far from the edges and the large carrier density in the present sample. The gate voltage dependence of the conductivity represents the average transport properties in the graphene device, where the charge density and scattering sources are inhomogeneously distributed. In contrast, the SdH oscillation in the magnetoresistance highlights the specific part of the sample where the carrier mobility and size of the Fermi surface are appropriate for observing each gate voltage condition.

4.4.3. Magnetoresistance at low magnetic fields

At low magnetic fields ($<1 \text{ T}$), steep decreases in the magnetoresistance were observed for both the antidot sample and the Ar⁺-irradiated sample, as shown in Figs. 4.9 and 4.10. These negative magnetoresistance values are attributed to a weak localization effect. Weak localization is caused by time-reversal symmetry breaking of elastic scattering paths, which enhances the conductivity by magnetic de-phasing of the standing

waves of charged carriers. Although negative magnetoresistance originating in weak localization usually saturates at a low magnetic field, that of the antidot sample does not saturate and remains negative between 0 and 15 T. A similar negative magnetoresistance was observed in graphite powders with approximate particle sizes of 30 nm [35]. This was explained by a decrease in scattering at the crystal boundaries as the applied magnetic field increases and the cyclotron radius of charge carriers decreases. The author analyzed the magnetoresistance by using the theoretical equation that describes weak localization for graphene [36],

$$\Delta\rho(B) = -\frac{e^2\rho(0)^2}{\pi h} \left[F\left(\frac{B}{B_\varphi}\right) - F\left(\frac{B}{B_\varphi + 2B_{iv}}\right) - 2F\left(\frac{B}{B_\varphi + B_{iv} + B_*}\right) \right], \quad \cdots(4.9)$$

with

$$F(z) = \ln z + \psi\left(\frac{1}{2} + \frac{1}{z}\right), \quad \cdots(4.10)$$

where ψ is the digamma function, B_x (x : φ , iv , $*$) is

$$B_x = \left(\frac{\hbar}{4eD}\right) \frac{1}{\tau_x}, \quad \cdots(4.11)$$

D is the diffusion constant, and τ_x with the subscript φ , iv , or $*$ corresponds to the inelastic scattering rate, intervalley scattering rate, or scattering rate associated with the intravalley transition, respectively. The scattering length L_x is calculated by using the relationship,

$$L_x = \sqrt{D\tau_x}. \quad \cdots(4.12)$$

The calculated values of D for the antidot and the Ar⁺-irradiated samples are approximately 30 cm² s⁻¹ and 80 cm² s⁻¹, respectively. The magnetoresistance data for the Ar⁺-irradiated and the antidot samples are fitted nicely by Eq. (4.9), as shown in Figs. 4.9 and 4.10, respectively. From the fitted parameter of B_x , the corresponding scattering lengths are calculated as a function of $(V_g - V_{\text{CNP}})$, as shown in Fig. 4.11a.

For the Ar⁺-irradiated sample, the inelastic electron–electron scattering length (L_φ) decreases as the carrier density decreases or the sample temperature increases, as shown in Fig. 4.11a. This is quite consistent with the nature of electron–electron interactions in graphene [37,38]. On the other hand the intervalley scattering length (L_{iv}) and the scattering length related to the intravalley transition (L_*) of the Ar⁺-irradiated sample are

independent of both the carrier density and the temperature. The independence of L_{iv} and L^* from n and T is consistent with the fact that defects and impurities are the sources of elastic scattering. Note that here L_{iv} is approximately equal to the defect spacing length $L_a = 40$ nm estimated from the Raman spectrum [39,40]. Therefore, the values of L_{iv} and L^* in the Ar⁺-irradiated sample are determined to be 40–50 nm.

On the basis of the agreement between L_{iv} and L_a in the Ar⁺-irradiated sample, the author fitted the magnetoresistance of the antidot sample by using Eq. (4.9) and setting L_{iv} equal to $L_a = 65$ nm. The results are plotted in Fig. 4.11b. The value of L^* is 10 nm. L_ϕ shows an asymmetric change depending on V_g . However, the weak localization effect requires that $L_\phi \gg L_{iv}, L^*$, and this condition is not satisfied in the range where $(V_g - V_{CNP})$ is positive. As described above, the positive range corresponds to the lower charge carrier mobility, which is due to charged impurities remaining in a sample area near the source–drain electrodes. Given that charged impurity scattering is the significant mechanism in the antidot sample, intervalley scattering because of the electrostatic potential of charged impurities. In contrast, the requirement for weak localization seems to be satisfied in the range where $(V_g - V_{CNP})$ is negative. The analysis of the weak localization effect confirmed that charged impurities and vacancy defects are the main scattering sources in the antidot and Ar⁺-irradiated sample, respectively.

4.5 Conclusions

The electron transport properties of antidot-nanopatterned and Ar⁺-irradiated graphene were investigated in terms of the carrier densities with respect to the backgate voltage.

In the antidot sample, the lower carrier mobility, irrespective of the smaller D band intensity of the Raman spectrum, reveals charged impurities to be the dominant scattering source. The gate voltage dependence of the conductivity in this sample is fitted well by the model for charged impurity scattering. The observed electron–hole asymmetry in the conductivity is explained by a spatially inhomogeneous distribution of charged impurities. In contrast, the gate voltage dependence of the conductivity in the Ar⁺-irradiated sample is well explained by the intervalley scattering induced by vacancy defects. This is consistent with the strong intensity of the Raman D band for this sample.

At high magnetic fields, SdH oscillations are observed only in the antidot sample, where charged impurities are the dominant scattering sources. The smaller change in the electron momentum during intravalley scattering causes less disturbance of the average cyclotron motion, whereas the larger change in the electron momentum due to vacancy defects, which are significant in the Ar⁺-irradiated sample, breaks the average cyclotron motion. The discrepancy between the oscillation frequencies and the carrier densities is attributed to the inhomogeneity of charged impurities and carrier densities in the sample.

At lower magnetic fields, both the antidot and the Ar⁺-irradiated samples show the weak localization effect. In the Ar⁺-irradiated sample, the condition for the scattering lengths obtained by theoretical fits is completely satisfied. Moreover, the inelastic scattering length depends on the carrier density and temperature, as explained by electron–electron interactions, whereas the elastic scattering lengths are almost independent of the carrier density and temperature. In addition, L_{iv} is approximately equal to the L_a value given by the Raman D band. This indicates that vacancy defects act as the dominant scatterers in the Ar⁺-irradiated sample. In contrast, in the antidot sample, the condition for the scattering lengths is not satisfied under the assumption of $L_{iv} = L_a$. The contribution of the intervalley scattering term is considered to be quite small; therefore, the intravalley scattering term due to charged impurities is considered to be significant.

Although edges are expected to affect carrier scattering in the antidot-nanopatterned graphene, the electron transport properties of the antidot sample were significantly influenced by charged impurities, which are inevitably introduced into the sample during fabrication.

4.6 Complement

The author used bilayer and single-layer graphenes for antidot and Ar⁺-irradiated samples, respectively. Single-layer graphene can be prepared easily for Ar⁺-irradiated samples because the preparation process is simple. In contrast, the author have seldom succeeded in the preparation and cleaning of single-layer antidot graphene sample because single-layer graphene is mechanically weak and chemically reactive. However, the electron-beam lithography technique, which was employed for preparing antidot nanostructures, allows the fabrication of antidots not only on the uppermost layer but also on the second layer as well, so that the characteristics of the antidots are almost the same for the first and the second layers. Accordingly, the author can treat these two layers as identical. Furthermore, as the physical processes that underlie the scattering are not significantly modified by the interlayer interaction, their essence is preserved. On the other hand, in the Ar⁺-irradiated sample, bilayer graphene is inappropriate as defects created on the second layer are different from those on the uppermost layer because of differences in the penetration of Ar⁺ ions. Thus, the author chose bilayer antidot graphene and single-layer Ar⁺-irradiated graphene to investigate the dominant scattering mechanism in each sample. In fact, the number of layers is not crucial to the analysis; discussion focuses on the comparison of inter- and intra-valley scattering sources.

Acknowledgment to Cambridge University Press

The study written in this chapter has been published in *Journal of Materials Research*, as Yasuhiko Kudo, Kazuyuki Takai, and Toshiaki Enoki (2013), Electron transport properties of graphene with charged impurities and vacancy defects, *Journal of Materials Research*, **28**, pp. 1097–1104, Copyright © Materials Research Society 2013, reproduced with permission. The author of this thesis sincerely acknowledge the permission of Cambridge University Press for the inclusion of this article in this thesis.

4.7 Figures in Chapter 4

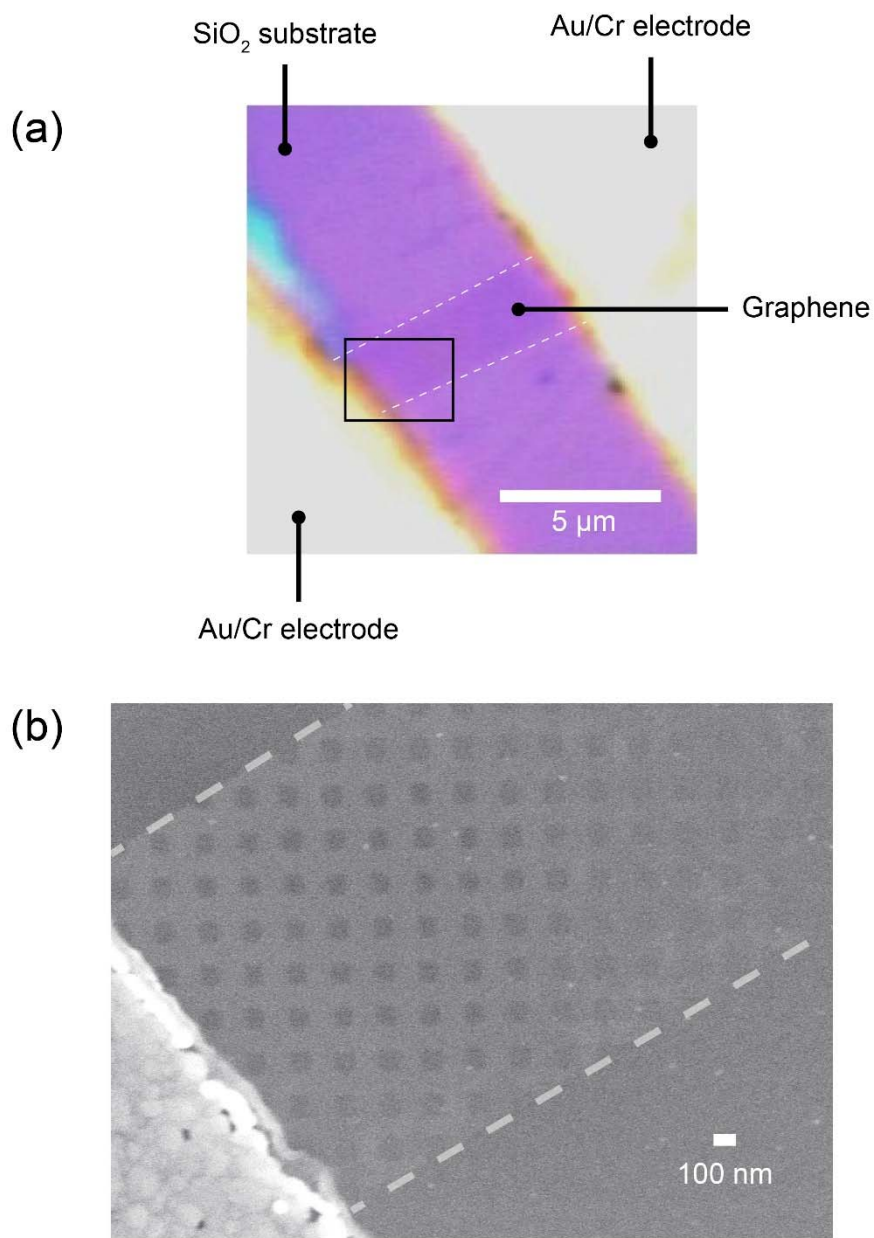


Figure. 4.1. (a) The optical microscope and (b) the scanning electron microscope images of an antidot graphene sample. The black square in (a) corresponds to the area of (b). Scale bar for each image is attached as white line.

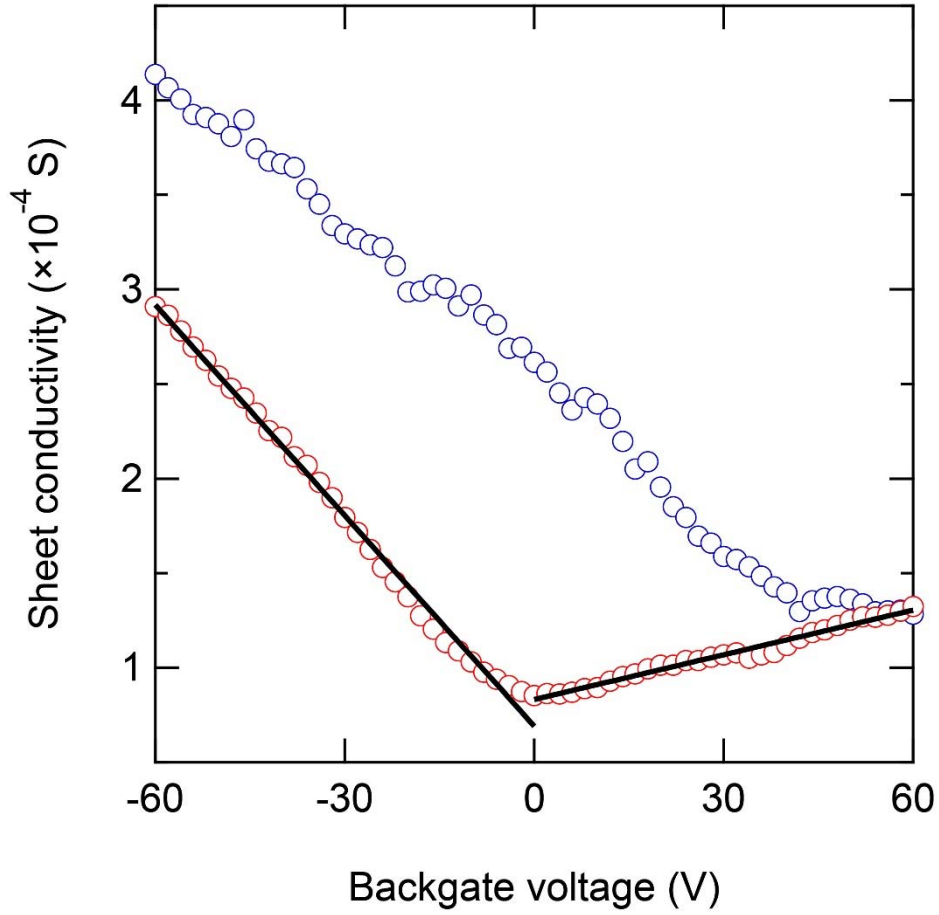


Figure 4.2. The V_g dependence of the sheet conductivity of the bilayer antidot sample measured at 1.5 K with zero magnetic field. The blue and the red circles denote the data obtained before and after the current-induced cleaning, respectively. The black curves represent theoretical fits by Eq. (4.6).

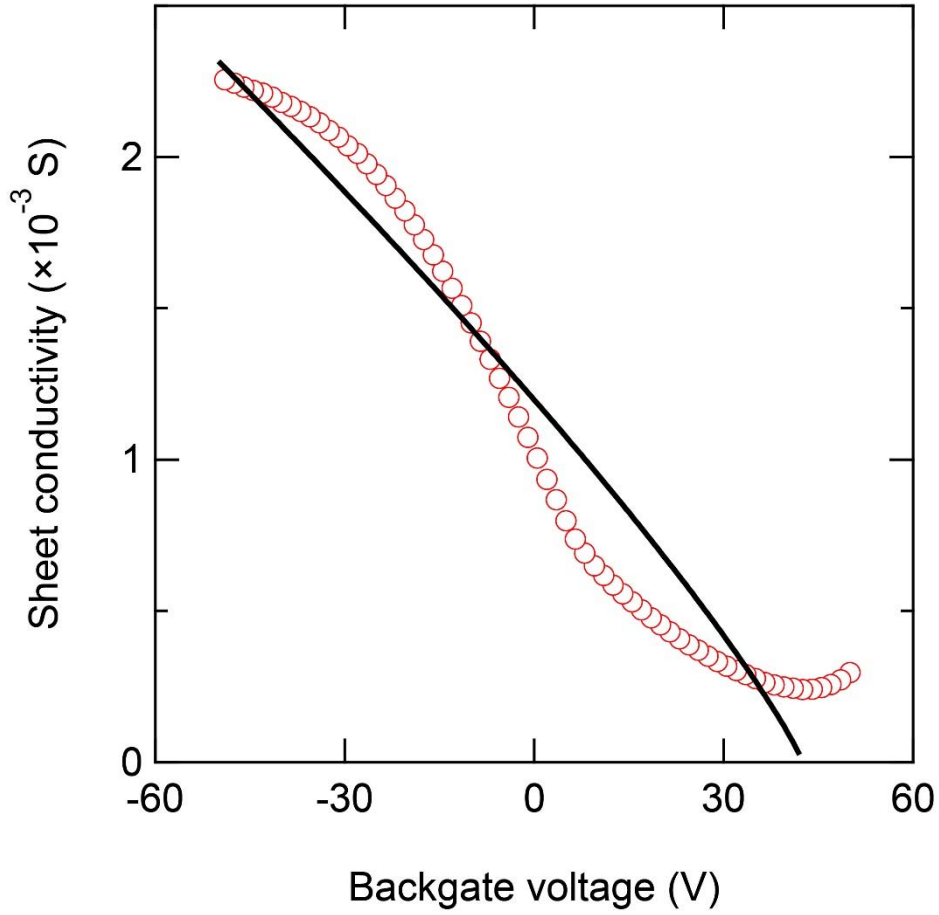


Figure 4.3. The V_g dependence of the sheet conductivity of the single-layer Ar^+ -irradiated sample measured at 2 K with zero magnetic field. The red circles denote the experimental data. The black curve denotes theoretical fit by Eq. (4.7).

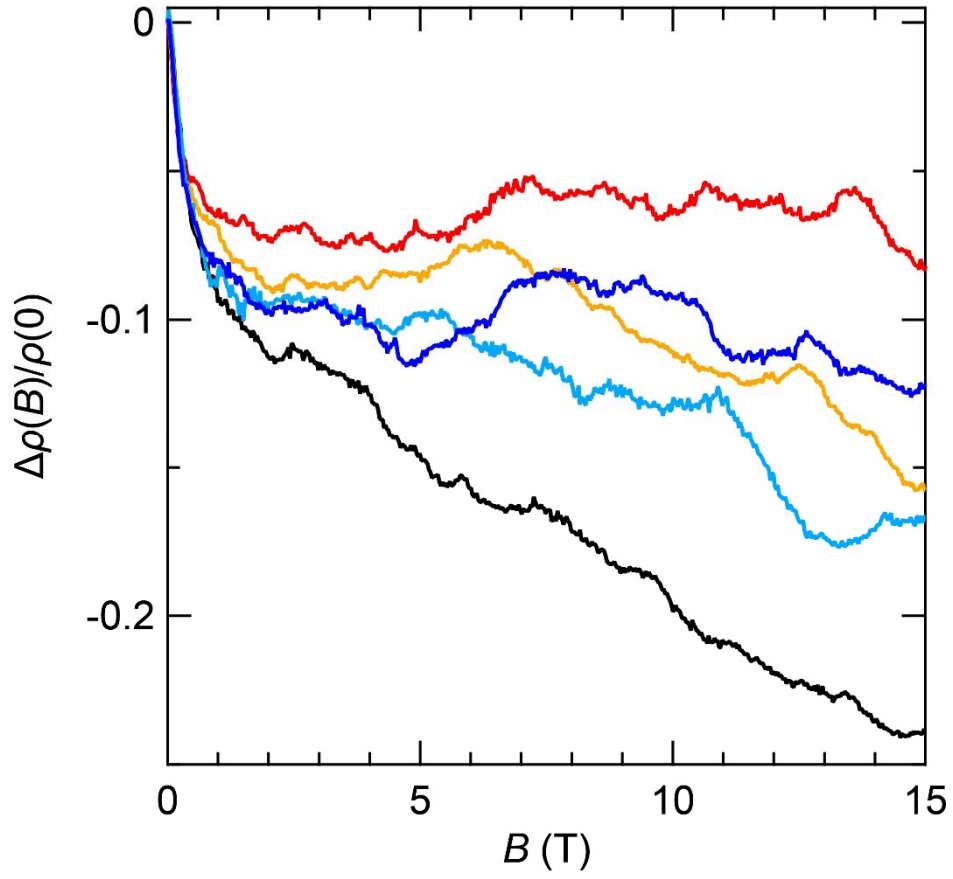


Figure 4.4. Magnetoresistance of the bilayer antidot sample measured at 1.5 K with $V_g = -50$ V, -30 V, 0 V, $+30$ V, and $+50$ V denoted by red, orange, black, light-blue, and blue curves, respectively.

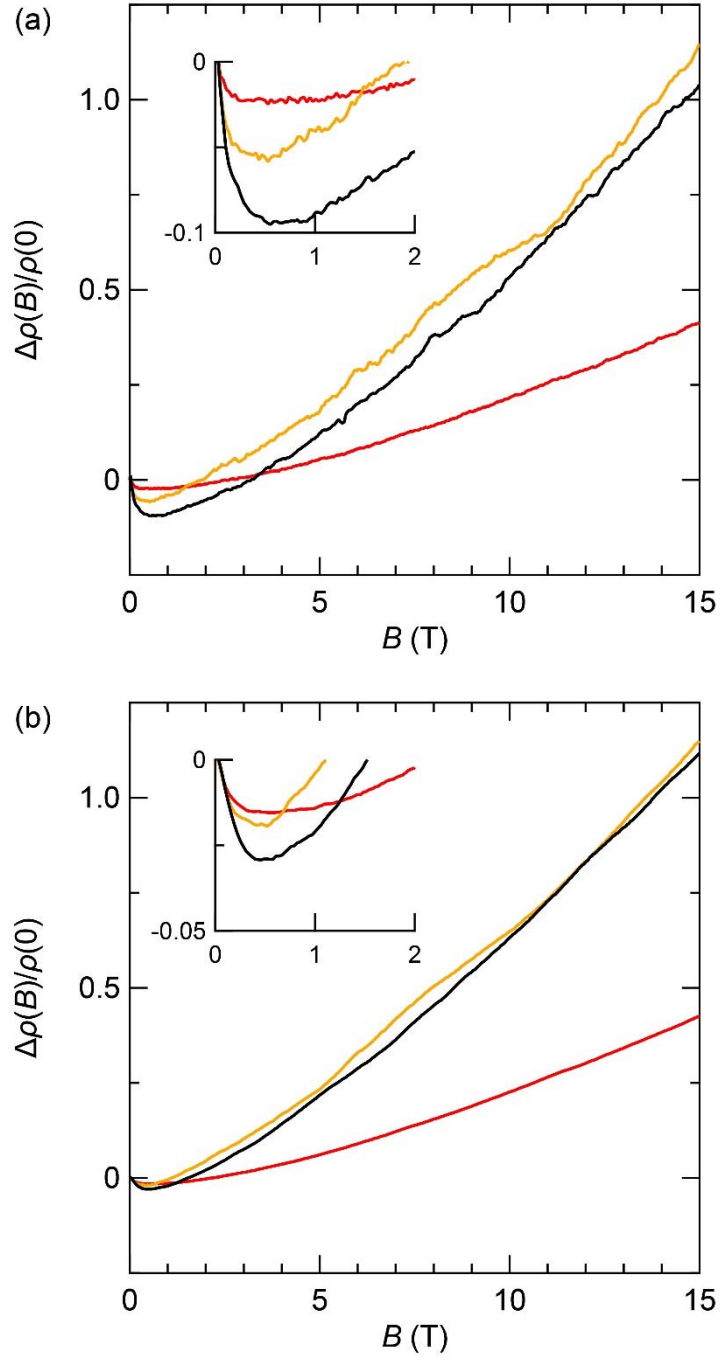


Figure 4.5. Magnetoresistance of the single-layer Ar⁺-irradiated sample measured at (a) 2 K and (b) 30 K with $V_g = 0$ V, +30 V, and +42 V denoted by red, orange, and black curves, respectively. The insets represent magnifications of low magnetic field regions from 0 T to 2 T.

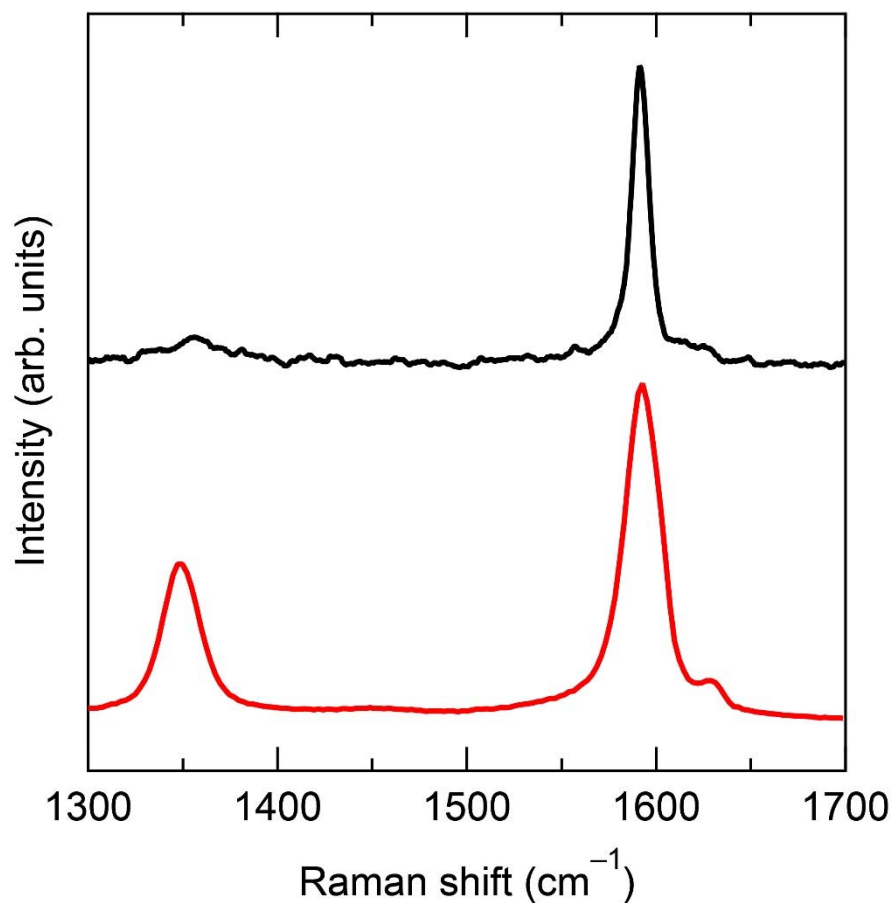


Figure 4.6. Raman spectra for the G and D bands of the antidot and the Ar⁺-irradiated samples denoted by the black and the red curves, respectively. In the spectrum of the antidot sample, the G and the D bands appear at 1591 cm⁻¹ and 1356 cm⁻¹, respectively, with corresponding widths of 9 cm⁻¹ and 34 cm⁻¹. In the Ar⁺-irradiated sample, the G and the D bands appear at 1592 cm⁻¹ and 1349 cm⁻¹, respectively, with corresponding widths of 21 cm⁻¹ and 23 cm⁻¹. In addition, the D' band appears at 1631 cm⁻¹ in the spectrum of the Ar⁺-irradiated sample. Its width is 5 cm⁻¹.

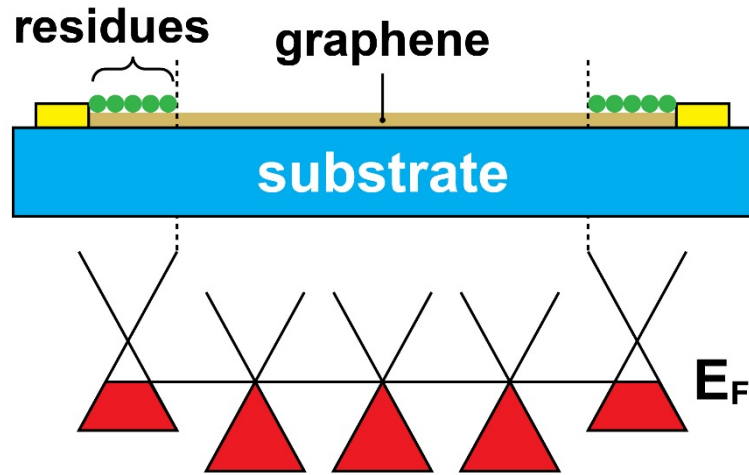


Figure 4.7. Schematic illustration of inhomogeneous distribution of charged impurities with a V_g of ~ 0 V. Impurities are likely to be retained by current-induced cleaning, causing residual modulation of the carrier density in the graphene near the metal electrodes.

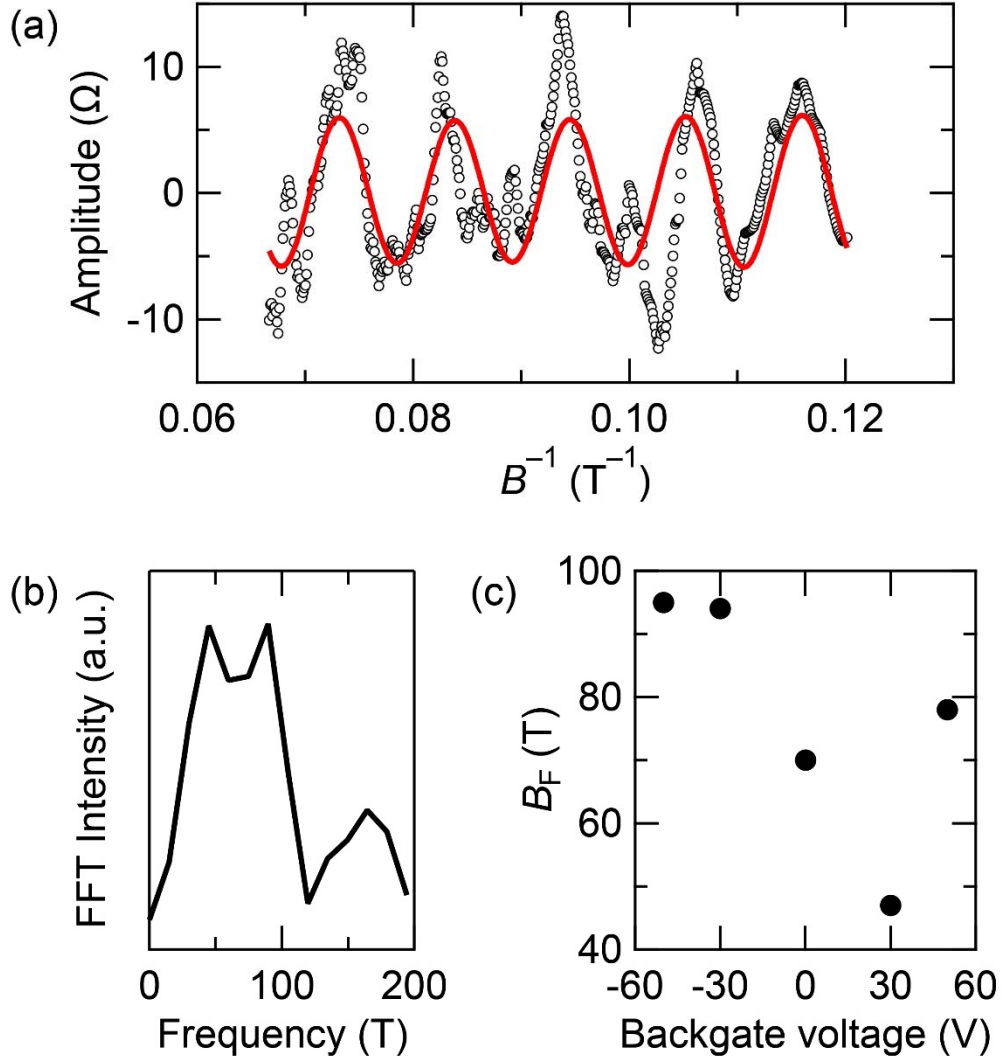


Figure 4.8. (a) SdH oscillation versus the inverse of the magnetic field observed in the antidot sample with $V_g = -50$ V at 1.5 K denoted as the circles. The red solid curve shows oscillation with the dominant frequency. (b) Power spectrum (*i.e.*, FFT intensity versus oscillation frequency) obtained with $V_g = -50$ V. (c) Dominant SdH oscillation frequencies observed with various backgate voltages.

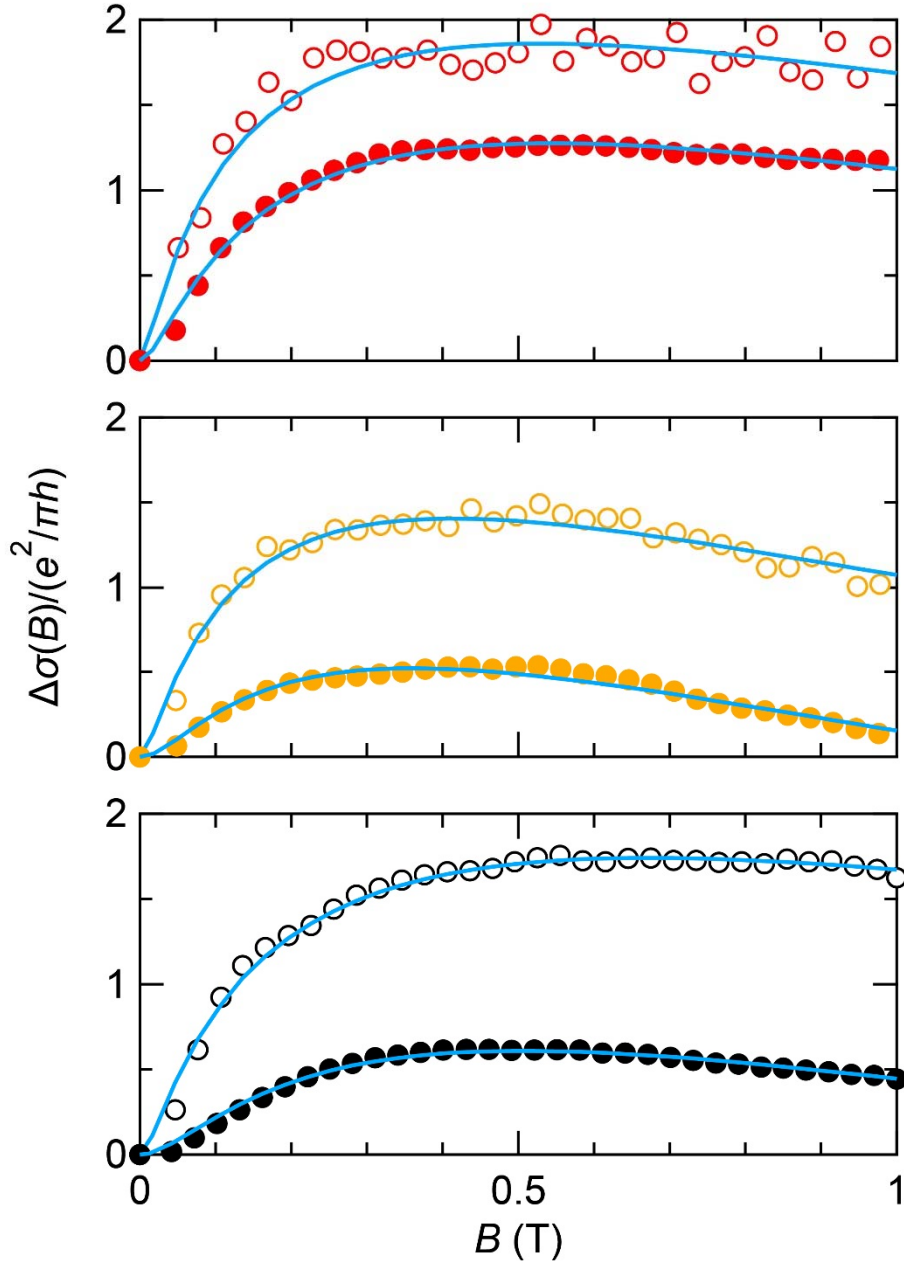


Figure 4.9. Magnetoresistance of the Ar⁺-irradiated sample measured with $V_g = 0$ V, +30 V, and +42 V (the red, the orange, and the black circles, respectively) at 2 K and 30 K (the empty and the filled circles, respectively). The solid curves represents the theoretical fits by Eq. (4.9).

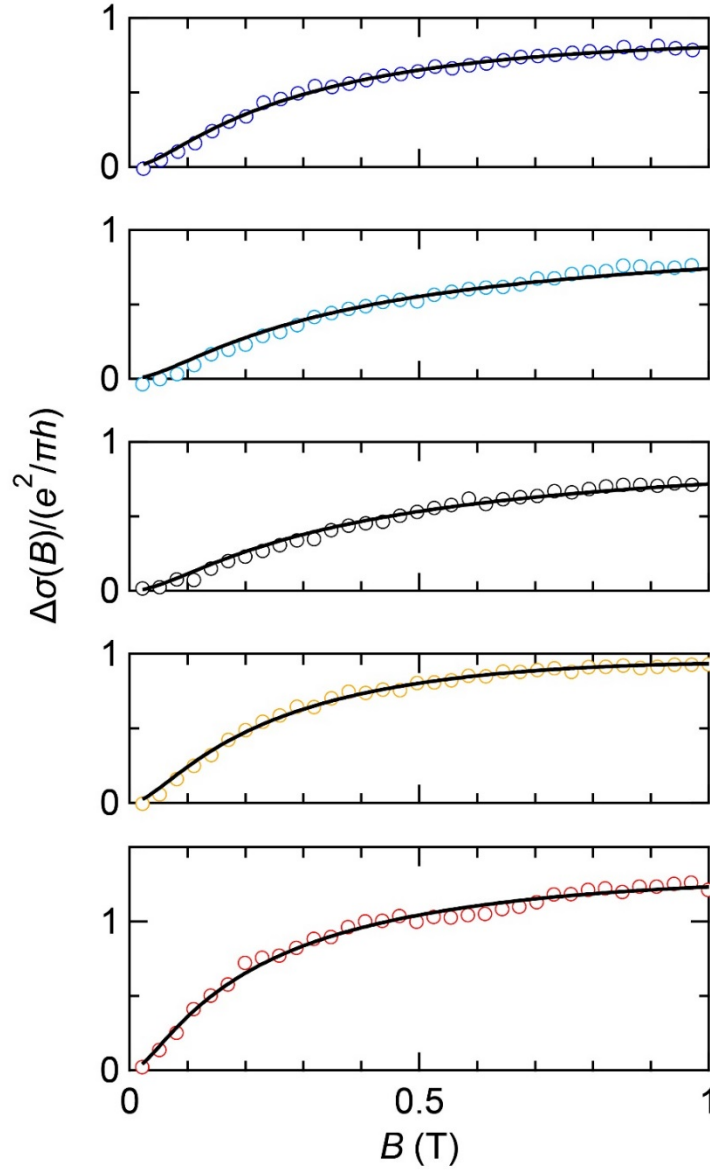


Figure 4.10. Magnetoresistance of the antidot sample measured at 1.5 K with $V_g = -50$ V, -30 V, 0 V, $+30$ V, and $+50$ V denoted by the red, the orange, the black, the light-blue, and the blue circles, respectively. The black solid curves represent the theoretical fits by Eq. (4.9).

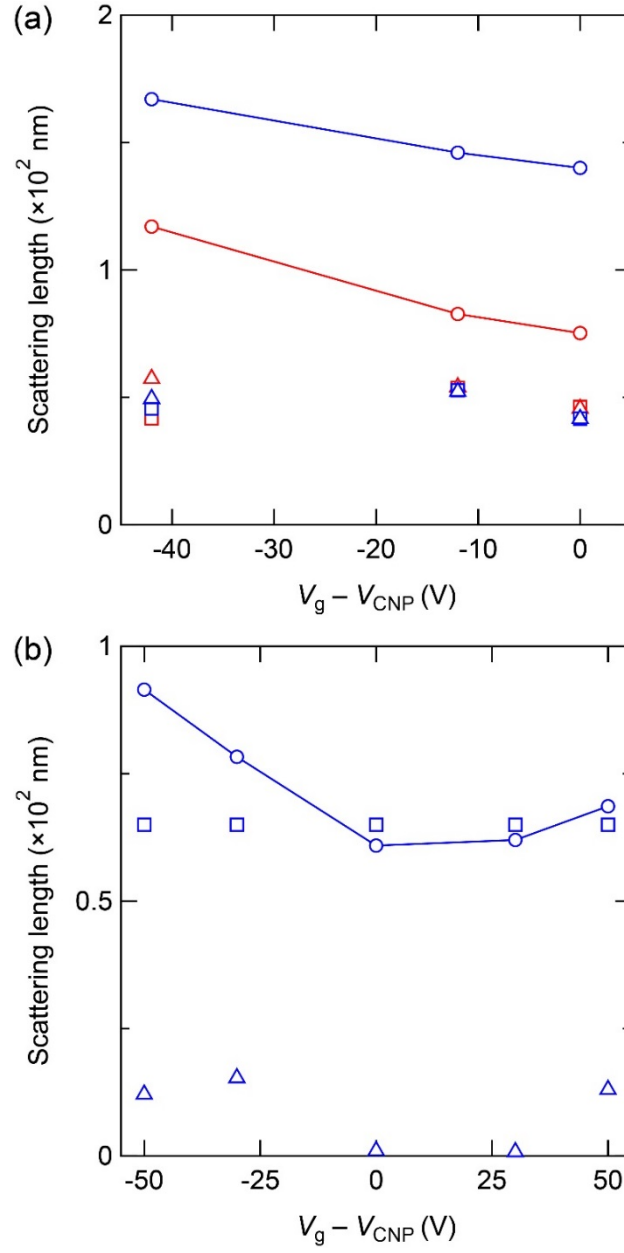


Figure 4.11. (a) Scattering lengths of the Ar⁺-irradiated sample and (b) the antidot sample obtained by fitting the magnetoresistance data shown in Figs. 4.9 and 4.10, respectively. The circles, the squares, and the triangles denote L_{φ} , L_{iv} , and L^* , respectively. In (a), the blue and the red symbols correspond to measurement temperatures of 2 K and 30 K, respectively. In (b) the measurements were performed at 1.5 K.

References in Chapter 4

- [1] K. S. Novoselov, A. K. Geim, S. V. Morozov, D. Jiang, Y. Zhang, S. C. Dubonos, I. V. Grigorieva, and A. A. Firsov, Electric field effect in atomically thin carbon films, *Science* **306**, 666 (2004).
- [2] K. S. Novoselov, A. K. Geim, S. V. Morozov, D. Jiang, M. I. Katsnelson, I. V. Grigorieva, S. V. Dubonos, and A. A. Firsov, Two-dimensional gas of massless Dirac fermions in graphene, *Nature* **438**, 197 (2005).
- [3] Y. Zhang, Y. W. Tan, H. L. Stormer, and P. Kim, Experimental observation of the quantum Hall effect and Berry's phase in graphene. *Nature* **438**, 201 (2005).
- [4] K. I. Bolotin, K. J. Sikes, Z. Jiang, M. Klima, G. Fudenberg, J. Hone, P. Kim, and H. L. Stormer, Ultrahigh electron mobility in suspended graphene, *Solid State Commun.* **146**, 351 (2008).
- [5] T. Ando, Screening effect and impurity scattering in monolayer graphene, *J. Phys. Soc. Jpn.* **75**, 074716 (2006).
- [6] J. H. Chen, C. Jiang, S. Adams, M. S. Fuhrer, E. D. Williams, and M. Ishigami, Charged-impurity scattering in graphene, *Nat. Phys.* **4**, 377 (2008).
- [7] T. Stauber, N. M. R. Peres, and F. Guinea, Electronic transport in graphene: a semiclassical approach including midgap states, *Phys. Rev. B* **76**, 205423 (2007).
- [8] J. H. Chen, W. G. Cullen, C. Jang, M. S. Fuhrer, and E. D. Williams, Defect scattering in graphene, *Phys. Rev. Lett.* **102**, 236805 (2009).
- [9] O. V. Yazyev, and L. Helm, Defect-induced magnetism in graphene, *Phys. Rev. B* **75**, 125408 (2007).
- [10] K. Takai, H. Sato, T. Enoki, N. Yoshida, F. Okino, H. Touhara, and M. Endo, Effect of fluorination on nano-sized π -electron systems, *J. Phys. Soc. Jpn.* **70**, 175 (2001).
- [11] J. H. Chen, L. Li, W. G. Cullen, E. D. Williams, and M. S. Fuhrer, Tunable Kondo effect in graphene with defects, *Nat. Phys.* **7**, 535 (2011).
- [12] M. Fujita, K. Wakabayashi, K. Nakada, and K. Kusakabe, Peculiar localized state at zigzag graphite edge, *J. Phys. Soc. Jpn.* **65**, 1920 (1996).
- [13] Y. Kobayashi, K. Fukui, T. Enoki, K. Kusakabe, and Y. Kaburagi, Observation of zigzag and armchair edges of graphite using scanning tunneling microscopy and spectroscopy, *Phys. Rev. B* **71**, 193406 (2005).
- [14] Y. Niimi, T. Matsui, H. Kambara, K. Tagami, M. Tsukada, and H. Fukuyama,

- Scanning tunneling microscopy and spectroscopy studies of graphite edges, *Appl. Surf. Sci.* **241**, 43 (2005).
- [15] T. Shen, Y. Q. Wu, M. A. Capano, L. P. Rokhinson, L. W. Engel, and P. D. Ye, Magnetoconductance oscillations in graphene antidot arrays, *Appl. Phys. Lett.* **93**, 122102 (2008).
 - [16] J. Bai, X. Zhong, S. Jiang, Y. Huang, and X. Duan, Graphene nanomesh, *Nat. Nanotechnol.* **5**, 190 (2010).
 - [17] X. Liang, Y. S. Jung, S. Wu, A. Ismach, D. L. Olynick, S. Cabrini, and J. Bokor, Formation of bandgap and subbands in graphene nanomeshes with sub-10 nm ribbon width fabricated via nanoimprint lithography, *Nano Lett.* **10**, 2454 (2010).
 - [18] M. Kim, N. S. Safron, E. Han, M. S. Arnold, and P. Gopalan, Fabrication and characterization of large-area, semiconducting nanoporated graphene materials, *Nano Lett.* **10**, 2454 (2010).
 - [19] J. Eroms, and D. Weiss, Weak localization and transport gap in graphene antidot lattices, *New J. Phys.* **11**, 095021 (2009).
 - [20] J. Moser, A. Barreiro, and A. Bachtold, Current-induced cleaning of graphene, *Appl. Phys. Lett.* **91**, 163513 (2007).
 - [21] L. G. Cançado, K. Takai, T. Enoki, M. Endo, Y. A. Kim, H. Mizusaki, A. Jorio, L. N. Coelho, R. Magalhães-Paniago, and M. A. Pimenta, General equation for the determination of the crystallite size L_a of nanographite by Raman spectroscopy. *Appl. Phys. Lett.* **88**, 163106 (2006).
 - [22] P. Blake, E. W. Hill, A. H. C. Neto, K. S. Novoselov, D. Jiang, R. Yang, T. J. Booth, and A. K. Geim, Making graphene visible, *Appl. Phys. Lett.* **91**, 063124 (2007).
 - [23] A. C. Ferrari, J. C. Meyer, V. Scardaci, C. Casiraghi, M. Lazzeri, F. Mauri, S. Piscanec, D. Jiang, K. S. Novoselov, S. Roth, and A. K. Geim, Raman spectrum of graphene and graphene layers, *Phys. Rev. Lett.* **97**, 187401 (2006).
 - [24] R. Saito, A. Jorio, A. G. S. Filho, G. Dresselhaus, M. S. Dresselhaus, and M. A. Pimenta, Probing phonon dispersion relations of graphite by double resonance Raman scattering, *Phys. Rev. Lett.* **88**, 027401 (2002).
 - [25] A. V. Baranov, A. N. Bekhterev, Y. S. Bobovich, and V. I. Petrov, Interpretation of certain characteristics in Raman spectra of graphite and glassy carbon, *Opt. Spectrosc.* **61**, 612 (1987).

- [26] C. Thomsen, and S. Reich, Double resonant Raman scattering in graphite, *Phys. Rev. Lett.* **85**, 5214 (2000).
- [27] K. Sugihara, Thermoelectric power of graphite intercalation compounds, *Phys. Rev. B* **28**, 2157 (1983).
- [28] L. G. Cançado, M. A. Pimenta, B. R. A. Neves, M. S. S. Dantas, and A. Jorio, Influence of the atomic structure on the Raman spectra of graphite edges, *Phys. Rev. Lett.* **93**, 247401 (2004).
- [29] S. Heydrich, M. Hirmer, C. Preis, T. Korn, J. Eroms, D. Weiss, and C. Schüller, Scanning Raman spectroscopy of graphene antidot lattices: evidence for systematic p-type doping. *Appl. Phys. Lett.* **97**, 043113 (2010).
- [30] S. V. Morozov, K. S. Novoselov, M. I. Katsnelson, F. Schedin, D. C. Elias, J. A. Jaszczak, and A. K. Geim, Giant intrinsic carrier mobilities in graphene and its bilayer, *Phys. Rev. Lett.* **100**, 016602 (2008).
- [31] S. Xiao, J. H. Chen, S. Adam, E. D. Williams, and M. S. Fuhrer, Charged impurity scattering in bilayer graphene, *Phys. Rev. B* **82**, 041406 (2010).
- [32] R. Nouchi, M. Shiraishi, and Y. Suzuki, Transfer characteristics in graphene field-effect transistors with Co contacts, *Appl. Phys. Lett.* **93**, 152104 (2008).
- [33] J. R. Hahn, H. Kang, S. Song, and I. C. Jeon, Observation of charge enhancement induced by graphite atomic vacancy: a comparative STM and AFM study, *Phys. Rev. B* **53**, 1725 (1996).
- [34] K. Takai, Y. Nishimura, and T. Enoki, Anomalous magnetotransport in nanostructured graphene, *Physica E* **42**, 680 (2010).
- [35] X. Zhang, Q. Z. Xue, and D. D. Zhu, Positive and negative linear magnetoresistance of graphite, *Phys. Lett. A* **320**, 471 (2004).
- [36] E. McCann, K. Kechedzhi, V. I. Fal'ko, H. Suzuura, T. Ando, and B. L. Altshuler, Weak-localization magnetoresistance and valley symmetry in graphene, *Phys. Rev. Lett.* **97**, 146805 (2006).
- [37] D. K. Ki, D. Jeong, J. H. Choi, H. J. Lee, and K. S. Park, Inelastic scattering in a monolayer graphene sheet: a weak-localization study, *Phys. Rev. B* **78**, 125409 (2008).
- [38] F. V. Tikhonenko, D. W. Horsell, R. V. Gorbachev, and A. K. Savchenko, Weak localization in graphene flakes, *Phys. Rev. Lett.* **100**, 056802 (2008).

- [39] J. Moser, H. Tao, S. Roche, F. Alzina, C. M. S. Torres, and A. Bachtold, Magnetotransport in disordered graphene exposed to ozone: From weak to strong localization, *Phys. Rev. B* **81**, 205445 (2010).
- [40] B. R. Matis, F. A. Bulat, A. L. Friedman, B. H. Houston, and J. W. Baldwin, Giant negative magnetoresistance and a transition from strong to weak localization in hydrogenated graphene, *Phys. Rev. B* **85**, 195437 (2012).

Chapter 5

Near-edge X-ray absorption fine structure study of the edge state on Ar⁺-irradiated graphite surface

5.1 Introduction

Although sp^2 -carbon-based family of compounds has always been in the stardom in various fields of materials science, the latest impact brought by the isolation of a single sheet of graphite, known as graphene [1–3], is of fundamental importance owing to its offering experimental stages for the elucidation on basic properties of sp^2 -carbon-based materials. Electronic behaviors in these materials originates from the unconventional electronic structure of graphene described by the massless Dirac equation in a two dimensional hexagonal bipartite lattice [4], combined with structural characteristics, such as dimensionality, disorder, presence and arrangement of guest species, and so forth. In addition, magnetic properties emerge significantly in nano-sized graphene and graphite, known as nanographene and nanographite, because of their possessions of edges. It has been theoretically predicted that a spin-polarized localized electronic state exists around zigzag-shaped edges and atomic vacancies, which are called the edge state, as a consequence of breaking symmetry between the two sublattices in the bipartite lattice of graphene [5–7]. The presence of the edge state has been experimentally validated by means of scanning tunneling microscopy (STM) and spectroscopy (STS) [8,9]. Magnetic properties in nanographite systems have been investigated utilizing electron spin resonance spectroscopy, magnetic susceptibility measurements with superconducting quantum interference device, and near-edge X-ray absorption fine structure (NEXAFS) spectroscopy [10–13]. These studies concluded that the origin of magnetic properties indeed lies in the edge state.

Until recently experimental studies focusing on the edge state had been limited in

nanographite-based systems, for example multi-layer nanoribbons and activated carbon fibers (ACFs). However, Chen *et al.* performed the observation of Kondo effect, which is the signature of localized magnetic moments interacting with conducting carriers, in single-layer graphene with atomic vacancies introduced by irradiation of noble-gas ions [14]. This study indicated the probability that the edge-state spins exist around vacancies. Several attempts of edge-enriched graphene fabrications have also been made with the aim of deriving the properties originating from the edge state as well as opening energy band gaps due to additional electronic confinements [15–20]. However, the contributions of the edge state seem to be concealed owing to not only the difficulties of the production of well-defined continuous zigzag edges but also contaminants included inevitably in samples during nanofabrication processes. The energetic advantage of armchair-shaped edges, of which the symmetric arrangement of the sublattices lead to the absence of the edge state [5,6], are also likely to play a significant role in disturbing the observations of the edge state. Because of these difficulties in experimental examination of graphene edges by means of nano-fabrications, the introduction of atomic vacancies is thought of as one of the most plausible methods. However, further experimental verifications are requisite for determination of the origin of localized spins as the edge-state spins around atomic vacancies.

Structural defects of graphite surfaces that are caused by bombardments of various ions with various energies have been investigated utilizing STM techniques [21–28]. It has been widely accepted that carbon vacancy defects and interstitial defects are created on the surface with their diameters ranging within a few nanometers. The interstitial defects are caused by trapping incident ions beneath the surface plane, which can be removed by heating up to approximately 900 K [26]. Focusing particular attention on the low-energy irradiations, it is possible to set limits to not only the vacancy diameters within a few sub-nanometers corresponding to single or at most few atomic scales but also to the depth of vacancy creation predominantly in the outermost layer. Thus, atomic vacancies with sublattice asymmetries in bipartite lattice are thought of as the origin of the edge state.

Although structural modifications by ion irradiations have been revealed in STM studies, STM information is limited in a quite local part of a sample and spectroscopic information is necessary to confirm the presence of the edge state with macroscopic

distribution. X-ray photoemission spectroscopy (XPS) has been utilized for ion-irradiated graphites. Several XPS studies have revealed that the C1s XPS spectra show asymmetric broadening by ion bombardments owing to the contribution of the defect-induced localized electronic states together with shake-up processes, oxidations, and so on [29–32], which make the derivation of edge state contribution rather complicated. Among electron spectroscopic techniques, NEXAFS spectroscopy, which probes the absorption of X-ray by transition of core electrons into unoccupied states, has been applied to a number of materials and has provided information of electronic structures of unoccupied states, molecular alignments at surfaces or thin films, and so on [33]. NEXAFS of graphite has been widely studied [34,35] and that of Ar⁺-irradiated graphite has also appeared partly in several studies on amorphous carbon films as reference spectra, without referring to the edge state [36,37]. Its advantage for observation of the edge state has been recently revealed using nanographite samples that have large contribution of the edge state by nature owing to a large ratio of edge carbon atoms to interior atoms [11,12]. Thus, the author hypothesized that the assignment of the edge state peak can be further confirmed when the edge state peak is observed upon creation of edges on the surface of graphite. Moreover, it is expected to unambiguously reveal that the edge state obviously emerge around atomic vacancies introduced by noble-gas irradiation.

In the present study, the author has employed the NEXAFS technique for the surface of highly-oriented pyrolytic graphite (HOPG) coupled with the introduction of structural defects by Ar⁺ irradiations with various acceleration energies, particularly focusing attention on the development of the lower-energy π^* shoulder, at which the edge state reportedly emerged [11,12]. The appearance of the edge state peak has been verified after 100-eV Ar⁺ irradiations, and the edge-state peak survived together with the broadened π^* peak due to amorphization on the surface irradiated with high-energy Ar⁺.

5.2 Experimental

Commercially available HOPG was employed in this study. An HOPG sample was fixed on a tantalum substrate and loaded into the chamber maintained in high vacuum (1.0×10^{-6} Pa). The Ta substrate was heated by electric current up to approximately 900 K for the removal of unintentional adsorbates from the sample surface. In order to introduce

defects to the sample, Ar⁺ ions were irradiated at the pressure of 1.0×10^{-4} Pa for 5 minutes with various acceleration voltages ranging from 100 V to 3 kV along the normal to the sample surface. An Ar⁺ irradiation was followed by heating the sample up to 900 K both to eliminate interstitial ions [26] and to avoid unintentional introduction of surface impurities. After a sequence of an Ar⁺ irradiation and following NEXAFS measurements, next sequence with a higher energy irradiation was performed. Carbon K-edge NEXAFS was measured at the soft X-ray beamline BL-7A in Photon Factory in Institute of Materials Structure Science, Tsukuba, Japan [38]. NEXAFS spectra were obtained by the partial electron yield (PEY) mode with an imaging-type microchannel plate detector [39], which mainly collected the C *KLL* Auger electrons. The total electron yield (TEY) mode was also employed for measurements, which counted sample photocurrent. PEY allows us to collect information on the uppermost surface, while the information from the surface to the interior of the sample can be obtained in TEY. Prior to the measurements, the photon energy was calibrated by setting the location of the C 1s to the π^* peak at 285.5 eV [11,12]. The angle of the X-ray incidence was fixed to 0° (*i.e.*, the normal to the surface plane) and 35° (*i.e.*, a magic angle $\sim 55^\circ$ with respect to the surface). The angular dependent terms in the probabilities of electronic transitions to various final states vanishes with the magic angle [33], resulting in a direct information of the electronic structure. The background of NEXAFS spectra were subtracted as a line. NEXAFS spectra were normalized by the edge jump at 370 eV.

5.3 Results

The C K-edge NEXAFS spectra were measured by the PEY and the TEY detection modes before and after the 5-minute Ar⁺ irradiations with kinetic energies from 100 eV to 3 keV. Figures 5.1 and 5.2 show the PEY spectra obtained with the angle of the X-ray incidence set to 35° and 0°, respectively. Figures 5.3 and 5.4 show the TEY spectra obtained with the incidence angle of 35° and 0°, respectively. In the pristine HOPG sample, of which spectra are denoted as black curves in Figs. 5.1, 5.2, 5.3, and 5.4, the excitation peak of the C 1s core-state electrons to the π^* unoccupied state appeared obviously at 285.5 eV with the grazing incidence (Figs. 5.1 and 5.3), whereas it was unnoticeable in the spectra with the normal incidence (Figs. 5.2 and 5.4). Another major

feature located in the energy range from 291 eV to 294 eV regardless of the angle of the incidence, which consisted of two distinct ingredients. The sharp feature at 291.8 eV was assigned to the σ^* core exciton [40,41], whereas the broad feature centered at 292.8 eV originated from the transition to the σ^* state [42]. In the PEY spectra but not in the TEY ones, there was an additional feature around 288 eV regardless of the angle of the incidence as shown in Figs. 5.1 and 5.2.

Changes in the NEXAFS spectra by the Ar⁺ irradiations were clearly observed. First of all, it should be noted that the intensity of the π^* peak reduced gradually with the increase of Ar⁺ kinetic energy in the spectra with the grazing incidence (Figs. 5.1 and 5.3). It reached the minimum at the 1-keV irradiation and remained unchanged after this irradiation. The 100-eV irradiated spectra (red curves in Figs. 5.1, 5.2, 5.3, and 5.4) had unexpectedly higher intensity of the π^* peak than the pristine spectra, which was caused by residual contaminants on the surface of the pristine sample. In contrast to the spectra with the grazing incidence, a little increase of the π^* region was observed with the normal incidence above the 1-keV irradiation (Figs. 5.2 and 5.4). The gradual decrease of the σ^* intensity was observed together with the disappearance of the splitting of the peaks. Spectral difference between the PEY and the TEY detections was found in the σ^* features. After the 500-eV irradiation (green curves in Figs. 5.1, 5.2, 5.3, and 5.4), the σ^* excitonic peak that appeared around 291.8 eV with a narrow width could not be resolved in the PEY spectrum (Figs. 5.1 and 5.2), whereas it still remained in the TEY ones until the 1-keV irradiation (Figs. 5.3 and 5.4). In addition, it was noticeable that the spectral feature around 288 eV, which was observed in the pristine HOPG sample with the PEY mode, disappeared immediately after 100-eV Ar⁺ irradiations (compare black and red curves in Figs. 5.1 and 5.2). Although the intensities of both the π^* and the σ^* peaks decreased in the spectra obtained with the grazing incidence as the Ar⁺ kinetic energy was increased, there were growing ingredients in the regions just below and above the π^* peak, and below the σ^* peak. The assignments of these features will be written later. Finally, the top of the π^* peak shifted gradually to the higher-energy side upon the increase of the Ar⁺ kinetic energy.

Figures 5.5 and 5.6 show Gaussian fits for the π^* region in the C K-edge NEXAFS spectra measured by the PEY and the TEY detections, respectively. The spectra of the pristine and the 100-eV irradiated samples were fitted with a single narrow Gaussian

curve, whereas the use of double Gaussians showed nice fits to the spectra for the 300-eV and higher-energy Ar⁺-irradiated samples. The light-gray ingredient was the main π^* transition. Its lower-energy shoulder with the position of 284.5 eV denoted as the dark-gray ingredient was assigned to the edge state of π -electron origin, which was definitely caused by structural defects introduced by the Ar⁺ bombardments [11,12]. The π^* ingredient appeared obviously to be broadened gradually upon increasing the Ar⁺ kinetic energy, along with the blue shift of the central energy of the π^* peak.

Figure 5.7a shows the variation of the integrated intensities of the π^* peak (I_{π^*}) and the edge state peak (I_{edge}) upon the Ar⁺ irradiations. I_{π^*} reduced with the increase of the Ar⁺ kinetic energy, whereas I_{edge} grew. The π^* peak reached its minimum intensity after the 1-keV irradiation in both the PEY and the TEY detections. In contrast, I_{edge} continued to increase gradually up to the 3-keV irradiation. Figure 5.7b shows the variation of the proportion of I_{edge} to I_{π^*} . Up to 500 eV, I_{edge} increased faster in the PEY spectra than the TEY spectra, whereas the difference between the PEY and the TEY detections decreased upon higher-energy Ar⁺ irradiations. Figure 5.8a represents the changes in the central energies of the π^* and the edge state peaks. The position of the π^* peak shifted from 285.5 eV to 286.0 eV when the kinetic energy of Ar⁺ ions increased up to 3 keV, so that the amount of the blue shift reached as much as 0.5 eV approximately. It should be noted that the position of the edge state ingredient little changed from its initial value of 284.5 eV. Figure 5.8b represents the evolutions of the widths of the π^* and the edge state peaks. The width of the π^* ingredient was 1.0 eV in the pristine HOPG sample. It increased strikingly with increasing Ar⁺ kinetic energy and nearly reached the maximum of 2.0 eV after the 1-keV irradiation. In contrast to the main π^* peak, the width of the edge state peak showed only a slight decrease.

Figure 5.9a shows the close-up of the π^* region in the C K-edge NEXAFS spectra measured by the PEY detection with the grazing incidence after continual 100-eV Ar⁺ irradiations for 60 minutes and 90 minutes in total. The PEY spectrum obtained after 60-minute dose was fitted with double Gaussians including the edge state ingredient. The ratio of I_{edge} to I_{π^*} was approximately equal to 0.06, which remained nearly unchanged after an additional 30-minute dose. On the other hand, a single Gaussian was sufficient to fit the TEY spectrum after 60-minute dose as shown in Fig. 5.9b. Even after an additional 30-minute dose, the edge state ingredient was not found by the TEY detections.

5.4 Discussion

The author observed an evolution in the C K-edge NEXAFS spectra in relation to the formation of structural defects for the HOPG samples upon Ar⁺ irradiation with various kinetic energies ranging from 100 eV to 3 keV. The reduction in I_{π^*} clearly reflects the destruction of the π network by Ar⁺ irradiation (Fig. 5.7a). 100-eV Ar⁺ irradiation reportedly produces atomic vacancies predominantly at the outermost layer of the sample [26–28]. Thus, the fully sp^2 -hybridized configuration of carbon atoms in the layers of the HOPG sample is retained upon low energy Ar⁺ irradiation, and the edge state ingredient is created as lower-energy shoulder of the π^* peak, which was previously assigned to the edge state [11,12]. The present results at 100-eV irradiation unambiguously confirms these features. In contrast, structural defects created by higher-energy irradiations have larger sizes and extend to deeper layers. The surface structure of the sample is largely destroyed, resulting in amorphous-like structures in which carbon atoms have a random coordination. This occurrence of structural randomness is supported by the rise of the π^* region in the spectra measured at normal incidence. Given that the π^* peak does not appear at normal X-ray incidence owing to the strong dependence of the X-ray polarization direction [34,35], the increase of the π^* intensity with normal incidence indicates that the parallel arrangement of graphene layers in graphite is broken by Ar⁺ bombardment. Accordingly, the surface of graphite irradiated by high energy Ar⁺ is regarded as amorphous-like carbon.

Here, the structural changes into the amorphous-like state is discussed in terms of the variation in the π^* and the σ^* peaks. Usually, amorphous carbon consists of sp^3 -, sp^2 -, and rare sp^1 -hybridized configurations of carbon atoms. The sp^3 configuration does not have a π^* transition in C K-edge NEXAFS spectra. However, when sp^3 -hybridized carbons become involved in fully sp^2 -hybridized graphite, structural distortions lead to a mixing of π and σ states, resulting in transitions to various π^* states [43,44]. This mixing was observed as a broadening of the π^* peak above the 500-eV irradiation, as shown in Fig. 5.8b. At this irradiation energy, the author observed that the splitting of the σ^* excitonic peak and the main σ^* peak disappeared in the PEY spectra, resulting in the broadened featureless shapes. This spectral change is again explained by the mixing of π and σ states, which causes multiple step edges of the σ^* transitions. The featureless shapes in the region of the σ^* transitions have been generally observed in amorphous carbon

[36,37,43,45,46]. Thus, after the 500-eV irradiation, the sample surface begins to form amorphous-like carbon, giving rise to a remarkable increase in the π^* width (Fig. 5.8b) and the disappearance of the characteristic σ^* features. Moreover, the sample surface is strongly damaged by 1-keV Ar⁺ irradiation because the width of the π^* peak nearly doubles upon 1-keV irradiation and nearly constant with further higher-energy irradiation. In addition to the broadening of the π^* peak, a blue shift of the central energy of the π^* peak was observed along with increasing Ar⁺ kinetic energy. This blue shift is quite surprising because the π^* position of HOPG is usually fixed and employed for the calibration of the incident photon energy. This blue shift can be addressed in relation to the deficit of the screening of core holes. On increasing the proportion of the sp^3 -hybridized carbon atoms, the concentration of the π electrons that participate in the screening of core holes reduces, resulting in a blue shift of the π^* peak [47].

Here, the problem of how the edge carbon atoms are terminated in created defects is referred to. When a carbon atom is eliminated from a layer of graphene, σ -dangling bonds are created, which are so reactive that they are expected to be immediately terminated by functional groups. This high reactivity is the reason why another Gaussian curve was not used to fit the σ -dangling bond peak, which was reportedly observed at 284.9 eV [12]. Under the present experimental conditions, hydrogen and oxygen are considered to be plausible species that terminate dangling bonds. According to former studies, various transitions related to the states of functional groups [48–53] can occur in addition to the interlayer state [42,54,55] in the intermediate between the π^* and the σ^* regions. In the present study, the PEY spectra of the pristine sample had a broad feature around 288 eV, nearly regardless of the angle of X-ray incidence, whereas the TEY spectra did not have such a feature, as shown in Figs. 5.1, 5.2, 5.3, and 5.4. Furthermore, this feature disappeared immediately after 100-eV Ar⁺ irradiation, and never reappeared. This observations suggest that the contribution of the interlayer state should be excluded. Indeed, Hua *et al.* theoretically reported that the spectral features between the π^* and the σ^* peaks are likely to be smeared out and should not appear in an ideal graphene sheet [56]. Due to the low reactivity of the graphite surface and the disappearance of the peak at 288 eV by 100-eV irradiation, residual contaminants containing hydrogen and oxygen-containing functional groups unintentionally resting on the surface should be responsible for this peak at 288 eV. The broadening of the π^* peak, in which the peak tail on the high-

energy side is extended to 286–287 eV, can originate from the functional groups. Actually, the $\sigma^*_{\text{C-H}}$ transition occurs in the approximate range of 286–288 eV [48–50], and the $\sigma^*_{\text{C=O}}$ and the $\sigma^*_{\text{C-O}}$ transitions are located over 287–291 eV [51–53]. Accordingly, the author has concluded that the amount of oxygen-containing functional groups is below the limit of the detection in the present experiments, and that the σ -dangling bonds are mainly terminated by hydrogen atoms.

Next, the edge state should be discussed. It was previously reported that the edge state of nanographite samples appears at 284.5 eV as a lower energy shoulder of the π^* peak in the C K-edge NEXAFS measurements [11,12]. In the present study, HOPG samples, which did not initially have a π^* shoulder, were employed and the rise of the lower-energy shoulder was clearly observed upon edge production on the surface of the sample by Ar⁺ irradiation. Thus, the assignment to the edge state is definitely verified. This assignment is particularly supported by the detection of the edge state only in PEY mode after 100-eV Ar⁺ irradiation, as shown in Fig. 5.9a in contrast to the TEY spectra in Fig. 5.9b. This is because each 100-eV Ar⁺ impact can eliminate at most a few carbon atoms predominantly from the outermost layer with the inside of the sample kept clean [26–28], and because the PEY mode is sensitive to C *KLL* Auger electrons having kinetic energies in the approximate range of 250–270 eV [57]. The mean free path of Auger electrons is about 0.8 nm in this energy range, corresponding to only 2–3 layers of HOPG.

The concentration of vacancies produced by Ar⁺ irradiation can be estimated. The number of 100-eV Ar⁺ impacts per unit area per unit time (Γ) is described by the ion current (I) and the spot size of the Ar⁺ beam (A) as $\Gamma = I / Ae$, where e is the elementary electrical charge. I and A were typically 10 nA and 20 mm², respectively, under the present experimental setup. Thus, $\Gamma = 3 \times 10^{15} \text{ m}^{-2} \text{ s}^{-1}$ is obtained. Additive effects of the ion current, for example secondary electron emission and secondary ionization of surrounding neutral Ar atoms by energetic Ar⁺ ions, are not taken into account. The 5- and 60-minute doses give 9.0×10^{17} , and 1.1×10^{19} impacts per unit area, respectively. The density of carbon atoms in a single layer of graphite is approximately $3.8 \times 10^{19} \text{ m}^{-2}$ (2 atoms in a unit cell of $0.246 \times \sqrt{3} / 2 \text{ nm}^2$). Under the assumption that the number of removed carbon atoms is approximately half of Ar⁺ impacts [27], the ratios of the removed carbon atoms to the total carbon atoms within the beam spot are 1% and 14% for 5- and 60-minute doses, respectively. For a 5-minute dose, the number of atomic

vacancies is so small that the edge state peak is likely to be below the limit of the detection in the present experimental setup. In contrast, nearly one carbon atom per a 6-membered ring is removed by a 60-minute dose. Accordingly, continuous edges as well as atomic vacancies, in which the sublattice symmetry [5,6] is broken with missing carbon atoms and/or carbon atoms not participating in the π -conjugations, are considered to be created on the surface of the sample in a concentration large enough to be observed, both of which result in the rise of the edge state contribution.

On approaching the amorphous-like carbon state with increasing Ar⁺ kinetic energy, $I_{\text{edge}}/I_{\pi^*}$ continues to be enhanced, whereas the width and the central energy of the edge state peak remained nearly unchanged as shown in Fig. 5.8. $I_{\text{edge}}/I_{\pi^*}$ has a direct correlation with the ratio of the edge carbon atoms to interior atoms, so that its increase is understood by the increase in the concentration of edges, in which the sublattice symmetry is broken by the introduction of defects. It should be addressed in terms of core-hole screening that the position of the edge state is as much as 1 eV below the π^* peak of the pristine HOPG (284.5 eV – 285.5 eV = –1 eV), and that the position and the width of the edge state peak remain unchanged upon Ar⁺ irradiation. Because the edge state belonging to the π -conjugation system has a large local density of states, the screening of a core hole is highly effective [47]. As a result, the edge state peak only slightly shifts upon amorphization in contrast to the π^* peak. In addition, it was indicated that the energy of the edge state peak with respect to the Fermi energy can slightly change owing to the charge transfer between the edge state and oxygen-containing functional groups [11]. Because during the present experiments, the proportion of oxygen-containing groups has appeared to be small, the energy distribution of the edge states with respect to the Fermi level has no charge transfer effect with oxygen-containing groups. What is interesting here is that the edge state contribution survives in damaged graphite, in which the intense Ar⁺ irradiation resulted in amorphization. This observation demonstrates that the edges of a degraded π -electron systems can be considered to possess the edge state.

5.5 Conclusions

The author has examined the evolution in the C K-edge NEXAFS spectra for HOPG samples irradiated by Ar⁺ ions with various kinetic energies ranging from 100 eV to 3 keV. The destruction of the π network of the HOPG sample upon Ar⁺ irradiation appears as a reduction in the intensity of the π^* peak. The significant broadening and the blue shift of the π^* peak upon high energy Ar⁺ irradiation can be explained in terms of the involvement of the sp^3 -hybridized configuration of carbon atoms, because this is what causes various π^* transitions due to the mixing of π and σ states along with a change in the σ^* transition region into broadened featureless shape. The sp^3 -hybridized configuration also reduces the concentration of π electrons that screen core holes. These variations show that the surface of the sample attains an amorphous-like structure in which there is randomness in the coordination number of carbon atoms. The occurrence of amorphization of the surface is also supported by the appearance of the π^* peak in the spectra obtained at normal incidence. Given that the spectral features related to the oxygen-containing functional groups were under the limit of the detection for the entire experiments, the author has concluded that the edge carbon atoms are mainly terminated by hydrogen atoms. Thus, the author has verified that the lower energy shoulder of the π^* peak is unambiguously assigned to the edge state peak that originates from defects distributed on the outermost layer. The observations that the central energy of the edge state peak is 1 eV below the π^* peak and the central energy and the width of the edge state peak does not change upon Ar⁺ irradiations can be understood in relation to the effective core-hole screening and the absence of charge transfer effects. The present study also demonstrates that edges in severely damaged graphite by Ar⁺ irradiation are able to support the edge state.

Acknowledgment to Elsevier

Part of the study written in this chapter has been accepted for publishing in *Carbon* (Elsevier), as Y. Kudo, M. Kiguchi, J. Takashiro, K. Takai, and T. Enoki, Development of edge state on graphite surface induced by Ar⁺ irradiation studied using near-edge X-ray absorption fine structure spectroscopy, *Carbon, in press* (<http://dx.doi.org/10.1016/j.carbon.2014.01.067>), Copyright 2014, Elsevier. The author of this thesis sincerely acknowledge the favor of Elsevier that accepts the inclusion of this article in this thesis.

5.6 Figures in Chapter 5

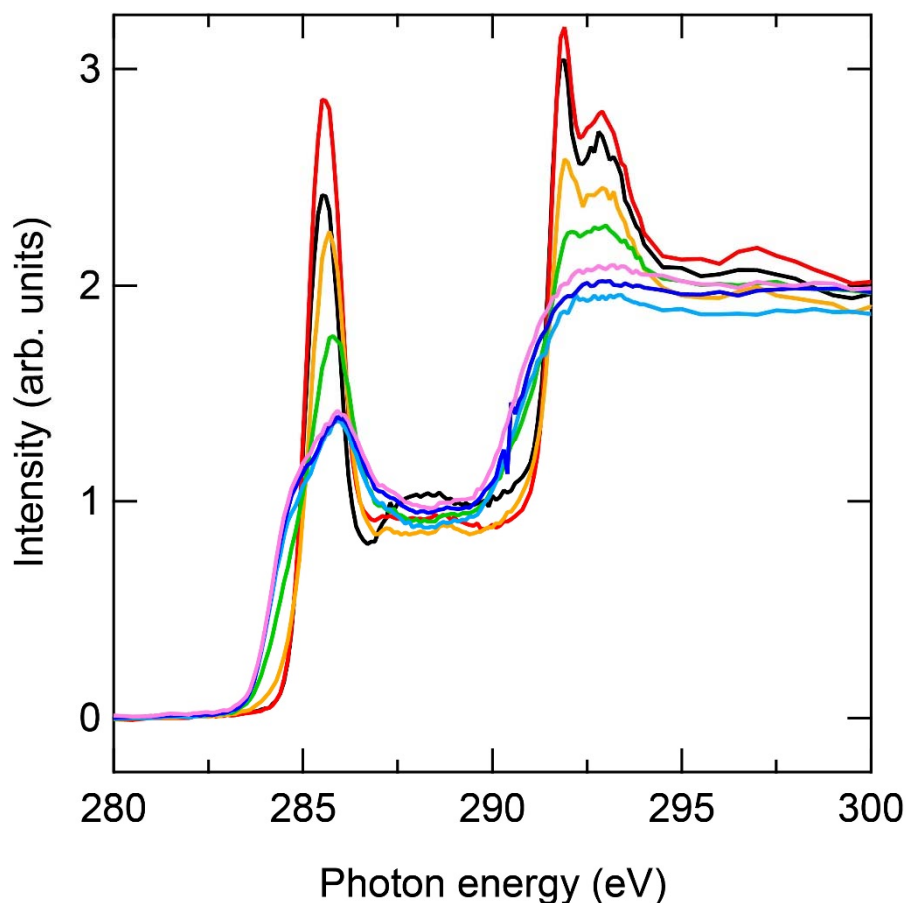


Figure 5.1. The C K-edge NEXAFS spectra measured by the PEY detection with the grazing incidence of X-ray. The black curve denotes the spectrum obtained from the pristine HOPG sample. The red, the orange, the green, the light-blue, the blue, and the pink curves denote the spectra obtained from the sample after Ar⁺ irradiations with kinetic energies of 100 eV, 300 eV, 500 eV, 1 keV, 1.5 keV, and 3 keV, respectively.

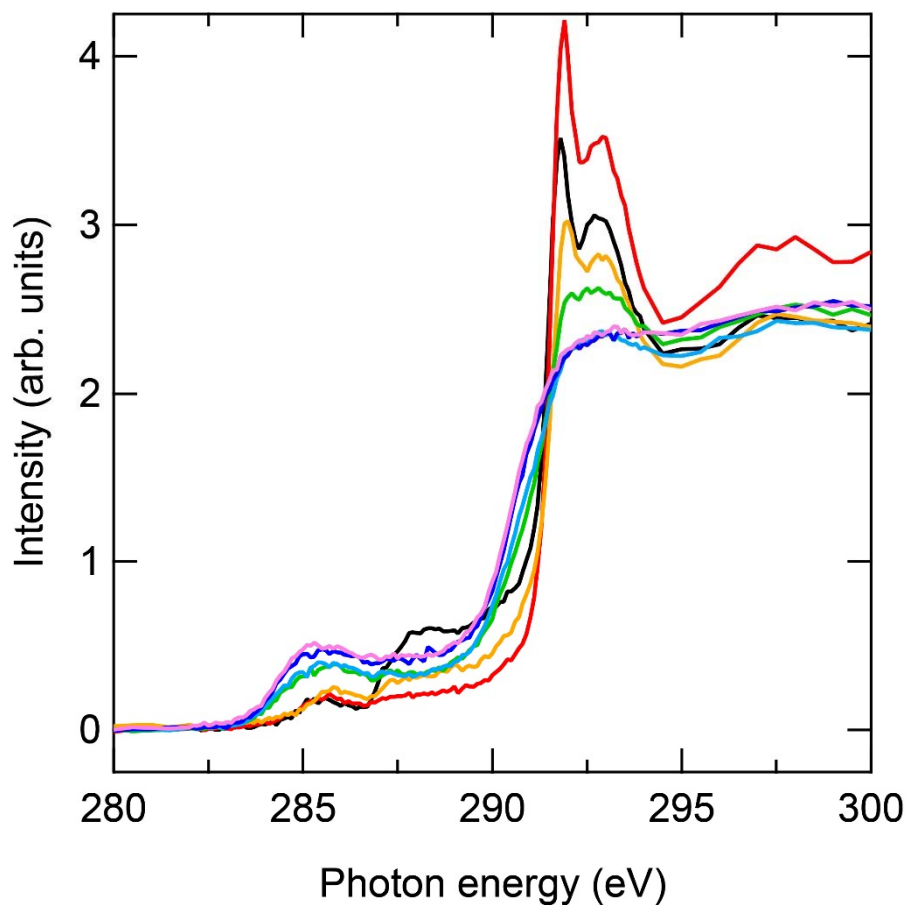


Figure 5.2. The C K-edge NEXAFS spectra measured by the PEY detection with the normal incidence of X-ray. The black curve denotes the spectrum obtained from the pristine HOPG sample. The red, the orange, the green, the light-blue, the blue, and the pink curves denote the spectra obtained from the sample after Ar⁺ irradiations with kinetic energies of 100 eV, 300 eV, 500 eV, 1 keV, 1.5 keV, and 3 keV, respectively.

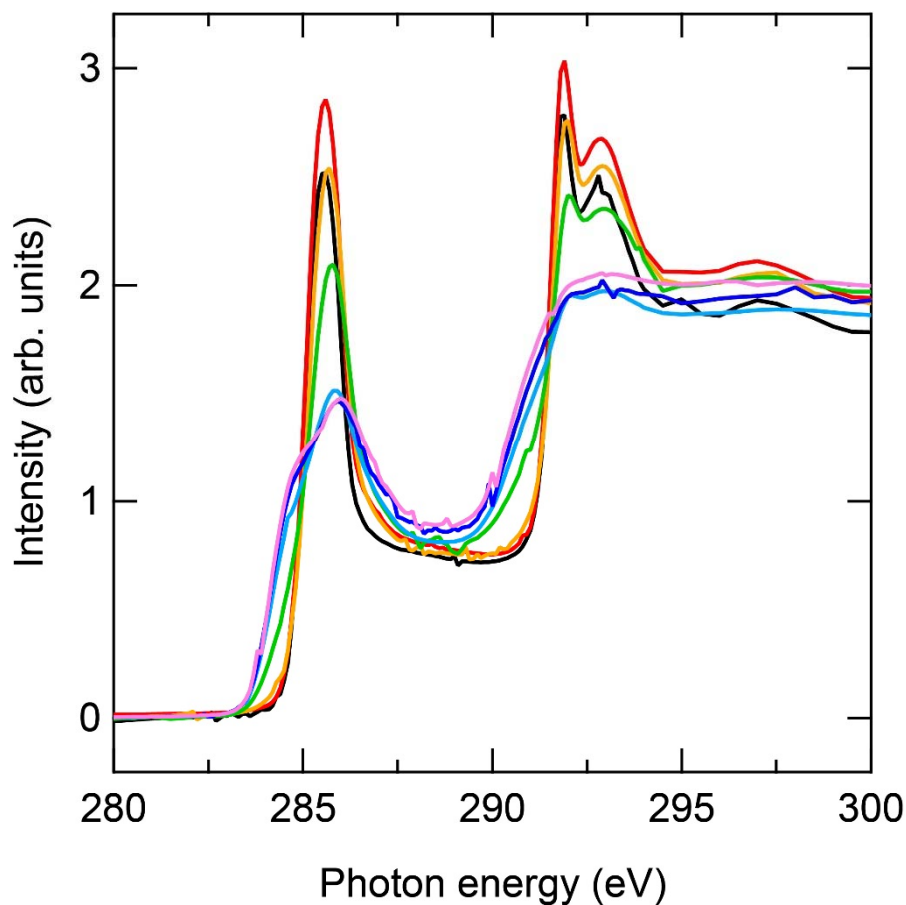


Figure 5.3. The C K-edge NEXAFS spectra measured by the TEY detection with the grazing incidence of X-ray. The black curve denotes the spectrum obtained from the pristine HOPG sample. The red, the orange, the green, the light-blue, the blue, and the pink curves denote the spectra obtained from the sample after Ar^+ irradiations with kinetic energies of 100 eV, 300 eV, 500 eV, 1 keV, 1.5 keV, and 3 keV, respectively.

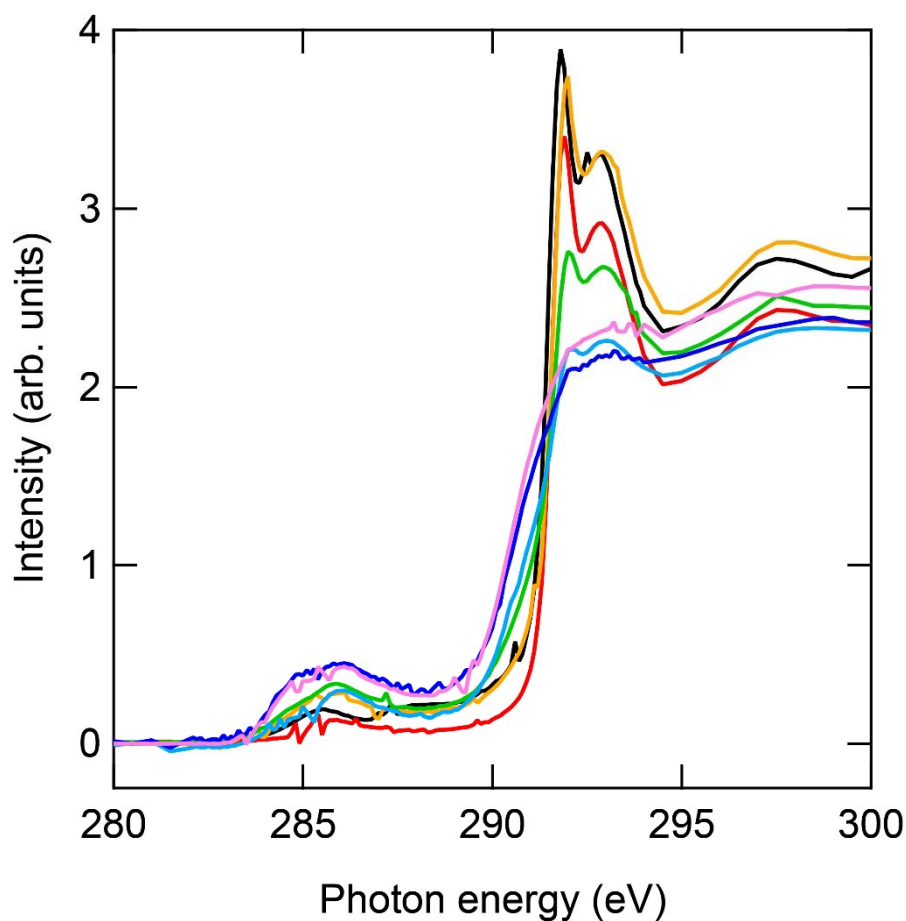


Figure 5.4. The C K-edge NEXAFS spectra measured by the TEY detection with the normal incidence of X-ray. The black curve denotes the spectrum obtained from the pristine HOPG sample. The red, the orange, the green, the light-blue, the blue, and the pink curves denote the spectra obtained from the sample after Ar⁺ irradiations with kinetic energies of 100 eV, 300 eV, 500 eV, 1 keV, 1.5 keV, and 3 keV, respectively.

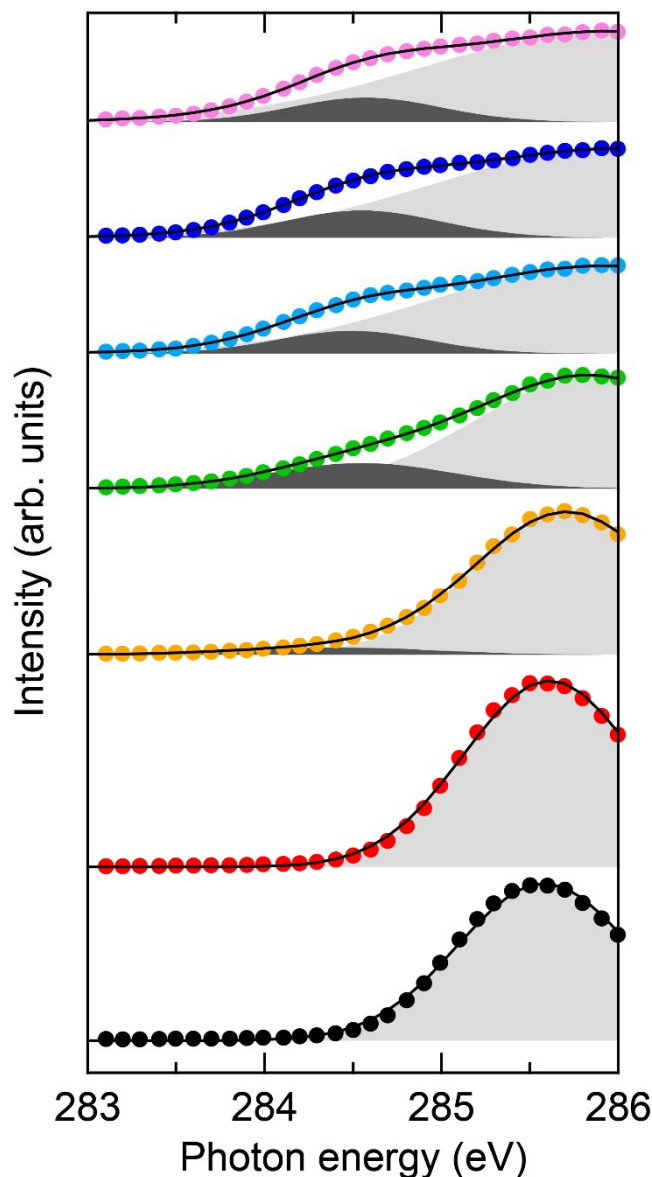


Figure 5.5. The close-up of the π^* region in the C K-edge NEXAFS spectra measured by the PEY detection with the grazing incidence of X-ray. The black, the red, the orange, the green, the light-blue, the blue, and the pink circles denote the experimentally obtained data for the pristine HOPG sample, and for 100-eV, 300-eV, 500-eV, 1-keV, 1.5-keV, and 3-keV Ar⁺-irradiated sample, respectively. The Gaussian fits are denoted as the light-gray and the dark-gray regions. The black curves represent the totals of the Gaussian fits.

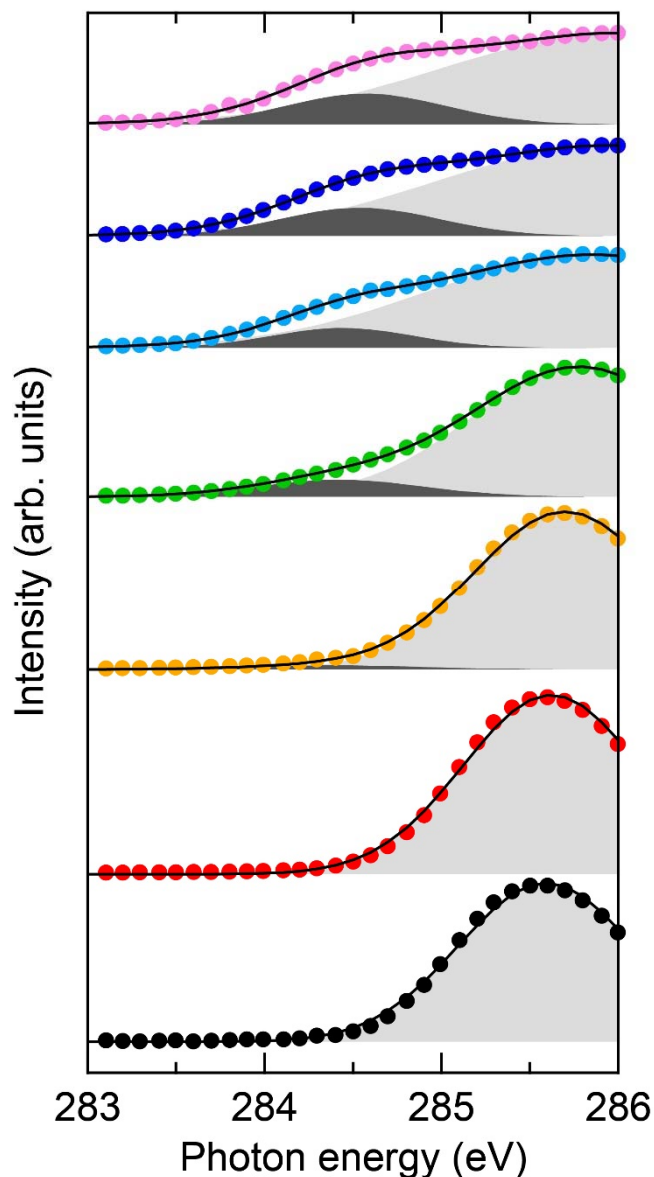


Figure 5.6. The close-up of the π^* region in the C K-edge NEXAFS spectra measured by the TEY detection with the grazing incidence of X-ray. The black, the red, the orange, the green, the light-blue, the blue, and the pink circles denote the experimentally obtained data for the pristine HOPG sample, and for 100-eV, 300-eV, 500-eV, 1-keV, 1.5-keV, and 3-keV Ar⁺-irradiated sample, respectively. The Gaussian fits are denoted as the light-gray and the dark-gray regions. The black curves represent the totals of the Gaussian fits.

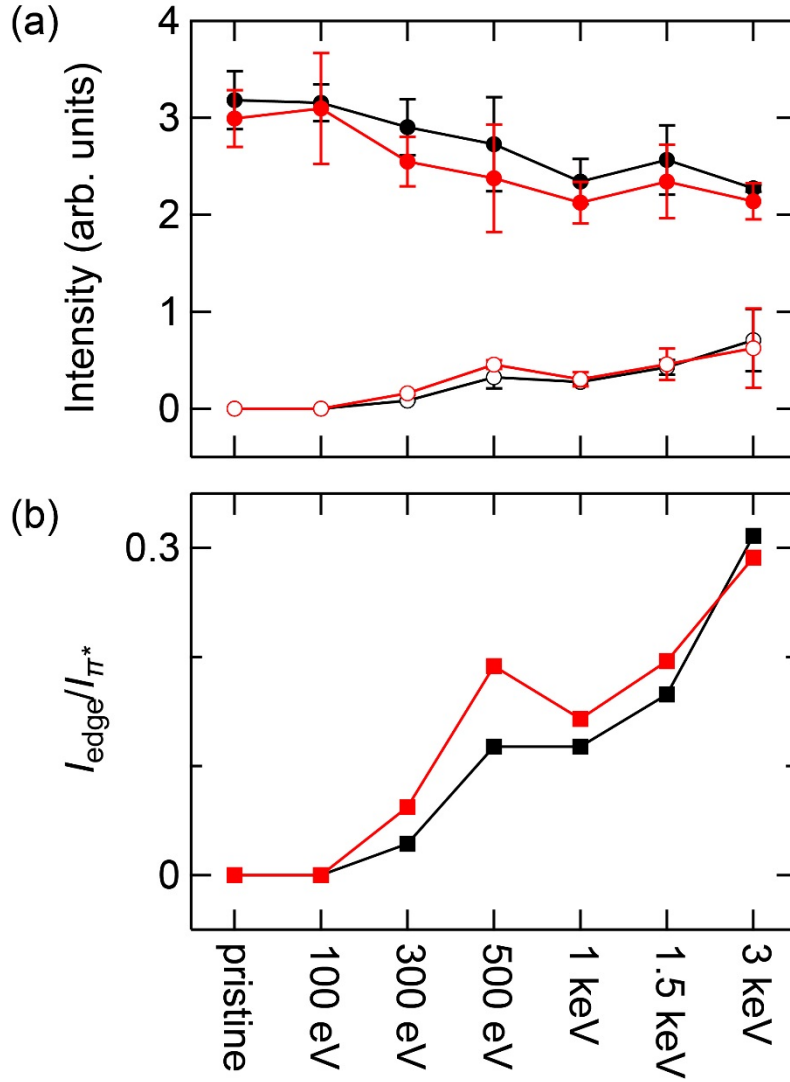


Figure 5.7. Variations of (a) the integrated intensities of the π^* peak and the edge state peak denoted by the filled and the empty circles, respectively, and (b) the ratio of the edge state to the π^* state denoted by the filled squares, upon Ar⁺ irradiations with various kinetic energies. The red and the black symbols correspond to the data measured with the PEY and the TEY detections, respectively.

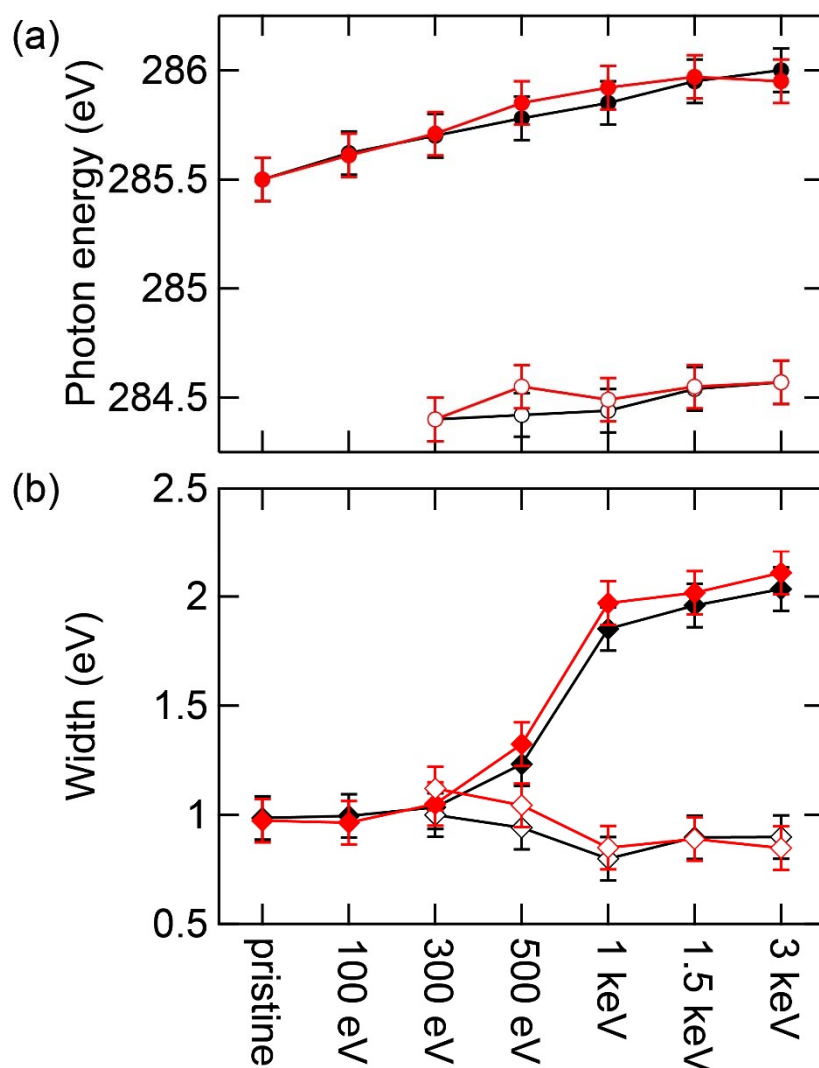


Figure 5.8. Variations of (a) the centers of the π^* and the edge state peaks denoted by the filled and the empty circles, respectively, and (b) the widths of the π^* and the edge state peaks denoted by the filled and the empty diamonds, respectively, upon Ar⁺ irradiations with various kinetic energies. The red and the black symbols correspond to the data measured with the PEY and the TEY detections, respectively. Experimental uncertainty of 0.1 eV for the peak positions and widths is included as error bars.

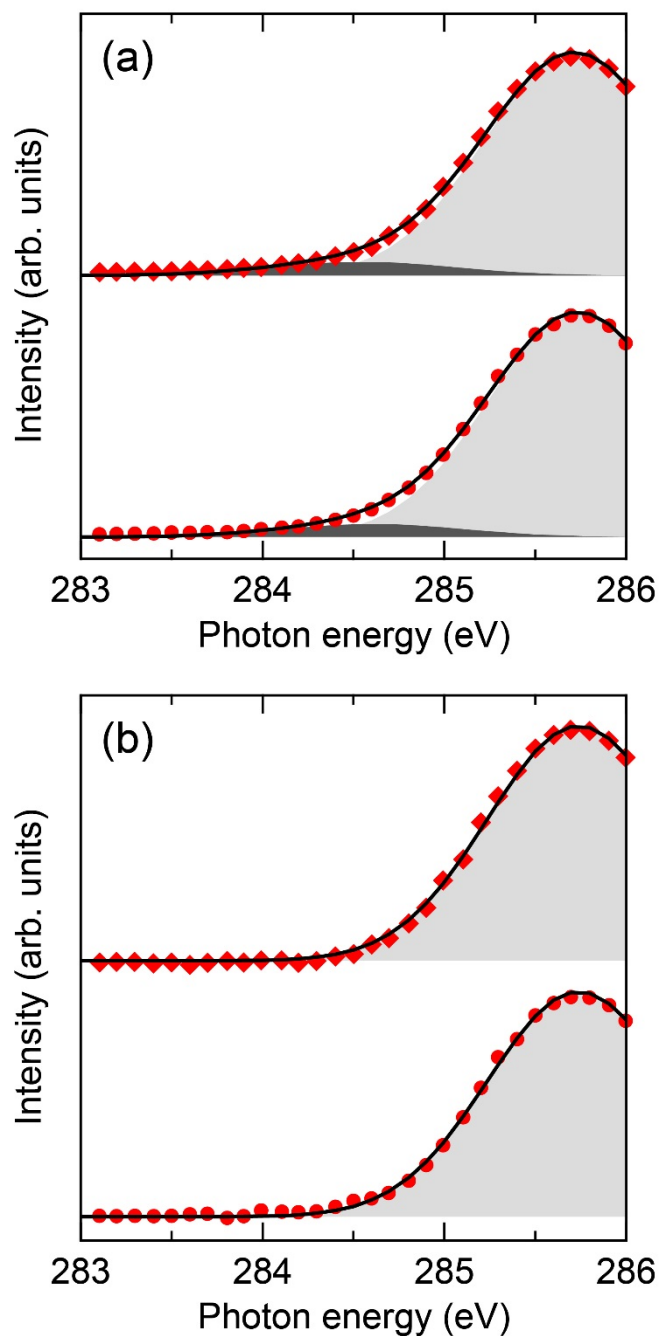


Figure 5.9. The close-up of the π^* region in the C K-edge NEXAFS spectra measured by (a) the PEY and (b) the TEY detections with the grazing incidence after continual 100-eV Ar⁺ irradiations for 60 minutes and 90 minutes, which are denoted as the red circles and the red diamonds, respectively. The Gaussian fits are denoted as the light-gray and the dark-gray regions. The totals of the Gaussian fits are represented by the black curves.

References in Chapter 5

- [1] K. S. Novoselov, A. K. Geim, S. V. Morozov, D. Jiang, Y. Zhang, S. V. Dubonos, I. V. Grigorieva, and A. A. Firsov, Electric field effect in atomically thin carbon films, *Science* **306**, 666 (2004).
- [2] K. S. Novoselov, A. K. Geim, S. V. Morozov, D. Jiang, M. I. Katsnelson, I. V. Grigorieva, S. V. Dubonos, and A. A. Firsov, Two-dimensional gas of massless Dirac fermions in graphene, *Nature* **438**, 197 (2005).
- [3] Y. Zhang, Y. W. Tan, H. L. Stormer, and P. Kim, Experimental observation of the quantum Hall effect and Berry's phase in graphene, *Nature* **438**, 201 (2005).
- [4] P. R. Wallace, The band theory of graphite, *Phys. Rev.* **71**, 622 (1947).
- [5] M. Fujita, K. Wakabayashi, K. Nakada, and K. Kusakabe, Peculiar localized state at zigzag graphite edge, *J. Phys. Soc. Jpn.* **65**, 1920 (1996).
- [6] T. Enoki and T. Ando, Physics and chemistry of graphene: graphene to nanographene, *Pan Stanford Publishing*, (Singapore, 2013).
- [7] O. V. Yazyev and L. Helm, Defect-induced magnetism in graphene, *Phys. Rev. B* **75**, 125408 (2007).
- [8] Y. Kobayashi, K. Fukui, T. Enoki, K. Kusakabe, and Y. Kaburagi, Observation of zigzag and armchair edges of graphite using scanning tunneling microscopy and spectroscopy, *Phys. Rev. B* **71**, 193406 (2005).
- [9] Y. Niimi, T. Matsui, H. Kambara, K. Tagami, M. Tsukada, and H. Fukuyama, Scanning tunneling microscopy and spectroscopy studies of graphite edges, *Appl. Surf. Sci.* **241**, 43 (2005).
- [10] T. Enoki and K. Takai, The edge state of nanographene and the magnetism of the edge-state spins, *Solid State Commun.* **149**, 1144 (2009).
- [11] V. L. J. Joly, M. Kiguchi, S. J. Hao, K. Takai, T. Enoki, R. Sumii, K. Amemiya, H. Muramatsu, T. Hayashi, Y. A. Kim, M. Endo, J. C. Delgado, F. L. Urías, A. B. Méndez, H. Terrones, M. Terrones, and M. S. Dresselhaus, Observation of magnetic edge state in graphene nanoribbons, *Phys. Rev. B* **81**, 245428 (2010).
- [12] M. Kiguchi, K. Takai, V. L. J. Joly, T. Enoki, R. Sumii, and K. Amemiya, Magnetic edge state and dangling bond state of nanographene in activated carbon fibers, *Phys. Rev. B* **84**, 045421 (2011).
- [13] S. J. Hao, K. Takai, V. L. J. Joly, and T. Enoki, Magnetism of HNO₃-adsorbed

- nanoporous network of nanographene sheets, *J. Phys. Chem. Solids* **73**, 1432 (2012).
- [14] J. H. Chen, L. Li, W. G. Cullen, E. D. Williams, and M. S. Fuhrer, Tunable Kondo effect in graphene with defects, *Nat. Phys.* **7**, 535 (2011).
- [15] M. Y. Han, B. Özyilmaz, Y. Zhang, and P. Kim, Energy band-gap engineering of graphene nanoribbons, *Phys. Rev. Lett.* **98**, 206805 (2007).
- [16] T. Shen, Y. Q. Wu, M. A. Capano, L. P. Rokhinson, L. W. Engel, and P. D. Ye, Magnetoconductance oscillations in graphene antidot arrays, *Appl. Phys. Lett.* **93**, 122102 (2008).
- [17] J. Eroms and D. Weiss, Weak localization and transport gap in graphene antidot lattices, *New J. Phys.* **11**, 095021 (2009).
- [18] J. Bai, X. Zhong, S. Jiang, Y. Huang, and X. Duan, Graphene nanomesh, *Nat. Nanotechnol.* **5**, 190 (2010).
- [19] K. Takai, Y. Nishimura, and T. Enoki, Anomalous magnetotransport in nanostructured graphene, *Physica E* **42**, 680 (2010).
- [20] Y. Kudo, K. Takai, and T. Enoki, Electron transport properties of graphene with charged impurities and vacancy defects, *J. Mater. Res.* **28**, 1097 (2013).
- [21] G. M. Shedd, and P. E. Russel, The effects of low-energy ion impacts on graphite observed by scanning tunneling microscopy, *J. Vac. Sci. Technol. A* **9**, 1261 (1991).
- [22] R. Coratger, A. Claverie, A. Chahboun, V. Landry, F. Ajustron, and J. Beauvillain, Effects of ion mass and energy on the damage induced by an ion beam on graphite surfaces: a scanning tunneling microscopy study, *Surf. Sci.* **262**, 208 (1992).
- [23] T. Li, B. V. King, R. J. MacDonald, G. F. Cotterill, D. J. O'Connor, and Q. Yang, A STM study of the effects of the ion incident angle and energy on surface damage induced by Ar⁺ bombardment of HOPG, *Surf. Sci.* **312**, 399 (1994).
- [24] J. Yan, Z. Li, C. Bai, W. S. Yang, Y. Wang, W. Zhao, Y. Kang, F. C. Yu, P. Zhai, and X. Tang, Scanning tunneling microscopy investigation of graphite surface damage induced by gold-ion bombardment, *J. Appl. Phys.* **75**, 1390 (1994).
- [25] D. Marton, H. Bu, K. J. Boyd, S. S. Todorov, A. H. A. Bayati, and J. W. Rabalais, On the defect structure due to low energy ion bombardment of graphite, *Surf. Sci. Lett.* **326**, L489 (1995).
- [26] J. R. Hahn and H. Kang, STM study of Ar⁺-induced defects produced by near-threshold energy collision, *Surf. Sci.* **357–358**, 165 (1996).

- [27] J. R. Hahn and H. Kang, Vacancy and interstitial defects at graphite surfaces: scanning tunneling microscopic study of the structure, electronic property, and yield for ion-induced defect creation, *Phys. Rev. B* **60**, 6007 (1999).
- [28] J. R. Hahn and H. Kang, Spatial distribution of defects generated by hyperthermal Ar⁺ impact onto graphite, *Surf. Sci. Lett.* **446**, L77 (2000).
- [29] D. Q. Yang and E. Sacher, s-p Hybridization in highly oriented pyrolytic graphite and its change on surface modification, as studied by X-ray photoelectron and Raman spectroscopies, *Surf. Sci.* **504**, 125 (2002).
- [30] D. Q. Yang and E. Sacher, Carbon 1s X-ray photoemission line shape analysis of highly oriented pyrolytic graphite: the influence of structural damage on peak asymmetry, *Langmuir* **22**, 860 (2006).
- [31] R. A. P. Smith, G. C. Smith, and P. Weightman, Effects of low energy argon ion irradiation on the carbon 1s photoelectron line of highly oriented pyrolytic graphite, *J. Electron Spectrosc. Relat. Phenom.* **152**, 152 (2006).
- [32] G. Speranza, L. Minati, and M. Anderle, The C1s core line in irradiated graphite, *J. Appl. Phys.* **102**, 043504 (2007).
- [33] J. Stöhr, NEXAFS spectroscopy, *Springer* (1992).
- [34] R. A. Rosenberg, P. J. Love, and V. Rehn, Polarization-dependent C(K) near-edge x-ray-absorption fine structure of graphite, *Phys. Rev. B* **33**, 4034 (1986).
- [35] S. Banerjee, T. H. Benny, S. Sambasivan, D. A. Fischer, J. A. Misewich, and S. S. Wong, Near-edge x-ray absorption fine structure investigations of order in carbon nanotube-based systems, *J. Phys. Chem. B* **109**, 8489 (2005).
- [36] R. Gago, I. Jiménez, J. M. Albella, A. C. Font, D. Cáceres, I. Vergara, J. C. Banks, B. L. Doyle, and L. J. Terminello, Bonding and hardness in nonhydrogenated carbon films with moderate sp³ content, *J. Appl. Phys.* **87**, 8174 (2000).
- [37] R. Gago, I. Jiménez, and J. M. Albella, Detecting with X-ray absorption spectroscopy the modifications of the bonding structure of graphitic carbon by amorphisation, hydrogenation and nitrogenation, *Surf. Sci.* **482–485**, 530 (2001).
- [38] K. Amemiya, H. Kondoh, T. Yokoyama, and T. Ohta, A soft X-ray beamline for surface chemistry at the Photon Factory, *J. Electron Spectrosc. Relat. Phenom.* **124**, 151 (2002).
- [39] K. Amemiya, S. Kitagawa, D. Matsumura, H. Abe, T. Ohta, and T. Yokoyama,

- Direct observation of magnetic depth profiles of thin Fe films on Cu(100) and Ni/Cu(100) with the depth-resolved x-ray magnetic circular dichroism, *Appl. Phys. Lett.* **84**, 936 (2004).
- [40] Y. Ma, P. Skytt, N. Wassdahl, P. Glans, D. C. Mancini, J. Guo, and J. Nordgren, Core excitons and vibronic coupling in diamond and graphite, *Phys. Rev. Lett.* **71**, 3725 (1993).
- [41] P. A. Brühwiler, A. J. Maxwell, C. Puglia, A. Nilsson, S. Andersson, and N. Mårtensson, π^* and σ^* excitons in C 1s absorption of graphite, *Phys. Rev. Lett.* **74**, 614 (1995).
- [42] D. A. Fischer, R. M. Wentzcovitch, R. G. Carr, A. Continenza, and A. J. Freeman, Graphitic interlayer states: a carbon K near-edge x-ray-absorption fine-structure study, *Phys. Rev. B* **44**, 1427 (1991).
- [43] I. Jiménez, R. Gago, and J. M. Albella, Fine structure at the X-ray absorption π^* and σ^* bands of amorphous carbon, *Diamond Relat. Mater.* **12**, 110 (2003).
- [44] G. Fanchini, V. Paret, A. Tagliaferro, and M. L. Thèye, Density of states and σ - π mixing in hydrogenated amorphous carbon films, *J. Non-Cryst. Solids* **299–302**, 858 (2002).
- [45] J. Díaz, S. Anders, X. Zhou, E. J. Moler, S. A. Kellar, and Z. Hussain, Combined near edge X-ray absorption fine structure and X-ray photoemission spectroscopies for the study of amorphous carbon thin films, *J. Electron Spectrosc. Relat. Phenom.* **101–103**, 545 (1999).
- [46] R. Gago, M. Vinnichenko, H. U. Jäger, A. Y. Belov, I. Jiménez, N. Huang, H. Sun, and M. F. Maitz, Evolution of sp^2 networks with substrate temperature in amorphous carbon films: experiment and theory, *Phys. Rev. B* **72**, 014120 (2005).
- [47] Z. Hou, X. Wang, T. Ikeda, S. F. Huang, K. Terakura, M. Boero, M. Oshima, M. Kakimoto, and S. Miyata, Effect of hydrogen termination on carbon K-edge x-ray absorption spectra of nanographene, *J. Phys. Chem. C* **115**, 5392 (2011).
- [48] A. Hoffman, A. Heiman, H. P. Strunk, and S. H. Christiansen, Microstructure and phase composition evolution of nano-crystalline carbon films: dependence on deposition temperature, *J. Appl. Phys.* **91**, 3336 (2002).
- [49] T. Y. Kim, C. S. Lee, Y. J. Lee, K. R. Lee, K. H. Chae, and K. H. Oh, Reduction of the residual compressive stress of tetrahedral amorphous carbon film by Ar

- background gas during the filtered vacuum arc process, *J. Appl. Phys.* **101**, 023504 (2007).
- [50] S. Ohmagari, T. Yoshitake, A. Nagano, S. A. Riyami, R. Ohtani, H. Setoyama, E. Kobayashi, and K. Nagayama, Near-edge X-ray absorption fine structure of ultrananocrystalline diamond/hydrogenated amorphous carbon films prepared by pulsed laser deposition, *J. Nanomater.* 876561 (2009).
- [51] A. Kuznetsova, I. Popova, J. T. Yates Jr., M. J. Bronikowski, C. B. Huffman, J. Liu, R. E. Smalley, H. H. Hwu, and J. G. Chen, *J. Am. Chem. Soc.* **123**, 10699 (2001).
- [52] S. Banerjee, T. H. Benny, M. Balasubramanian, D. A. Fischer, J. A. Misewich, and S. S. Wong, Ozonized single-walled carbon nanotubes investigated using NEXAFS spectroscopy, *Chem. Commun.* 772 (2004).
- [53] H. K. Jeong, L. Colakerol, M. H. Jin, P. A. Glans, K. E. Smith, and Y. H. Lee, Unoccupied electronic states in graphite oxides, *Chem. Phys. Lett.* **460**, 499 (2008).
- [54] D. Pacilé, M. Papagno, A. F. Rodríguez, M. Grioni, L. Papagno, Ç. Ö. Girit, J. C. Meyer, G. E. Begtrup, and A. Zettl, Near-edge X-ray absorption fine-structure investigation of graphene, *Phys. Rev. Lett.* **101**, 066806 (2008).
- [55] M. Papagno, A. F. Rodríguez, Ç. Ö. Girit, J. C. Meyer, A. Zettl, and D. Pacilé, Polarization-dependent C K near-edge X-ray absorption fine-structure of graphene, *Chem. Phys. Lett.* **475**, 269 (2009).
- [56] W. Hua, B. Gao, S. Li, H. Ågren, and Y. Luo, X-ray absorption spectra of graphene from first-principles simulations, *Phys. Rev. B* **82**, 155433 (2010).
- [57] T. W. Haas and J. T. Grant, Chemical effects on the KLL Auger electron spectrum from surface carbon, *Appl. Phys. Lett.* **16**, 172 (1970).

Chapter 6

Electron transport study on hydrogen adsorption effect at vacancies in graphene

6.1 Introduction

As described in Chapters 4 and 5, Ar^+ irradiation to graphene can be used to derive significant scattering contribution of edges of atomic vacancies to the electrical conductivity in contrast to nanofabrications, and the edge state emerges pronouncedly at such atomic vacancies. In addition to these findings on the issue of the geometrical structure of graphene, chemical aspects of graphene are mentioned in this chapter. From the point of view of both fundamentals and future applications, tuning the electronic and the magnetic structure of the edge state via chemical functional groups is of increasing interest and importance. However, experimental approaches on graphene-edge decoration by functional groups is still considerably challenging. A technique that can control various functional groups bound to atomic vacancies needs establishing. As a beginning point, hydrogen, which gives the most primal chemical structure of graphene edges, is highlighted. In fact, hydrogenation of edges was previously performed in the studies on observation of the edge state at continuous step edges of graphite using scanning tunneling microscope [1,2]. In these studies [1,2], graphite surface was exposed to a H flow generated by cracking H_2 , as utilized for hydrogenation of silicon surface to make mono-hydride surface. However, it is unclear whether this method is applicable or not to electrical conductivity measurements of graphene with macroscopic distribution of atomic vacancies. Electrical conductivity of graphene with tuning the Fermi energy by a backgate voltage include fruitful information particularly on scattering sources, although it is averaged information over a sample, therefore, it should be carefully addressed whether the hydrogenation process causes or not unintentional structures at the interior

as well as the vacancies in graphene.

Apart from edge functionalization, the importance of decorating the interior carbons of graphene should be also referred to. Since the electronic structure of graphene in the vicinity of the Fermi energy is composed of p_z orbitals of carbons that spread out of the plane of graphene, molecular adsorption affects significantly the electronic properties of graphene. Electron transport studies have been performed upon adsorptions of various molecules, showing the sensitivity of graphene to chemical doping by adsorbates [3–5], which makes graphene potential gas sensors. Among various gas molecules, hydrogen has been of particular interest in terms of controlling properties of graphene in virtue of making graphane [6]. Graphane is hydrogenated graphene, or infinitely fused cyclohexane, in which the p_z orbitals are employed to form C–H bonds, *i.e.*, sp^2 -hybridized configuration in graphene is changed into sp^3 , as shown in Fig. 6.1 [7]. Graphane is electrical insulator with energy band gap of ~ 3.5 eV [7], is easily prepared from graphene by exposure to H plasma and can be reversibly transformed to graphene by annealing [6]. Combined with patterning techniques [8], a single sheet of the composite of graphene and graphane is hopeful for applications in carbon electronics.

In addition to electronic devices, hydrogen on graphene has attracted enormous attention in terms of developing hydrogen storage materials [9], because hydrogen is expected as clean and abundant energy source unlike fossil fuel. To be simplified, there are two requirements for practical hydrogen storage material, namely, density and reversibility. The density is usually evaluated as the gravimetric density ($W_{\text{H}_2} / (W_{\text{container}} + W_{\text{H}_2})$; W denotes the weight) and the volumetric density ($W_{\text{H}_2} / V_{\text{container}}$; V denotes the volume), both of which should be large. The reversibility means the ability of the storage material to adsorb and desorb hydrogens in moderate conditions. For the densities, the use of light elements is a plausible way. However, chemical bond between hydrogen and light elements are usually strong as seen in organic substances or graphane. In contrast, adsorption of H_2 on graphite or nanotube is known to be weak [10]. Focusing attention on graphene-based materials, this remarkable difference is explained as physisorption and chemisorption. Physisorption of H_2 onto graphene has reportedly a small barrier of less than 0.1 eV, resulting in the ease of diffusion and desorption of physisorbed molecules [11]. On the other hand, dissociative chemisorption of H_2 is a pathway to stable adsorption like graphane produced via exposure to reactive H plasma

[6]. However, dissociative chemisorption of H_2 is theoretically expected to have a barrier higher than 3.3 to 3.9 eV onto a basal plane of graphene [12], and it only have the chances at the sites with structural disorders such as edges, vacancies, and ripples [13–18]. In particular, zigzag edges can allow H_2 to dissociatively adsorb without a barrier [14]. Meanwhile, there is a drawback that chemisorbed hydrogen requires high temperature to desorb [6,8], In order to achieve favorable balance between the densities and the reversibility using graphene, a new method of tuning the chemical activity of graphene is needed.

Recently, it has been theoretically reported that chemisorption of H_2 onto graphene can be controlled by an electric field perpendicular to the graphene plane [19]. Liu *et al.* [19] employed a model of Li-doped graphene and manifested that the binding strength of H_2 on the Li-doped graphene can be switched by the direction of an electric field. Following calculations have shown that the presence of electric field can work significantly for adsorption of hydrogen onto graphene [20] and nitrogen-doped graphene [21,22]. Additionally, such an electric field is likely to induce and stabilize structural corrugation in graphene [23], which can be active sites for H_2 adsorption [16–18]. Although the application of perpendicular electric fields can be an answer to the control of the chemical activity of graphene, experimental information is lacking due to high difficulty.

The present study highlights the decoration around atomic vacancies by hydrogen with the aim of establishing a method applicable to the decoration by various functional groups, and moreover in anticipation of experimentally elucidating the effects of functional groups on the edge state in graphene. In this study, effects of H or H_2 exposure to graphene have been examined in terms of the backgate-voltage dependence of the electrical conductivity. The electrical conductivity measurement has been employed because the changes in electron scattering characteristics of vacancies are expected upon hydrogenation treatments and because electron transport properties in graphene are sensitive to presence of adsorbates [3–5]. When graphene was hole-doped state by a backgate voltage, H_2 adsorption was significantly induced, resulting in a considerable amount of electron donation. Adsorbed H_2 appeared to desorb spontaneously if the backgate-aided hole-doped state of graphene was turned off. These results suggest that the backgate-induced weak chemisorption of H_2 onto graphene is related to the control of

chemical activity of graphene by electric fields. For the introduction of atomic vacancies, single-layer graphene samples were irradiated by 100 eV Ar^+ beam. It has been shown that exposures of Ar^+ -irradiated graphene to H or H_2 lead to quite distinct results. A large amount of electron donation observed via H exposure is considered to be due to unknown effects of impurities or substrates. In contrast, H_2 exposure to Ar^+ -irradiated graphene did not show the feature of electron donation. Theoretical calculations have indicated that charge transfer does exist in a C–H bond at a vacancy but the transferred electrons are not conducting. Owing to this agreement, H_2 exposure to Ar^+ -irradiated graphene is considered to realize the selective hydrogenation around atomic vacancies without damaging the interior. Moreover, this molecular exposure method is likely to be applicable to various functionalization.

6.2 Experimental

Graphene samples were deposited on a SiO_2/Si substrate by mechanical exfoliation of kish graphite. Single-layer sheets were identified by taking the ratio of optical contrasts. For making a field-effect-transistor (FET) device, Au/Cr electrodes (30 nm and 5 nm thick, respectively) were attached to a single-layer graphene sample using photolithography technique. The Si layer was used as the backgate electrode for tuning the Fermi energy of the graphene sample. A graphene FET sample was loaded into a vacuum chamber with the base pressure below 1.0×10^{-9} Torr. Prior to the following electrical conductivity measurements, contaminants on the sample were removed by annealing the entire chamber up to 150°C with flowing H_2 and Ar gases (1:10) into the chamber at the total pressure of 1.0×10^{-7} Torr. This condition was confirmed to clean the sample sufficiently by electrical measurements. After this cleaning, the variation of the backgate dependence of the conductivity of the graphene FET sample was measured at room temperature upon creation of vacancies and hydrogenation.

For introducing atomic vacancies into the sample, a 100 eV Ar^+ ion beam was irradiated at the argon pressure of 1.0×10^{-7} Torr for a few seconds. The following hydrogenation of the sample was performed by two methods. One was an exposure of the sample to an H flow, which was produced by cracking H_2 with a heated tungsten filament. The other method was done without cracking, namely an exposure of the sample to a H_2

atmosphere. The latter method was also applied to graphene FET samples before the introduction of vacancies.

6.3 Results and discussion

6.3.1 Atomic hydrogen exposure to graphene having atomic vacancies

Figure 6.2 shows the backgate-voltage (V_g) dependences of the conductivity of a graphene sample, which were measured at room temperature. The black circles represent the data for the pristine sample. The data measured after the following 100 eV Ar^+ irradiation for 5 minutes are denoted as red circles. Then, after the further following H exposure for 5 minutes, the data denoted as blue were obtained. Here, an H flow was generated by introducing H_2 at the pressure of 1.0×10^{-5} Torr and by cracking with heated W filament. As previously used in Chapter 4, the amount of atomic vacancies created in graphene can be estimated using the following theoretical equation [24],

$$\sigma(n) = \frac{2e^2}{\pi h} \left| \frac{n}{n_d} \right| (\ln k_F R)^2, \quad \cdots (6.1)$$

where σ is the conductivity, n is the concentration of charge carriers, e is the elementary electrical charge, h is the Planck constant, n_d is the concentration of atomic vacancies, k_F is the Fermi wave number, and $R = 0.25 \text{ nm}$ is the diameter of a single atomic vacancy. The black solid curves in Fig. 6.2 show the fits by Eq. (3.1) to the data of the Ar^+ -irradiated sample. These fits give $n_d \sim 8 \times 10^{12} \text{ cm}^{-2}$.

It should be noted that an exposure to H flow changed drastically the backgate voltage that gave the minimum conductivity, namely the charge neutrality point (V_{CNP}). In the pristine sample, V_{CNP} was nearly equal to -13 V . After Ar^+ irradiation, V_{CNP} moved to -19 V because of the Ar^+ -aided removal of residual contaminants. Then, the following H exposure moved V_{CNP} out of the range of the V_g sweep (-50 V to $+50 \text{ V}$). This shift of V_{CNP} toward negative side corresponds to the occurrence of conducting electron donation. Here it should be noticed that the mobility of electrons, which can be approximated as the slope of the trace in the V_g region from -50 V to 0 V , is quite similar to that for the Ar^+ -irradiated sample. The mobility of both traces are nearly $2.0 \times 10^3 \text{ cm}^2 \text{ V}^{-1} \text{ s}^{-1}$. Provided that the exposure to H adds impurities such as on-plane C-H bonds like graphane

[6,25,26], the mobility must decrease. Because the mobility remains unchanged, it should be concluded that additional impurities are not involved, and that hydrogenation occurs only around vacancies. Based on this assumption, the value of V_{CNP} after H exposure is estimated by extrapolating the trace, as shown as the blue dashed curve in Fig. 6.2. The expected V_{CNP} is at -90 V. The shift of ~ -70 ($= -90 \text{ V} - (-19 \text{ V})$) corresponds to the amount of electron donation of $\Delta n = 7.5 \times 10^{10} \times \Delta V_{\text{CNP}} \sim 5.3 \times 10^{12} \text{ cm}^{-2}$ calculated in terms of the field-effect-modulated concentration of carriers. Note that the thickness of the SiO_2 layer of the substrate was 285 nm , for this sample. Thus, the averaged amount of electron donation per a vacancy is calculated to be as much as $0.6e$. This remarkable feature of the electron donation will be further discussed below in comparison with the case of H_2 exposure after Ar^+ irradiation.

6.3.2 Gate-controlled adsorption of hydrogen molecule on graphene

Prior to the application of H_2 to Ar^+ -irradiated graphene samples, interaction with H_2 and pristine graphene (*i.e.*, without atomic vacancies) was examined. Recently, it was reported that when graphene was exposed to H_2 at atmospheric pressures, V_{CNP} shifted toward the negative side [27]. In this report, graphene prepared by chemical vapor deposition technique was also employed, which were much more defective therefore reactive than exfoliated graphene, and the authors mentioned that they could observe clear evidence of dissociative adsorption of H_2 on graphene [27]. However, totally different results have been obtained in the present conditions.

Figure 6.3 shows a schematic illustration of a typical procedure for exposure of a graphene sample to H_2 at the pressure of $1.0 \times 10^{-6} \text{ Torr}$ for various durations. During exposure, a backgate voltage ($V_{\text{g,ad}}$) was applied. Right after $V_{\text{g,ad}}$ was turned off and H_2 was evacuated, the conductivity of the sample was measured with sweeping V_{g} . Figure 6.4 shows the backgate-voltage dependence of the conductivity of a pristine graphene after exposure to H_2 for 5, 10, 15, and 30 minutes with $V_{\text{g,ad}} = +30 \text{ V}$, and Fig. 6.5 shows results for the identical sample upon the similar procedures but with $V_{\text{g,ad}} = -30 \text{ V}$. Here, a crucial difference can be seen. When the sample was electron-doped by $V_{\text{g,ad}} > V_{\text{CNP}}$ (Fig. 6.4), V_{CNP} did not shift. In contrast, when the sample was hole-doped by $V_{\text{g,ad}} < V_{\text{CNP}}$ (Fig. 6.5), V_{CNP} shifted significantly toward the negative side, corresponding to the

donation of conducting electrons to the sample. Moreover, repetition of the conductivity measurements revealed that the shifted V_{CNP} returned to the initial position, that is to say, the electron donation disappeared spontaneously. Interestingly, the observed electron donation is definitely the opposite of the case of O_2 , which causes hole donations. The hole donation by O_2 exposure has been revealed to be induced by $V_{\text{g,ad}} > V_{\text{CNP}}$ and suppressed by $V_{\text{g,ad}} < V_{\text{CNP}}$ [4]. This feature is also the opposite of the present case of H_2 exposure. Furthermore, the hole donation by O_2 exposure never disappear spontaneously, as an as-prepared graphene samples usually show hole-doped feature in the conductivity.

As mentioned above, the exposure-duration dependence of the V_{CNP} shift was clearly observed. In addition, the V_{CNP} shift was also dependent of $V_{\text{g,ad}}$. Figure 6.6 shows the backgate-voltage dependence of the conductivity of a different single-layer graphene sample measured before and after exposure to H_2 for 15 minutes at the pressure of 1.0×10^{-6} Torr with various $V_{\text{g,ad}}$. In the case of $V_{\text{g,ad}} = V_{\text{CNP}}$ the shift of V_{CNP} was negligible, and non-zero $V_{\text{CNP}} - V_{\text{g,ad}}$ were associated with the magnitude of the V_{CNP} shift. In these measurements, the shifted V_{CNP} also returned to the initial position after several hours. Moreover, an interesting fact was found. Figure 6.7 shows the data for the identical sample upon the similar procedures except for the time difference between the evacuation of H_2 and the stopping $V_{\text{g,ad}}$. The shifts of V_{CNP} measured by this process were approximately equal to those measured without the time difference. In other words, if $V_{\text{g,ad}}$ was retained, the shift of V_{CNP} was also retained.

The source of the observed electron donation is considered to be H_2 adsorption because of the absence of the other possibilities. In order to confirm the occurrence of electron donation by adsorbed H_2 , the electron and the hole mobilities were derived for the identical sample in Figs. 6.6 and 6.7. These mobilities were calculated by functional fits to the V_{g} -dependent conductivity traces. From the simple Drude equation, $\sigma = e\mu n$ (σ : conductivity, μ : mobility), the mobility is obtained as the slope of σ versus n , *i.e.*, V_{g} . Thus, the linear regions of the measured conductivity traces (the regions very close to and far from V_{CNP} were excluded) were linearly fitted. As shown in Fig. 6.8, electron mobility decreased and the hole mobility remained unchanged with the decrease of $V_{\text{g,ad}} - V_{\text{CNP}}$, whereas both of the mobilities decreased for positive $V_{\text{g,ad}} - V_{\text{CNP}}$. The decrease of $V_{\text{g,ad}} - V_{\text{CNP}}$ corresponds to the increase of the electron donation. The asymmetry in the magnitude of the reduction in the electron and the hole mobilities was previously reported

and attributed to the signature of electrical charge of adsorbed impurities [28,29]. According to the previous reports [28,29], the electron mobility shows more sensitive reduction than the hole mobility in the presence of positively-charged impurities. For the present results, the increase only in the electron mobility indicates the presence of positively charged adsorbates, namely, the electron donation by adsorbed H₂ molecules.

Figure 6.8 also shows the temporal changes in the mobilities. The reduction in the electron mobility was disappeared after V_{CNP} returned to the initial position. This result indicates that the reduction in the electron mobility is strongly correlated with the amount of electron donation, *i.e.*, the amount of adsorbed H₂. In addition, the insensitivity of the hole mobility to adsorbed H₂ is shown. In fact, positively charged impurity also reduce the hole mobility, which has been experimentally examined using potassium ions [28]. However, there is obvious difference between H₂ and potassium ions adsorbed on graphene. Potassium ions do not desorb spontaneously. The strength of chemical interaction between H₂ and graphene differs from that between potassium ions and graphene, so that the scattering mechanism for conducting electrons in graphene should be different. Further effort is requisite for the elucidation of the scattering nature of adsorbed H₂. Figure 6.8 also shows the decreases in both of the electron and the hole mobilities for positive $V_{\text{g,ad}} - V_{\text{CNP}}$, of which the origin is considered as adsorption of O₂ remaining in the vacuum chamber.

The structure of adsorbed hydrogen needs to be addressed. Due to the charge transfer interaction, physisorption is omitted. For consideration of dissociative chemisorption that is probably absent owing to the high barriers [12], a good example would be graphane [6]. Reportedly, the transformation of graphene into graphane by reactive hydrogen plasma is reversible by annealing up to 450°C [6]. This fact indicates that hydrogen atoms bonded to the interior carbon atoms of graphene need a temperature higher than a few 100°C to desorb. On the other hand, Kim *et al.* [27] mentioned their observation of electron donation as a consequence of dissociative adsorption of H₂ at vacancy defects, *i.e.*, edges. When it comes to hydrogens bound to edge carbon atoms, heat treatment at more than 1000°C is requisite for dissociation [30]. Therefore, the spontaneous recovery of the V_{CNP} shifts in the present study is not the case of dissociative chemisorption.

The remaining possibility should be non-dissociative chemisorption of H₂. In fact, the opposing hole donation by O₂ has been explained in terms of non-dissociative

chemisorption [4]. The opposite charge of donated carriers is likely to reflect the relative electronegativity of O and H with respect to C, although the spontaneous disappearance of electron donation by hydrogen is distinct from the case of O₂. Then, the catalysts that strengthen the interaction between clean graphene and physisorbed H₂ to cause charge transfers need to be understood. As mentioned above, the combination of electric fields and structural disorders is a possible candidate. Here, an electric-field effect is referred to.

In an ideal model of a parallel-plate capacitor, an electric field exists only between the plates because electric fields above one plate and below the other plate are compensated. However, in a graphene FET device, it was stated that a V_g can create a non-uniform electric field above the graphene in addition to a uniform electric field between the graphene and the backgate electrode, as shown in Fig. 6.9 [31]. The strength of the non-uniform electric field is approximately 10% of that of the uniform one [31]. The electric field in the SiO₂ layer (E) with a V_g is given by

$$E = \frac{n_q}{\epsilon_0 \epsilon_{\text{SiO}_2}} = \frac{V_g}{d}, \quad \cdots (6.2)$$

where n_q is the charge density, ϵ_0 is the vacuum permittivity, $\epsilon_{\text{SiO}_2} = 3.9$ is the relative permittivity of SiO₂, and d is the thickness of the SiO₂ layer. Here $d = 90$ nm was employed. Thus, the stray electric field above the graphene (E_{stray}) is given by $E_{\text{stray}} = 0.10E \sim 1.0 \times 10^6 \times V_g \text{ V} \cdot \text{m}^{-1}$. Figure 6.10 shows the dissociative adsorption pathways of H₂ onto the surface of graphene under the absence or the presence of an electric field [20]. The electric field is defined as F , of which the positive direction is from the plane of graphene to the adsorbed hydrogen. Namely, $V_{g,\text{ad}}$ -aided hole-doped state in the present study corresponds to the positive value of F . F is expressed as the unit of a.u., where $1 \text{ a.u.} = 5.14 \times 10^{11} \text{ V} \cdot \text{m}^{-1}$. Thus, the present condition of a $V_{g,\text{ad}}$ as a few 10 V corresponds to the order of 10^{-5} a.u. of F . In fact, both Figs. 6.10a and 6.10b show large reaction barriers (E_{bar}) and reaction energies (E_R), so that the dissociative chemisorption of H₂ is very unlikely even if the presence of $F = +0.01$, which is three order of magnitude larger than the present condition. However, it should be noticed that the state labeled as ‘1’ in Fig. 6.10b has a lower energy and a smaller separation from the graphene than the initial structure (IS). Here IS is taken as a physisorbed H₂, which has the separation of ~ 0.26 nm from the graphene surface [20]. This result in Fig. 6.10b suggests that the

bonding between adsorbed H₂ and the graphene is considerably strengthened with respect to the physisorption case. Unfortunately, the magnitude of strengthening, the possibility and the amount of charge transfer in the present conditions cannot be estimated because Ref. [20] was not focusing on the structure '1', and because precise theoretical calculations are strongly requisite.

6.3.3 Hydrogen molecule exposure to graphene having atomic vacancies

Under the assumption that H₂ dissociatively react at atomic vacancies spontaneously [14,15], and according to the present finding that $V_{g,ad}$ -aided adsorbed H₂ can easily desorb, H₂ exposure to Ar⁺-irradiated graphene was investigated.

Figure 6.11 shows the backgate-voltage dependence of the conductivity of a single-layer graphene sample. For the pristine sample, V_{CNP} appeared at $\sim +17$ V. Then, the pristine sample was exposed to H₂ with $V_{g,ad} = +17$ V, resulting in the trace denoted as the black dotted curve in Fig. 6.11. V_{CNP} little shifted, as expected. The reason for the small reduction in the conductivity is unclear. Then, the sample was irradiated by 100 eV Ar⁺ beam for 10 seconds and immediately followed by the exposure to H₂ with $V_{g,ad} = +17$ V for 15 minutes. The data right after these procedures are denoted as the red dashed curve, and the data measured after a few hours are denoted as the red solid curve in Fig. 6.11. For the red dashed curve, a slight shift of V_{CNP} was observed ($\sim +15$ V, *i.e.*, the shift was -2 V). This slight V_{CNP} shift disappeared soon, as can be seen in the red solid curve. The repetition of the identical procedures gave the very similar changes as shown as the blue dashed and solid curves in Fig. 6.11.

Figure 6.12 shows the data for the identical sample in Fig. 6.11 measured the similar procedures. Prior to Ar⁺ irradiation (the red data in Fig. 6.11), the pristine sample was exposed to H₂ with $V_{g,ad} = 0$ V, resulting in a slight negative shift of V_{CNP} and its recovery, as expected (the green dotted curve in Fig. 6.12). Following the red and blue data in Fig. 6.11, the similar Ar⁺ irradiation and hydrogenation procedures except for $V_{g,ad} = 0$ V were repeated. The data after this repetition is denoted as the green dashed and solid curves in Fig. 6.12. Compared with the green dotted and dashed curves in Fig. 6.12, the shift of V_{CNP} after Ar⁺ irradiation and hydrogenation was again larger than that after hydrogenation process. Although the reason why the shifted V_{CNP} did not return to the

initial location after Ar^+ irradiation and hydrogenation is unclear, the remaining shift of V_{CNP} and Eq. (6.1) give the estimation of the amount of electron donation and the defect density, leading to the amount of the charge transfer per a vacancy of less than $0.006e$.

From these results in Figs. 6.11 and 6.12, it is obviously seen that exposure to H_2 after Ar^+ irradiation does not cause a significant amount of electron donation in contrast to the case of exposure to H flow. In addition, it can be said that the amount of electron donation after Ar^+ irradiation and hydrogenation procedures is larger than that after exposure to H_2 with each $V_{\text{g,ad}}$.

According to theoretical calculations, the charge transfer occurs in the C–H bonds around a vacancy, with the possible magnitude of as much as $0.5e$ [32]. The carbon atom is negatively charged and the hydrogen atom is positive. This value is, in fact, comparable to that obtained by exposing Ar^+ -irradiated graphene to H flow ($0.6e$). However, theoretical studies also suggests that the transferred electrons are unlikely to be conducting, thus localized [32], which supports the results obtained by Ar^+ irradiation and H_2 exposure. Based on the agreement with theoretical results, it has been concluded that atomic vacancies in graphene are selectively hydrogenated by means of H_2 exposure.

The large amount of the electron donation that was observed using H flow needs to be ascribed to other origin. In the previous section, the probability of the involvement of charged adsorbates is omitted by considering the mobility invariance. However, due to the denial of transfer of conducting electrons by selective hydrogenation around vacancies using H exposure, the presence of charge transfer interaction should be considered between graphene and adsorbates that does not reduce the mobility of carriers. In the present case, adsorbed hydrogen atoms are most likely. One relevant experiment was reported. Katoch *et al.* examined electron transport characteristics of graphene exposed to an H flow at low temperature, resulting in an invariance of the mobility along with the electron donation [33]. This observation indicated that H could be adsorbed onto graphene giving rise to charge transfer without significantly enhancing electron scattering events. Moreover, Katoch *et al.* observed the disappearance of the electron donation when the temperature was increased to room temperature. This disappearance was not observed in the present study, so that the adsorbed states should be differ. However, Katoch *et al.* did not reveal the adsorbed structure of H on graphene, and such information is still lacking. Further experimental and theoretical verification is requisite for adsorbed states

of H as well as H₂ on graphene.

Although the absence of electron donation is revealed in graphene having hydrogenated vacancies, attention should be paid to the larger V_{CNP} shift observed immediately after Ar⁺ irradiation and H₂ exposure than the V_{CNP} shift of $V_{\text{g,ad}}$ -induced H₂ adsorption onto the pristine graphene. Structural relaxation is a possible reason for this point. Given that a single atomic vacancy has three surrounding carbon atoms each of which can form another covalent bond, two H₂ is necessary to terminate the dangling bonds, probably leading to desorption of an excess hydrogen atom. This speculation is only one of various possible hydrogenation reaction pathways, so that further theoretical and experimental effort is required to confirm the hydrogenation processes.

6.4 Conclusions

Effects of H or H₂ exposure to graphene have been examined in terms of the V_{g} dependence of the electrical conductivity. When graphene is hole-doped state by an application of $V_{\text{g,ad}}$, H₂ adsorption has appeared to be significantly induced, resulting in a considerable amount of conducting electron donation. Adsorbed H₂ can desorb spontaneously if $V_{\text{g,ad}}$ is turned off. These results suggest that the $V_{\text{g,ad}}$ -induced weak chemisorption of H₂ onto graphene is related to the control of chemical activity of graphene by electric fields. For the hydrogenation of atomic vacancies in graphene, it has been shown that exposures of Ar⁺-irradiated graphene to H or H₂ lead to quite distinct results. A large amount of electron donation observed via H exposure is considered to be due to electron-donating impurities. In contrast, H₂ exposure to Ar⁺-irradiated graphene does not show the feature of electron donation after stabilization. Theoretical calculations have indicated that charge transfer does exist in a C–H bond at a vacancy but the transferred electrons are not conducting. Owing to this agreement, H₂ exposure to Ar⁺-irradiated graphene is considered to realize the selective hydrogenation around atomic vacancies without damaging the interior. Moreover, this molecular exposure method is likely to be applicable to various functionalization.

6.5 Figures in Chapter 6

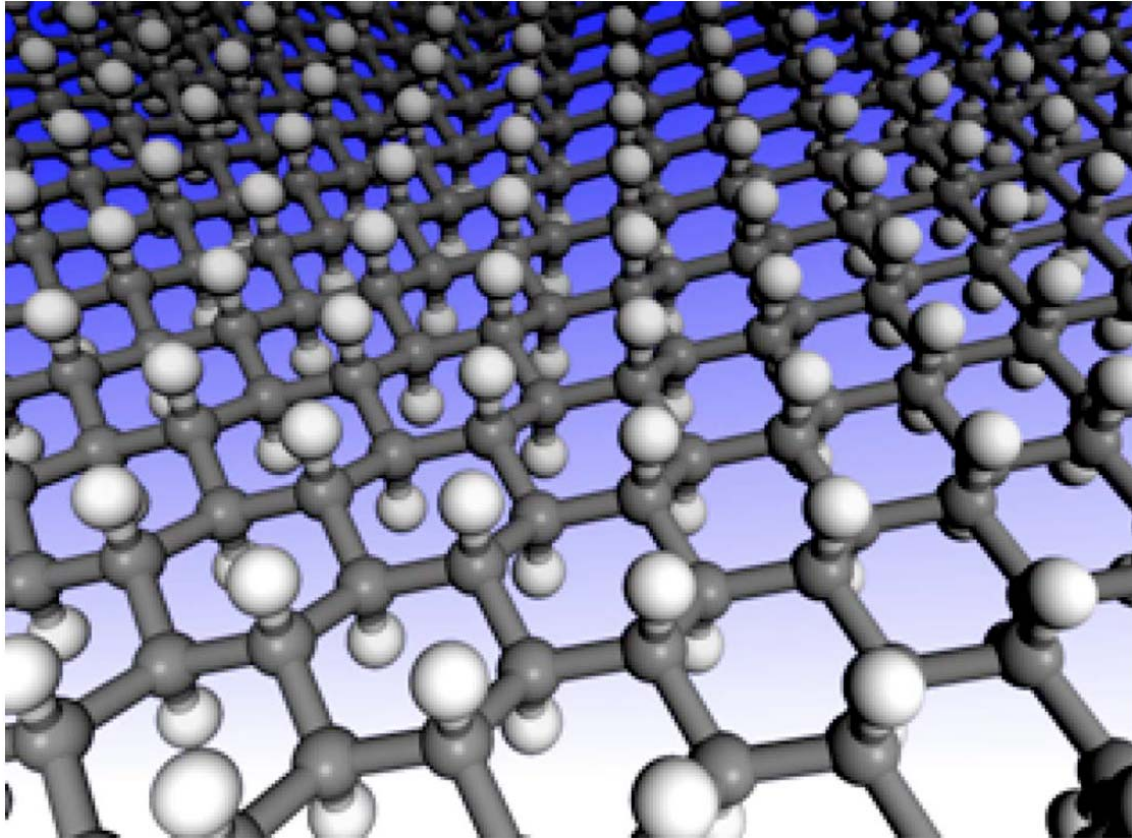


Figure 6.1. Illustration of the structure of graphane. Reprinted figure with permission from J. O. Sofo, A. S. Chaudhari, and G. D. Barber, Graphane: a two-dimensional hydrocarbon, *Physical Review B* **75**, 153401 (2007) [7]. Copyright (2007) by the American Physical Society.

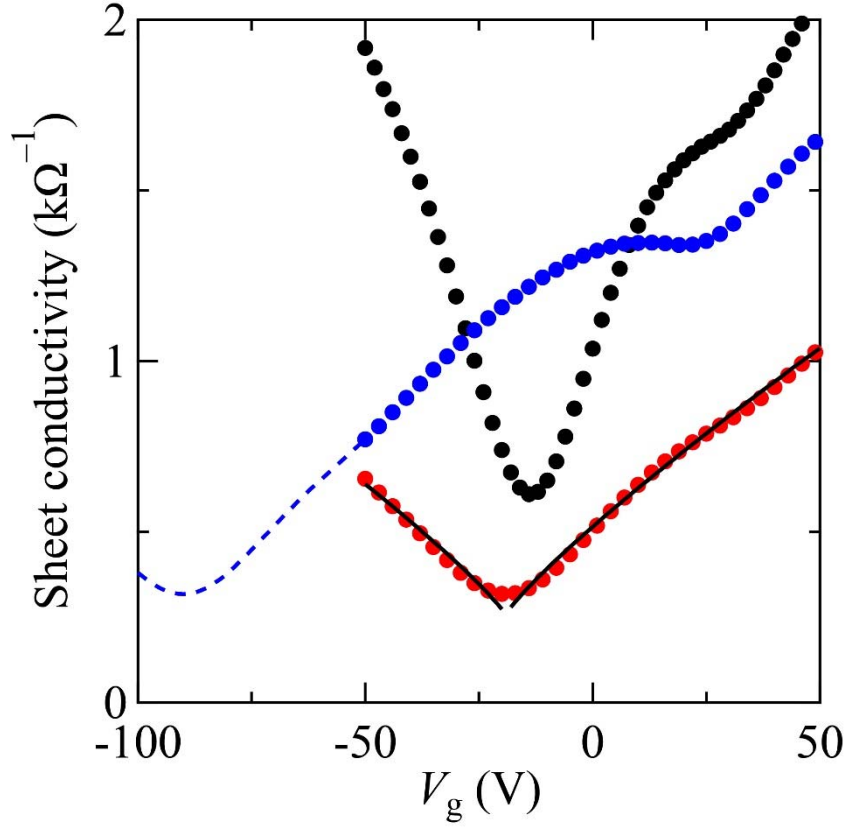


Figure 6.2. The backgate-voltage dependence of the conductivity of a single-layer graphene sample. The black, the red, and the blue circles denote the data measured for the pristine sample, for the sample irradiated by 100-eV Ar^+ beam, and for the Ar^+ -irradiated sample exposed to H flow, respectively. The black solid curves are theoretical fits to the red data. The blue dashed curve denotes the extrapolation of the blue data.

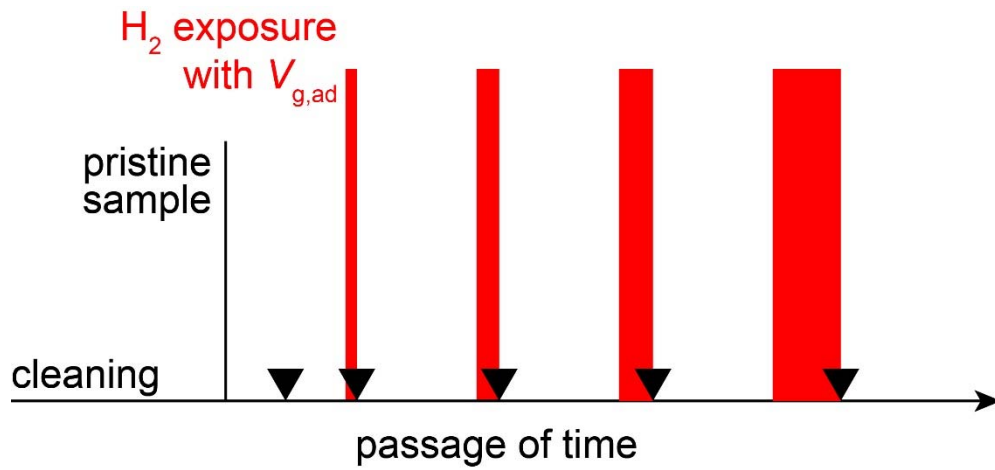


Figure 6.3. Schematic illustration of a typical experimental procedure for exposure of graphene to H₂ for various durations. The down-triangles denote electrical conductivity measurements with V_g sweep. The data shown in Figs. 6.3 and 6.4 were measured immediately after exposure.

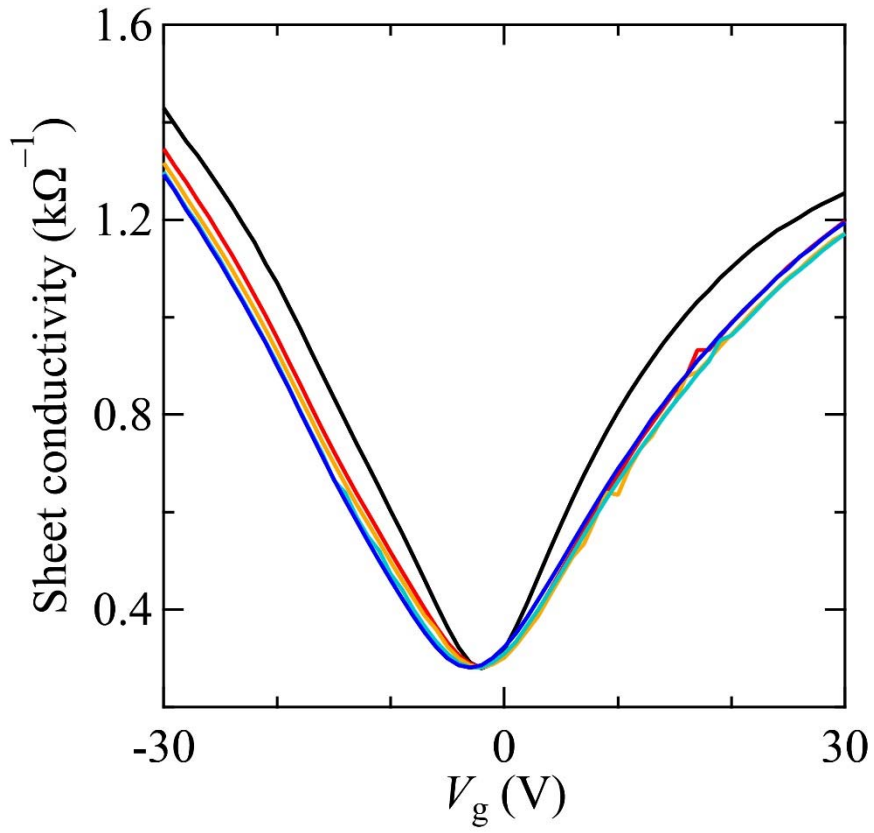


Figure 6.4. The backgate-voltage dependence of the conductivity of a single-layer graphene sample. The black trace denotes the data for the pristine sample. The red, the orange, the light-blue, and the blue traces denote the data measured after exposure to H_2 at a pressure of 1.0×10^{-7} Torr for 5, 10, 15, and 30 minutes, respectively, with an application of $V_g = +30$ V.

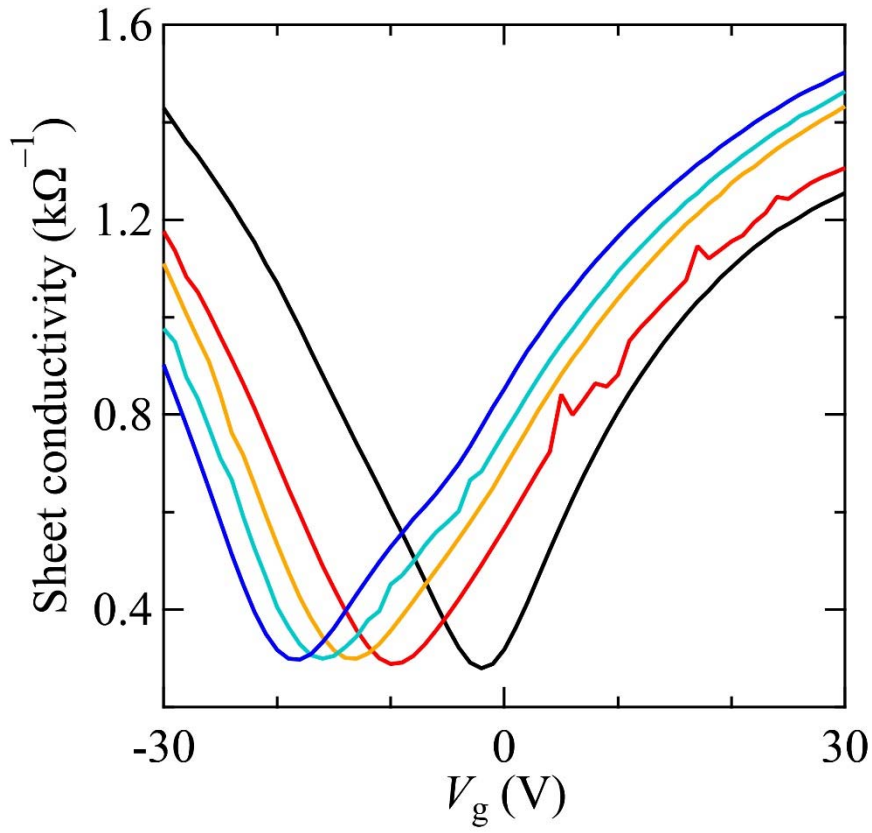


Figure 6.5. The backgate-voltage dependence of the conductivity of the same graphene sample shown in Fig. 6.2. The black trace denotes the data for the pristine sample. The red, the orange, the light-blue, and the blue traces correspond to the same condition of H_2 exposure with the data in Fig. 6.2, except for the applied backgate voltage during exposure $V_g = -30$ V.

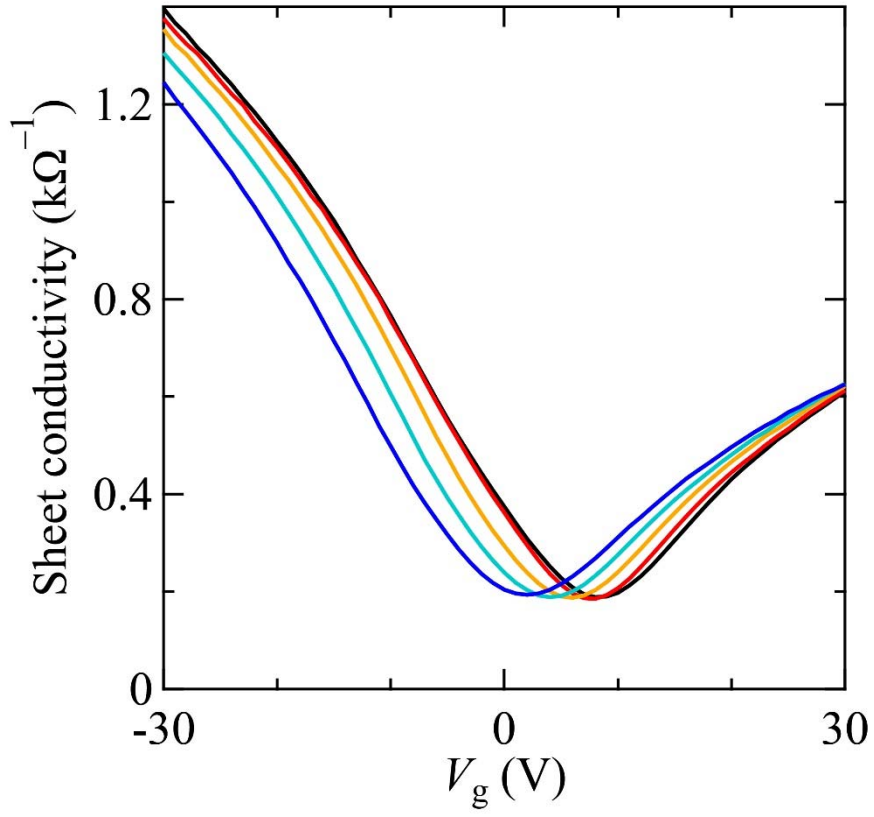


Figure 6.6. The backgate voltage dependence of the conductivity of a single-layer graphene sample. The black trace denotes the data for the pristine sample. The red, the orange, the light-blue, and the blue traces denote the data for the sample exposed to H_2 for 15 minutes with $V_{g,ad} = V_{CNP}$ (+8 V), -10 V, -20 V, and -30 V, respectively.

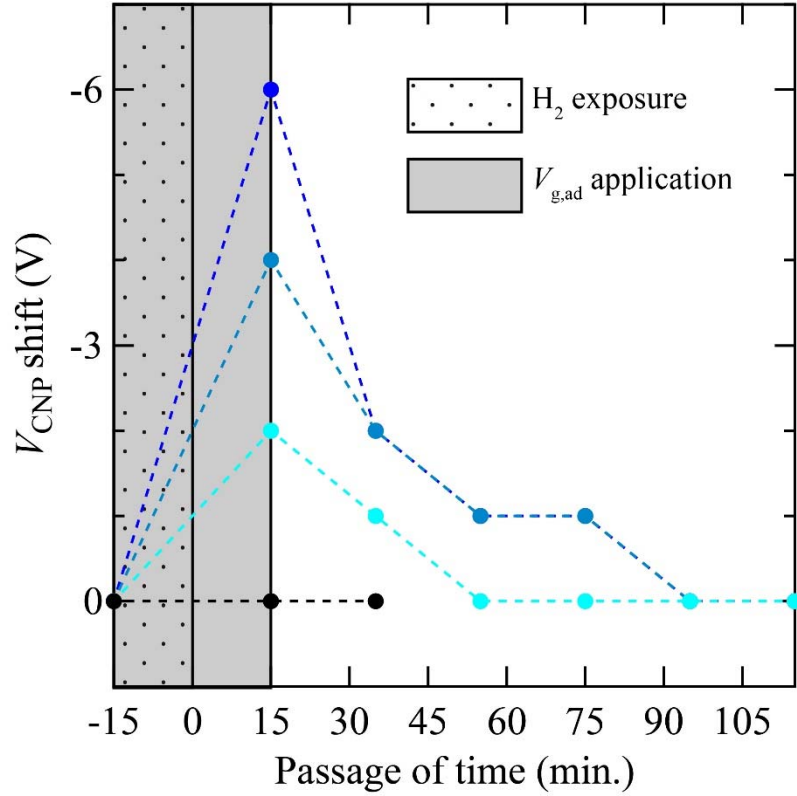


Figure 6.7. A plot of the shift of V_{CNP} upon exposure to H_2 versus the passage of time (t) measured with the identical sample in Fig. 6.6. The black, the light-blue, the middle-blue, and the blue circles correspond to the data with $V_{\text{g,ad}} = V_{\text{CNP}} (+8 \text{ V})$, -10 V , -20 V , and -30 V , respectively. At $t = -15$, the application of $V_{\text{g,ad}}$ and the introduction of H_2 at the pressure of $1.0 \times 10^{-6} \text{ Torr}$ were started. At $t = 0$, H_2 was evacuated. Then, at $t = 15$, $V_{\text{g,ad}}$ was stopped and the conductivity was measured. The conductivity measurements were repeated until the V_{CNP} shift became zero. It took 20 minutes for each shot of the conductivity measurement.

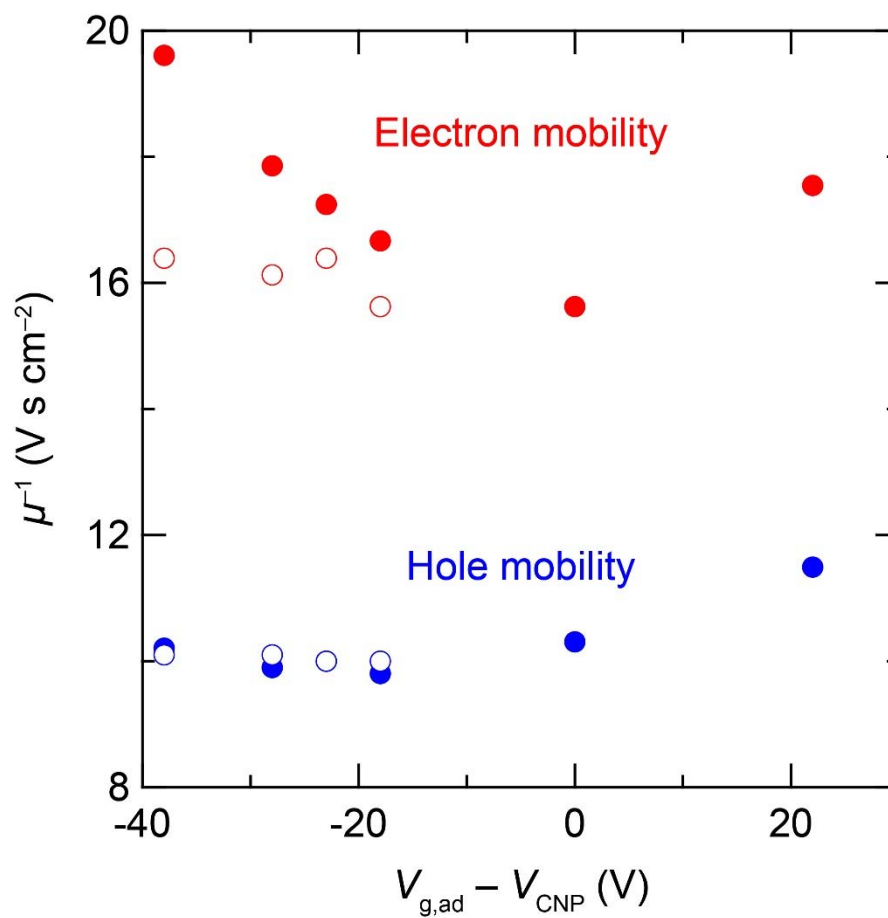


Figure 6.8. A plot of inversed electron and hole mobilities obtained with the identical sample in Fig. 6.6. The red and the blue circles denote the electron and the hole mobilities, respectively. The filled and the empty circles denote the data measured immediately after H_2 exposure and after the recovery of V_{CNP} , respectively.

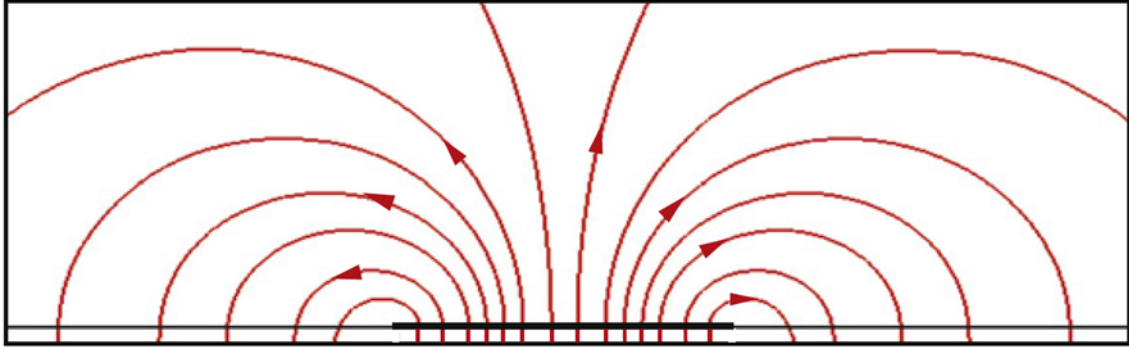


Figure 6.9. Electric field around a graphene FET device when a V_g is applied. The thick black line denotes the graphene. The silicon backgate layer is the bottom of the image. A SiO₂ layer is between the graphene and the silicon layer. The red curves denote the electric field. Reprinted from *Carbon*, **49**, A. A. Kaverzin, S. M. Strawbridge, A. S. Price, F. Withers, A. K. Savchenko, and D. W. Horsell, Electrochemical doping of graphene with toluene, 3829, Copyright (2011), with permission from Elsevier [31].

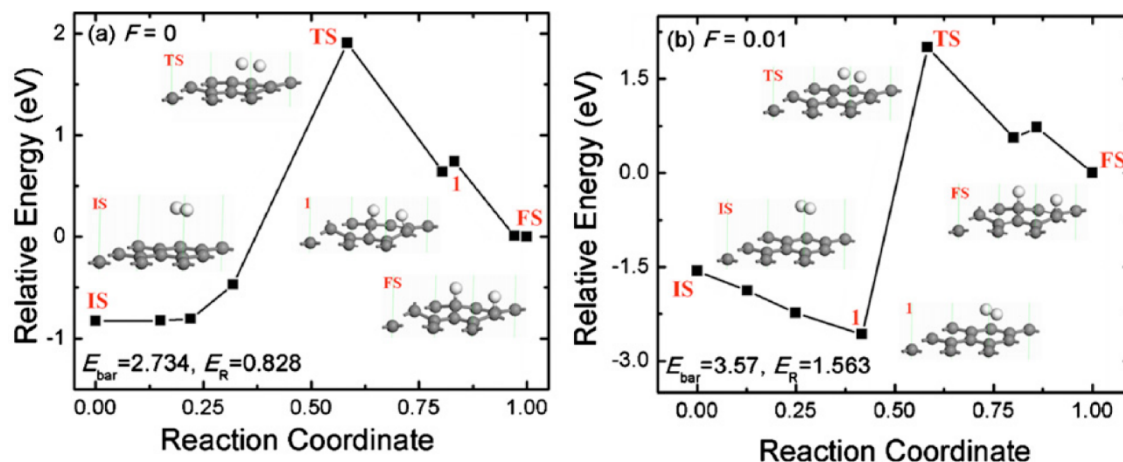


Figure 6.10. The pathways of dissociative adsorption of H_2 onto graphene under (a) the absence and (b) the presence of an electric field perpendicular to the graphene plane. The energy is taken with respect to the final structure (FS). IS and TS are the initial structure and the transition state, respectively. E_{bar} and E_R are the dissociation barrier energy (TS–IS) and the reaction energy (FS–IS), respectively, in the unit of eV. The insets denote structures at various stages of the reaction coordinates. Carbon and hydrogen atoms are denoted as the gray and the white spheres. The positive direction of the electric field (F) is taken as the direction from the graphene plane to the adsorbed hydrogen. F is in the unit of a.u., where $1 \text{ a.u.} = 5.14 \times 10^{11} \text{ V} \cdot \text{m}^{-1}$. Reprinted with permission from Z. M. Ao and F. M. Peeters, Electric field: a catalyst for hydrogenation of graphene, *Applied Physics Letters* **96**, 253106 (2010) [20]. Copyright 2010, AIP Publishing LLC.

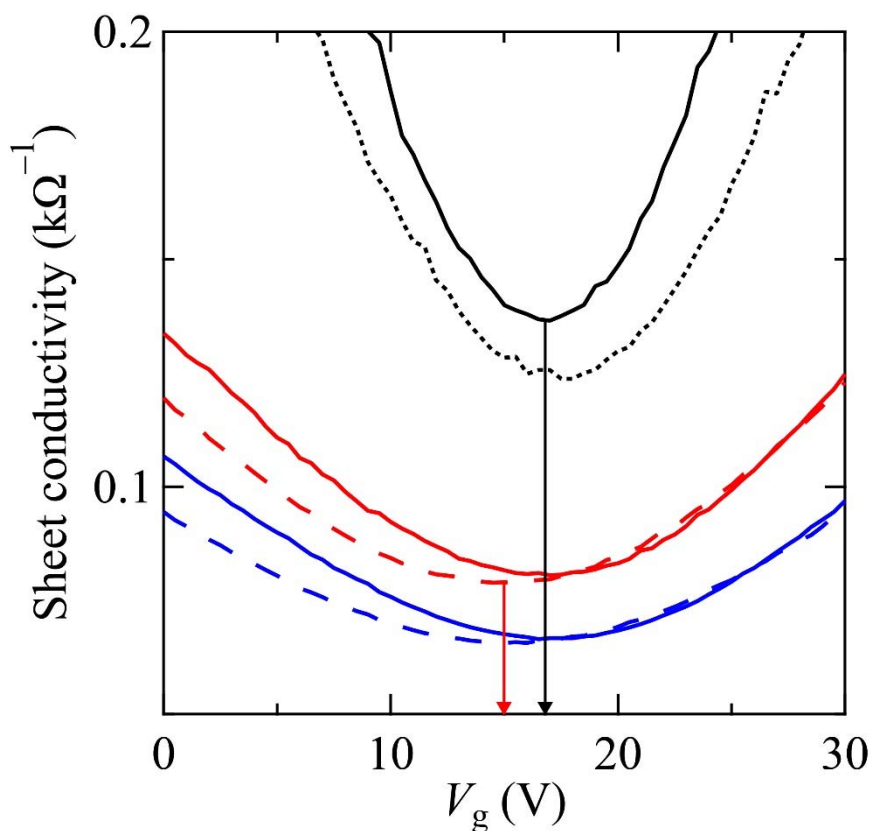


Figure 6.11. The backgate-voltage dependence of the conductivity of a single-layer graphene sample in the backgate range between 0 V and +30 V. The black solid curve denotes the data for the pristine sample. The initial V_{CNP} was at $\sim +17$ V, as indicated by the black arrow. The black dotted curve represents the data measured after an exposure of the pristine sample to H_2 with $V_{\text{g,ad}} = V_{\text{CNP}}$ for 15 minutes at the pressure of 1.0×10^{-6} Torr. The red dashed curve denotes the data for the sample after 100 eV Ar^+ irradiation for 10 seconds and the immediately following exposure to H_2 with $V_{\text{g,ad}} = V_{\text{CNP}}$ for 15 minutes at the pressure of 1.0×10^{-6} Torr. The shifted V_{CNP} located at $\sim +15$ V, as indicated by the red arrow. The red solid curve is the data measured a few hours after the data of the red dashed curve. The blue dashed and solid curve denote the data after one repetition of the identical procedure.

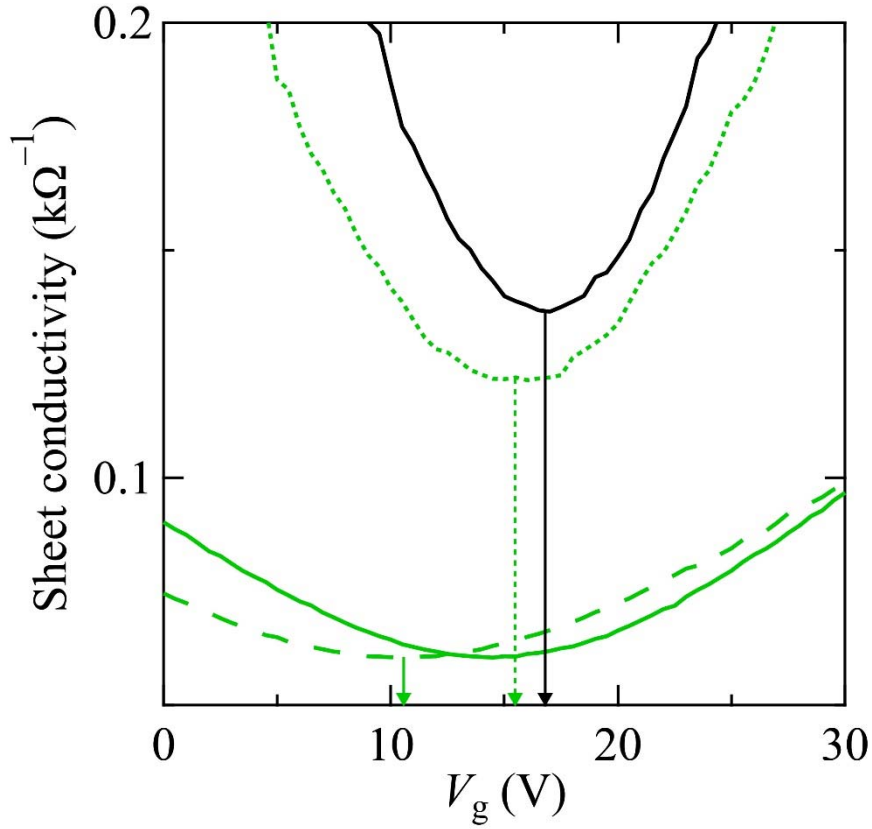


Figure 6.12. The backgate-voltage dependence of the conductivity of the identical sample in Fig. 6.11. The black solid curve is the data for the pristine sample. The green dotted curve is the data measured after an exposure of the pristine sample to H_2 with $V_{g,ad} = 0$ V for 15 minutes at the pressure of 1.0×10^{-6} Torr. The shifted V_{CNP} was at $\sim +15.5$ V as indicated by the green dotted arrow, and it returned to the initial value. The green dashed curve denotes the data for the sample after the second repetition of the Ar^+ irradiation and hydrogenation procedures written in Fig. 6.11 except for $V_{g,ad} = 0$ V. The shifted V_{CNP} located at $\sim +11$ V as indicated by the green solid arrow. The green solid curve is the data measured a few hours after the data of the green dashed curve. The final location of V_{CNP} was at $\sim +15$ V.

References in Chapter 6

- [1] Y. Kobayashi, K. Fukui, T. Enoki, K. Kusakabe, and Y. Kaburagi, Observation of zigzag and armchair edges of graphite using scanning tunneling microscopy and spectroscopy, *Phys. Rev. B* **71**, 193406 (2005).
- [2] Y. Kobayashi, K. Fukui, T. Enoki, and K. Kusakabe, Edge state on hydrogen-terminated graphite edges investigated by scanning tunneling microscopy, *Phys. Rev. B* **73**, 125415 (2006).
- [3] F. Schedin, A. K. Geim, S. V. Morozov, E. W. Hill, P. Blake, M. I. Katsnelson, and K. S. Novoselov, Detection of individual gas molecules adsorbed on graphene, *Nat. Mater.* **6** 652 (2007).
- [4] Y. Sato, K. Takai, and T. Enoki, Electrically controlled adsorption of oxygen in bilayer graphene, *Nano Lett.* **11**, 3468 (2011).
- [5] I. Silvestre, E. A. de Morais, A. O. Melo, L. C. Campos, A. M. B. Goncalves, A. R. Cadore, A. S. Ferlauto, H. Chacham, M. S. C. Mazzoni, and R. G. Lacerda, Asymmetric effect of oxygen adsorption on electron and Hole mobilities in bilayer graphene: long- and short-range scattering mechanisms, *ACS Nano* **7**, 6597 (2013).
- [6] D. C. Elias, R. R. Nair, T. M. G. Mohiuddin, S. V. Morozov, P. Blake, M. P. Halsall, A. C. Ferrari, D. W. Boukhvalov, M. I. Katsnelson, A. K. Geim, and K. S. Novoselov, Control of graphene's properties by reversible hydrogenation: evidence for graphane, *Science* **323**, 610 (2009).
- [7] J. O. Sofo, A. S. Chaudhari, and G. D. Barber, Graphane: a two-dimensional hydrocarbon, *Phys. Rev. B* **75**, 153401 (2007).
- [8] Y. Wang, X. Xu, J. Lu, M. Lin, Q. Bao, B. Özyilmaz, and K. P. Loh, Toward high throughput interconvertible graphane-to-graphene growth and patterning, *ACS Nano* **4**, 6146 (2010).
- [9] V. Tozzini and V. Pellegrini, Prospects for hydrogen storage in graphene, *Phys. Chem. Chem. Phys.* **15**, 80 (2013).
- [10] H. Kajiura, S. Tsutsui, K. Kadono, M. Kakuta, M. Ata, and Y. Murakami, Hydrogen storage capacity of commercially available carbon materials at room temperature, *Appl. Phys. Lett.* **82**, 1105 (2003).
- [11] J. S. Arellano, L. M. Molina, A. Rubio, and J. A. Alonso, Density functional study of adsorption of molecular hydrogen on graphene layers, *J. Chem. Phys.* **112**, 8114

- (2000).
- [12] Y. Miura, H. Kasai, W. Diño, H. Nakanishi, and T. Sugimoto, First principles studies for the dissociative adsorption of H₂ on graphene, *J. Appl. Phys.* **93**, 3395 (2003).
 - [13] W. A. Diño, Y. Miura, H. Nakanishi, H. Kasai, T. Sugimoto, and T. Kondo, H₂ dissociative adsorption at the armchair edges of graphite, *Solid State Commun.* **132**, 713 (2004).
 - [14] W. A. Diño, H. Nakanishi, H. Kasai, T. Sugimoto, and T. Kondo, H₂ dissociative adsorption at the zigzag edges of graphite, *e-J. Surf. Sci. Nanotech.* **2**, 77 (2004).
 - [15] A. Allouche and Y. Ferro, Dissociative adsorption of small molecules at vacancies on the graphite (0001) surface, *Carbon* **44**, 3320 (2006).
 - [16] D. W. Boukhvalov and M. I. Katsnelson, Enhancement of chemical activity in corrugated graphene, *J. Phys. Chem. C* **113**, 14176 (2009).
 - [17] H. McKay, D. J. Wales, S. J. Jenkins, J. A. Verges, and P. L. de Andres, Hydrogen on graphene under stress: molecular dissociation and gap opening, *Phys. Rev. B* **81**, 075425 (2010).
 - [18] X. Gao, Y. Wang, X. Liu, T. L. Chan, S. Irle, Y. Zhao, and S. B. Zhang, Regioselectivity control of graphene functionalization by ripples, *Phys. Chem. Chem. Phys.* **13**, 19449 (2011).
 - [19] W. Liu, Y. H. Zhao, J. Nguyen, Y. Li, Q. Jiang, and E. J. Lavernia, Electric field induced reversible switch in hydrogen storage based on single-layer and bilayer graphenes, *Carbon* **47**, 3452 (2009).
 - [20] Z. M. Ao and F. M. Peeters, Electric field: a catalyst for hydrogenation of graphene, *Appl. Phys. Lett.* **96**, 253106 (2010).
 - [21] Z. M. Ao and F. M. Peeters, Electric field activated hydrogen dissociative adsorption to nitrogen-doped graphene, *J. Phys. Chem. C* **114**, 14503 (2010).
 - [22] Z. M. Ao, A. D. H. Nieves, F. M. Peeters, and S. Li, The electric field as a novel switch for uptake/release of hydrogen for storage in nitrogen doped graphene, *Phys. Chem. Chem. Phys.* **14**, 1463 (2012).
 - [23] Z. Wang, L. Philippe, and J. Elias, Deflection of suspended graphene by a transverse electric field, *Phys. Rev. B* **81**, 155405 (2010).
 - [24] J. H. Chen, W. G. Cullen, C. Jang, M. S. Fuhrer, and E. D. Williams, Defect scattering in graphene, *Phys. Rev. Lett.* **102**, 236805 (2009).

- [25] Z. H. Ni, L. A. Ponomarenko, R. R. Nair, R. Yang, S. Anissimova, I. V. Grigorieva, F. Schedin, P. Blake, Z. X. Shen, E. H. Hill, K. S. Novoselov, and A. K. Geim, On resonant scatterers as a factor limiting carrier mobility in graphene, *Nano Lett.* **10**, 3868 (2010).
- [26] M. Jaiswal, C. H. Y. X. Lim, Q. Bao, C. T. Toh, K. P. Loh, and B. Özyilmaz, Controlled hydrogenation of graphene sheets and nanoribbons, *ACS Nano* **5**, 888 (2011).
- [27] B. H. Kim, S. J. Hong, S. J. Baek, H. Y. Jeong, N. Park, M. Lee, S. W. Lee, M. Park, S. W. Chu, H. S. Shin, J. Lim, J. C. Le, Y. Jun, and Y. W. Park, N-type graphene induced by dissociative H₂ adsorption at room temperature, *Sci. Rep.* **2**, 690 (2012).
- [28] J. H. Chen, C. Jang, S. Adam, M. S. Fuhrer, E. D. Williams, and M. Ishigami, Charged-impurity scattering in graphene, *Nat. Phys.* **4**, 377 (2008).
- [29] D. S. Novikov, Numbers of donors and acceptors from transport measurements in graphene, *Appl. Phys. Lett.* **91**, 102102 (2007).
- [30] J. Takashiro, Y. Kudo, S. Kaneko, K. Takai, M. Kiguchi, T. Enoki, T. Ishii, and T. Kyotani, unpublished results.
- [31] A. A. Kaverzin, S. M. Strawbridge, A. S. Price, F. Withers, A. K. Savchenko, and D. W. Horsell, Electrochemical doping of graphene with toluene, *Carbon* **49**, 3829 (2011).
- [32] K. Kusakabe and G. K. Sunnardianto, unpublished results.
- [33] J. Katoch, J. H. Chen, R. Tsuchikawa, C. W. Smith, E. R. Mucciolo, and M. Ishigami, Uncovering the dominant scatterer in graphene sheets on SiO₂, *Phys. Rev. B* **82**, 081417 (2010).

Chapter 7

General conclusions

Graphene is a first isolated macroscopic two-dimensional crystalline material. The honeycomb arrangement of carbon atoms in graphene construct the unconventional electronic structure represented by the relativistic massless Dirac equation in the vicinity of the Dirac point. On cutting infinite graphene into small fragments, the edge state emerges at the energy of the Dirac point. The edge state is localized around zigzag-shaped edges and has localized spins due to the asymmetry of the bipartite sublattice. In addition, the high reactivity at graphene edges together with the sensitivity of the edge state to functional groups gives rise to the chances of incorporating the exotic physics in graphene and its edges with chemistry [1].

Traditional experimental studies on the edge state have employed nanographite-based samples that have abundant edges by nature, so that they have focused attention on magnetic properties originating from the edge state. However, there have been several drawbacks. Nanographite-based materials show definitely distinct characteristics in electron transport from graphene. Electronic properties in the vicinity of the Dirac point are of particular interest, but the Fermi energy of nanographite-based samples cannot be precisely tuned by means of, *e.g.*, backgate voltage, which is typically utilized in graphene studies. For chemical modification of edges, nanographite-based samples initially have edges randomly terminated by, *e.g.*, oxygen-containing groups, so that cleaning edges requires quite high temperature and decorating edges requires highly active chemical species, *e.g.*, F_2 . In contrast to these disadvantages of nanographite-based materials, making the edge state emerge in graphene is strongly advantageous, although experimental approaches are lacking. In this thesis, it has been examined how electronic phenomena originating from edges can be observed in graphene having artificial edges and whether the edge state actually emerges at the edges. Moreover, the method of chemically controlling the edge state has been explored.

The first scope of this thesis is to conclude what kind of nanostructure of graphene can have a large contribution of edges. For this objective, artificial nanofabrication by

electron-beam lithography and the following reactive oxygen etching was employed to fabricate 100-nm-sized antidot graphene samples. For comparison, graphene samples having atomic vacancies were prepared by means of 100-eV Ar^+ irradiation, which produces mostly single-atomic vacancies in the outermost layer. Under the hypothesis that the contribution of edges appears as scattering mechanisms of conducting carriers, the electrical conductivities of these samples were measured at low temperature under a magnetic field with the concentration of charge carriers tuned by a backgate voltage. Raman spectroscopy was also utilized to estimate electron scattering sources in these samples, indicating that the D band due to the intervalley scattering event significantly appeared for Ar^+ -irradiated samples, and that it was unexpectedly weak for antidot samples. The characteristics in the conductivities were discussed in terms of the position of the Fermi energy, which was successfully and precisely defined with respect to the Dirac point. Considering the results of the Raman measurements, the backgate-voltage dependences of the conductivities for antidot sample and Ar^+ -irradiated sample were fitted by the charged-impurity scattering regime and the vacancy-edge scattering regime, respectively, leading to nice agreements. In high magnetic fields, magnetic oscillations of the resistivity were observed only for antidot sample not for Ar^+ -irradiated sample. This fact supported the strong scattering by defects in Ar^+ -irradiated sample and the weak scattering by charged impurities in antidot sample. In addition, antidot sample showed unanticipatedly irregular dependence of the frequencies of the magnetic oscillations upon the backgate voltage. This finding suggests inhomogeneous distribution of charged impurities over a sample. In low magnetic fields, both samples showed steep reduction in the resistivity, which were attributed to the weak localization effect caused by scatterers. Characteristic scattering lengths were derived via theoretical fits for weak localization effect observed in low magnetic fields. The inter- and the intra-valley scatterings due to vacancies were effective for Ar^+ -irradiated sample, while the intra-valley scatterings by charged impurities were significant in antidot sample. Then, it has been concluded that dominant scattering sources in antidot samples and Ar^+ -irradiated samples are charged impurities and edges of vacancies, respectively, so that the contribution of the edge state can be expected in graphene with atomic vacancies. These results have been published [Y. Kudo, K. Takai, and T. Enoki, Electron transport properties of graphene with charged impurities and vacancy defects, *Journal of Materials Research* **28**, 1097–1104 (2013)],

and written in Chapter 4.

The second scope is to verify the emergence of the edge state over a macroscopic area of a sample surface upon the creation of atomic vacancies. In order to understand how the edge state contribution emerges upon creation of structural defects, the surface of graphite has been observed using near-edge X-ray absorption fine structure (NEXAFS) spectroscopy upon Ar^+ irradiation with various kinetic energies. The appearance of the edge state ingredient has been obviously observed as the lower-energy shoulder of the π^* peak upon 100 eV Ar^+ irradiation. As the kinetic energy of Ar^+ ions were stepwisely increased to 3 keV, the drastic changes in the π^* and the σ^* peaks were observed. The broadening of the π^* and the σ^* peaks indicates the mixing of π and σ states as a consequence of structural transformation into amorphous-like state. This fact means the involvement of sp^3 configurations into fully sp^2 -hybridized carbons in graphite. Given that the increase of sp^3 carbons decrease the concentration of conducting electrons, the observed blue shift of the π^* peak has been explained in terms of the reduction of the core-hole screening. Interestingly, the contribution of the edge state has appeared to remain even in the severely damaged amorphous-like state, which indicates the survival of substantial extent of the π -conjugation network in the present conditions. These results have been submitted [Y. Kudo, M. Kiguchi, J. Takashiro, K. Takai, and T. Enoki, Development of edge state on graphite surface induced by Ar^+ irradiation studied using near-edge X-ray absorption fine structure spectroscopy, *Carbon*, *in press* (2014), <http://dx.doi.org/10.1016/j.carbon.2014.01.067>], and written in Chapter 5.

By virtue of these studies, Ar^+ irradiation to graphene has appeared to be the most reliable method for the emergence of the edge state contribution over a single-layer graphene. In addition to this finding about geometrical structure of graphene having the edge state, artificial control of vacancy-decorating functional groups is expected to offer a way of tuning the electronic and the magnetic properties of the edge state. Therefore, the third scope of this thesis is set to establish a method for decorating the vacancies in Ar^+ -irradiated graphene, which should be applicable to various functionalizations. Hydrogenation was chosen as a beginning point. Electrical conductivity measurements were again employed in terms of backgate-aided control of carrier density, in anticipation of detecting evolutions in scattering behaviors. Hydrogenation process was performed *in-situ* by exposing Ar^+ -irradiated graphene samples to an H flow or H_2 . In addition to these

experiments, H₂ adsorption onto pristine graphene samples was also examined with an application of a backgate voltage during exposure to H₂. When a graphene sheet was hole-doped state by a backgate voltage during H₂ exposure, a considerable amount of electron donation was discovered. In contrast, backgate-aided electron-doped state did not show such electron donation. The amount of the electron donation was appeared to be controlled by a duration of exposure and an applied backgate voltage. Then, the electron-donating source has attributed to the adsorption of H₂. The presence of charge transfer excludes the physisorption. The high reaction barrier omits the dissociative chemisorption. Thus, a non-dissociative chemisorption is a possible state of H₂ on graphene. What strengthens the bonding between H₂ and graphene is considered to be leakage of electric fields and structural disorders. Apart from the case of pristine graphene, when an H flow was exposed to Ar⁺-irradiated graphene, a quite large amount of electron donation was observed. The amount per a vacancy has been estimated as 0.6*e*. In contrast, H₂ exposure to Ar⁺-irradiated graphene did not show a significant feature of electron donation. According to a theoretical calculation, the charge transfer effect occurs in the C–H bond at a vacancy in graphene, as much as 0.5*e* per a vacancy. However, it also states that the transferred electrons are unlikely to be conducting. Thus, it has appeared that the case of H₂ exposure agrees with the theoretical results. It has been concluded that backgate-controlled H₂ adsorption onto the surface of graphene may open a way of utilizing graphene as hydrogen storage material, and that hydrogenation of vacancies in graphene can be performed by exposing to H₂. Moreover, this simple method is probably applicable to other gas species. These results have been written in Chapter 6. To be validated, more detailed experimental and theoretical effort is strongly requisite, which can precisely track the hydrogen adsorption reaction pathways.

To be summarized, the author has succeeded to verify the carrier scattering sources in artificial nanostructured graphene and graphene having randomly distributed atomic vacancies as inevitably involved charged impurities and edges of vacancies, respectively. Furthermore, the author has succeeded to confirm the emergence of the edge state over a wide area upon creation of vacancies by means of X-ray absorption spectroscopy. Finally, the author has suggested the creation of atomic vacancies in graphene immediately followed by molecular exposure as a method of artificially decorating edges with various functional groups. The author hopes that these discoveries contribute to the fundamental

understanding and future application of the edge state in graphene.

Perspective

The difficulty in experimental studies on the edge state of graphene can be attributed to the difficulty of creating zigzag-shaped edges in a graphene. There has been no method that can provide selectively a significant number of zigzag edges into a graphene sheet, although several recent progresses are hopeful [2,3].

This thesis has revealed that the edge state (*i.e.*, a significant amount of zigzag edges) can be emerged by ion irradiation to graphene, and that chemical tuning of the edge state will be possible by arbitrary functional groups bound to the edge carbon atoms. Ion-irradiated graphene samples can be investigated by means of electrical conductivity measurements with the Fermi energy controlled precisely by a gate voltage. Thus, one can examine scattering properties of conduction electrons by localized electronic spins of the edge state in terms of, *e.g.*, the Kondo effect [4]. Here, because the edge-state spins are strongly affected by functional groups attached to the edge carbons, intentional functionalization is crucially requisite. As supposed by this thesis, the creation of atomic vacancies and immediately following exposure of gaseous agents will lead to arbitrary functionalization of atomic vacancies, so that edge-state properties with arbitrary functional groups can be studied. This finding in this thesis needs to be further confirmed by experimental characterization of chemical structures of decorated vacancies with various functional groups upon various reaction conditions. Local probe techniques, *i.e.*, STM and AFM, can answer to this point. Of course, theoretical calculations are also going to work indispensably for this objective. As a consequence, electrical conductivity measurements of graphene having arbitrarily decorated vacancies, of which atomically resolved structures can be validated by STM/AFM and theoretical approaches, are expected to elucidate the electron scattering mechanisms by the edge-state spins.

In close relation to this topic, the size of vacancy and an interaction between vacancies are interesting. It is generally recognized that irradiation of low-energy ions creates single-atomic vacancies. Enlarging the atomic vacancies increases considerably the ratio of the edge carbon atoms to the interior ones, so that the electron transport

property is likely to change significantly with respect to that in graphene having single-atomic vacancies. As an example, the repetition of oxidation and thermal decomposition can be considered. An exposure of Ar^+ -irradiated graphene to oxygen leads to the attachment of the carbonyl ($>\text{C}=\text{O}$) and the hydroxyl ($-\text{OH}$) groups to vacancies as the majority. These oxygen-containing functional groups can be removed with the carbon atoms by heating up to $\sim 1000^\circ\text{C}$. The repetition of O_2 exposure and heating may be utilized as atom-by-atom etching method of vacancies. Regarding an interaction between vacancies, on the other hand, when two atomic vacancies are sufficiently close to each other, an overlap of wave functions is expected as in the case of narrow zigzag nanoribbons [5]. It will be an attractive and important theme how the interaction between vacancies changes depending on distance, functional groups, and so on.

For the further advances, it should be again stressed that the accurate definition of edge structures is necessary. For this purpose, STM or AFM apparatus is indispensable. Then, it needs to be coupled with other measurement methods. As an example, scanning gate microscopy (SGM) can be considered. Topinka *et al.* employed AFM technique for the SGM experiment [6,7]. The sample was a GaAs-based two-dimensional electron system having a nanostructure of a quantum point contact (QPC). Topinka *et al.* examined the conductivity of the QPC sample as a function of the position of the metal-coated cantilever with tuning the potential of the cantilever. The biased cantilever works as a scattering potential. The magnitude of the reduction of the conductivity depends on the position of the biased cantilever. When the cantilever locates on a conduction path, the conductivity significantly decreases, and vice versa. Consequently, the path of conducting electrons can be visualized with a resolution of ~ 20 nm. The essential advantages of SGM for studying the edge state of graphene are the abilities of determining the edge structure and applying a potential with an arbitrary strength on an arbitrary position. One of ideal experiments can be the following. An ion-irradiated graphene field-effect device is prepared. The conductivity can be measured in terms of backgate voltage, which controls the Fermi energy homogeneously over the entire sample. Then, focusing attention on an atomic vacancy having the edge state, the biased cantilever can modify the edge state only at the atomic vacancy with the other edges unchanged. Thus, the interaction between the single edge state and conducting electrons are consider to be examined.

Although these ideas are extremely challenging at present, the author strongly believe

that they will bring invaluable understanding on the edges of graphene. The author again sincerely hopes that this thesis will give contributions to forthcoming advances in the science of graphene.

References in Chapter 7

- [1] T. Enoki and T. Ando, Physics and chemistry of graphene: graphene to nanographene, *Pan Stanford publishing* (2013).
- [2] L. Xie, L. Jiao, and H. Dai, Selective etching of graphene edges by hydrogen plasma, *J. Am. Chem. Soc.* **132**, 14751 (2010).
- [3] Z. Shi, R. Yang, L. Zhang, Y. Wang, D. Liu, D. Shi, E. Wang, and G. Zhang, Patterning graphene with zigzag edges by self-assembled anisotropic etching, *Adv. Mater.* **23**, 3061 (2011).
- [4] J. H. Chen, L. Li, W. G. Cullen, E. D. Williams, and M. S. Fuhrer, Tunable Kondo effect in graphene with defects, *Nat. Phys.* **7**, 535 (2011).
- [5] K. Wakabayashi, M. Fujita, H. Ajiki, and M. Sigrist, Electronic and magnetic properties of nanographite ribbons, *Phys. Rev. B* **59**, 8271 (1999).
- [6] M. A. Topinka, B. J. LeRoy, S. E. J. Shaw, E. J. Heller, R. M. Westervelt, K. D. Maranowski, and A. C. Gossard, Imaging coherent electron flow from a quantum point contact, *Science* **289**, 2323 (2000).
- [7] M. A. Topinka, B. J. LeRoy, R. M. Westervelt, S. E. J. Shaw, R. Fleischmann, E. J. Heller, K. D. Maranowski, and A. C. Gossard, Coherent branched flow in a two-dimensional electron gas, *Nature* **410**, 183 (2001).